Faculty of Engineering
Imperial College London

Microstructural Analysis of Hydride Precipitation in Zirconium Alloys

Saïd El Chamaa

Supervisors: Dr Catrin Mair Davies and Dr Mark R. Wenman

A thesis submitted in part fulfilment of the requirements for the degree of
Doctor of Philosophy
in the Faculty of Engineering at Imperial College London, 2020

Declaration

I hereby declare that this thesis and the work reported herein was composed by and originated entirely from me. Information derived from the published and unpublished work of others has been acknowledged in the text and references are given at the end of thesis.

Copy Right Statement

The copyright of this thesis rests with the author. Unless otherwise indicated, its contents are licensed under a Creative Commons Attribution-Non Commercial-No Derivatives 4.0 International Licence (CC BY-NC-ND).
Under this licence, you may copy and redistribute the material in any medium or format on the condition that; you credit the author, do not use it for commercial purposes and do not distribute modified versions of the work.
When reusing or sharing this work, ensure you make the licence terms clear to others by naming the licence and linking to the licence text.
Please seek permission from the copyright holder for uses of this work that are not included in this licence or permitted under UK Copyright Law.

Abstract

Zirconium alloy cladding and structural materials are central to the structural integrity of nuclear fuel pins as well as dry storage of spent fuel rods. However, zirconium alloys are susceptible to hydrogen pick-up in the reactor environment and its operation lifetime can be severely compromised by a hydride embrittlement mechanism. In this project, the effects of microstructurally local stress raisers on hydride precipitation, in Zr-4 and commercially pure zirconium, such as second phase particles (SPPs) and grain boundaries (GBs) were studied in unloaded samples and ones containing long range stress concentration features (SCFs) such as loaded notches. In unloaded Zr-4 and commercially pure Zr, quantification of hydride precipitates as a function of grain boundary density and SPP content, show that for smaller grain specimens, there was a higher proportion of inter-granular hydrides, relative to intra-granular hydrides, due to the higher GB density. But, as the grains were grown in size to produce blocky-α microstructures, the proportion of intra-granular hydrides increased; this effect was slightly more observed for Zr-4 specimens with a higher SPP content than in commercially pure Zr. Results also show that not all GBs are favourable sites for hydride precipitation, an observation attributed to the different energy at GBs between grains of different crystallographic orientations.

Further studies relating to the microstructural effects on hydride precipitation, were then performed on as-received and blocky-α Zr-4 microstructures after undergoing three thermomechanical cycles at a maximum temperature of 350°C and at loads ranging between 2 and 8 MPa$\sqrt{}$m. Thermomechanical cycling of Zr-4 'V' (1 mm notches with 45° flank angle and 50 µm root radius) and 'U' (1 mm notches with 700 µm root radius) notched specimens showed that the microstructure interacts with stresses at notch regions to produce a higher hydride number density and hydride area fraction than in the specimen bulk. Furthermore, results show that blocky-α Zircaloy-4 specimens showed no hydride reorientation at all applied loads and the increase in hydride number density from the bulk towards the notches in blocky-α Zr-4, was found to be lower than that in as-received Zr-4 specimens. Hydride quantification results can be used to parameterise predictive hydride embrittlement numerical and analytical models with microstructural data that relate to hydride precipitation sites around different notch acuities.

Finally, a method of incorporating microstructural effects into a finite element model was introduced via a computational framework that incorporates atomic scale anisotropy through elastic dipole tensors. A crystal plasticity polycrystalline finite element model was then employed to provide computational insights into the effects of plasticity and polycrystallinity on the steady state hydrogen distribution profiles in blocky-α microstructures. Results show that the plastic zone and the effective plastic strain in blocky-α grains are highly dependent on the crystallography of the notch tip grain. Plasticity was found to reduce the hydrostatic stress and deplete hydrogen concentration in hard crystals ahead of 'V'

and ‘U’ notch geometries. Grain boundaries were also found to have an effect on hydrostatic stress distribution that in-turn effects hydrogen concentration profiles and therefore hydride precipitation. Results between model and experimental blocky-α micrograph were found to be in a good agreement, as hydride precipitates can be seen at GBs of large hydrostatic stress from the model and vice versa.

A key outcome of the project will be to quantify and qualify hydride precipitation DHC models that can be used to support industrial safety assessments.

Acknowledgements

I would first like to thank my supervisors Dr Catrin M Davies and Dr Mark R Wenman of Imperial College London for their constant support and guidance. I also would like to thank the EPSRC and Rolls-Royce for their support and supervision.

I must express my very profound gratitude to my family and friends for providing me with unfailing support and continuous encouragement throughout my years of study and through the process of researching and writing this thesis. This accomplishment would not have been possible without them. Thank you.

To my family and friends,

Contents

List of Tables **ix**

List of Figures **xviii**

Nomenclature **xix**

1 Introduction **1**
1.1 Background . . . 1
1.1.1 Hydride Precipitation in Zr . . . 1
1.2 Nuclear Power for Electricity Generation . . . 2
1.2.1 Overview of Fission Reactions . . . 2
1.2.2 Fission Reactor Technology . . . 3
1.3 Zirconium in the Nuclear Industry . . . 6
1.3.1 Development of the Zircaloys™ . . . 7
1.3.2 Alloying Addition and Grain Size Effects . . . 8
1.3.3 Corrosion and H Embrittlment of Zr alloys . . . 9
1.4 Research Aims and Objectives . . . 11
1.5 Publications . . . 12
1.6 Conferences . . . 12

2 Literature Review **14**
2.1 Outline . . . 14
2.2 Crystallography . . . 14
2.3 Texture Evolution . . . 15
2.4 Elastic Properties . . . 16
2.5 Plastic Deformation in HCP Crystals . . . 18
2.6 Mechanical Properties of Zr Alloys . . . 21
2.7 Grain Growth in Zirconium Alloys . . . 23
2.7.1 Abnormal Grain Growth . . . 24
2.7.2 Grain Growth *via* Annealing . . . 25
2.7.3 Second Phase Particles and Grain Growth . . . 26
2.8 Hydrogen Embrittlement . . . 28
2.8.1 Hydrogen Ingress . . . 28
2.8.2 Hydrogen diffusion in Zr . . . 31
2.8.3 Solubility . . . 32
2.8.4 Hydrogen Interstitial and Diffusion . . . 40
2.9 Hydrides in Zirconium . . . 43
2.9.1 Phases in Zr . . . 43
2.9.2 ZrH_x Morphology and Orientations . . . 43
2.9.3 Hydride Precipitation Sites . . . 45
2.9.4 Mechanical Properties of zirconium hydrides . . . 46

2.10 Hydride Reorientation . . . 48
2.10.1 Conditions . . . 48
2.11 Delayed Hydride Cracking (DHC) . . . 50
2.11.1 DHC Initiation . . . 53
2.12 Hydride Precipitation Models . . . 54
2.13 Summary . . . 55
2.13.1 Research Strategy . . . 56

3 Experimental Methodology 58
3.1 Introduction and Objectives . . . 58
3.2 Metallographic Characterisation Techniques of As-received and Grain Size Enhanced Zircaloy-4 and Zircadyne-702 . . . 59
3.2.1 Optical Microscopy . . . 59
3.2.2 Scanning Electron Microscopy . . . 59
3.2.3 Electron Back-scatter Diffraction . . . 60
3.3 Mechanical Properties Characterisation . . . 63
3.3.1 Hardness Testing . . . 64
3.4 Electro-chemical Hydrogen Charging . . . 65
3.4.1 Hydride and SPP Characterisation in Non-Cycled Samples . . . 67
3.5 Thermo-mechanical Testing . . . 71
3.5.1 Sample Preparation . . . 71
3.5.2 Mechanical Cycle . . . 74
3.5.3 Thermal cycle . . . 75
3.6 Choice of Thermo-mechanical Cycling Parameters . . . 77
3.6.1 Applied Load . . . 77
3.6.2 Applied Temperature . . . 77
3.6.3 Hydrogen Concentration . . . 78
3.7 Hydride and SPP Characterization and Quantification . . . 78

4 Computational Methodology 80
4.1 Finite Element Modelling of Mechanical Loading . . . 80
4.1.1 Boundary Conditions . . . 80
4.1.2 Stress Analysis . . . 81
4.1.3 Hydrogen Diffusion Modelling . . . 84

5 Hydride Precipitation Sites – Microstructural Hierarchy 87
5.1 Outline . . . 87
5.2 Introduction . . . 87
5.3 Microstructural Characterisation . . . 89
5.3.1 Zr-4 . . . 89
5.3.2 Zr-702 . . . 94
5.4 SPP Characterisation . . . 96
5.5 Mechanical Characterisation . . . 101
5.5.1 Zr-4 and Zr-702 Mechanical Properties . . . 101
5.6 Hydride Quantification and Discussion . . . 103
5.7 Conclusions . . . 111

6 Quantification of Stress-driven Hydride Precipitation in As-received and 'Blocky-α' Zr-4 Microstructures 113
6.1 Outline . . . 113
6.2 Introduction . . . 113

6.3 Results and Discussion . . . 116
6.3.1 Microstructure . . . 116
6.3.2 Hydride Distribution . . . 117
6.3.3 Hydride Quantification: As a function of K . . . 118
6.3.4 Hydride Quantification at $K = 8$ MPa$\sqrt{\text{m}}$: As a function of grain boundary and SPP density . . . 126
6.3.5 Hydride Quantification at Twins . . . 128
6.3.6 Discussion of Hydride Nucleation Sites Hierarchy . . . 130
6.4 Conclusions . . . 133

7 Computational Stress Analysis of Notch-Tip Hydrogen Profiles in Zr-4 134
7.1 Outline . . . 134
7.2 Introduction . . . 135
7.3 Modelling Approach and Setup . . . 137
7.3.1 Stress State of Notched Zirconium . . . 138
7.3.2 Stress Analysis . . . 139
7.3.3 Atomistic-to-Continuum Coupling . . . 142
7.4 Results . . . 144
7.5 Discussion . . . 144
7.6 Conclusions . . . 147
7.7 Analysis of Anisotropic Stress-Driven Hydrogen Equilibrium Profiles using a Crystal Plasticity Model . . . 149
7.8 Crystal Plasticity Modelling Incorporating Atomistic Analysis . . . 149
7.8.1 CPFE Model Setup . . . 150
7.9 Results . . . 151
7.9.1 Hydrogen Profiles in Monocrystalline Structures . . . 151
7.9.2 Hydrogen Profiles in Polycrystalline Structures . . . 153
7.10 Thermomechanical Cycling Effect on Hydrogen Concentration . . . 157
7.10.1 Computational Results versus Experimental Hydride Distribution . . . 157
7.11 Discussion . . . 157
7.12 Conclusions . . . 160

8 Overall Discussion 161
8.1 Hydride Precipitation Sites in Zr-4 and Commercially Pure Zr . . . 161
8.2 Hydride Precipitation Sites in Loaded Zr-4 . . . 164
8.3 Microstructural Incorporation in Hydrogen Models . . . 165

9 Overall Conclusions and Future Work 167
9.1 Future Work . . . 168
9.1.1 Quantification of Hydride Precipitation Sites . . . 168
9.1.2 Hydride Precipitation Sites in Thermomechanically Cycled Zr-4 Specimens . . . 168
9.1.3 Hydrogen Stress Driven Diffusion Modelling Incorperating Microstructural hcp Anisotropy . . . 169

10 Appendix A 173
10.1 Hydride Precipitation near Second Phase Particles; SEM + EDX analysis . . . 173
10.2 Full Test Matrix . . . 182
10.3 Fortran Codes Used For Atomistic to Continuum Scale Coupling . . . 183
10.3.1 Anisotropic - Prismatic . . . 183
10.3.2 Anisotropic - Basal . . . 184
10.4 Chemical Analysis Certificates of Zr-4 and Zr-702 . . . 185

10.5 Polycrystal Plasticity Modeling 187
10.5.1 Crystal Plasticity Method 187

List of Tables

1.1 List of common commercial reactors with their corresponding features [1]. 6
1.2 The comparison of the approximate macroscopic cross section and UTS for some metals with respect to zirconium [1]. 7
1.3 Composition of the Zircaloy family containing Sn and α/β Zr-Nb alloys, Zirlo™ and M5™ (alloying elements in wt.%). Adapted from [2, 3]. 8

2.1 Elastic constants and Young's moduli for mono crystal pure zirconium in different crystal orientations at room temperature [4] 18
2.2 Typical yield strength values for cold worked Zr-4 and Zr-2 alloys [5]. 23
2.3 Typical yield strength values for cold worked Zr-2.5Nb CANDU pressure Tubes [5]. . . 23

3.1 The chemical composition of Zr-4 and Zr-702. The full chemical composition of both materials is presented in Appendix A, measured by AMG Analytical ltd. 58
3.2 Test matrix highlighting notch geometries, applied stress intensity factor and microstructural variables. 73
3.3 List of parameters used for hydride and SPP quantification. 79

5.1 The chemical composition of Zr-4 and Zircadyne-702. (Zr: balance). The full chemical composition of both materials is presented in Appendix A, measured by AMG Analytical ltd. 88
5.2 The SPP number density (ρ_{SPP}) in Zr-4 and Zr-702 samples with as-received grain sizes (l_{G}<30µm). The standard deviation (SD) is also presented. 98
5.3 Tensile properties of Zr-4 and Zr-702 in the RD and TD, as-received grain size, at 20°C and 350°C. 102

6.1 Macro-hydride number density and intra-granular hydride fraction after 3 thermo-mechanical cycles at K= 8 MPa$\sqrt{\mathrm{m}}$ in as-received and blocky-α Zr-4 in the bulk and around the 'V' and 'U' notches. 126

7.1 List of parameters and variables required for this multiscale stress analysis. Adapted from [6]. 139

10.1 Test matrix for specimens with C_H of ∼120 wppm, thermomechanically cycled 3 times. 182
10.2 Test matrix for specimens with C_H of ∼120 wppm, thermomechanically cycled 3 times. Specimens cycled at K= 2 where recycled at K= 4 and 6 182

List of Figures

1.1 A schematic representation of a chain nuclear fission reaction which begins with a neutron colliding with an fissionable atomic nucleus and forcing it into a state of instability [7]. 3
1.2 Schematic of a nuclear power plant A component-by-component breakdown of a PWR nuclear reactor design [8]. 4
1.3 Schematic diagrams of a PWR fuel rod and radial temperature profile in the fuel rod. Adapted from [7]. 5
1.4 Corrosion kinetics curve of zirconium alloy cladding in the PWR core. First and second transitions are shown by dotted lines. Adapted from [9]. 11

2.1 (a) Unit cell structure of the HCP α crystal structure with (0001) basal planes, (b) a 2D scheme of close packed layer of A with positions where the B or C layers may be stacked and (c) the B layer now on top of an A layer. Adapted from [9]. 15
2.2 (a) Schematic of the hot rolling process during Zircaloy fabrication. (b) A simplified pole figure corresponding to the (0002) basal plane texture of Zircaloy-4 rolled and annealed sheet [10, 11]. 17
2.3 Texture of two zirconium alloys, namely (a) Zr-4 and (b) commercially pure zirconium (Zr-702), with pole figure colour scale in multiples of random texture. The average grain size of >1400 grains measured by EBSD of Zr-4 is 15 µm and of Zr-702 is 30 µm. Adapted from [12]. 17
2.4 Polar plot (a) of Young's modulus versus sample orientation and (b) shows the corresponding {0002} pole figure in the transverse (T) and longitudinal (L) directions of the Zr tube samples. Adapted from [4, 13]. 19
2.5 Main crystallographic planes of the HCP crystal lattice. (a) Purple: basal planes {0001}. (b) Blue: prismatic plane type I $\{10\bar{1}0\}$. Red: pyramidal plane type I order I $\{10\bar{1}1\}$. (c) Green: prismatic plane type II $(11\bar{2}0)$. Yellow: pyramidal plane type II order I $(11\bar{2}0)$. Adapted from [9]. 20
2.6 (a) Schematic of a twin boundary, whereby circles represent atoms in 2D planes that can undergo various twinning modes (b) in HCP zirconium. Adapted from [7, 9]. . . . 22
2.7 (a) A scheme of the Zr tube cladding radial texture along with 3D micrographs showing re-orientation of hydrides in Zircaloy-4 cladding of 230 wppm from (b) as-hydrided to (c) after eight thermal cycles. Adapted from [14]. 24
2.8 IPF EBSD maps showing an example of a lower (a) bimodal grain size distribution than a higher (b) one. The arrow in (b) shows an island grain with an as-received grain size inside a large grain. Adapted from [15]. 26
2.9 The hydrostatic stress field generated by a coherent β-Nb SPP, modelled using a 2D discrete dislocation plasticity simulation during SPP precipitation, that happens at high temperature during alloy processing [16]. 27
2.10 The absorption of hydrogen by-product due to oxidation, into Zr-4. Adapted from [7, 17]. 29
2.11 Tetragonal (a) and monoclinic (b) lattice unit cells along with (c) an EBSD phase map showing monoclinic ZrO_2 in green, tetragonal ZrO_2 in red and zirconium metal in blue [18]. 31

2.12 Comparison of hydrogen diffusivity data for a range of Zr and Zr alloys in different conditions across a range of temperatures. The standard deviation of best-fit curves is ±15% for normal conditions and ±5% for transverse and longitudinal. Adapted from [7, 19]. 33
2.13 Compilation of terminal solubility data below 550°C for pure zirconium, Zircaloy-2 and Zircaloy-4. Adapted from [20]. 34
2.14 The hysteresis in the terminal solid solubility of hydrogen in Zircaloy-2 and Zircaloy-4 observed using differential scanning calorimetry, where ΔH_c is the difference in hydrogen concentration at a given temperature between the heat-up curve (blue) and the cool-down curve (red). Adapted from [21]. 35
2.15 Comparisons between $TSS_{d/p,irradiated}$ and $TSS_{d/p,unirradiated}$ for Zircaloy-2. Adapted from [7]. 37
2.16 Hydrogen solubility data for oxygen strengthened Zircaloy-4. Adapted from [21]. . . . 39
2.17 Interstitial sites in HCP crystals. The sites are defined by the centre of the polyhedra and triangle or by colored circles. Red corresponds to octahedral sites/faces and blue corresponds to terahedral ones. Adapted from [9]. 42
2.18 Zirconium-hydrogen phase diagram [22]. 44
2.19 Optical image (a) of a longitudinal section of Zr2.5%Nb highly textured pressure tube alloy containing ∼300 wppm, showing a clear macro-hydride precipitation in the circumferential-axial plane of the tube. The stacking of micro-hydrides to form macro-hydrides can be seen using TEM (b) that also shows the habit planes for both micro and macro-hydrides [23]. 45
2.20 Nominal stress/strain curves for the compressive deformation of $ZrH_{1.66}$ in temperatures ranging from 22 to 453 °C. Adapted from [24]. 47
2.21 Temperature-dependence of K_{IC} for δ-hydrides in pure zirconium and Zr-2.5%Nb. Adapted from [25]. 48
2.22 Number of cycles to DHC initiation as a function of the peak notch tip tensile stress. Adapted from [26]. 53

3.1 Useful SEM signals generated by electron–atom interactions. Secondary electrons (SE), back-scattered electron (BE) and X-rays are generated and detected by SE, BSE and EDX detectors. The electron volume interaction with atoms in shown in orange that reaches a depth of 5000 nm at an beam accelerating voltage of 20 keV. 61
3.2 Electron back-scattered diffraction patterns (EBSPs) (a) are shown for a polycrystalline Zircaloy-4 sample at a step size of 1.5 µm, with (b) generated bands, representing crystallographic planes, from the individual grain selected from (a) along (c) the corresponding orientation of the hcp crystal in that selected $-Zrgrain.$ 62
3.3 The dimensions of tensile (a) specimens used to determine the yield and tensile strength of Zr-4 and Zr-702 material. The RD and TD orientations of the tensile dogbone specimens is shown in the Zr-4 plate (b) along with the vacuum chamber (c) used for high temperature testing at 350°. 64
3.4 Relationship between hydriding time vs hydride layer for Zr-4 charging under a current density of 1 kA m^{-2}. The red dashed line, shows that hydriding Zr-4 for 24 hours produces a hydride layer thickness of 10 µm. Adapted from [22]. 66
3.5 Electro-chemical hydrogen charging set-up used to introduce hydrides in zirconium specimens; (a) the anode Pt mesh and the cathode Zr sample were spot welded onto Pt and Zr wires respectively. The attraction between H^+ ions and the electrons is shown in (b) resulting in the formation of an adhesive hydride layer at the negative electrode [27]. 68

3.6 (a) Optical micrograph of a 10-20 µm hydride layer, visible along the sample cross-section. The hydride layer, produced via electro-chemical hydrogen charging, diffuses (b) throughout the sample thickness showing alignment along the sample RD. 68
3.7 Polarised optical micrograph of as-received Zr-702 used for macro-hydride characterisation. 69
3.8 Blocky-α microstructure containing inter, intra and transgranular hydrides. The latter is considered to be in the same category as intragranular hydrides. 69
3.9 Image processing using the Fiji ImageJ software [28]. 70
3.10 (a) Orientations of samples with respect to the plate. The 'U' and 'V' notch geometries are shown in (b) and (c) where ρ represents the notch root radius with values of 700 µm and 50 µm respectively. (d) shows the four-point bending set-up whereby the upper fixed rollers and the lower loading rollers are shown in black circles with a diameter of 3 mm. 73
3.11 A scheme that shows the four-point bending rig whereby the distance between the loading rollers is half the distance between the upper rollers. 74
3.12 Convention used in definition of spatial coordinates for a notch where d is the distance from position $\rho/2$. 76
3.13 Profiles of the thermal and stress intensity cycles at a K= 8 MPa$\sqrt{}$m for as-received Zr-4 specimens. 76

4.1 Images of the 2D mesh and boundary conditions for the (a)(b) 'V' and (c)(d) 'U' notch models. P corresponds to the applied force and u_x corresponds to the displacement in the x direction. 82
4.2 Images of (a)(b) the 3D mesh for the 'V' notch with boundary conditions. 82
4.3 Comparison of the σ_{xx} stresses at K= 8 MPa$\sqrt{}$m at the 'V' notch tip from the 2D (a) plane stress and (b) plane strain models with the (c) surface and (d) mid-plane of the 3D model. 83
4.4 (a) 'V' notch triaxiality ($\sigma_{Mises}/\sigma_{hyd}$) in comparison to (b) the 'U' notch distribution in plane stress conditions at K= 8 MPa$\sqrt{}$m. 83
4.5 (a) 'V' notch triaxiality ($\sigma_{Mises}/\sigma_{hyd}$) in comparison to (b) the 'U' notch distribution in plane strain conditions at K= 8 MPa$\sqrt{}$m. 84
4.6 'V' and 'U' notch triaxiality ($\sigma_{Mises}/\sigma_{hyd}$) at (a)(c) the surface and at (b)(d) the mid-plane of the 3D models at K= 8 MPa$\sqrt{}$m. 85
4.7 'V' and 'U' notch hydrostatic stress distribution at (a)(c) the surface and at (b)(d) the mid-plane of the 3D models at K= 8 MPa$\sqrt{}$m. 86

5.1 Secondary electron micrographs of Zr-4 samples with (a) as-received small grains (1753 grains with an average size of ∼15 µm) and (b) annealed large grains (59 grains with an average size of 411 µm). 89
5.2 Inverse pole figure, IPF$_{RD}$ (a) and IPF$_{ND}$ (b) revealing the as-received Zr-4 equiaxed grain structure. Their corresponding pole figures (c) highlight the expected Zr-4 rolling texture. (step size: 1 µm, accelerating voltage: 20 keV and number of grains analysed: 1582). 90
5.3 Maps of IPF$_{RD}$ (a) and IPF$_{ND}$ (b) revealing the blocky-α Zr-4 grain structure. Their corresponding pole figures (c) highlight the apparently textureless microstructure. (step size: 2 µm, number of grains analysed: 59). 91
5.4 Grain average misorientation (GAM) maps of (a) as-received Zr-4 sample and (b) blocky-α grains sample, whereby the misorientation angle ranges between 0.0° (blue) to 5.0° (red) as shown in the colour scale bar. 92
5.5 Grain orientaion spread of as-received (a) and blocky-α (b) Zr-4 specimens. 93

5.6 Maps of IPF_{RD} (a) and IPF_{ND} (b) revealing the as-received Zr-702 equiaxed grain structure. Their corresponding pole figures (c) highlight the expected Zr-4 rolling texture. (step size: 1 µm, number of grains analysed: 929). 94
5.7 Maps of IPF_{RD} (a) and IPF_{ND} (b) revealing the blocky-α Zr-702 grain structure. Their corresponding pole figures (c) highlight the textureless microstructure. (step size: 2 µm, number of grains analysed: 148). 95
5.8 Grain average misorientation (GAM) maps of (a) as-received Zr-702 sample and (b) blocky-α grains Zr-702 sample, whereby the misorientation angle ranges between 0.0° (blue) to 5.0° (red) as shown in the colour scale bar. 96
5.9 (a) Back-scattered SEM image of as-received Zr-4 specimen taken at ×2.5k magnification showing the bright zirconium background and the relatively dark particles. A small region from (a) was magnified to ×12.5k to show the substructure of the particles that were found to have small darker regions within. Binary images of (a) and (b) used for SPP number density and size distribution analysis are shown in (c) and (d), respectively. The arrow in (c) highlights a hollow particle that is taken into account during analysis while the noise in (d) is not considered in the analysis. 98
5.10 BS SEM images at a magnification of 10,000× of (a) as-received Zr-4 (b) grain growth annealed Zr-4. Their corresponding thresholded binary images are shown in (c) and (d) that highlight the size and number density reduction of SPPs from as-received to blocky-α microstructures. 99
5.11 The number of second phase particles (SPPs) per μm^2 in blocky-α grain specimens of grain sizes >250 µm. Error bars show the standard deviation (SD) of SPP number density (ρ_{SPP}). 99
5.12 The SPP area distribution in (a) as-received Zr-4 with l_G= 15 µm and (b) blocky-α specimen with l_G= 770 µm. The median SPP area in as-received samples was found to be 0.15 μm^2 and 0.22 μm^2 in recrystallised ones. 100
5.13 The SPP area distribution in (a) as-received Zr-702 with l_G= 32 µm and (b) blocky-α specimen with l_G= 602 µm. The median SPP area in as-received samples was found to be 0.14 μm^2 and 0.29 μm^2 in blocky-α microstructures. 100
5.14 Tensile testing stress-plastic-strain curves for Zr-4 and Zr-702 as-received grain size at two different temperatures for the rolling direction (RD) and transverse direction (TD) of plate. 101
5.15 The experimental Vickers hardness number (VHN) for (A) as-received and (B) blocky-α grained (B) Zr-4 and Zr-702 is shown in blue columns. The experimental 0.2% yield strength is shown for as-received materials while a theoretical yield based on the Hall-Petch equation is shown for all specimens. NB the 0.2% yield strength for blocky-α specimens was not experimentally produced. 103
5.16 (a) Secondary electron micrographs of Zr-4 in the RD-TD plane (average grain size ∼15 µm). Blocky-α grains containing hydrides in Zr-4 are shown in (d). Binary images of the micrographs used for hydride analysis are respectively shown (b) and (e) with noise and (c) and (f) without noise, revealing the black macro-hydride features. The arrow in (a) shows an inta-granular hydride in as-received Zr-4 while arrows 1, 2 and 3 in (d) show twin boundary hydrides (twins produced during grinding above 15 N), intra-granular hydrides and inter-granular hydrides respectively. 104
5.17 Hydride distributions parameterised by grain size and SPP content, as represented by the proportion of intra-granular hydrides for Zr-702 and Zr-4 specimens of differing average grain sizes. Vertical error bars show the standard deviation of the proportion of intra-granular hydrides. The graph shows two regions split by a vertical dashed line, whereby region (A) is for as-received grain sizes and (B) for specimens containing blocky-α grains. 105

5.18 Types of intra-granular hydrides; Arrow (1) shows two macro-hydrides precipitating fully inside a grain and decorating crystal planes. (2) and (3) show macro-hydrides precipitating intragranually in one grain and crossing the GB into another. In the case of (2) there is a clear change of hydride orientation as the hydride crosses the GB from one grain to another. Arrow (4) shows a similar hydride behaviour but with a small degree of intergranular precipitation when crossing grains, also with a change of hydride orientation after crossing. And finally, arrow (5) shows an intra-granular hydride that does not cross into another grain, instead continues to precipitate at the GB. 106
5.19 Micro-hydride precipitates at and around SPPs (a) in as-received Zr-4. The corresponding binary image (b) shows circular black SPPs surrounding lenticular micro-hydrides that appear to stack on top of each other. EDX maps of Fe (c) and Cr (d) atoms give a good indication of the SPP location. 107
5.20 Macro-hydride precipitates at and around SPPs (a) in blocky-α Zr-4. The corresponding binary image (b) shows circular black SPPs surrounding large macro-hydrides. EDX maps of Fe (c) and Cr (d) atoms give a good indication of the SPP location. 108
5.21 Macro-hydride precipitates at and around SPPs (a) in blocky-α Zr-4. The corresponding binary image (b) shows circular black SPPs surrounding macro-hydrides. EDX maps of Fe (c) and Cr (d) atoms give a good indication of the SPP location. 109
5.22 The macro-hydride area distribution in Zr-4 for an as-received sample with $l_{\mathrm{G}} \simeq$15 µm and an enhanced grain size sample with $l_{\mathrm{G}} \simeq$720 µm. The modal area of hydrides in as-received Zr-4 is 8 µm^2 and 230 µm^2 in blocky-α specimen. 110
5.23 The macro-hydride area distribution in Zircadyne-702 for an as-received sample with $l_{\mathrm{G}} \simeq$30 µm and an enhanced grain size sample with $l_{\mathrm{G}} \simeq$800 µm. The modal area of hydrides in as-received Zr-702 is 28 µm^2 and 100 µm^2 in blocky-α specimen. 111

6.1 A schematic showing the terminal solid solubility of precipitation and dissolution of hydrogen in Zr versus temperature in K. 116
6.2 Secondary electron micrograph of V-notch region of electro-polished, non-hydrided Zr-4 (a) as-received specimen and (b) recrystallised specimen containing 'blocky-α' grains. . 117
6.3 Map of IPF$_{RD}$ of a V-notched recrystallised Zr-4 specimen after thermo-mechanical cycling (a) containing 82 grains, whereby arrows labelled (1) show T1 mechanical twins and arrow (2) shows small grains due to abnormal grain growth. The grain size distribution (b) is shown for the recrystallised specimen shown in (a) that contains 'blocky-α' and some abnormal grains. 117
6.4 T1 twins in Zr grains with 85° misorientation between the <c> axes of the parent grain and the twin. 118
6.5 Thresholded optical images showing hydride precipitation in the bulk of (a) as-received and (b) blocky-α microstructure of a Zr-4 specimen on the ND-TD plane. 119
6.6 Thresholded images showing Zr-4 specimens in the TD-ND plane of the plate on the left flank of (a) the 'V' notch and (b) the 'U' notch specimen after 3 thermo-mechanical cycles at K= 8 MPa$\sqrt{}$m. 119
6.7 Thresholded images showing Zr-4 specimens in the TD-ND plane of the plate with (a) 'V' notch and (b) 'U' notch after 3 thermo-mechanical cycles at K= 8 MPa$\sqrt{}$m. . . . 120
6.8 The macro-hydride number density after three thermo-mechanical cycles with K ranging from 2 to 8 MPa$\sqrt{}$m in as-received Zr-4 in the bulk, around 'V' and around 'U' notched specimens. Error bars show the standard deviation in hydride number density. 121
6.9 FE prediction of hydrostatic stress profiles below 'V' and 'U' notch-tips for as-received Zr-4 at 350°C. 121
6.10 Hydrostatic stress profile around 'V' notches at (a) K= 2, (b) K= 4, (c) K= 6 and (d) K= 8 MPa$\sqrt{}$m. The box in (d) highlights the size of the enhanced hydrostatic stress notch tip region. 122

6.11 Hydrostatic stress profile around 'U' notches at (a) K= 2, (b) K= 4, (c) K= 6 and (d) K= 8 MPa$\sqrt{}$m. The box in (d) highlights the size of the enhanced hydrostatic stress notch tip region. 123
6.12 The macro-hydride number density after three thermo-mechanical cycles with K ranging from 2 to 8 MPa$\sqrt{}$m in blocky-α (l_G= 700-900 µm) Zr-4 in the bulk, around 'V' and around 'U' notched specimens. Error bars show the standard deviation in hydride number density. 124
6.13 SE SEM micrographs of a blocky-α specimen in the bulk (a) and at the notch-tip (b). 124
6.14 The intra-granular hydride number density (%) after three thermo-mechanical cycles with loads ranging from 2 to 8 MPa$\sqrt{}$m in (a) as-received (b) recrystallised (l_G= 700-900 µm) Zr-4 in the bulk, around 'V' and around 'U' notched specimens. Error bars show the standard deviation in intra-granular hydride fraction. 125
6.15 The hydride area fraction (%) after three thermo-mechanical cycles with loads ranging from 2 to 8 MPa$\sqrt{}$m in (a) as-received (b) recrystallised (l_G= 700-900 µm) Zr-4 in the bulk, around 'V' and around 'U' notched specimens. 125
6.16 The macro-hydride number density after three thermo-mechanical cycles K= 8 MPa$\sqrt{}$m in blocky-α Zr-4 in the bulk, around 'V' and around 'U' notched specimens. 127
6.17 Optical images showing blocky-α Zr-4 specimens with an average grain size (l_G) of 700-900 µm, containing 100-130 wppm, in the TD-ND plane of the plate with (a) 'V' notch and (b) 'U' notch after 3 thermo-mechanical cycles at K= 8 MPa$\sqrt{}$m. Arrows labelled (1) show twins containing macro-hydride precipitates within blocky-α grains. Arrows (2) and (3) show inter and intra-granular hydrides respectively at percentages of ∼30% and ∼70% respectively around the notches after cycling in comparison to a ratio of ∼40% and ∼60% respectively in the bulk. 129
6.18 Optical images showing blocky-α Zr-4 specimens with a grain size (l_G) of 700-900 µm, containing 100-130 wppm, in the TD-ND plane of the plate showing (a) bulk region of a 'V' notch specimen and (b) bulk region of a 'U' notch, after 3 thermo-mechanical cycles at K= 8 MPa$\sqrt{}$m. Arrows labelled (1) show twins containing macro-hydride precipitates within blocky-α grains. 129
6.19 (a) Thresholded optical image of a blocky-α thermo-mechanically cycled (×3) 'U' notch specimen. Mechanical T1 type twins shown were found to contain macro-hydride features. The area distribution of twin hydrides (b) shows the median at 270-300 µm^2, a value that is dependent on grain size. 130

7.1 The unit cell of hexagonal α-zirconium showing the distinct crystallographic planes. The anistropic properties of α-zirconium are attributed to its non-ideal c/a ratio of 1.593, which itself is fundamentally a consequence of its electronic structure. 136
7.2 Schematic breakdown of the multiscale stress analysis. Adapted from [6]. 138
7.3 σ_{xx} (MPa) distribution maps at notch-tips in Zircaloy-4 specimens at K= 8 MPa$\sqrt{}$m. All three notches have the same root radius $R = 50\,\mu$m but different flank angles (ϕ). (a) $\phi = 45°$. (b) $\phi = 30°$. $\phi = 20°$. 140
7.4 ϵ_{xx} (a)(c)(e) and ϵ_{yy} (b)(d)(f) distribution maps at notch-tips in Zircaloy-4 specimen at K= 8 MPa$\sqrt{}$m. (a, b) $\phi = 45°$. (c, d) $\phi = 30°$. (e, f) $\phi = 20°$. 141
7.5 A hydrogen interstitial occupying a tetrahedral site in hexagonal α-zirconium. The hydrogen anion forms three equivalent bonds with the zirconium atoms on the basal plane and a fourth nonequivalent bond with a zirconium atom along the transverse c-direction; the tetrahedral interstitial possesses a trigonal symmetry. Adapted from [6]. 143
7.6 The hydrogen concentration profile at the tip of a V-notch of root radius $R = 50\,$µm with flank angles of (a) 45° (b) 30° and (c) 20°, all at K= 8 MPa$\sqrt{}$m. The (x, y)-plane of the simulation cell is the basal plane. The dashed square highlights the notch-tip hydrogen enhanced region. 145

7.7 The hydrogen concentration profile at the tip of a V-notch of root radius $R = 50\,\mu m$ with flank angles of (a) 45° (b) 30° and (c) 20° all at $K = 8$ MPa$\sqrt{m}$. The (x, y)-plane of the simulation cell is the prism plane. 146
7.8 A 3D FE model (a), highlighting the displacement and loading boundary conditions, with a simplified loading configuration of four-point bending. A truncated quasi-2D plane stress model (b) which has a reduced microstructure embedded at the notch tip. The full model tensile stress distribution (c) on the bottom half sample is compared with the truncated model along path C-C' (d) [29]. 151
7.9 Effective plastic strain (a)(d), on a relatively hard monocrystal plane (prism), and its effect on hydrostatic stress (b)(e) and hydrogen concentration distribution (c)(f) at 'U' and 'V' notch tips at $K = 8$ MPa$\sqrt{m}$. The arrows in black highlight the depletion in σ_{hyd} and C_H ahead of notch tips due to plasticity. 152
7.10 Effective plastic strain (a)(d), on a soft monocrystal plane (basal), and its effect on hydrostatic stress (b)(e) and hydrogen concentration distribution (c)(f) at 'U' and 'V' notch tips at $K = 8$ MPa$\sqrt{m}$. 153
7.11 Blocky-α Sample 1 (a) and Sample 2 (b) loaded to the elastic stage t_e and plastic onset t_p (c). 154
7.12 The distribution profiles of the total strain component, ϵ_{11}, (a, b), the effective plastic strain, $\tilde{\epsilon}^p$, (c, d), the hydrostatic stress σ_{hyd} (e, f) and the hydrogen equilibrium hydrogen concentration (C_H), in notch tip blocky-α Sample 1 at the elastic stage t_e and plastic onset t_p. 155
7.13 The distribution profiles of the total strain component, ϵ_{11}, (a, b), the effective plastic strain, $\tilde{\epsilon}^p$, (c, d), the hydrostatic stress σ_{hyd} (e, f) and the hydrogen equilibrium hydrogen concentration (C_H), in notch tip blocky-α Sample 2 at the elastic stage t_e and plastic onset t_p. 156
7.14 Simulated hydrogen concentration (C_H) map (a) after three thermo-mechanical cycles of Sample 1, compared with its SEM micrograph (b). The hydrostatic stress (σ_{hyd}) distribution highlights the tensile and compressive regions that interact with hydrogen diffusion (c). The white line highlight the tensile GBs. The cycling profile and the time of which simulation parameters are chosen is shown in sub-figure (d). 158

9.1 Simulated micrographs of the notch-tip hydrogen profile as a function of the notch acuity. (a) corresponds to a 'V' notch geometry and (b) 'U' notch one [30]. 171
9.2 Simulated micrographs of notch-tip hydrogen profiles as a function grain size. (a) $l_G = 50\,\mu m$ and (b) $l_G = 200\,\mu m$ [30]. 171

10.1 SPPs in as-received Zr-4 (a) with EDX analysis of Zr (b), Fe(c) and Cr (d). 173
10.2 SPPs in hydrided as-received Zr-4 (a) with EDX analysis of Zr (b), Fe(c) and Cr (d) with its corresponding spectrum. 174
10.3 SPPs in as-received Zr-4 highlighting a vertical SPP precipitation RD pattern (a) with EDX analysis of Zr (b), Fe(c) and Cr (d) with its corresponding spectrum. 175
10.4 SPPs in hydrided as-received Zr-4 highlighting several vertical SPP precipitation RD pattern (a) with EDX analysis of Zr (b), Fe(c) and Cr (d) with its corresponding spectrum. 176
10.5 SPPs in blocky-α Zr-4 highlighting micro-hydride precipitation near SPPs (a) with EDX analysis of Zr (b), Fe(c) and Cr (d) with its corresponding spectrum. 177
10.6 SPPs in hydrided blocky-α Zr-4 highlighting micro-hydride precipitation near SPPs (a) with EDX analysis of Zr (b), Fe(c) and Cr (d) with its corresponding spectrum. 178
10.7 SPPs in blocky-α Zr-4 highlighting micro-hydride precipitation near SPPs (a) with EDX analysis of Zr (b), Fe(c) and Cr (d) with its corresponding spectrum. 179
10.8 SPPs in hydrided blocky-α Zr-702 highlighting micro-hydride precipitation near SPPs (a) with EDX analysis of Zr (b), Fe(c) and Cr (d) with its corresponding spectrum. . . 180

10.9 SPPs in blocky-α Zr-702 highlighting micro-hydride precipitation near SPPs (a) with EDX analysis of Zr (b), Fe(c) and Cr (d) with its corresponding spectrum. 181

Nomenclature

$[l_G]$	Average grain size [µm]
E	Energy [J]
$[H]$	Hydrogen concentration [wppm]

Greek Symbols

ζ	Trigonal hydride phase
γ	Face centered tetragonal hydride phase
δ	Face centered cubic hydride phase
ϵ	Face centered tetragonal hydride phase

List of Abbreviations

AGR	Advanced Gas-cooled Reactor
bcc	body centred cubic
bct	body centred tetragonal
BWR	Boiling Water Reactor
CANDU	CANada Deuterium Uranium
DHC	Delayed Hydride Cracking
VHN	Vickers Hardness Number
fcc	face centred cubic
fct	face centred tetragonal
hcp	hexagonal close packed
PWR	Pressurised Water Reactor
RBMK	Reaktor Bolshoy Moshchnosti Kanalnyy
VVER	Vodo-vodyanoi Energetichesky Reaktor
SEM	Scanning Electron Microscope

TSS Terminal Solid Solubility

UTS Ultimate Tensile Strength

$\langle$hkil$\rangle$ Family of directions

(hkil) Individual plane

[hkil] Individual direction

{hkil} Family of planes

Chapter 1

Introduction

1.1 Background

Zirconium alloys have been used in the nuclear industry as nuclear fuel cladding and structural materials due to their corrosion resistance, neutron transparency and reasonable mechanical properties. Zirconium alloy development has been progressing since the beginning of its introduction into the nuclear industry leading up to numerous current commercial grades. This project focuses on hydrogen embrittlement of the alloy, with the aim to quantitatively link hydride precipitation to microstructural features, thus enabling parameterisation of predictive models of hydrided microstructures for safety assessments.

1.1.1 Hydride Precipitation in Zr

The focus of this project is to study, quantify and if possible identify microstructural and stress concentration features that effect hydrogen diffusion and hydride precipitation in zirconium alloys. The study quantifies hydride precipitation and hydrogen concentration at a topological hierarchy of stress raisers classified as long range stress concentrating features such as volumetric flaws (notches) and microstructurally local stress-raisers constituting defects at the nano and microscale such as grain boundaries and second phase particles. Hydride precipitation has an negative effect on the mechanical properties of zirconium alloys and as such is important in understanding embrittlement as a precursor to delayed hydride cracking (DHC).

1.2 Nuclear Power for Electricity Generation

Nations started to focus on nuclear energy for electricity generation in the early 1950s [31]. The more recent concern of the cost-resource relationship for fossil fuels, and the need to reduce our level of dependence on them, has brought nuclear energy to be part of the energy mix. Although the nuclear industry provides clean energy for electricity generation, misconceptions have partly kept the industry from becoming a major energy source in many countries.

1.2.1 Overview of Fission Reactions

The process of nuclear fission involves heavy parent nuclei found in fissionable materials; each heavy parent nucleus undergoes a division that results in the production of unstable daughter nuclei. Upon any successful nuclear reaction event the release of energy depends on the nuclear binding force per nucleon. Generally a positive amount of energy is only released from a nuclear fission event if the parent nuclei are sufficiently heavy.

Fissile isotopes can be defined as atoms containing nuclei with an even number of protons and an odd mass number; this nucleon criterion allows the fissionable parent nucleus to divide into two lighter daughter nuclei should it absorb an additional neutron. Typical fissile fuel material include the isotopes of the elements uranium (U) and plutonium (Pu) [32]. A fissile isotope such as U-235 undergoes a nuclear transmutation event, triggered after absorbing a thermal neutron, that transforms the nucleus to a state of nuclear instability. For example, a typical fission reaction

$$U^{235} + n \longrightarrow U^{236*} \longrightarrow Ba^{141} + Kr^{92} + 3n \tag{1.1}$$

creates fission products that include two or more daughter nuclei as well as additional neutrons. These additional neutrons can potentially cause a subsequent fission event in another fissile nucleus if the energies of the produced neutrons are reduced to a favourable thermal energy region [33]. If there is a critical mass of fissile fuel, that is, a critical number of fissionable nuclei within the material, then it is possible to initiate a self-sustaining chain reaction of fission events, a process previously observed to happen in nature [34]. A chain reaction can produce large amounts of heat for a relatively small mass of fissile fuel. Fission events produce radioactive daughter nuclei which is harmful to the surroundings and so appropriate safety precautions must be taken. These challenges for ensuring a safe nuclear fission chain reaction must be addressed by the design of a nuclear reactor, which requires a careful

selection of integral materials for different purposes. Figure 1.1 shows a fission reaction between one neutron and a fissionable atomic nucleus. The nucleus then splits, producing an exothermic process that creates kinetic energy as well as releasing additional neutrons. This process then repeats itself as thermal neutrons collide with other fissionable atomic nuclei.

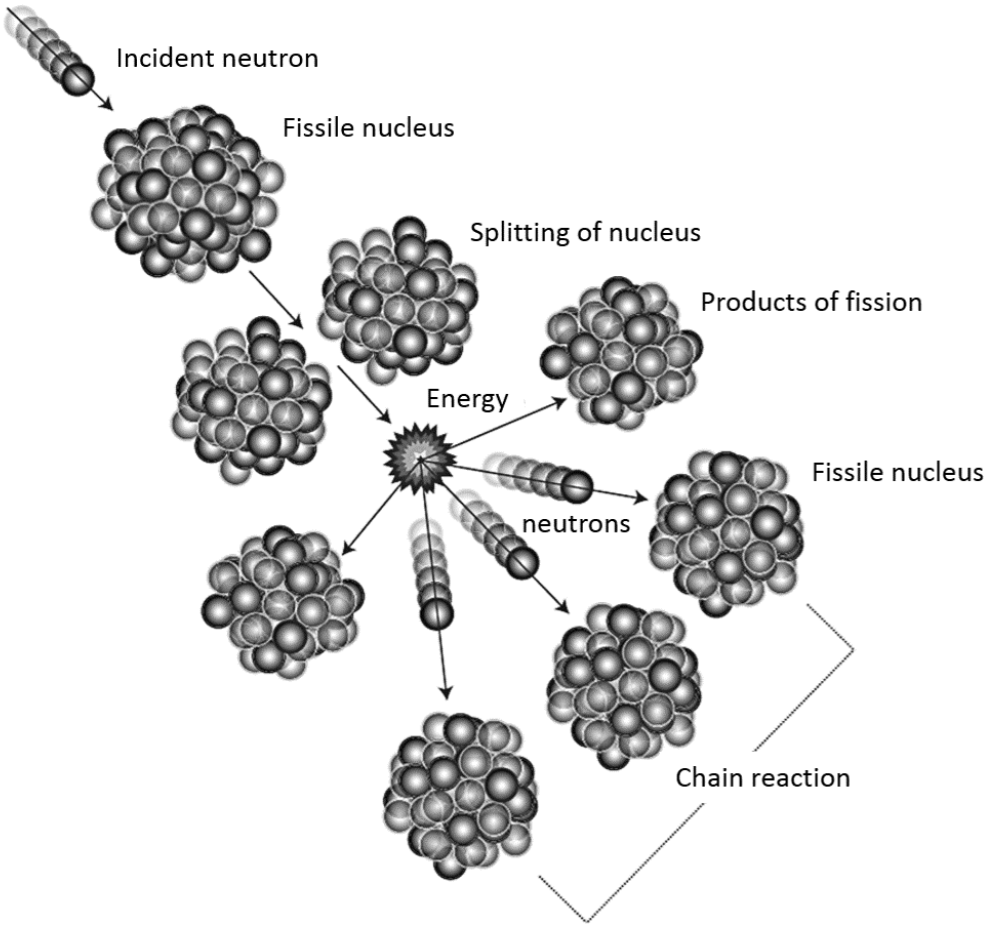


Figure 1.1: A schematic representation of a chain nuclear fission reaction which begins with a neutron colliding with an fissionable atomic nucleus and forcing it into a state of instability [7].

1.2.2 Fission Reactor Technology

Commercial nuclear fission reactors come in various types (shown in Table 1.1) that are categorised into generations. Pressurised water reactor (PWR) is a well know type introduced during the development period of propulsion reactors for US submarines [35, 36]. The primary circuit of PWRs contains water at ∼300°C under pressure while steam is generated in the secondary circuit. The cooling and heat transfer processes happen when primary loop passes through the steam generator. Water acts as both

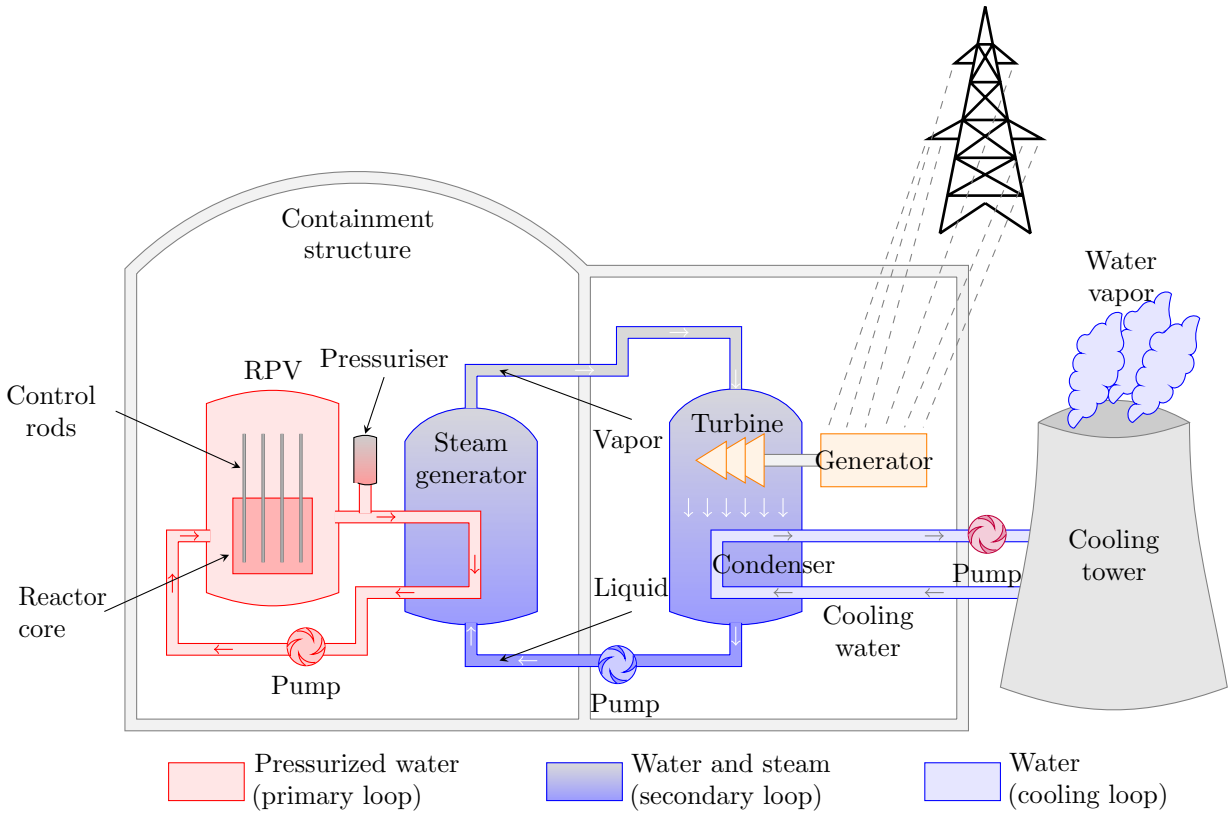


Figure 1.2: Schematic of a nuclear power plant A component-by-component breakdown of a PWR nuclear reactor design [8].

a coolant and a moderator, causing neutrons to reach low kinetic energies and thus become thermal neutrons. Moderation is achieved by the repetitive elastic collisions of fast neutrons with nuclei of light atoms of small cross-section for neutron absorption. Light atoms are more efficient in moderation than heavier ones due to simple principles of conservation of energy and momentum [9]. PWRs include the following key components as shown in Figure 1.2:

- Nuclear fissile fuel: UO_2 pellets of 10 mm in height (containing fissile 3-6% ^{235}U) arranged vertically in fuel rods.
- Neutron moderator: Reduces the kinetic energy of neutrons. Water acts as the moderator in PWRs, other common moderators in other designs include heavy water (D_2O) and graphite (C).
- Control rods: Neutron absorbers (e.g B, Hf, Ag, In or Cd) with a high neutron absorption cross-section, used to control the fission rate.
- Fuel cladding material: Houses fuel pellets in the shape of a vertical rod and has a small neutron absorption cross-section (zirconium alloys in PWRs).
- Pressure vessel: Steel vessel containing the reactor core.

- Steam generator: Part of the heat exchange system where the coolant transfers the heat from the reactor, producing steam, to run the turbines.

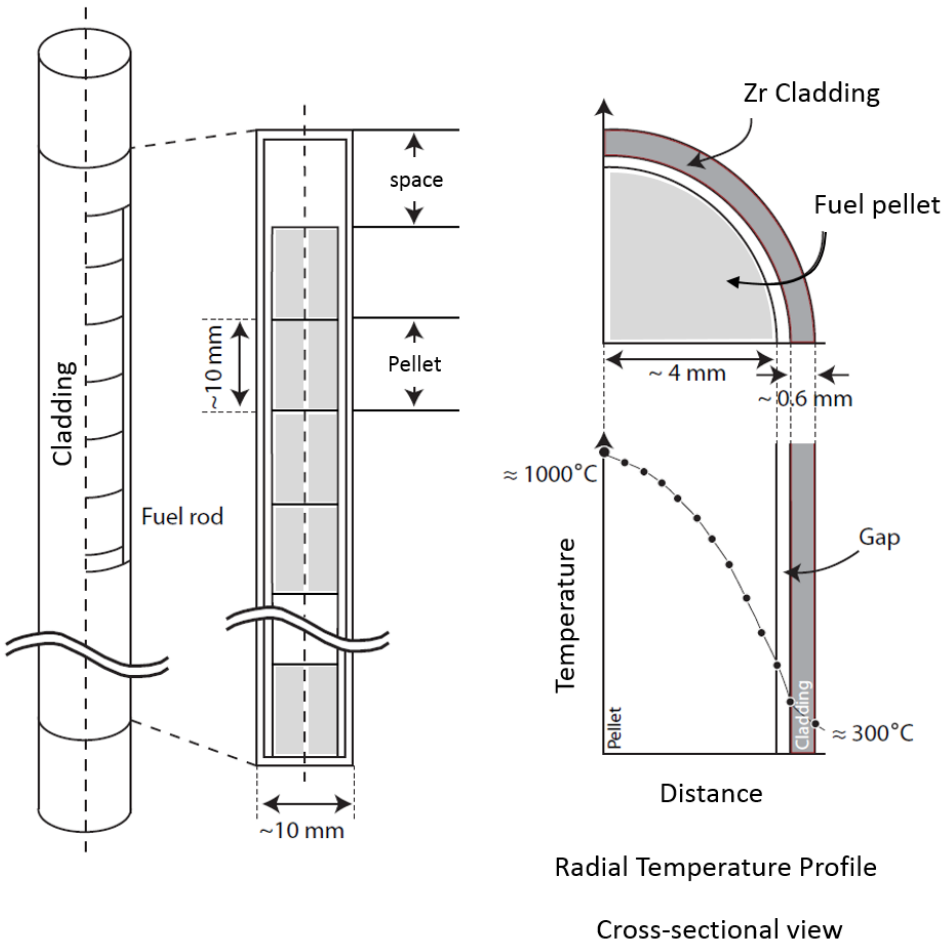


Figure 1.3: Schematic diagrams of a PWR fuel rod and radial temperature profile in the fuel rod. Adapted from [7].

Zirconium alloys fuel cladding material in PWR fuel rods contain fuel pellets that reach 1000°C plus during reactor operation. The temperature on the outer surface of the cladding is 350°C. This thermal gradient from the centre of the pellet to the cladding is shown in Figure 1.3 causes significant effects of the mechanical properties, the microstructural evolution and the corrosion processes occurring in both the fuel and cladding.

Table 1.1: List of common commercial reactors with their corresponding features [1].

Design	Fuel	Coolant	Moderator	Cladding	Number Built
PWR	UO_2	H_2O	H_2O	Zr Alloy	>400
BWR	UO_2	$H_2O_{(l+g)}$	H_2O	Zr Alloy	>78
CANDU	UO_2	H_2O/D_2O	D_2O	Zr Alloy	37
RBMK	UO_2	H_2O	Graphite	Zr Alloy	21
AGR	UO_2	CO_2	Graphite	Stainless steel	14
GCR	U	CO_2	Graphite	Mg Alloy	39
Boiling water reactor (BWR); Canada Deuterium Uranium (CANDU); Reaktor Bolshoy Moshchnosti Kanalnyy (RBMK).					

1.3 Zirconium in the Nuclear Industry

The paramount decision of using zirconium metal in nuclear reactors as fuel cladding and structural materials, came from Admiral Rickover of the US Navy for the USS Nautilus [37]. This decision was made in December 1947, when Rickover learned the great potential behind this material when alloyed using some transition metals. Initial nuclear propulsion reactors utilised aluminium and beryllium alloys as fuel cladding due to their low neutron absorption cross-section [38]. However, the ultimate tensile strength (UTS) of these alloys was proved to be inadequate. Generally, a suitable material for nuclear fuel cladding and fuel assembly must:

- Be resistant to corrosion in water and steam under reactor core conditions.
- Withstand a negative thermal gradient of around 40-50°C.
- Maintain structural integrity during reactor operation; have a relatively high mechanical strength.
- Have a small thermal neutron capture cross-section.
- Exhibit acceptable radiation tolerance.

Other base metals such as titanium and nickel readily absorb neutrons and hence have poor neutron economy. Table 1.2 shows the neutron economy and strength of various other metals and highlights its suitability for reactor applications when compared to more conventional and commercially available structural materials [1, 7].

In the early 1930s, zirconium was known to have a high melting temperature of 1,855°C with high resistance against chemical attack, however, it was considered to have poor ductility, low corrosion resistance and a natural 2% hafnium content, which has an extremely high cross-section for neutron

Table 1.2: The comparison of the approximate macroscopic cross section and UTS for some metals with respect to zirconium [1].

Base metal	Neutron economy: Macroscopic thermal neutron cross-section (cm^{-1})	Ultimate tensile strength (MPa) at 300°C
Zr	0.01	900
Fe	0.17	1100
Ni	0.31	1100
Ti	0.26	1000
Al	0.014	90
Mg	0.005	90
Be	0.001	350

absorption [39]. Subsequently, this led to the use of stainless steel in some designs as cladding materials, which then later caused an increase in fuel enrichment to compensate for the neutron loss in the cladding. After 1945, and due to the improvements made in the hafnium separation process and the discovery of the alloying effect of iron, chromium, niobium and nickel to improve corrosion resistance, zirconium became the strongest candidate. Since then, zirconium alloys have been broadly used as neutron transparent cladding materials for fuel rods in light water reactors, and structural materials in other water-cooled reactors like Canada deuterium uranium (CANDU) and reaktor bolshoy moshchnosti kanalnyy (RBMK).

As research advanced, some major properties of zirconium alloys have been changing towards better mechanical and corrosion resistant material, by altering the composition of the alloying elements or by changing the way this material is manufactured and in turn contolling grain size and texture. Optimising properties of zirconium alloys allows the fuel burn-up in the reactor core to increase, leading to more economic reactor operations [40].

1.3.1 Development of the Zircaloys™

Zircaloy-1 was the first Zr-base alloy developed in the early 1950s. Zircaloy-1 contains 2.5 wt% Sn to counteract the damaging effects of impurities such as N, increasing its corrosion resistance. However, it was later discovered that corrosion resistance in the long term was inadequate and thereafter efforts started to find a new alloy composition that withstands the corrosive reactor environment [41]. Later in 1952, an ingot of test alloy was accidentally contaminated with stainless steel, and therefore small amounts of Fe, Cr and Ni, showed some promising corrosion resistance properties. This fortunate

accident produced Zircaloy-2 (1.5%Sn-0.15%Fe-0.05%Ni-0.1%Cr), a new alloy that has been used, with only small compositional variations, in several water cooled-reactors up to the current time [37]. After Zircaloy-2, Zircaloy-3 was made with a reduced Sn and removed Ni content because Ni increases H pick-up [42]. Zircaloy-3 (0.25%Sn-0.25%Fe), was however found to have an unacceptable UTS and was hence discarded. Finally, Zircaloy-4, one of the development in the Zircaloy family, which contains 1.5% Sn, 0.24% Fe, 0.1% Cr and 120 ppm Si [43, 44]. Zircaloy-4 has very low Ni content like Zircaloy-3 and a higher Fe content than Zircaloy-2. Zircaloy-4 was found to have very good high temperature corrosion resistance as Zircaloy-2 with low H pick-up extent like Zircaloy-3. Si was added to enhance the formation of a uniform protective oxide layer [7, 45].

During the development period of the Zircaloy family, α/β Zr-Nb alloys were also being developed and used in other reactor designs [44]. Zr alloys containing Nb were primarily used as pressure tubes in reactors such as CANDU, VVER and RBMK. Unlike the α-Zr stabiliser Sn, that is a key alloying addition in the Zircaloy family, Nb is a strong β-Zr stabiliser and one that reduces the rate of H pick-up [46]. Nb was also found to improve the mechanical properties of Zr-based alloys in comparison to Sn, which lead to the development of Zirlo™ by Westinghouse and M5™ by Areva both with chemical compositions containing 1 wt% Nb along with small amounts of other transition metals such as Fe and Cr for improved corrosion resistance [9, 47, 48]. Table 1.3 shows alloy composition of the Zircaloy family, M5™ and Zirlo™. Another Nb containing alloy is Zr-2.5wt%Nb which does not have a trademark name and is used in calandria pressure tubes for CANDU reactors due to its high yield stress.

Table 1.3: Composition of the Zircaloy family containing Sn and α/β Zr-Nb alloys, Zirlo™ and M5™ (alloying elements in wt.%). Adapted from [2, 3].

Element	Zircaloy-1	Zircaloy-2	Zircaloy-3	Zircaloy-4	M5™	ZIRLO™
Nb	–	–	–	–	1	1
Sn	2.5	1.5	0.25	1.5	0.01	1
Fe	–	0.15	0.25	0.2	0.05	0.11
Cr	–	0.1	0.1	0.1	0.015	<0.01
O	0.14	0.14	0.14	0.14	0.18	0.15

1.3.2 Alloying Addition and Grain Size Effects

Alloying elements in zirconium alloys are generally added to:

- improve corrosion resistance;

- increase mechanical strength;
- maintain phase stability;
- reduce H pick-up.

However, due to their low solubility in the Zr solid solution alloying elements of Fe, Ni and Cr in particular precipitate out of the hcp Zr phase to produce a uniform distribution of intermetallic second phase particles (SPPs) [49]. The main SPPs found in Zr-4 are $Zr(Cr,Fe)_2$ [50, 51], which are also found in Zr-2 along with $Zr_2(Fe,Ni)$. SPPs have diameters ranging between 10 nm and 1 µm and have a volume fraction of about 0.5% in Zr-4 [52]. Not only were SPPs found to significantly affect the mechanical and corrosion properties of Zr alloys, but were also thought to act as favorable low energy sites for hydride precipitation most likely due to local stress fields they create [16, 30].

Alloying additions in zirconium alloys contribute towards an increased mechanical strength of the material, however, and more importantly, a fine grain size needs to be produced to maintain a high yield stress and toughness during in-reactor service. Grain size in as-fabricated zirconium alloys is at the range of tens of micrometers. Grains, separated by grain boundaries, can however grow in size at temperatures near and below the Zr-$\alpha \rightarrow \beta$ transition to produce the large so called blocky-α grains that disrupt the uniform as manufactured fine grain distribution and alter the mechanical properties and the hydride nucleation site dynamic of the alloy. The size of blocky-α grains is in the range of hundreds of micrometers and so can be detrimental, as they can grow to span the entire tube wall thickness of the fuel cladding. This of course compromises the structural integrity and increases the in-service likelihood of tube failure [12].

1.3.3 Corrosion and H Embrittlment of Zr alloys

The water coolant in contact with zirconium alloy cladding in water reactors is considered as a harsh physical and chemical environment due to high temperatures and pressures. The water solution or water/steam mix both associated with corrosion rates and H-pick amount, contain the following:

- boric acid shims (added/removed to control rate of burn-up);
- lithium hydroxide alkali solution to balance pH;
- free hydrogen atoms to form H_2O with free oxygen atoms or other free radicals;

- organic contaminants;
- free radicals formed after water radiolysis;

The lifetime of zirconium fuel cladding and consequently the fuel assembly lifetime is limited by the rate of oxidation and H ingress. When water/steam reacts with Zr, hydrogen by-products of this oxidation reaction are produced as shown in the following ionic equations:

$$Zr + 2O^{2-} \rightarrow ZrO_2 + 4e^- \tag{1.2}$$

$$4H^+ + 4e^- \rightarrow 4H \tag{1.3}$$

Equation 1.2, the anode half reaction, shows a typical oxidation process whereby the metal loses four electrons. Equation 1.3, the cathode, shows the reduction process that produces four hydrogen atoms or two hydrogen diatomic molecules. The overall redox equation is as follows:

$$Zr + 2H_2O \rightarrow ZrO_2 + 4H \tag{1.4}$$

Considering the anodic reaction in equation 1.3, the zirconium oxide (ZrO_2) corrosion film produced was identified to be made up of non-uniform distribution of stable monoclinic and metastable tetragonal phases. The growth of this oxide film, which has an initial thickness of tens of nm ranging up to 1 µm, has variable rates during the lifetime of the alloy. The oxide starts forming at a high rate and then saturates, after a time period of weeks, to a less protective state that causes a break-away process. This gives rise to a parabolic curve, and its process is the repeated as shown in Figure 1.4 [53].

Research advancements in Zr alloys development has significantly improved their corrosion resistance, mainly by altering the content of alloying elements [54, 55]. As a result, the limiting factor for operational lifetime of zirconium fuel cladding and structural materials is often no longer associated with oxidation, but instead the concentration or fraction of hydrogen atoms entering through the oxide layer into the metal matrix and therefore hydride precipitation. Zr cladding has a durable hydrogen absorption ability at temperatures above 500°C, however, this property of this alloy can still cause some significant problems when the hydrogen level in the system surpasses its solubility limit especially at high burn-ups. The solubility of hydrogen in zirconium decreases sharply with a decrease in temperature as the solubility decreases from 50 at. % at 500°C to 0.7 at. % at 300°C and to 10^{-4} at room temperature [20]. The solubility issue leads to the detrimental brittle hydride precipitation that is the driving force of

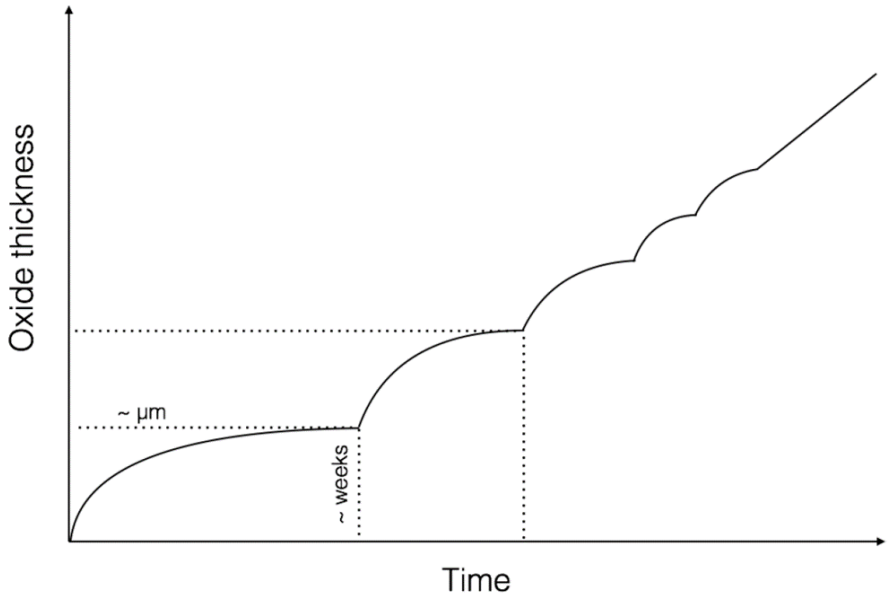


Figure 1.4: Corrosion kinetics curve of zirconium alloy cladding in the PWR core. First and second transitions are shown by dotted lines. Adapted from [9].

delayed hydride cracking (DHC) [40]. Hydride embittlement causes a threat to the structural integrity of the Zr components specially during reactor shut down or during end of life storage where hydride concentrations can reach high levels. Previous Zr component DHC failures in Zr-2.5wt%Nb cap welds and pressure tubing have sparked research initiatives by industry and the academic community to develop and improve our understanding of hydride precipitation, re-orientation and embrittlement.

1.4 Research Aims and Objectives

The aim of this work is to quantify hydride precipitation in different microstructural settings that can be used to parameterise predictive delayed hydride cracking models of different geometries and thermo-mechanical load cycles. In addition, this project aims to provide a computational framework that incorporates microstructural effects of zirconium in a hydrogen diffusion model. To achieve these aims a combination of numerical models and experimental analysis will be performed.

The objectives of this project are outlined as:

1. Experimentally determine the effects of microstructure on hydride distribution in as-received and blocky-α Zr-4 and commercially pure zirconium without external loading, with the aim of studying the potency of inter and intra-granular hydride precipitation sites. (Chapter 5).

2. Experimentally determine the effects of notch acuity on hydride distribution in as-received and

blocky-α Zr-4 when subjected to thermo-mechanical loading, considering the effects of material texture, grain size and SPP distribution. (Chapter 6).

3. Develop a continuum based finite element model to compute notch-tip hydrogen profiles with microstructural effects to predict the hydrogen stress-driven diffusion towards notches, a sub-process of delayed hydride cracking. (Chapter 7).

1.5 Publications

The following papers have been produced and contributed to parts of this doctoral thesis:

1. S. Chamaa, M. Patel, C. M. Davies, and M. R. Wenman. The Effect of Grain Boundaries and Second-Phase Particles on Hydride Precipitation in Zirconium Alloys. MRS Advances, 3(31):1749–1754, 2018. ISSN 20598521. doi: 10.1557/adv.2018.111.

2. S. Chamaa, M. Patel, M. R. Wenman, and C. M. Davies. Multiscale Stress-Diffusion Analysis of Notch-Tip Hydrogen Profiles in Zircaloy-4. ASME 2018 Pressure Vessels and Piping Conference, pages V06BT06A013–V06BT06A013. American Society of Mechanical Engineers. 2018

3. L. Reali, S. Chamaa, D. S. Balint, C. M. Davies, and M. R. Wenman. Deformation and fracture of zirconium hydrides during the plastic straining of Zr-4. MRS Advances 5, no. 11 (2020): 559-567.

4. Y. Liu, W. Wan, S. Chamaa, M. R. Wenman, C. M. Davies and F. P.E. Dunne. Strain Rate Sensitivity Analyses in Polycrystalline Zircaloy-4. Submitted.

5. Y. Liu, S. Chamaa, M. R. Wenman, C. M. Davies and F. P.E. Dunne. Creep, Cyclic Plasticity and Hydrogen in Zircaloy-4. In progress.

1.6 Conferences

Some work discussed in this thesis has been presented at the following conferences, reviews and meetings:

1. ASME Pressure Vessel and Piping (PVP) conference ‘Multiscale Stress-Diffusion Analysis of Notch-Tip Hydrogen Profiles in Zircaloy-4’. Prague (2018)

2. MRS 'The Effect of Grain Boundaries and Second-Phase Particles on Hydride Precipitation in Zirconium Alloys'. Boston (2017)

3. Rolls-Royce Nuclear University Technology Centre Annual Review - Rolls-Royce plc 'The Effect of Microstructure on Hydride Precipitation" Derby (2017)

4. Universities' Nuclear Technology Forum (UNTF) 'Microstructural Analysis of Hydride Precipitation in Zirconium Alloys' Liverpool (2017)

5. JNC Winter School 'The Effect of Microstructure on Hydride Precipitation' Solihull (2016, 2017, 2018 and 2019)

Chapter 2

Literature Review

2.1 Outline

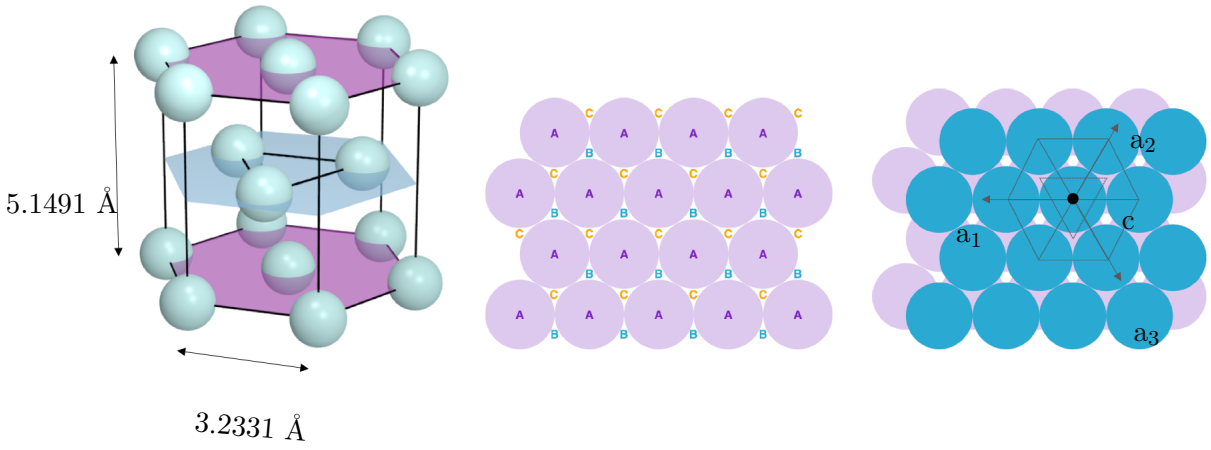
In this chapter a literature review is provided. Key experimental and computational research outputs on zirconium alloys, hydrogen and hydride precipitation in Zr since the 1950s are discussed. The chapter starts by reviewing the atomic structure, crystallography, texture and other microstructural properties of Zr (Part I). The chapter then reviews how these properties influence the material behaviour and its interaction with hydrogen and hydrides, leading up to the problem of hydrogen embrittlement through to the DHC phenomena (Part II).

Part I: Crystallography and Microstructure of Zirconium alloys

2.2 Crystallography

Zirconium (Zr) has a hexagonal close packed (HCP) α crystal structure at room temperature, with a P63/mmc space group as shown in Figure 2.1. At high temperatures, a body centred cubic (*bcc*) structure, the β phase, is stable. The $\alpha \rightarrow \beta$ transition occurs at 863°C for Zr, ~1000°C below its melting point. Consequently, for nuclear reactor applications, the metal is usually in the hexagonal α phase. The room temperature lattice parameters in the HCP crystals a and c have been determined to be 3.23 Å and 5.15 Å respectively resulting in (c/a) ratio of 1.59 [56]. Therefore HCP metals exhibit some deviation from the ideal c/a ratio (the ratio for which the bond distance between one plane and another is the same as the in-plane one - Ideal c/a= 1.63) resulting in strong anisotropic thermal, elastic and plastic properties. Figure 2.1 also shows the HCP A-B-A-B staking of close packed planes,

where A and B are two of the three equivalent sites [9].



(a) HCP unit cell (b) Closed packed plane (c) HCP staking

Figure 2.1: (a) Unit cell structure of the HCP α crystal structure with (0001) basal planes, (b) a 2D scheme of close packed layer of A with positions where the B or C layers may be stacked and (c) the B layer now on top of an A layer. Adapted from [9].

2.3 Texture Evolution

The crystallographic micro-texture of zirconium alloys has a direct influence on the material mechanical properties and corrosion behaviour. Texturing zirconium alloy components for nuclear applications has been a key step in optimising the structural integrity of the materials. The texture is produced during the several fabrication steps that include thermomechanical treatments at temperatures ranging between 500 and 825°C [57, 58]. Texture can be described as non-random orientation of grains due to the rotation of the crystallographic axes of grains towards preferred orientations relative to the processing axes; this in particular is called deformation texture and is important when considering Zr plate or tube formation. The grain rotation can also take place during heat treatments above the recrystallisation point of the deformed material resulting in an annealed texture. Texture in zirconium alloys is important as it effects the yield strength, creep properties, fatigue and stress corrosion cracking resistance, hydride orientation and irradiation induced growth behaviour [41, 59].

The texture of a hot rolled recrystallised zirconium alloy sheet is known as the Zr $(0002)_{\alpha-Zr}$. The compressive stress exerted by the upper and lower rollers on the sheet, cause the c-axis of the HCP crystals to rotate 30-40° from the normal direction (ND) of the plate towards its transverse direction (TD) as shown in Figure 2.2(a) [10]. The 0001_{Zr} pole figure displays two asymmetric peaks of basal

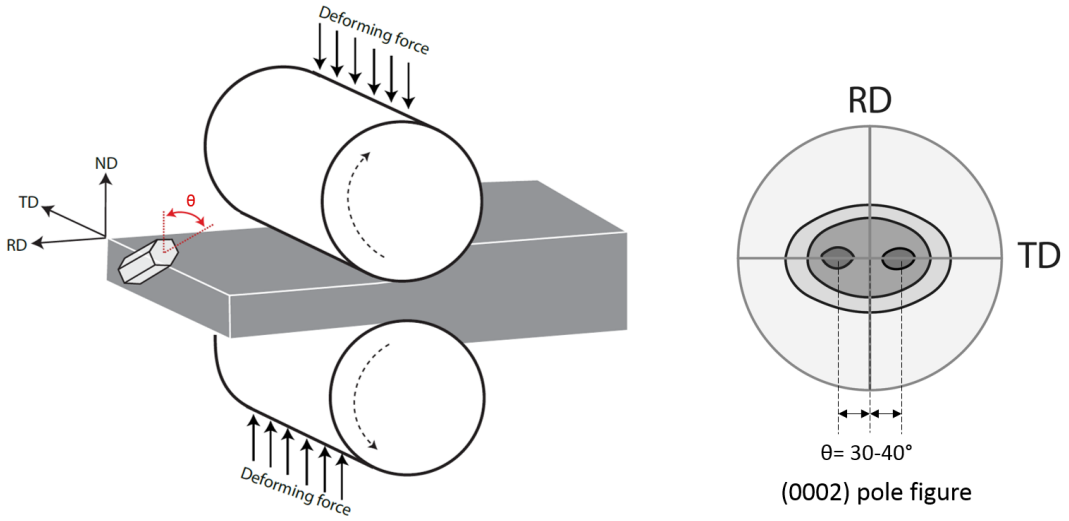
pole density, close to the sample ND at the centre of the pole figure, which shows the typical texture of zirconium alloys that is produced during thermomechanical treatments during the fabrication process. The asymmetry of the basal peaks indicate microscopic fluctuation in grain orientation for the spread of grains analysed within the sample volume [60]. The typical basal texture of Zr $(0002)_{\alpha-Zr}$ can be measured by electron back-scatter diffraction (EBSD) explained in Chapter 3. The textures of Zr-4 and commercially pure zirconium, Zircadyne-702 (Zr-702), hot rolled and recrystallised plates used in this study are shown in Figure 2.3(a)(b). Plate directions are referred to as the rolling, normal and transverse directions (RD, ND and TD).

The texture of the zirconium alloy tube components is determined by the fabrication route which consists of four pilgering steps with intermediate annealings as follows: (1) Cast ingot, (2) β-quenching at 1050°C, (3) hot extrusion at 825 °C, (4) first annealing at 760 °C for 4 hours, (5) 1^{st} pilgering 80% reduction, (6) second annealing at 650 °C for 4 hours. (7) 2^{nd} pilgering 70% reduction, (8) third annealing at 575 °C for 3 hours, (9) 3^{rd} pilgering 58% reduction and (10) final annealing at 500°C for 10 hours. The texture of the tube produced has the c-axis of the hcp crystals perpendicular to the axial tube direction. The orientation of hydrides precipitating can be ruled by this texture. Circumferential hydrides (parallel to the hoop stress) are considered to be less harmful than radial hydrides (perpendicular to the hoop stress), and so the texture is made to accommodate desirable hydrides [11, 58].

2.4 Elastic Properties

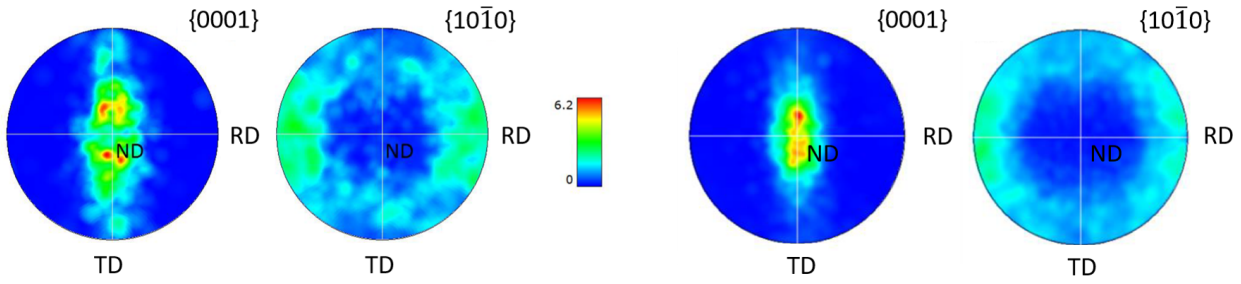
Zirconium alloys used in nuclear water reactors as fuel cladding and structural materials are subjected to several types of stresses including thermal, mechanical and irradiation during reactor operation [61]. Understanding the elastic and plastic deformation mechanisms in the textured and untextured HCP Zr microstructures is important, specially when deformation mechanisms have an effect on hydrogen diffusion and hydride precipitation in Zr [40].

The elastic properties of zirconium alloys are typically effected by temperature, texture, as well a showing a slight dependence on neutron irradiation [4]. The elastic moduli or Young's modulus of Zr2.5wt%Nb was found by Pan et al. to have a relationship with the material crystallographic texture as shown in Figure 2.4 [4]. The relationship was tested for CANDU pressure tube material using ultrasonic resonance and not only showed the variation in the elastic properties as a function of sample orientation but also as a function of temperature. Figure 2.4 shows that the Young's modulus



(a) (b)

Figure 2.2: (a) Schematic of the hot rolling process during Zircaloy fabrication. (b) A simplified pole figure corresponding to the (0002) basal plane texture of Zircaloy-4 rolled and annealed sheet [10, 11].



(a) (b)

Figure 2.3: Texture of two zirconium alloys, namely (a) Zr-4 and (b) commercially pure zirconium (Zr-702), with pole figure colour scale in multiples of random texture. The average grain size of >1400 grains measured by EBSD of Zr-4 is 15 µm and of Zr-702 is 30 µm. Adapted from [12].

has highest values at 20, 200 and 400°C at an orientation parallel to the transverse direction, where the basal pole for the majority of the α-Zr crystals are aligned [7].

Another study by Fisher et al. [62] used the ultrasonic wave velocity technique to measure the anisotropic elastic constants of five independent elastic moduli in single crystals in pure zirconium in

different orientations at room temperature. The study shows that the highest stiffness constant is at C33 = 164.8 GPa, which is parallel to the transverse direction in rolled plates, which agrees with Figure 2.4 where also the highest Young's modulus values were recorded parallel to the transverse direction. Stiffness constants were found to be highly dependent on temperature, and are reported to decrease as temperature increases [63]. At room temperature, the Young's modulus of mono-crystals, which depends on the angular orientation of HCP crystals, is reported to be highest (∼125 GPa) when the angle between the basal pole [0002] and the loading axis are parallel (0°). The Young's modulus was calculated by combining single crystal elastic constants. The Young's modulus of mono-crystals decrease to ∼89 GPa as the angle between the basal plane normal and the loading axis increase to 52.5°. Finally it increases back again to 99 GPa as the orientation of the HCP crystal approaches $[10\bar{1}0]$ at 90°. Table 2.1 highlights the stiffness constants for the 5 independent elastic moduli and the maximum and minimum Young's moduli (E) values in pure Zr at 20° [4].

Finally, to study the effects of alloying additions and texture at a range of temperature (20-300°) on the elastic properties of Zr alloys, Northwood et al. [63] conducted measurements in Zircaloy-2, Zr-1.15 wt% 0-0.1 wt% Fe and Zr-2.5 wt% Nb polycrystals. Northwood et al. found that the Young's modulus and shear modulus decreased linearly with increasing temperature with weak dependence on alloy composition. Northwood et al. also compared their results with previous work that calculated polycrystalline constants from single crystal elastic constants. There was good agreement (±5% deviation) in the Young's modulus and shear modulus between directly measured values from bulk samples [63], and values calculated from combining single crystal elastic constants and texture measurements [4]. This means that the elastic behavior of Zr alloys is not greatly dependent on polycrystallinity possibly due to a weak interaction between grains in the elastic regime [64].

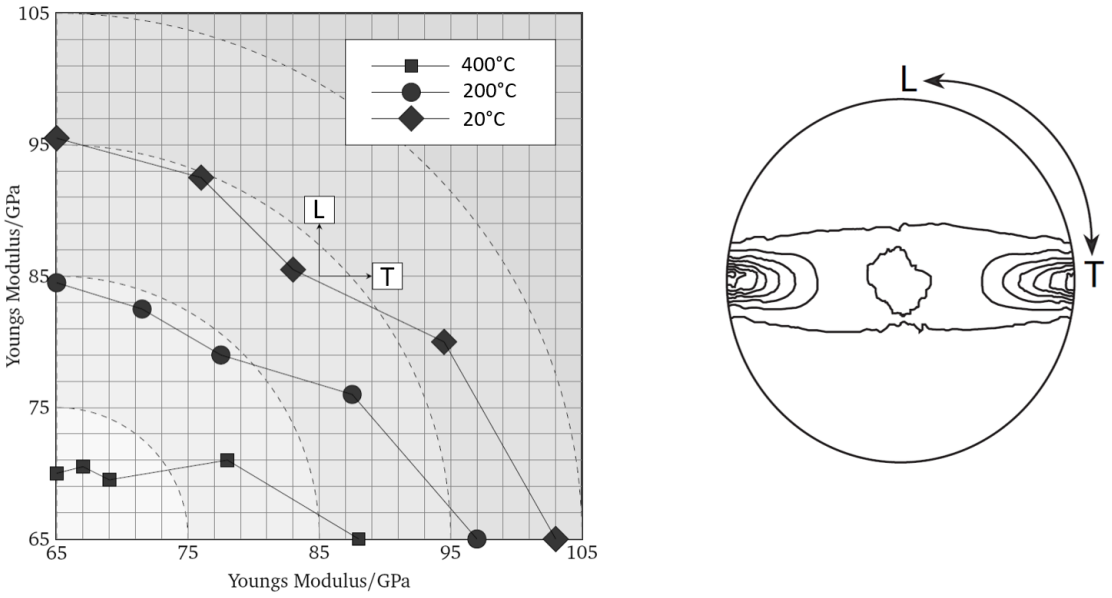
Table 2.1: Elastic constants and Young's moduli for mono crystal pure zirconium in different crystal orientations at room temperature [4]

Elastic Constant	C11	C12	C13	C33	C55	$E_{[10\bar{1}0]}$	$E_{[0001]}$	E_{min}
Value (GPa)	143.4	72.8	65.3	164.8	32.0	99.1	125.3	89.0

E_{min} correspond to the minimum Young's modulus value (E) at an angle between the basal plane normal and the loading axis of 52.5°.

2.5 Plastic Deformation in HCP Crystals

The non-ideal c/a ratio of Zr has significant effects on plastic deformation in HCP crystal lattices due to its relation to atomic density, elastic anisotropy, stacking fault energy and relative orientation of the



(a) (b)

Figure 2.4: Polar plot (a) of Young's modulus versus sample orientation and (b) shows the corresponding {0002} pole figure in the transverse (T) and longitudinal (L) directions of the Zr tube samples. Adapted from [4, 13].

applied stress axis [7, 65]. There are two primary deformation mechanisms in HCP crystals, namely, slip and twinning. The activation and dominance of both mechanisms depends on which requires the least stress to initiate and sustain plastic deformation in a particular direction, at a given temperature.

2.5.0.1 Slip

Slip often appears in crystal planes at regions of high planar atomic density and shortest lattice vector. Slip occurs as a result of dislocation motion through the crystal lattice along a particular plane in a particular direction. Slip systems can therefore be accurately described by the slip plane and the displacement or Burgers vector. In hexagonal metals, slip systems include basal, prism and pyramidal slip, shown in Figure 2.5. In Zr, the most common slip systems at low temperatures are basal slip $\{0001\}\ \langle 11\bar{2}0\rangle$ and prismatic slip $\{10\bar{1}0\}\ \langle 11\bar{2}0\rangle$. Although various studies have shown that the main slip system in Zr at room temperature is on $\{10\bar{1}0\}$ prismatic planes with $\langle 11\bar{2}0\rangle$ $\langle$a$\rangle$ type Burgers vector, and it is rarely seen in [0001] basal planes [40, 66, 67]. These two slip systems are however limited to two independent systems, and therefore fail to satisfy the von Mises criterion of slip that states that "in order for a material to undergo deformation without cracking, each grain within a polycrystal

must contain at least five active independent slip systems" [68]. Pyramidal ⟨c+a⟩ slip systems and twinning modes must therefore play important roles in contributing to the room temperature ductility of polycrystalline zirconium [64]. At higher temperatures, first-order ⟨a⟩ pyramidal slip $\{10\bar{1}1\}$ $\langle 12\bar{1}0\rangle$ and second-order ⟨c+a⟩ pyramidal slip $\{11\bar{2}2\}$ $\langle 11\bar{2}3\rangle$ become more favourable.

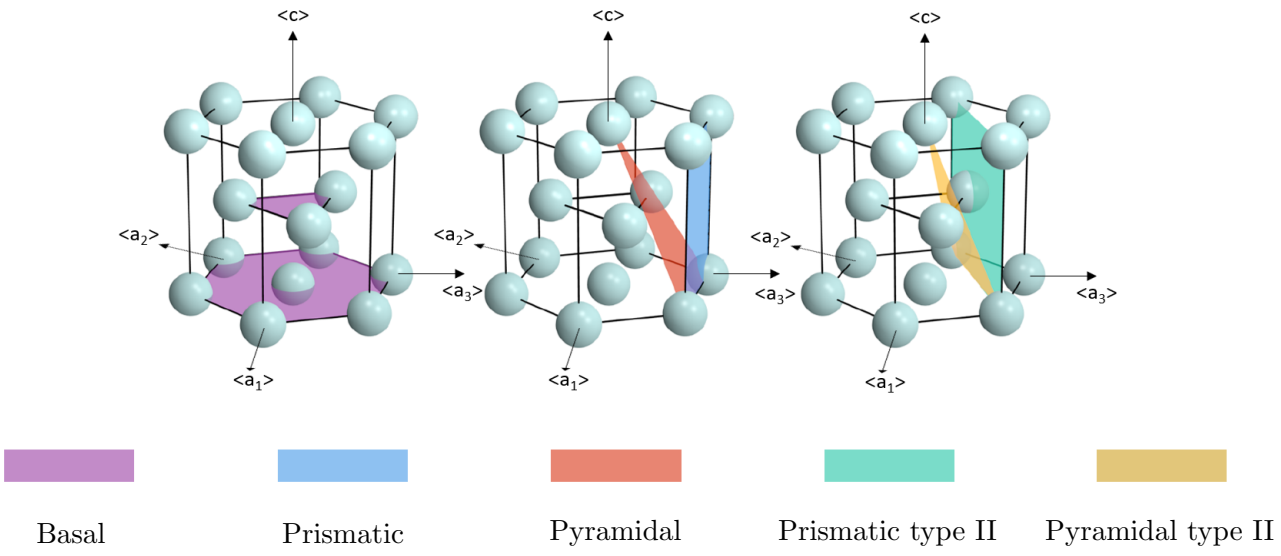


Figure 2.5: Main crystallographic planes of the HCP crystal lattice. (a) Purple: basal planes {0001}. (b) Blue: prismatic plane type I $\{10\bar{1}0\}$. Red: pyramidal plane type I order I $\{10\bar{1}1\}$. (c) Green: prismatic plane type II $(11\bar{2}0)$. Yellow: pyramidal plane type II order I $(11\bar{2}0)$. Adapted from [9].

2.5.0.2 Twinning

Twin modes are often an alternative deformation mechanism when the activation of a slip system is unfavourable. Twinning allows deformation parallel to the unit cell ⟨c⟩ axis, which prismatic ⟨a⟩ slip cannot allow [64]. Twinning often dominates over slip in hexagonal metals due to their limited number of close packed slip systems [69]. The process of deformation twinning produces a crystal lattice that mirrors that of its parent. This occurs when there is a reorientation of the parent lattice by atomic displacements, equivalent to a simple shear on every plane which produces a coordinated shear transformation in a crystalline material. Twin types can be classed as either compressive (C1, C2) or tensile (T1, T2) twins, which accommodate shear strain either to contract or extend the ⟨c⟩ axis of the HCP unit cell. This strain accommodation may possibly effect the hydride precipitation dynamic in polycrystals as will be discussed later. Figure 2.6 shows a simplified scheme of the twin mechanism along with HCP twinning modes. The predominant twin type in zirconium is the T1 mode, also shown in Figure 2.6.

Considering the effect of grain size on twin deformation, Kaschner and Gray [70] observed no grain size dependence on twinning at both room temperature or 77 K. Capolungo et al. [71] also show similar results after producing a statistical study on T1 twins in high-purity polycrystalline zirconium. Capolungo et al. show that the incidence of twinning is not found to be dependent on grain size. Small grain sizes were found to be nearly as likely to exhibit twins as large ones. Twin thickness was also measured and was found to be relatively constant across the samples for a given strain level and insensitive to grain area, which according to the author, explains why the twin area fraction in twinned grains was independent of grain area.

Song and Gray [72] also investigated the effects of grain size on twinning in pure zirconium, and found that twins are dominant in small grained microstructures (15 µm grain size) at all strain levels and rates (2 to 20% at 0.001 and 0.1 s^{-1}). However, in materials containing large grain sizes (75 µm grain size) they observed that deformed large grains promote slip-dominated deformation, before transitioning to twinning-dominated deformation. The grain size dependent behaviour of twin deformation is due to longer dislocations pile-ups being possible in large grains, which increases the pile-up stress and allows slip transfer across grain boundaries. If the grain size is large enough, slip transfer occurs before the twinning critical resolved shear stress is reached which causes the deformation to transition to a twin dominated. The critical resolved shear stress for twinning is independent on grain size of the material [72].

2.6 Mechanical Properties of Zr Alloys

The mechanical properties along with microstructural effects, play an important part in the degradation mechanisms in Zr alloys such as in DHC [40]. Firstly, the Zircaloys used as fuel cladding materials can exhibit a significant microstructural and mechanical anisotropy due to the development of a preferred orientation or texture during mechanical fabrication processes. On the other hand, studies by Schofield et al. [5], on electron beam weld metal samples that are not subject to mechanical working during fabrication, a near random texture can be expected and therefore show little mechanical anisotropy behaviour. The random texture in the weld metal samples has been confirmed by microtexture measurements. Mechanical properties however have not been reported on random textured Zr microstructures such as in beam weld samples.

The manufacturing process for the Zircaloys involves several high temperature annealing stages, mentioned in Section 2.3, which results in finished components with a low yield strength. Neutron

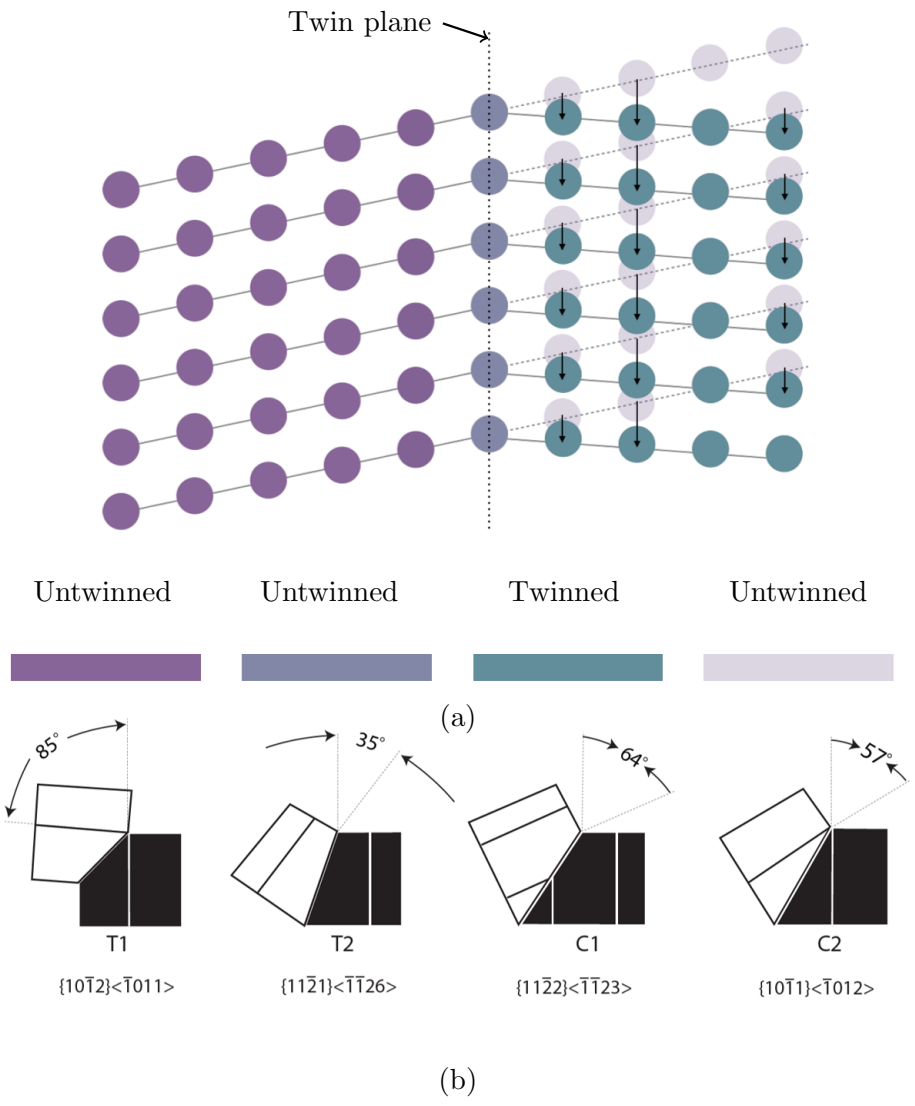


Figure 2.6: (a) Schematic of a twin boundary, whereby circles represent atoms in 2D planes that can undergo various twinning modes (b) in HCP zirconium. Adapted from [7, 9].

irradiation was found to have an effect on the mechanical properties of Zircaloy-4 tube components by mainly increasing the yield strength at room and at high temperatures. Zr components, used as fuel cladding, are known to have a strong crystallographic texture (resolved basal pole Kearns factors: 0.6 radial, 0.33 circumferential and 0.07 axial) from the extrusion and cold drawing processes. The tube has a large fraction of the HCP grains with the basal pole near the radial direction of the tube as schematically shown in Figure 2.7(a). The tubes are stronger in the circumferential direction than the axial direction. The effect of neutron irradiation on the yield strength of cold drawn Zircaloy-4/Zircaloy-2 and Zr2.5wt%Nb at 30 and 300°C are shown in Tables 2.2 and 2.3 respectively. Table 2.3 also shows the effect of texture on the yield strength. Texture is also known to effect hydride precipitation in Zr alloys and has been extensively reported in literature to form well aligned hydride

Table 2.2: Typical yield strength values for cold worked Zr-4 and Zr-2 alloys [5].

Yield Strength (0.2% proof stress) (MPa)		
Temperature (°C)	Zircaloy-2 and Zircaloy-4	
	Un-irradiated	Irradiated
30	380	710
300	146	476

Table 2.3: Typical yield strength values for cold worked Zr-2.5Nb CANDU pressure Tubes [5].

Yield Strength (0.2% proof stress) (MPa)			
Temperature (°C)	Zr-2.5%Nb		
	Test Direction	Unirradiated	Irradiated
30	Axial	779	1089
	Circumferential	555	-
300	Axial	504	804
	Circumferential	355	-

platelets in highly textured materials due to the basal plane hydride precipitation [40]. The platelets can readily re-orientate under the influence of temperature and applied stress from the circumferential to the radial direction, as shown in Figure 2.7(b)(c), which will be explored further in Part II of this chapter.

2.7 Grain Growth in Zirconium Alloys

Zirconium alloys have been used as fuel cladding and structural materials partly due to their good mechanical properties that stems from a fine uniform grain size. A uniform fine grain size also contributes in minimising stresses caused by thermal expansion and irradiation, and ensure a uniform homogeneous strain rate along in-service Zr cladding components. If the average grain size of polycrystalline zirconium alloys increase or an abnormal grain growth occurs, the structural integrity of components will be severely affected [72].

The yield strength of Zr decreases as grain size increase [72]. This is consistent with the Hall-Petch equation, that has a room temperature coefficient for pure Zr, reported by Armstrong [73] and shown in Equation 2.1:

$$\sigma_y = 29.42 + \frac{7.89}{\sqrt{D}} \tag{2.1}$$

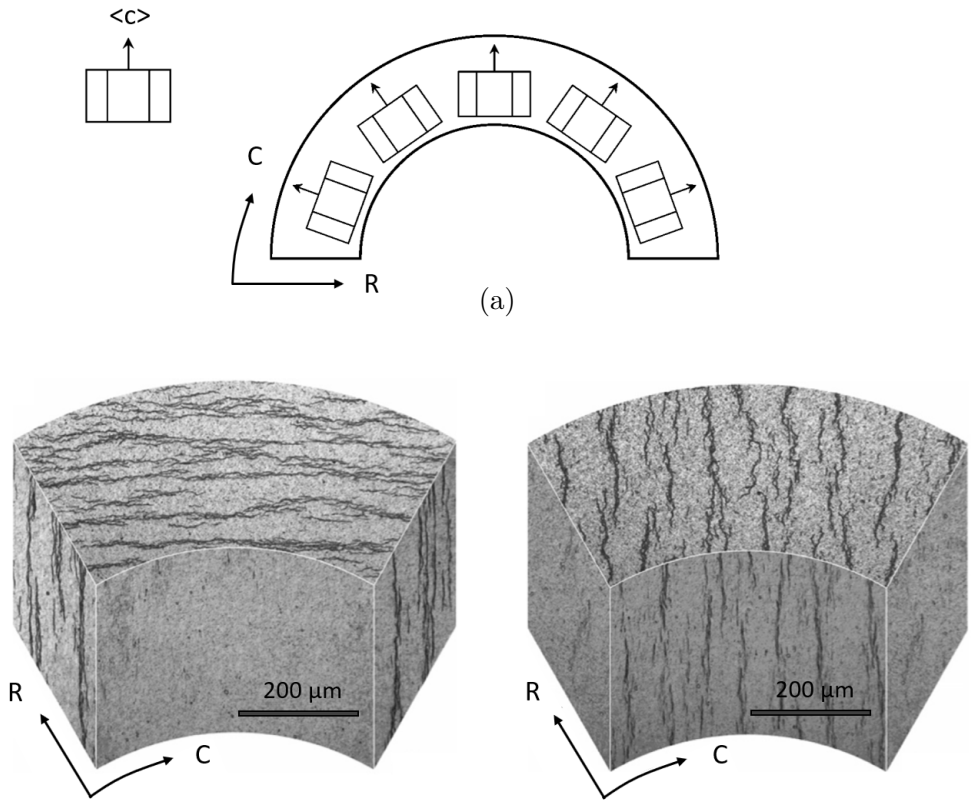


Figure 2.7: (a) A scheme of the Zr tube cladding radial texture along with 3D micrographs showing re-orientation of hydrides in Zircaloy-4 cladding of 230 wppm from (b) as-hydrided to (c) after eight thermal cycles. Adapted from [14].

where σ_y is the yield stress in MPa for an average zirconium grain diameter D in mm. The equation does not take into account the texture of the material and the alloying elements or impurities that tend to increase the tensile or yield strength of the alloy [74]. Using Equation 2.1 a predicted yield strength of 85 MPa is calculated if the grain size of Zr is 20 µm.

2.7.1 Abnormal Grain Growth

Some grains in polycrystalline zirconium alloys, can grow abnormally at high temperatures to form large grains known as blocky-α grains (>300 µm). If blocky-α grains abnormally form in Zr-4 fuel cladding tubes or in structural Zr-4 components containing welds, the structural integrity of the components can be detrimentally affected:

1. Large grain size leads to degradation in yield strength and thermal expansion properties in

anisotropic Zr [72, 75].

2. Causing a reduced number of grain boundaries which generally impacts the mechanical properties of components, specifically yield and tensile strength [72].

3. Causing changes to ageing regimes such as irradiation growth and creep [75].

4. Effecting hydride embrittlement mechanisms, by either providing a favourable (near basal planes) or non-favourable crystal orientation for hydrides to precipitate [76, 77]. Reorientation of hydrides in blocky-α microstructures to cause DHC, has not yet been reported in literature.

2.7.2 Grain Growth *via* Annealing

In this project the Zr material used is in the form of hot-rolled and partially recrystallised plates. Recrystallisation *is the formation of new grains in a deformed material by migration of high angles grain boundaries (>10-15°) to reduce the stored energy of a system.* Strain energy from plastic deformation in microstructures is eliminated from the nucleation and growth of new grains by primary recrystallisation [78]. Grain growth to form blocky-α grain sizes in Zr alloys was found to occur on further annealing after recrystallisation [12]. Uniform grain growth again occurs due to the migration of high angle grain boundaries (>10-15°) but this time driven by the reduction of grain boundary interfacial energy. In uniform grain growth the smallest grains shrink and are consumed by larger neighboring grains, so that the average size of grains increase. Normal grain growth is a continuous transformation, which means that it occurs homogeneously and simultaneously throughout the stress free parent metal [78].

Non-uniform grain growth in Zr, also know as abnormal grain growth or secondary recrystallisation, occurs when normal/uniform grain growth is suppressed or pinned by microstructural particles such as SPPs. The pinning effect causes a small amount of grains to grow and consume small adjacent ones, leading to a bimodal grain size distribution. Figure 2.8 shows an example of microstructures with unimodal and bimodal grain size distribution [15]. The driving force for abnormal grain growth is the same as for normal grain growth which is the reduction of grain boundary area [78]. Research work by Tong et al. [64] and Gray et al. [79] have shown that grains in commercially pure zirconium and Zr-4 can grow at 800-830°C in inert atmosphere (below the α to $\alpha+\beta$ transus temperature) after 336 hours, to produce uniform blocky-α microstructures with no abnormal grains. This technique of grain growth is used in the experimental work performed here to study the effect of reducing the grain boundary

area on hydride precipitation and therefore study the grain boundary hydride nucleation potency after reducing the number of available intergranular hydride precipitation sites per unit volume.

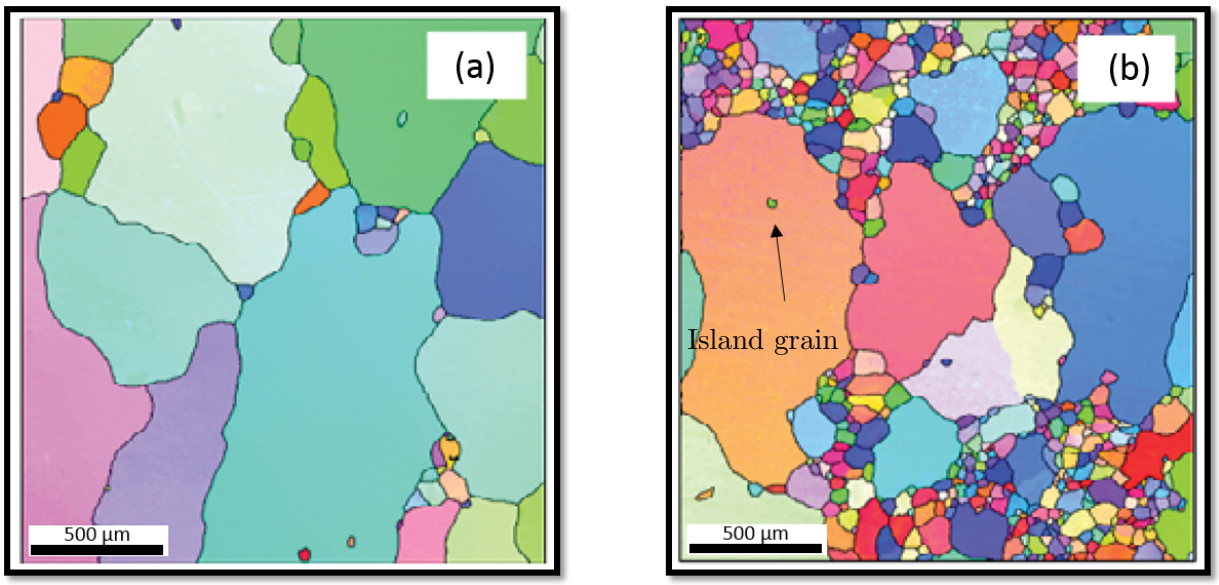


Figure 2.8: IPF EBSD maps showing an example of a lower (a) bimodal grain size distribution than a higher (b) one. The arrow in (b) shows an island grain with an as-received grain size inside a large grain. Adapted from [15].

2.7.3 Second Phase Particles and Grain Growth

SPPs found in Zr-4 are $ZrFe_2$, $ZrCr_2$ and $Zr(Cr, Fe)_2$ [52]. SPPs have diameters ranging between 10 nm and 1 µm as mentioned in Chapter 1 and have a volume fraction of ∼0.5% [52]. SPPs were found to have positive effects on the mechanical properties and oxidation rates of Zr alloys but negative effects on hydride precipitation, as they act as microstructurally local stress-raisers, in other words, heterogeneous sites for hydrides to precipitate at [16].

An attempt to quantify the hydrostatic stress field generated by a 0.4 µm diameter SPP in Zr has been done using discrete dislocation plasticity (DDP) model by Reali et al. [16], as shown in Figure 2.9. The model simulates a coherent β-Nb SPP using 2D DDP, point sources of dislocation dipoles (2D version of a Frank-Read source emitting loops) are randomly distributed around the particle, and so are point obstacles. The particle stress triggers plastic relaxation around it. Figure 2.9 shows the stress profile produced by an SPP on the basal plane, with strong compression inside the particle and large tensile stress ring around it.

Finally, according to studies by Washburn [80], Smith [81] and Zener [82], SPPs were found to have effects on grain growth in Zr. These effects include:

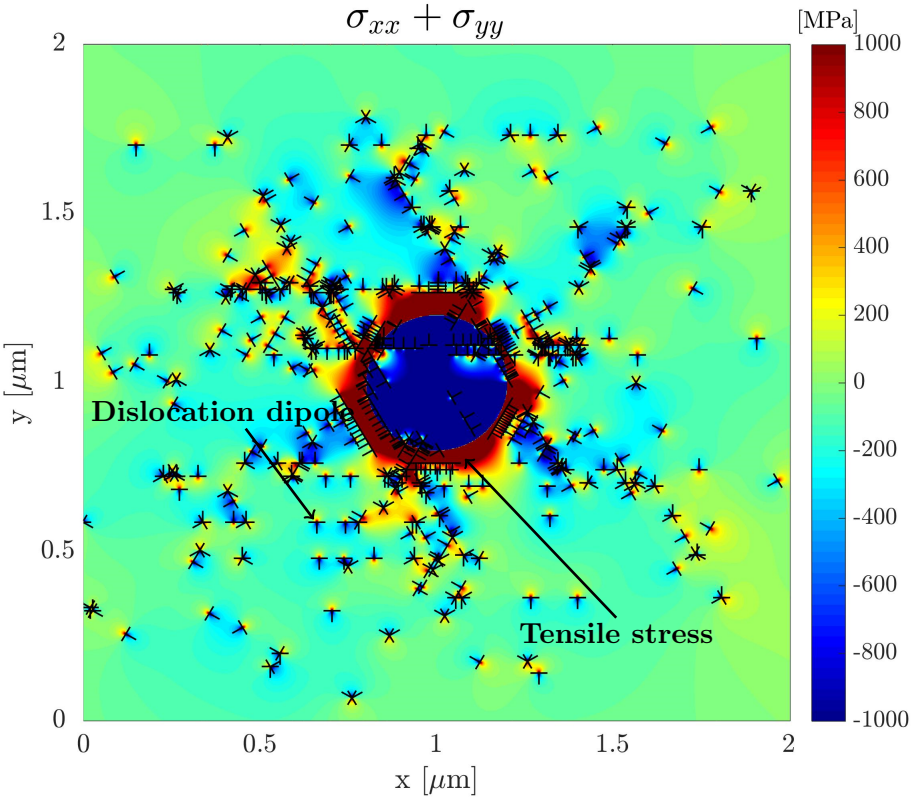


Figure 2.9: The hydrostatic stress field generated by a coherent β-Nb SPP, modelled using a 2D discrete dislocation plasticity simulation during SPP precipitation, that happens at high temperature during alloy processing [16].

1. Causing an incubation period for grain growth in Zircaloy-4

2. and causing growth of grains to stagnate leading to the inhibition of normal or abnormal grain growth. This is known as the Zener pinning effect and it occurs when *"grain boundary is moving through a matrix with second-phase particles, there is a tendency for the grain boundary to stick at the particles"* [82–84].

The level of SPP pinning, assuming a uniform SPP distribution, can be expressed by the dimensionless constant,

$$\psi = \frac{3F_v\bar{R}}{d} \tag{2.2}$$

where F_v is the SPP volume fraction (0.5% in Zr-4), d is the SPP diameter (~0.5 µm in as-received Zr-4) and $\bar{R}$ is the average grain diameter (15 µm in Zr-4). A high value of ψ (≈45 in Zr-4) indicates strong pinning, and ψ= 0 indicates no pinning [64, 82]. In single phase materials with no SPPs, normal grain growth will always occur to reduce interfacial energy. A positive value of ψ slows down the rate of

grain growth by exerting a pinning pressure which retards or inhibits grain boundary motion [64, 82].

Part II: Zirconium-Hydrogen System

2.8 Hydrogen Embrittlement

2.8.1 Hydrogen Ingress

Hydrogen atoms in the reactor core can be generated via any of the following H producing mechanisms [85]: (1) Zr corrosion reactions, (2) radiolysis of H_2O molecules in the coolant, (3) dissolved coolant hydrogen and (4) fuel oxidation.

2.8.1.1 *Zr Corrosion*

The chemical equation shown in Figure 2.10 outlines the generation of hydrogen by-products as a result of Zr oxidation. The parameter hydrogen pick-up fraction (HPUF) also known as $f_{Hpick-up}$ in the context of hydrogen in zirconium is commonly and solely used to refer to the ratio of hydrogen that enters the material over the total hydrogen produced due to the corrosion reaction only [86] where,

$$f_{Hpick-up} = \frac{H_{abs.}}{H_{corr.}}. \tag{2.3}$$

According to Flanagan et al. Zr-4 absorbs ∼15% of the hydrogen oxidation by-products as shown in Figure 2.10 [17]. The Figure only shows the theoretical hydrogen pick-up fraction for Zr-4, a value which varies with alloy content, coolant chemistry and may also vary under different reactor conditions. The other 85% of hydrogen atoms tends to recombine with another hydrogen atom to produce H_2 and dissipate through the water coolant.

Considering the main product of the equation in Figure 2.10, ZrO_2, that is regarded as a thin protective oxide layer (during pre-transition) of meta-stable nano-crystalline tetragonal zirconium oxide. This meta-stable layer which forms at the Zr-water interface later transforms into predominantly monoclinic phase under the equilibrium conditions of operational temperatures. Tetragonal-ZrO_2 is stabilised within the oxide via compressive stress-states due to the metal/oxide interface, reduced grain sizes and dissolved alloying elements [87]. ZrO_2 acts as the first barrier to hydrogen absorption into the zirconium metal. Figure 2.11(a) and (b) show both tetragonal and monoclinic phases respectively as

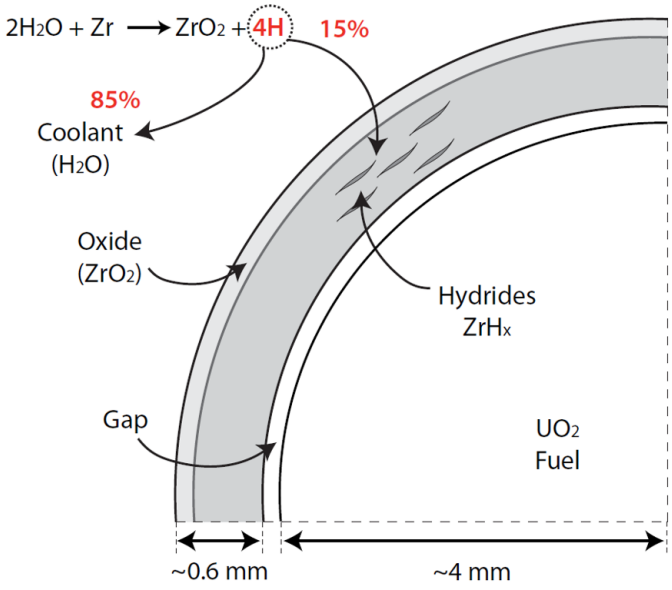


Figure 2.10: The absorption of hydrogen by-product due to oxidation, into Zr-4. Adapted from [7, 17].

found in ZrO_2. Tetragonal and monoclinic structures were found using synchrotron X-ray diffraction, TEM and transmission-EBSD to have tendencies to form in equiaxed and columnar grain morphologies respectively [88] as shown in Figure 2.11(c) [45, 89]. Referring to hydrogen ingress, the oxide layer was found to decrease hydrogen diffusivity as its volume fraction increases [90]. This phenomenon was also observed on deuterium ingress through the oxide layer [91].

Other than the oxide layer at the Zr/water interface, alloy composition was also found to have an effect on Zr corrosion and H pick-up. Correlations between H pick-up and alloy composition were established during the early development stages of zirconium alloys when Ni was found to increase H pick-up [37, 47, 92]. It was this breakthrough that lead to the development of Zircaloy-4 from Zircaloy-3 that contained a high Ni content which prevented the latter from reaching a commercial life. Since then, many studies have attempted to characterise the effects of intermetallic second phase particles (SPPs) on the corrosion and H pick-up in Zr [93–99]. A study by Tagstrom et al. [100, 101] on irradiated Zr-2 materials with 4 different SPP distribution, have shown that the number density of SPPs plays an important role in H pick-up as each particle acts as a favorable site for hydrogen ingress when the oxide barrier is thin. The size and shape of SPPs was also studied by Tagstrom et al., which was found to be less important with regards to H ingress, and both number density and size distribution were found to have smaller effects when the oxide layer begins to thicken. Studies on SPP size, morphology and distribution have shown that SPPs, even at small volume fractions (<0.2% in

Zr-702 and <0.5% in Zr-4 [48]), have a large effect on hydrogen ingress.

A recent study by Yao et al. [102] in an effort to better understand the role of SPPs in the hydrogen uptake of 4 alloys, Zr-4, Zr-2, N36 and N18, and four heat treatments for each alloy to produce specimens with different SPP size distributions and area fractions, has shown that the hydrogen pick-up fraction increases with samples containing a higher volume fraction of SPPs of small and large sizes. This trend was, however, reported to be compositionally dependent. Yao et al. also reported three different SPP particles namely, $Zr(Fe,Cr)_2$, $Zr_2(Fe,Ni)$ and $Zr(Fe,Nb)_2$ which have a strong ability for hydrogen absorption than α and β-Zr. They conclude thereafter, by suggesting that more hydrogen is absorbed in the SPPs than in the Zr matrix during the first stages of reactor operations (thin oxide layer, high temperatures, low neutron irradiation conditions), which is then released into the Zr matrix when the conditions change (SPP oxidises or dissolves due to irradiation or the temperature is reduced after an operating cycle) [9, 102]. Finally, a density functional theory study on the hydrogen accommodation in Zr-4 and Zr-2 SPPs by Burr at al. [103] has shown that $ZrCr_2$ and $ZrFe_2$, the boundary phases of the $Zr(Cr,Fe)_2$ solid solution are unfavourable for H accommodation compared to α-Zr. Conversely, $Zr_2(Fe,Ni)$ solid solution accommodate hydrogen readily, even compared to α-Zr. Thus, the presence of $Zr(Cr,Fe)_2$ SPPs will aid the transport of H through the oxide, while $Zr_2(Fe,Ni)$ SPPs do not, trapping the migrating H until these SPPs are dissolved or oxidised [103].

2.8.1.2 *Radiolysis of H_2O molecules in the coolant*

Radiolysis of water produces hydrogen peroxide along with diatomic hydrogen molecules *via* reaction 2.4 [85]:

$$2H_2O \rightarrow H_2O_2 + H_2 \tag{2.4}$$

Radiolysis alters the steam/hydrogen ratio as more hydrogen is produced. This contributes to the internal hydriding of the cladding [104].

2.8.1.3 *Dissolved coolant hydrogen*

Hydrogen was also found to be dissolved in the coolant of PWRs at 10 to 60 cm^3/kg. It was however calculated that this amount of hydrogen would make less of a contribution than radiolytically produced hydrogen in the amount of hydrogen ingress into Zr [85, 104].

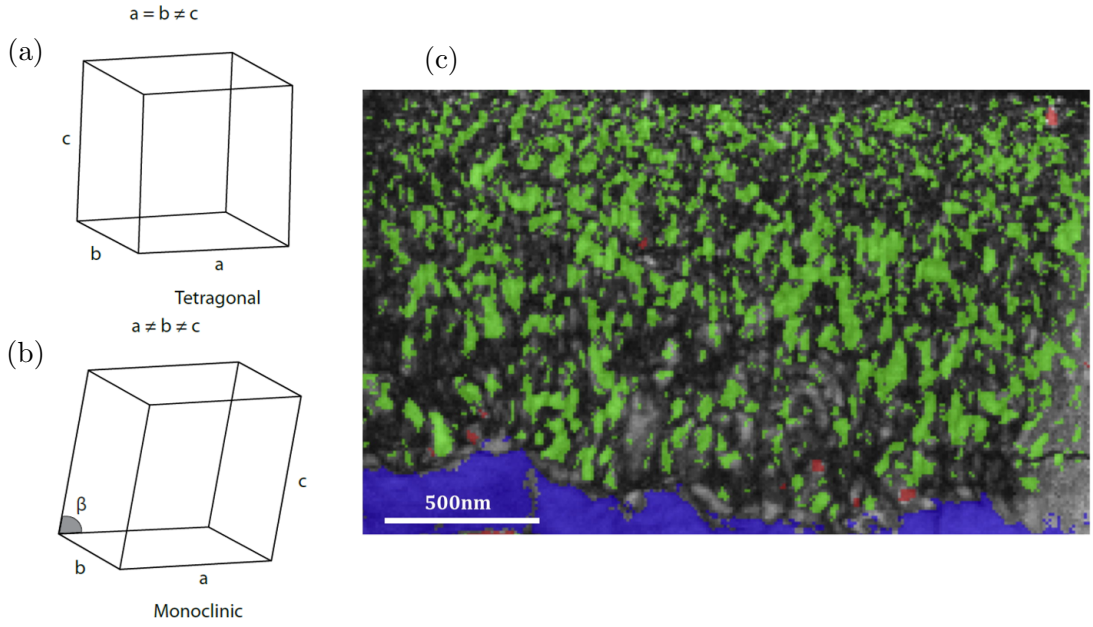


Figure 2.11: Tetragonal (a) and monoclinic (b) lattice unit cells along with (c) an EBSD phase map showing monoclinic ZrO_2 in green, tetragonal ZrO_2 in red and zirconium metal in blue [18].

2.8.2 Hydrogen diffusion in Zr

Once hydrogen passes through the oxide layer at the Zr/water interface to enter the Zr matrix, they diffuse throughout the cross-section of the cladding *via* entropy/stress-driven diffusion following Equation 2.5, where J is the hydrogen flux,[22]:

$$J = \frac{-DC_x}{RT}[RT\frac{dlnC_x}{dx} + \frac{Q^*}{T}\frac{dT}{dx} - V\frac{dP}{dx}] \tag{2.5}$$

where, C_x is the hydrogen concentration at any point along x (mol.m^{-3}), D is the hydrogen diffusivity (defined below in Equation 2.6),

Q^* is the heat-of-transport of hydrogen (∼10 kcal.mol^{-1} [19]), R is the universal gas constant (8.314 m^2.kg.s^{-1}.K^{-1}.mol^{-1}), T is temperature (K), V is the volume of transport of hydrogen, and P is the hydrostatic stress.

Diffusion Equation 2.5, considers two important factors that effect hydrogen diffusion, namely heat and stress. The hydrostatic stress gradient in Zr alloy components governs the diffusion process of hydrogen. When stress is absent, the migration of hydrogen is found to be governed by both temperature and concentration gradients. Although, stress cannot be truly absent in the microstructure, local

microstructural stress raisers such as SPPs and grain boundaries may also produce local hydrostatic stress gradient that effects hydrogen diffusion. Assuming stress in the microstructure is negligible, Hydrogen would tend to migrate via standard entropy driven diffusion from high concentration to low concentration and towards cold regions; once hydrogen diffuses towards cold regions, they start forming hydride phases once outside the solubility limit, and hence introducing new hydrogen concentration gradient in the solution. As the hydride concentration increases at cold regions in the matrix, a hydrogen flux is created from hot to cold regions [105]. The hydrogen diffusion rate in Zr tube cladding materials under reactor conditions is considered very fast at 1 mm/h.

The diffusion constant, D ($cm^2.s^{-1}$), for hydrogen can be defined by Equation 2.6 [19],

$$lnD = lnD_0(-\frac{Q^*}{RT}) \tag{2.6}$$

where, D_0 is a pre-exponential factor (7×10^{-3} $cm^2.s^{-1}$), Q^* is the heat-of-transport of hydrogen in a metal (activation energy for diffusion) ($kcal.mol^{-1}$), and T is the temperature (K).

Figure 2.12 shows the trends in the rate of hydrogen diffusion in pure zirconium, Zr-2 and Zr-4 as a function of material composition and microstructures [19]. Grain size, cold work, crystallographic texture and compositional variations have been found to have little effect on diffusivity in both Zircaloys. Transverse and normal directions have shown low activation energies for diffusion (gradient= activation energy) and are considered a potential consequence of the texture generated via processing, such that the degree of diffusion parallel to the c-axis is at its smallest in the longitudinal direction of the plate which contains the smallest concentration of c-axes. [19].

2.8.3 Solubility

The solubility limit of hydrogen in zirconium at room temperature is very low and was quantified by Kearns et al. to be just 1 appm [20]. Above this amount, hydrogen atoms precipitate out of the solid solution and form hydride (ZrH_x) phases.

The terminal solid solubility of hydrogen (TSS_H) in α-Zr is a function of temperature, and can be calculated using Equation 2.7 [7]:

$$TSS^H_{\alpha-Zr} = Aexp(\frac{-E_H}{T}) \tag{2.7}$$

where A is a constant, E_H is the difference in partial molar heat of solution of hydrogen in solid solution and partial molar heat of solution of hydrogen in hydrides [106] and T is the temperature in

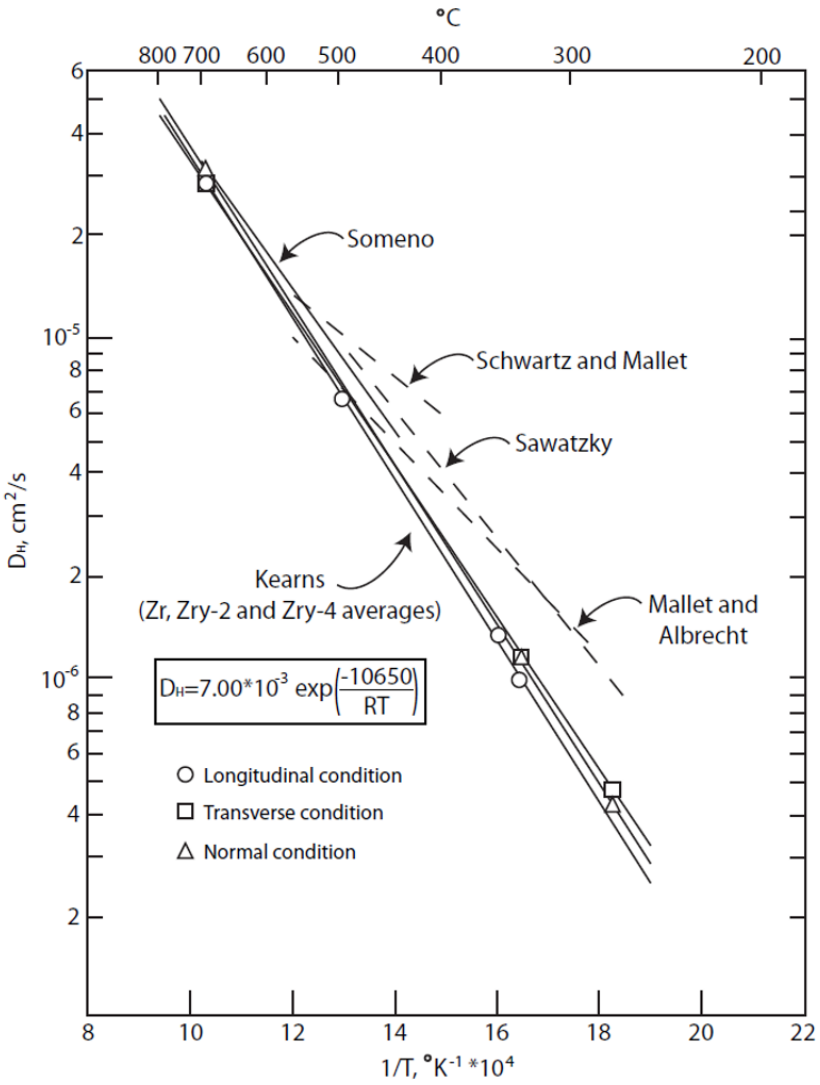


Figure 2.12: Comparison of hydrogen diffusivity data for a range of Zr and Zr alloys in different conditions across a range of temperatures. The standard deviation of best-fit curves is ±15% for normal conditions and ±5% for transverse and longitudinal. Adapted from [7, 19].

K.

Figure 2.13 presents Kearn's mean solubility curves of hydrogen in three zirconium materials. Results from Kearn's study and other previous investigations into hydrogen solubility are compiled into curves shown in Figure 2.13 [107–116]. The small variation in slope between pure zirconium and Zircaloy-2/4 suggests a negligible effect of SPPs which can therefore allow the assignation of a single Arrhenius curve, encompassing all data sets. This is presented by Equation 2.8 where R is 1.987 cal mol^{-1} and T is temperature in Kelvin. [20]:

$$TSS^{H}_{\alpha-Zr} = 1.2 \times 10^{5} exp(\frac{-8550}{RT}) \tag{2.8}$$

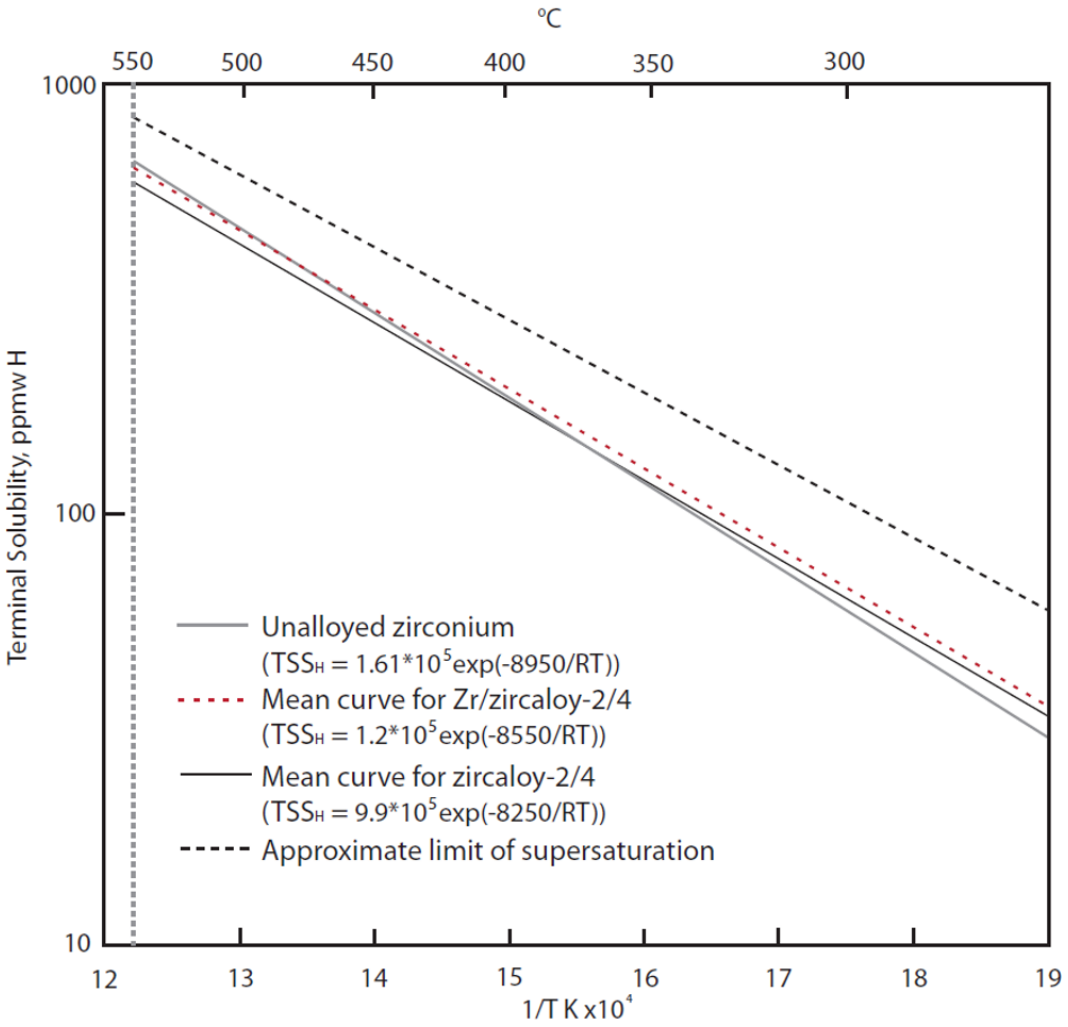


Figure 2.13: Compilation of terminal solubility data below 550°C for pure zirconium, Zircaloy-2 and Zircaloy-4. Adapted from [20].

Solvus, is another term used instead of hydrogen terminal solid solubility limits in zirconium. Solvus or TSS, which are functions of temperature (T), are the points at which the concentration of hydrogen in solution in α-Zr is in equilibrium with ZrH_x precipitates. At the solvus at any given T, the chemical potentials of hydrogen in α-Zr and ZrH phases are equal. In the α-Zr/H system there are two solvi, one for precipitation on cooling and the other for dissolution on heating. This postulated to be because of the elastic/plastic strain energy associated with the accommodation of the large volume expansion on hydride precipitation, governed by the misfit strains ($\sim$16%) [117]. Some of this strain energy is irrecoverable on dissolution and results in the hysteresis in a cooling - heating cycle [5]. At a given temperature

the hydrogen concentration in solution measured on heat-up, TSS_d or C_d, is lower than that measured on cool-down, TSS_p or C_p as shown in Figure 2.14. From the thermodynamic point of view, the difference between hydride dissolution on heating and hydride precipitation on cooling must in reality be due to microstructural energy barriers associated with nucleating a new phase that can only be overcome by increasing the difference in Gibbs energy of the two phases achieved by significant undercooling.

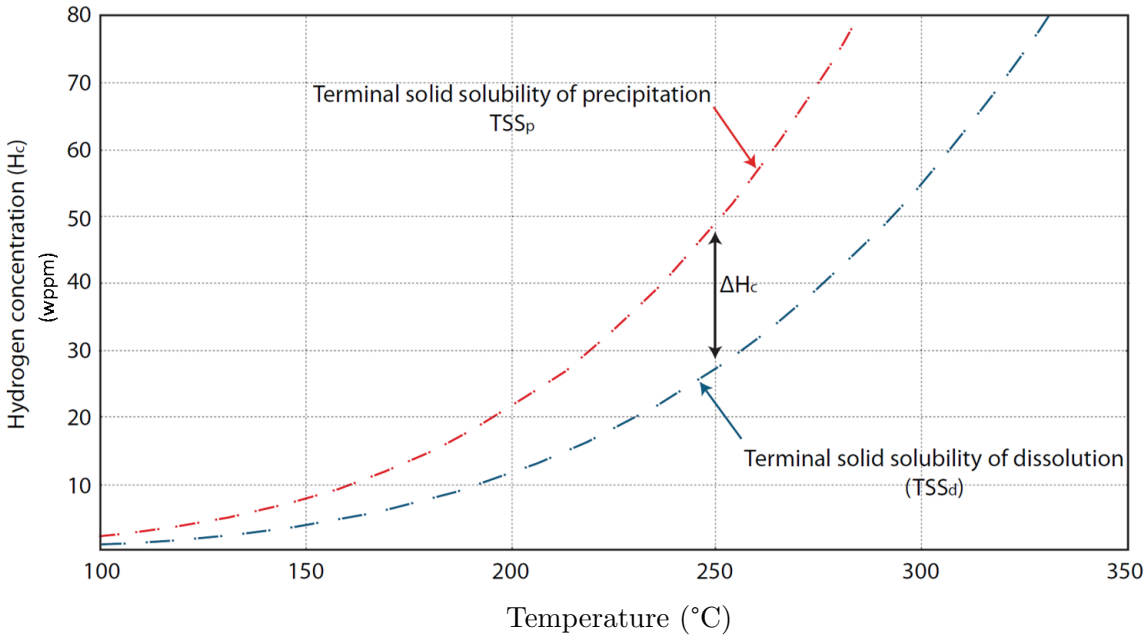


Figure 2.14: The hysteresis in the terminal solid solubility of hydrogen in Zircaloy-2 and Zircaloy-4 observed using differential scanning calorimetry, where ΔH_c is the difference in hydrogen concentration at a given temperature between the heat-up curve (blue) and the cool-down curve (red). Adapted from [21].

Hydrogen solubility in Zr can be effected by the following factors: (1) Irradiation, (2) stress, (3) oxygen content, (4) alloying elements, (5) point defects and (6) hydrogen getterers.

1. Irradiation

Irradiation has been found to have an effect on the TSS values of hydrogen in Zr. Irradiation was found to increase the TSS levels for both dissolution and precipitation as shown in Figure 2.15. Mean values for C_d and C_p for stress-free bulk unirradiated and irradiated Zircaloy-2 are given by the following equations [21]:

For unirradiated Zircaloy:

$$C_d = 106446.7 \times exp(\frac{-359891}{RT}) \tag{2.9}$$

$$C_p = 138746 \times exp(\frac{-34467.5}{RT}) \tag{2.10}$$

For irradiated Zircaloy:

$$C_d = 24236.1 \times exp(\frac{-28193.6}{RT}) \tag{2.11}$$

$$C_p = 212.1 \times exp(\frac{-8343.9}{RT}) \qquad (for\ T{<}170°C) \tag{2.12}$$

$$C_p = 66350.1 \times exp(\frac{-29574.6}{RT}) \qquad (for\ T{>}170°C) \tag{2.13}$$

where C_d and C_p are in wppm and T is the temperature in Kelvin.

In unirradiated materials such as ones used in this project, at a temperature of 20°C, TSS_d and TSS_p are <1 wppm and approximately 5 wppm respectively. At a temperature of 350°C dissolution and precipitation limits increase to approximately 60 wppm and 124 wppm respectively. Irradiation of Zr specimen was found to increase hydrogen solubility due to a mechanism rationalised as irradiating defect trapping, as suggested by Vizcaino et al. [118].

2. Stress

Dominant stress concentration features (SCFs) in Zr specimens, such as notches, cracks or defects, have a long range effect on hydrogen diffusion/transport along with an effect on hydrogen solubility and is now considered during cooling stages. In thermodynamic equilibrium: The chemical potential of hydrogen in the stressed hydride at notches is equal to the chemical potential of hydrogen in α-Zr in the relatively unstressed bulk. (partial molar volumes of hydrogen in solid solution in α-Zr and in ZrH_x are approximately equal ($V_{H\alpha} \approx V_{H\delta}$)) [5, 119, 120].

During cooling:

$$RTlnC_{p\sigma} = -(g_{H,\alpha} - g_{H,\delta}) - (\sigma - \sigma_0)V_{H\alpha} + \frac{\overline{W^c_{acc}}}{x} \tag{2.14}$$

where σ and σ_0 are the hydrostatic tensile stress at SCFs such as notches and in the unstressed bulk respectively, $C_{p\sigma}$ is the hydrogen concentration in the bulk that is in equilibrium with hydrogen in the stressed hydride at the notch, $\overline{W^c_{acc}}$ is the accommodation energy on precipitation averaged over

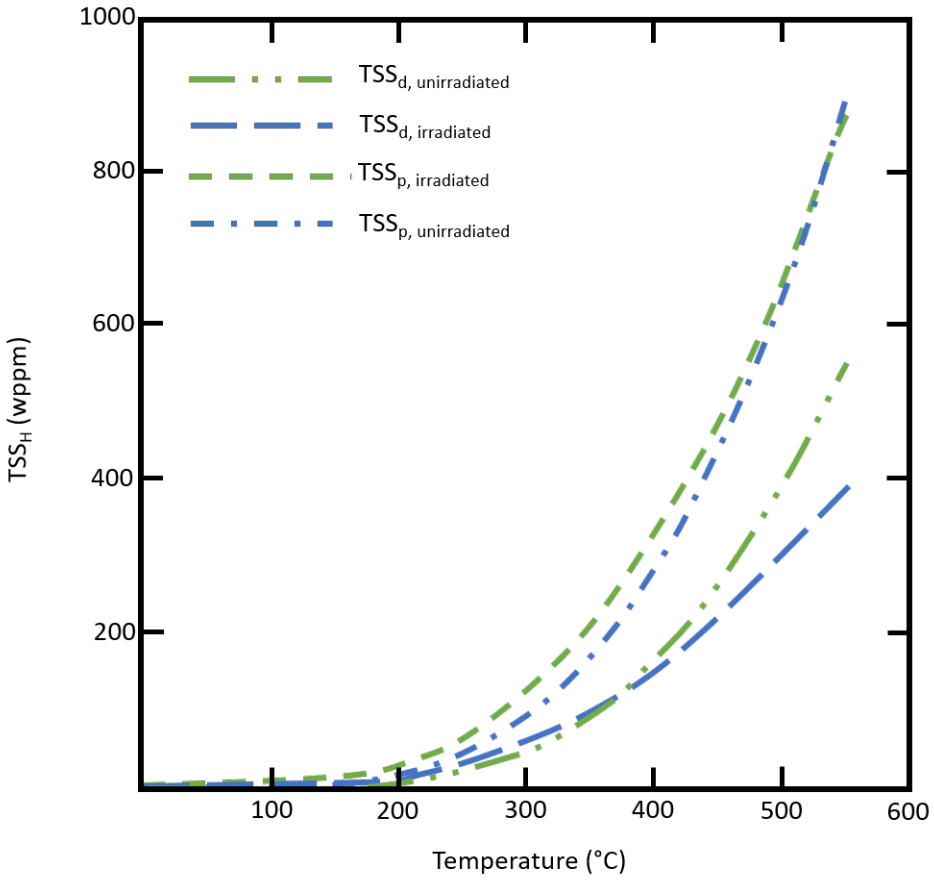


Figure 2.15: Comparisons between $\mathrm{TSS}_{d/p,irradiated}$ and $\mathrm{TSS}_{d/p,unirradiated}$ for Zircaloy-2. Adapted from [7].

all orientations relative to the applied stress, $g_{H,\alpha}$ and $g_{H,\delta}$ are the chemical potentials per mole of H in α-Zr and δ-Zr respectively and $V_{H\alpha}$ is the partial molar volume of H in α-Zr. In thermodynamic equilibrium:

$$(g_{H,\alpha} - g_{H,\delta}) - \frac{\overline{W^c_{acc}}}{x} = Q_{p\sigma} - T\Delta S_c \tag{2.15}$$

where ΔS_c is the entropy and Q_{pa} the heat of solution of ZrH_x in α-Zr in the presence of stress. Assume that the entropy terms are independent of stress we find for the precipitation solvus that:

$$C_{p\sigma} = \frac{Bexp - (Q_{p\sigma} + \Delta\sigma V_{H\alpha})}{RT} \tag{2.16}$$

where $\Delta\sigma = (\sigma$ - $\sigma_0)$. The heat of solution $Q_{p\sigma}$ is related to that at zero stress by the equation:

$$Q_{p\sigma} = Q_p - \overline{W^c_{acc}} + W^c_{acc} \tag{2.17}$$

from which it follows to:

$$C_{p\sigma} = C_p exp - \frac{(\Delta\sigma V_{H\alpha})}{RT} \times exp(\frac{\overline{W^c_{acc}} - W^c_{acc}}{RT}) \tag{2.18}$$

Thus if the accommodation energy, averaged over all stress orientations, is independent of stress ($\overline{W^c_{acc}} = \mathrm{W}^c_{acc}$), the effect of stress will come from only the following hydrostatic stress term: $\delta\sigma V_{H\alpha}$. The equation can therefore simplify to:

$$C_{p\sigma} = C_p exp(-\frac{(\Delta\sigma V_{H\alpha})}{RT}) \tag{2.19}$$

Given that, during cooling, $C_{p\sigma}$ defines the bulk concentration and C_p the SCF (local) concentration, Equation 2.20 can be rearranged to give a ratio of the local hydrogen concentration at the SCF to the bulk hydrogen concentration. However equation 2.20 can only be used for simplistic isotropic analysis of the hydrogen diffusion profile around the notch tip; it does not explicitly account for the spatial variation, HCP anisotropy and polycrystalline heterogeneity [40, 121]:

$$\frac{C_{HL}}{C_{HB}} = exp[\frac{V_H(\sigma_{HL} - \sigma_{HB})}{RT}] \tag{2.20}$$

where,

C_{HL}: Local hydrogen concentration at the peak stress location.

C_{HB}: Bulk hydrogen concentration remote from the stress concentration.

V_H: Partial molar volume of hydrogen in zirconium (1.67×10^{-6} $\mathrm{m^3\ mol^{-1}}$) [40].

σ_{HL}: Local hydrostatic stress at the stress concentration (Pa).

σ_{HB}: Bulk hydrostatic stress (negligible, relative to stress at SCF).

R: 8.314 kJ $\mathrm{mol^{-1}K^{-1}}$.

One important aim of this project is to highlight the importance of incorporating microstructural effects on hydrogen diffusion and hydride precipitation in the less stressed bulk and where stress gradients are introduced through SCFs. As mentioned previously SCFs in the form of notches, cracks or defects, are not the only stress raisers in Zr components; local microstructural features such as SPPs and grain boundaries, that exist due to alloying addition and polycrystallinity respectively, also produce microscale stresses that alter the hydrogen diffusion and hydride precipitation dynamic. Furthermore, hydrogen diffusion anisotropy in Zr, which has not been previously captured in theoretical

and numerical models, is also explored in this study.

3. Oxygen Content

An increased oxygen content in the Zr matrix was experimentally and computationally shown to increase hydrogen solubility as shows in Figure 2.16 [21, 118, 122]. According to McMinn et al., the reason for an increase hydrogen solubility with an increased oxygen content is the trapping of hydrogen at solute oxygen atoms, similar to the irradiation defect trapping mechanism proposed by Vizcaino et al. [118], or due to an increase in matrix strength. It is worth mentioning here that oxygen atoms that prefer to sit in octahedral sites of the HCP crystal also have an effect on hydrogen diffusion, for reasons later explained [118].

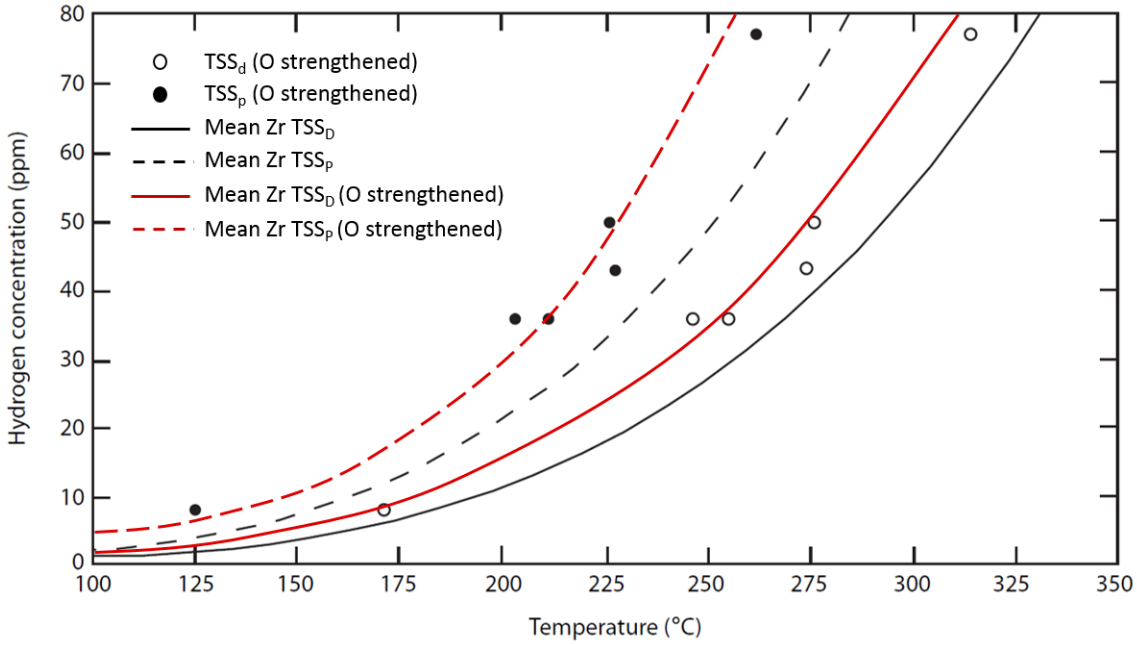


Figure 2.16: Hydrogen solubility data for oxygen strengthened Zircaloy-4. Adapted from [21].

4. Alloying Elements

Early studies on the influence of alloying additions on hydrogen solubility by Kearns and Kammenzind, have shown little effects [20, 123]. However, in 2005, a study by Muta et al. [124] on pure Zr and Zircaloy-2 of various alloying element concentrations, have shown, by means of a differential scanning calorimeter, that TSS_H for Zircaloy-2 is larger than that for pure zirconium, Ni or Cr additions increase TSS_H and finally Fe and Sn have no effect on the solubility.

5. Point Defects

Defects in the zirconium lattice such as vacancies can result in a hydrogen trapping mechanism that causes an increase in hydrogen solubility [125]. It was found by Christensen et al. that up to

nine hydrogen atoms can be trapped by a single vacancy in α-Zr leading to an increased solubility. Other defects, including dislocation loops, slip systems and grain boundaries, can also act as sinks for hydrogen, causing higher degrees of effect on solubility [7].

6. Hydrogen Gettering

Some alloying elements may getter hydrogen in zirconium and cause an increase in solubility limit of hydrogen. If the alloying element getterer has a low solubility in zirconium matrix itself and does not form intermetallic compounds, it would be present in the form of discrete particles that would act as internal sinks for hydrogen but not otherwise interfere with the alloy. For nuclear applications the getter should also have a reasonably low capture cross-section for thermal neutrons and Yttrium has been suggested by Coleman et al. [126] to fulfill gettering requirements. Research on yittrium hydrides have also been conducted by Beck et al. that showed that the free energy of yittrium hydride formation is lower than that for zirconium hydrides [127], however when the concentration of yittrium was similar to that of hydrogen at 1.44 at% the getter may combine with oxygen instead of hydrogen thus not being a highly effective getterer [126].

2.8.4 Hydrogen Interstitial and Diffusion

Both theoretical and experimental work seem to suggest that hydrogen atoms preferentially occupy tetrahedral sites in hexagonal Zr owing to the anisotropy of the crystal structure. The tetrahedral sites have a trigonal symmetry; the H atoms form three equivalent bonds with the Zr atoms on the basal plane and one non-equivalent bond with the Zr atom along the axial ⟨c⟩-direction. Hydrogen atoms can also occupy octahedral sites (Figure 2.17(a)), which are larger than tetraheral ones (Figure 2.17(b)) [9]. The free energy difference between octahedral and tetrahedral site occupancy is very small, only a few kJ mol^{-1} [125]. Figure 2.17(c) shows the trigonal site of the octaheral basal face and the hexahedral site of the tetrahedral basal face. Another planar defect is found on the remaining faces of the polyhedra (which are shared between octahedra and tetrahedra), this is termed the non-basal trigonal site (Figure 2.17(d)).

Hydrogen atoms diffuse in solution from one interstitial site to another generally via a combination of entropy driven diffusion at high temperatures (from high to low concentrations) or stress driven diffusion at temperatures approaching the TSS_p point (from low to high hydrosatic tensile stress). A computational study by Christensen et al. has demonstrated that the solubility of hydrogen in zirconium increases under tensile strain and decreases under compressive strain proving that hydrogen is thermodynamically driven from regions of compressive strain to regions of tensile strain [125]. The

diffusion of hydrogen towards high tensile stress regions, leads to the precipitation of the detrimental zirconium hydrides, explored in the next section.

Considering Equation 2.20, hydrogen diffusion from a high tensile to a lower tensile (or compressive) region is treated in theoretical studies in isotropic systems due to the assumption of treating hydrogen interstitials as misfitting spheres without accounting for the tetrahedral interstitialcy and trigonal symmetry [30]. Studies by Khoda-Bakhsh and Ross [128] indicate that distortions created by tetraheral hydrogen interstitials in zirconium is that of an elongated sphere in which theoretically agrees with the notion of partial isotropy in basal plane diffusion, and anisotropy in the prism/pyramidal plane diffusion [30]. This means that hydrogen diffusion anisotropy in HCP microstructures must be accounted for as a step towards incorporating microstructural effects in theoretical models.

In order to model the hydrogen diffusion anisotropy, Equation 2.20 can be adjusted to account for the elastic interaction energy, between the non-spherical misfit diffusing hydrogen and the lattice, which mediates stress-driven diffusion [30]. Hydrogen tetrahedral interstitials create a local elastic misfit distortion in HCP crystals, which may or may not interact with other sources of elastic fields in the lattice, such as microstructurally local stress raisers, SPPs and GBs, or higher dimensional stress concentrators such as notches and cracks. This interaction defines an elastic interaction energy, and when large, hydrogen diffusion will be biased in one direction to reduce the interaction energy in the system.

2.8.4.1 Hydrogen Models

Density Functional Theory

Firstly, density functional theory (DFT) studies by Lumley et al. [129, 130] on H-H interactions suggest that hydrogen prefers a bimodal concentration distribution within the Zr lattice, suggesting that H-H interaction in solution can be regarded to be small in dilute solutions. Lumley et al. add that as hydrogen concentration in the lattice increase, the energy barrier for hydride formation, which is high at low hydrogen concentrations, will decrease, making hydride precipitation more energetically favourable. Other DFT studies by Burr et al. [103] on hydrogen and SPPs in Zr, suggest that $Zr(Cr,Fe)_2$ SPPs are unfavourable for H accommodation compared to α-Zr while $Zr_2(Fe,Ni)$ solid solution accommodates hydrogen readily [131]. Burr et al. investigated the solubility of H in the intermetallic phases, and calculated the solution enthalpies for H in the most favourable interstitial site in each of the intermetallic phases, and compared the data with the solution enthalpy of hydrogen

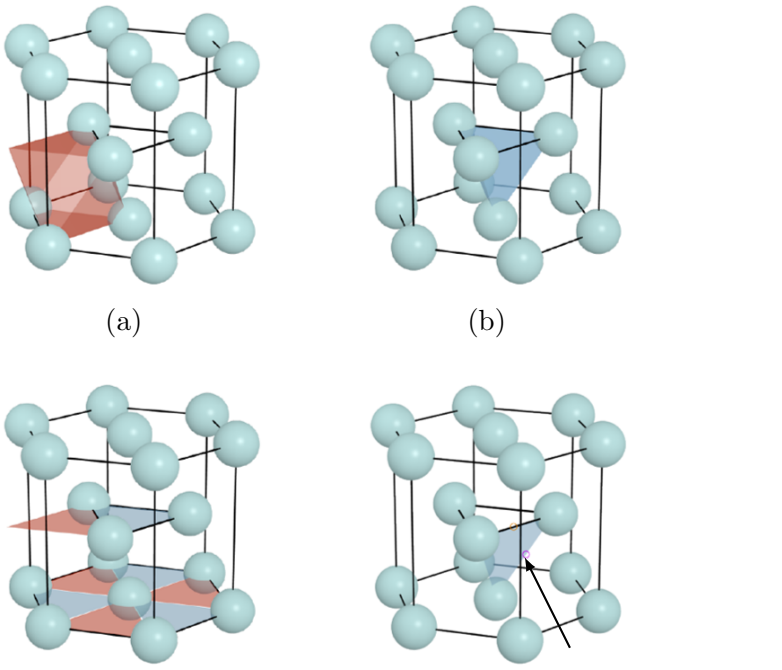


Figure 2.17: Interstitial sites in HCP crystals. The sites are defined by the centre of the polyhedra and triangle or by colored circles. Red corresponds to octahedral sites/faces and blue corresponds to terahedral ones. Adapted from [9].

in α-Zr.

Finite Element Modelling

Current finite element modelling (FEM) models of hydrogen diffusion in notched zirconium specimens typically compute the stress state and simulate the kinetics of stress-driven diffusion [132, 133]. FEM studies have so far ignored continuum scale anisotropy because the FE models do not account for the anisotropic crystallography of Zr at the atomic scale or the anisotropic polycrystallinity of Zr at the microscale. This requires the use of more advanced FE-based crystal plasticity models in which the compatibility stresses due to misoriented HCP crystals can be computed. Simulating the kinetics of hydrogen stress-driven diffusion, interstitial hydrogen atoms are usually modelled as a spherical misfits, an assumption which does not account for the atomistic scale anisotropy associated with the tetrahedral interstitial. Atomistic scale anisotropy is exhibited in the hydrogen diffusivity, which varies along the different crystallographic directions [6]. As zirconium alloy reactor components have a polycrystalline microstructure, hydrogen diffusion can be affected by the texture of many misorientated HCP crystals. Therefore, the hydrogen diffusivity may vary depending on the zirconium

alloy microstructure [40, 134]. Currently there exists a variety of commercial zirconium alloy materials, each of which has different microstructural properties [135]. Chapter 7 of this thesis establishes a multiscale framework for continuum stress-diffusion analysis which incorporates the atomistic scale anisotropy and polycrystallinity so that microstructural effects in different textures and grain structure can be simulated.

2.9 Hydrides in Zirconium

2.9.1 Phases in Zr

Zirconium hydrides are divided into three known phases and one transitional phase of different crystal structures and compositions. Hydride phases precipitate by their dependence on temperature along with cooling rate and hydrogen concentration [136]. The most important phase is known as the stable delta phase (δ-phase: $ZrH_{1.5-1.7}$) and is considered to be the non-stoichiometric most commonly observed, face centred cubic (*fcc*) phase. Other phases are called the gamma and the epsilon phases (γ-phase: ZrH and ϵ-phase: ZrH_2) thought to be stable and metastable respectively having a face centred tetragonal (*fct*) crystal structure. Finally, the zeta phase (ζ-phase: $ZrH_{0.5}$), that is now known to be metastable and trigonal in structure and is believed to be a transitional phase between α-Zr and δ or γ hydrides, however this is thought to be dependent on the alloy, its hydrogen concentration and cooling rate [136]. This ζ-phase was hypothesised in 2009 by Zhao et al. [137] to be crucial when it comes to the stress reorientation phenomenon of hydrides. This has been concluded after the observation of a highly strained field around these ζ-hydrides, and depending on the cooling rate of the material the ζ-hydrides can either transform into the γ-phase at fast cooling or the δ-phase at slow cooling. Ultimately, most literature agrees that the two hydride phases that are mostly associated with cracking in zirconium alloys are the δ and γ-phases. Figure 2.18 shows the hydrogen-zirconium system equilibrium phase diagram highlighting different phases of hydrides in Zr at different temperatures [138].

2.9.2 ZrH_x Morphology and Orientations

The morphology and orientation of ZrH_x, and factors effecting them, are important to quantify and understand as they can effect the degree of hydride embrittlement. The following factors have been reported in literature to impact morphology and orientation:

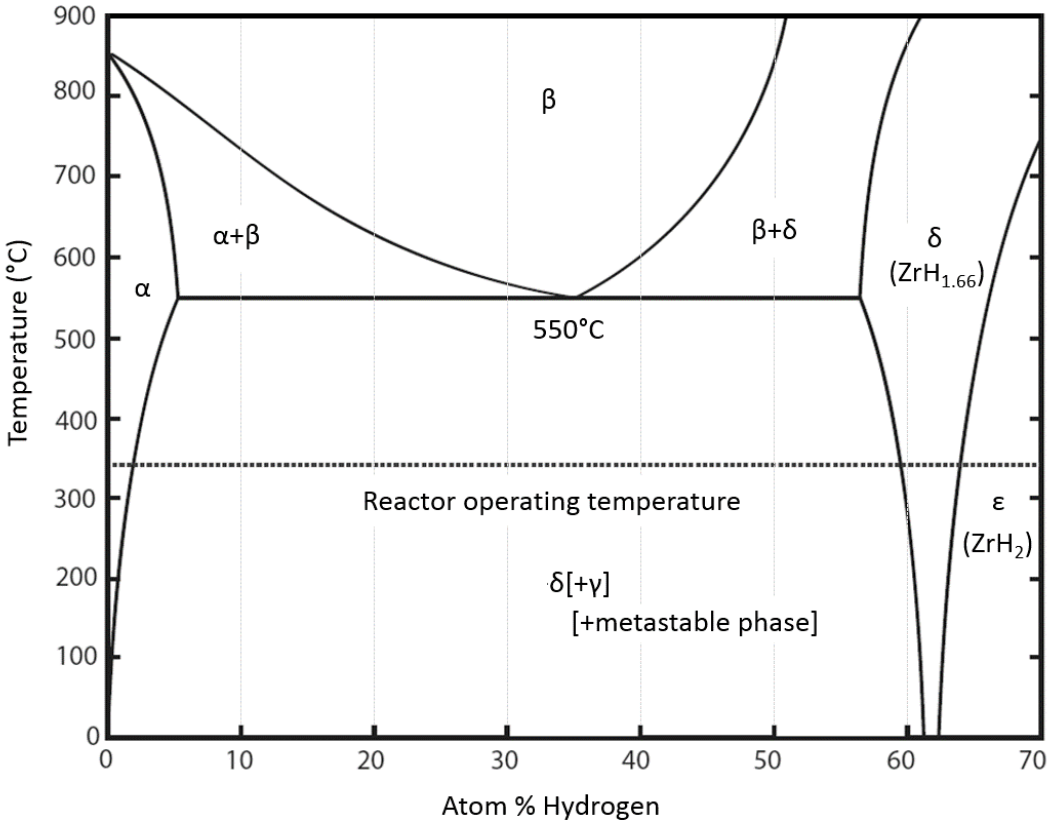


Figure 2.18: Zirconium-hydrogen phase diagram [22].

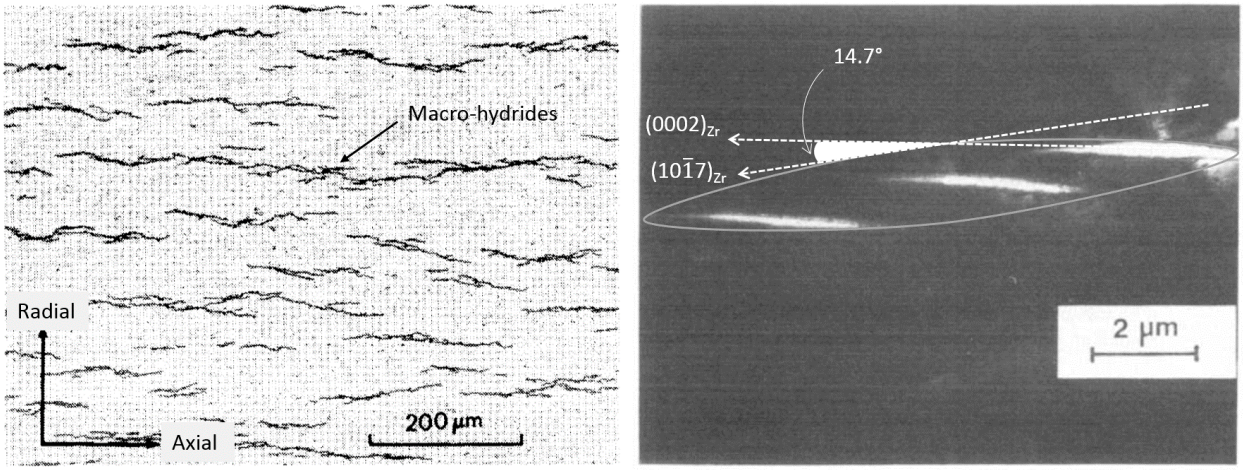
1. Cooling rate [139, 140].

2. Alloy and its fabrication history [141, 142].

3. Residual stresses from cold work [14, 143].

4. The level and direction of applied stress during hydride precipitation (mainly during cool-down). [144].

Macro-hydrides, observed using optical microscopy, were found to be made up of a collection of stacked micro-hydrides nucleating and precipitating on basal HCP planes. The orientation relationship between micro-hydrides and the α-Zr matrix has been reported in literature via electron microscopy studies, to be $\{0001\}_{\alpha-Zr}\|\{111\}_{\delta-ZrH}$, $\langle 11\bar{2}0\rangle_{\alpha-Zr}\|\langle 1\bar{1}0\rangle_{\delta-ZrH}$ [40, 142, 145]. The stacking nature of micro-hydrides precipitating on basal planes, results in the formation of macro-hydrides with a habit plane $(10\bar{1}7)$, which is around 15° from the basal plane as shown in Figure 2.19 [23, 76, 146].



(a) (b)

Figure 2.19: Optical image (a) of a longitudinal section of Zr2.5%Nb highly textured pressure tube alloy containing ∼300 wppm, showing a clear macro-hydride precipitation in the circumferential-axial plane of the tube. The stacking of micro-hydrides to form macro-hydrides can be seen using TEM (b) that also shows the habit planes for both micro and macro-hydrides [23].

2.9.3 Hydride Precipitation Sites

Hydrides in pure and alloyed zirconium were readily found to precipitate within grains, between them, or both, at sites displaying high energy such as grain boundaries and dislocations [145]. A study on hydride precipitation at grain boundaries has shown that hydrides prefer to precipitate at grain boundaries that are only aligned with the habit planes of the macro-hydrides in stress free samples [147]. This is however, dependent on the alloy and the hydrogen concentration in the samples. Other studies have described grain boundaries between grains as interfaces between misorientated crystals along which the atomic structure is locally distorted which suggests that grain boundaries are a localised stress-raisers which may be under either tension or compression. Stress-raisers, such as grain boundaries, dislocations, slip systems, twin boundaries and SPPs, may therefore act as favourable sites for hydrogen diffusion and thereafter hydride precipitation at low temperatures [40, 145, 146]. Generally, defects that may act as favourable intragranular hydride precipitation sites may include SPPs and dislocations [30, 148]. Intergranular sites are limited to grain boundaries, of which increase in density per unit volume as grain size decreases. The ratio between hydrides at intergranular sites and intragranular ones is highly dependent on thermal treatments and cooling rates. Slow cooling rates promotes the formation of intergranular hydrides at high energy grain boundaries, and fast rates predominantly causes the formation of intragranular hydrides [149]. The size distribution of hydrides is also affected by cooling

rates, along with applied stress [149]. In stressed samples, hydrides precipitate in regions that minimise the applied stress such as grain boundaries or intra-granular near-basal orientations perpendicular to the applied stress [23]. This tendency for hydrides to minimise the stresses at their precipitation site, gives rise to a hierarchy of preferred micro-hydride nucleation sites, in other words a competition between sites at long range stress-raisers (notches), that tend to produce dominant stress fields when loaded that can have a long range effect on hydrogen diffusion, and microstructurally local stress-raises (GBs, twins and SPPs), that produce a local stress field with a short range hydrogen diffusion effect [16]. Local stress-raisers also have a hierarchy of hydride nucleation potency, these can be classified as principle or subsidiary sites. Around or at a grain boundary many micro-hydride needles would nucleate and the subsequent autocatalysis would lead to a formation of a macroscopic hydride which is often seen in experimental work [148]. Intergranular hydrides have more influence on hydride-induced failure than intragranular ones as cracks are more likely to nucleate around intergranular hydrides because the slip system of the intergranular hydrides and the adjacent grains do not coincide. This situation induces higher stress and incompatible strain into the hydrides [150]. A strategy to quantify the potency of hydride precipitation sites as a function of grain size and SPP content is developed in chapters 5 and 6 to study the intra/intergranular precipitation dynamic and the competing effects on hydride precipitation between long range and local stress raisers.

2.9.4 Mechanical Properties of zirconium hydrides

2.9.4.1 Yield Strength

A study by Beck and Mueller [127] in 1960, on the tensile properties of bulk zirconium hydride specimens within composition ranges of $ZrH_{0.7}$ and $ZrH_{1.9}$ at the temperature range of 25 to 500°C, showed that macro-plastic deformation was not observed in δ and γ-phase hydrides. This indicates extreme brittleness of ZrH_x especially at compositional ranges of x=1.53-1.70 [40, 127]. Puls, Shi and Rabier [151] have studied the effect of varying x (H/Zr ratio) on zirconium hydride yield strength in Zr2.5%Nb, and they found that the yield strength decreases from 80-90 MPa for Zr2.5%Nb-$H_{1.3-1.6}$ to 50-60 MPa for Zr2.5%Nb-$H_{1.7-2}$. Temperature was also found to effect the yield of zirconium hydrides. Stress-strain curves obtained via compression testing of $ZrH_{1.66}$ in temperatures ranging from 22 to 453°C. Results show that $ZrH_{1.66}$ exhibits a high yield strength at all temperatures with increasing trend in ductility from a negligible amount at room temperature to a relatively higher value at 453°C as shown in Figure 2.20 [24]. Plasticity was clearly found to be present above 300°C, which suggest

that the degree of hydride embrittlement reduces at temperature above 300°C.

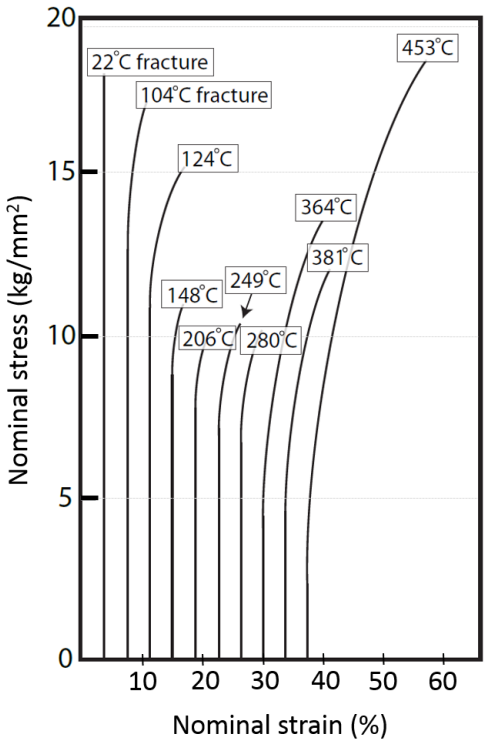


Figure 2.20: Nominal stress/strain curves for the compressive deformation of $ZrH_{1.66}$ in temperatures ranging from 22 to 453 °C. Adapted from [24].

2.9.4.2 Fracture Toughness

Due to the brittleness of zirconium hydrides relative to the Zr matrix, fracture toughness (K_{IC}) is therefore very low. Simpson and Cann [25] tested the fracture toughness of $ZrH_{1.66}$ in pure zirconium and Zr-2.5%Nb at room temperature and 300°C. They found that the fracture toughness of these δ-ZrH is 1 MPa$\sqrt{m}$ at room temperature and 3 MPa$\sqrt{m}$ at 300°C, as shown in Figure 2.21.

A study by Davies and Stearns [152] not only shows that hydrides reduce fracture toughness and ductility of Zr alloys, but specifically shows that as the amount of hydrides precipitated in preferred orientation increase, the fracture toughness decrease. The study was done on cold worked Zircaloy-2 pressure tubes whereby preferred hydride orientations are hydrides that align perpendicular to the principal applied stress. Radially oriented hydrides in fuel cladding zirconium alloys have been reported in literature as detrimental, as they cause crack propagation. Textured zirconium alloy tubes are generated to allow hydrides to precipitate circumferentially but hydrides manage to reorientate to

radial ones possibly due to ratcheting (thermally induced hydride reorientation usually after by a series of thermomechanical cycles during which hydrides repeatedly precipitate and dissolve). Hydride reorientation, explained in the next section, has been a large problem in industry and a topic of research since the 1960s [40].

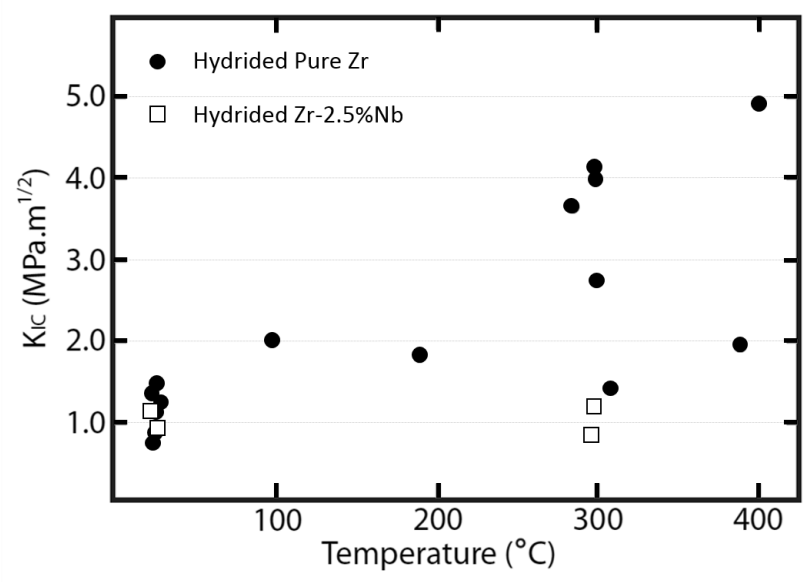


Figure 2.21: Temperature-dependence of K_{IC} for δ-hydrides in pure zirconium and Zr-2.5%Nb. Adapted from [25].

2.10 Hydride Reorientation

2.10.1 Conditions

2.10.1.1 *Stress*

It is established in literature, that hydride reorientation is dependent on the texture of zirconium alloys and occurs at a threshold tensile stress that varies with temperature. Simpson et al. [153] have quoted a minimum tensile stress for hydride reorientation in Zr-2.5%Nb tubes at 138 MPa without thermal cycling and as low as 50 MPa with thermal cycling. Other experiments on the threshold stress required for hydride reorientation were done by Schofield [5]. Schofield tested irradiated textureless Zircaloy-2 "V" notch specimens containing electron beam welds, that were loaded in four-point bending to an outer fibre stress of 550 MPa at temperatures between 290°C and 60°C. Results show that after 10 thermal ratcheting cycles, extensive hydride reorientation was observed throughout the tensile region. Schofield also conducted the same tests but on unirradiated weld Zircaloy-2 specimens, with a 0.2% offset yield

stress ($\sigma_{0.2}$) of ≈380 MPa and 146 MPa at 30 and 300°C respectively. Results shows that hydride reorientation was not prominent due to the relatively low yield stress in unirradiated material [5]. This latter observation is not yet fully understood and is explored in this project via thermomechanical testing of soft blocky-α hydrided microstructures.

2.10.1.2 *Grain Size and Cold Work*

Hydride reorientation in zirconium is reported in literature to be mainly controlled by texture, however, a study by Kearns and Wood [154] have shown that grain size and cold work (a simulant of irradiation damage) also play a role. Cold work introduces defects in the form of dislocations in zirconium alloys that lead to internal stresses. These stresses can either act as tensile concentration sites that can easily accommodate the volume change due to hydride precipitation, or compressive concentration sites that can also accommodate hydrides (specially at high wppmH) but far less favorable. The latter sites, when external high stresses are applied under cooling, can cause hydrides to precipitate out of them and re-precipitate at locations where the maximum strain energy can be relieved [7, 23]. Such locations can be considered to be energetically favoured sites for precipitation, such as dislocations (introduced via cold work) which results in intragranular hydrides.

Grain size was found by Kearns and Wood [154] to have a more dominant role in hydride reorientation than cold work. The trend was found to be a decrease in the reorientation as grain size increases. The reason for this observation is not fully understood, and is an area explored in this project. In addition previous work showed mostly qualitative trends; Chapters 4 and 5 aim to quantify the role of grain boundaries and other microstructural features in hydride precipitation.

2.10.1.3 *Hydrogen Content*

A study in 2008 on the effect of hydrogen concentration on hydride reorientation was done by Chu et al. [14] on Zircaloy-4 tube cladding specimens with concentrations of 130 to 600 wppm, thermally cycled for 24 hours at a constant hoop stress of 160 MPa for 0, 1, 4 and 12 cycles. Chu et al. have suggested that the concentration of hydrogen in Zr has an effect on hydride reorientation; the higher the hydrogen content in Zircaloy-4 cladding specimens the more susceptibility to hydride reorientation on cooling under a constant load is observed. At relatively low concentrations (130 wppm), after 12 thermal cycles at a constant stress, 75% of hydride were found to reorientate. At slightly higher hydrogen concentrations, the amount of reoriented hydride increase to 100% at 250 and 300 wppm. This observation was linked the different terminal solid solubity of hydrogen at different concentrations.

When the hydrogen concentration in the specimen is at 130 wppm, the temperature required for hydride nucleation and precipitation, which has a crucial effect of hydride reorientation, occurs only when the specimen was cooled to below 350°C. But in the specimens containing 250-300 wppm, precipitation immediately started once they were slowly cooled from the holding temperature of 400°C. The hydrogen diffusion rates therefore were relatively higher in the latter specimens at higher temperatures and the effect of stress on the hydride reorientation was significantly higher. Consequently, a smaller fraction of reoriented hydrides was obtained in specimens of lower hydrogen concentration of 130 wppm due to the lower hydrogen diffusion rates below 350°C. Finally, at 600 wppm reorientation decreases to a low 20%. The author proposed that this was a result of hydrides occupying unfavorable sites in as-hydrided specimens at 600 wppm at 0 cycles which limits the number of sites available for reorientation. Thus above 300 wppm the maximum amount of reoriented hydrides was inversely proportional to hydrogen concentration which agrees with other studies by Kearns et al. and Hardie et al. [154, 155].

2.10.1.4 *Thermal Cycling*

Previous studies have shown the effect of thermal cycling on hydride reorientation in Zircaloy-4 cladding specimens [14, 151, 156]. Texture, as mentioned, plays an important role in producing circumferential hydrides as the c-axis of the HCP crystals align perpendicular to the circumferential direction, however after several thermal cycles, the hydrides that have reoriented to locations where the strain energy can be relieved (in the radial direction if a large hoop stress in applied), were found to increase in concentrations to form stringers of reoriented hydrides. This was found to be due to a process called hydride ratcheting, whereby "successive thermal cycling can increase the amount of precipitated hydrides at stress concentration features if complete dissolution of the hydrogen inventory is not achieved (hydride phases are still present) at the peak temperature of the thermal cycle" [156].

2.11 Delayed Hydride Cracking (DHC)

DHC is a (slow) time-dependent crack growth mechanism in pure zirconium and zirconium alloys in which hydrogen atoms in solution diffuse from area of low hydrostatic tensile stress to higher ones [40]. Hydrogen atoms accumulate or cluster leading to the precipitation of zirconium hydrides once the diffused hydrogen concentration increase sufficiently, in the high tensile stress region, above the TSS_p. Brittle hydrides then accumulate and grow in size at the SCF until they fracture and result in a propagated crack that would introduce a new tensile stress region to repeat the mechanism.

Experiments on DHC indicate that fracture initiation happens when the hydride volume fraction at local tensile stress regions is high. DHC was confirmed by the observation of radiation leaks due to failures in several Zr components including (1) CANDU pressure tubes that had fractured following crack initiation in rolled joints, (2) BWR fuel pin cladding that had split axially due to the presence of massive hydride blisters and (3) weld caps in Zr-2.5%Nb components possibly due to large grains in the weld structure [5, 157]. The extensive literature on DHC is attributed to the multiscale nature of the mechanism. DHC involves three primary sub-processes. The first process is the atomistic scale diffusion of dissolved hydrogen atoms in the Zr matrix via either:

1. Stress-driven diffusion driven by the hydrostatic stress gradient towards tensile stress regions. The applied stress must be above a threshold value, which is temperature dependent, that causes hydrogen to diffuse, which later precipitates as hydrides below the TSS_p that align perpendicular to the principal stress. The biased hopping mechanism of hydrogen atoms during stress-driven diffusion occurs due to the misfit strain energy, caused by a hydrogen in the interstitial site of a Zr HCP crystal, that leads to hydrogen atoms avoiding hydrostatic compressive regions and migrating towards tensile regions [40]. If the applied stress is below the threshold value, then hydrogen will continue to diffuse via entropy driven diffusion from high to low concentration or from hot to cold regions. In the case of a tensile stress applied at a notch, the tensile stress acts as hydrostatic stress, drawing off the hydrogen in solution from the bulk to the notch region and thereby increasing the hydrogen concentration at the notch or C_{HL} when compared to that in the bulk region as such [5, 121, 158]:

$$C_{HL} = C_{HB} exp(\frac{V_H \Delta\sigma}{RT}) \tag{2.21}$$

where V_H is the partial molar volume of hydrogen in zirconium, $\Delta\sigma$ the difference in the hydrostatic stress between the bulk and the crack tip, C_{HB} is the hydrogen concentration in the bulk region. It is worth mentioning again, that this equation is isotropic and it does not account for the Zr alloy microstructure. Essentially, this equation would give the same results for different alloy microstructures of different chemistry, as long as the hydrostatic stress was the same. This equation is being modified in Chapter 7 through the multiscale theory and simulation

to introduce a model that attempts to account for the HCP anisotropy and the microstructural polycrystallinity.

2. Entropy-driven diffusion from regions of high concentration to low concentration. This type of diffusion is dominant in unloaded samples, but can also occur when an external tensile stress is applied. Hydrogen atoms that have already precipitated as hydrides at SCFs (after a high hydrogen volume fraction is reached) cause a reduction in hydrogen concentration, which may therefore lead to the diffusion of hydrogen from high to low concentrations (entropy-driven diffusion). In other words, stress-driven diffusion may be considered as a combination of the usual entropic-driven diffusion of hydrogen in the solid solution, which is usually random, and the effects of biased driving force, such as a tensile stress gradient, which provides some direction along which the hydrogen atoms tend to move towards. But some randomness always remains because temperature is non-zero and so entropy still controls some aspects of the diffusion.

Hydrogen diffusion from one tetraherdal interstitial site to another through the Zr lattice via both diffusion methods, with tetraheral sites being energetically favourable in the anisotropic HCP crystal [128], describes a mechanism known as stress-driven diffusion [40, 159, 160]. Following hydrogen stress-driven diffusion, hydrides precipitate when the solvus for hydride precipitation is reached near the SCF via a mechanism known as diffusion-controlled precipitation [161]. This is the second process of DHC, whereby the microscale precipitation of hydrides occurs when the solvus is reached at SCFs (long range stress-raisers) and local energetically favourable heterogeneous nucleation sites (local stress-raisers). Hydrides were found to relieve the stress when they precipitate and therefore a competition between precipitation sites arise depending on their energy levels [14]. This competition or nucleation potency is studied in this project, particularly in Chapters 4 and 5. The amount of hydride precipitated at SCFs depends on:

1. Stress levels at the site of precipitation.
2. Temperature and duration of applied temperature.
3. Thermal history (number of previous thermal cycles applied).
4. Presence of diffusable hydrogen.

The final process is the continuum scale fracture which corresponds to crack initiation and propagation in the hydride-rich regions. This project focuses on the first two processes of DHC described above.

2.11.1 DHC Initiation

Cracking initiation at a SCF due to hydride reorientation has been extensively studied for CANDU pressure tube Zr-2.5%Nb material by Sagat et al. [26] and in Zr-2 by Schofield [5], and are reviewed in the following section.

2.11.1.1 DHC Experimental Data

Sagat et al. [26] have studied DHC initiation in Zr-2.5%Nb pressure tube notched specimens containing ≈130 wppm of bulk hydrogen concentration. Sagat et al. tested seven different notch depths ranging between 0.05 mm to 1.0 mm and four different root radii 0.05 mm, 0.18 mm, 0.3 mm and 0.64 mm. Specimens with all combinations of the aforementioned notch geometries were subject to a constant dead weight load and were thermally cycled, on a weekly basis, between 295°C and 60°C. An extended hold of ∼5 days was applied during the cooling transient at a temperature of 250°C.

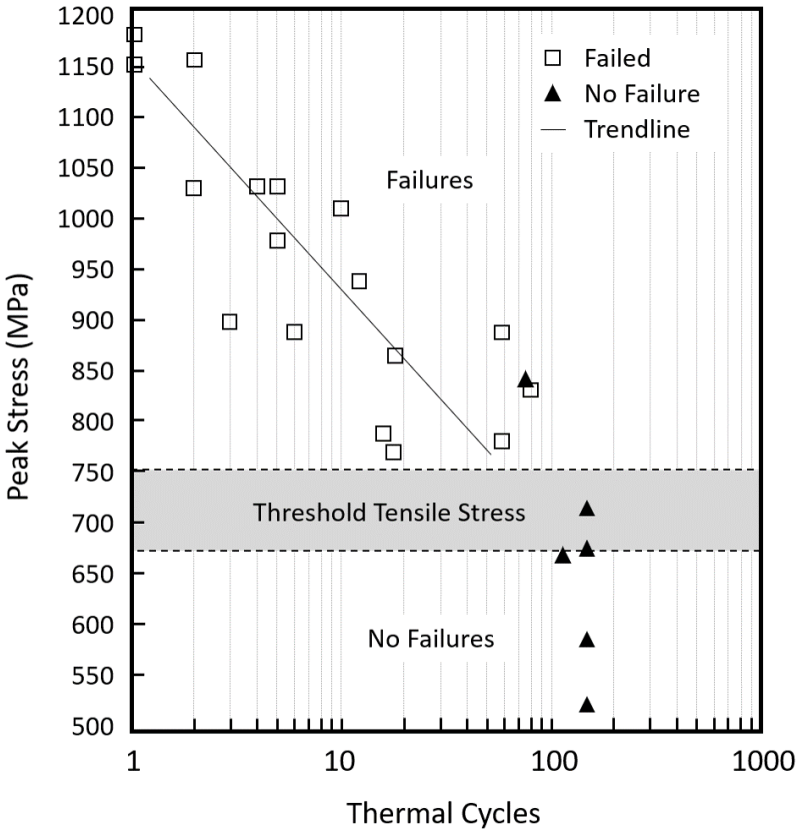


Figure 2.22: Number of cycles to DHC initiation as a function of the peak notch tip tensile stress. Adapted from [26].

Figure 2.22 shows results are of tests that lasted ∼4.5 years. The trendline for cracked or failed

specimen data indicates a reduction in the maximum notch tensile stress required for failure, as the number of thermal cycles increase. The results also show that a threshold tensile stress between 675 and 750 MPa is required for DHC initiation.

Similar work by Schofield et al. [5] who carried out an extensive programme of testing to investigate the potential for DHC initiation from 'V' and 'U' notches in irradiated textureless Zircaloy-2 electron-beam weld at a range of stress intensity factors (8-20 MPa$\sqrt{m}$) and a range of thermal cycles (10-198). Results from Schofield's test programme firstly show that hydride reorientation in irradiated Zr-2 samples can occur at the order of 50 MPa notch tip tensile stress, while hydride reorientation in softer (annealed and unirradiated) material does not occur at such low stresses. DHC initiation was found by Schofield to be detrimentally effected by cold holds below 60°C. Notch geometry effects were also found by Schofield to effect hydride precipitation; local notch tip crystallography can inhibit hydride re-orientation at a sharp 'V' notches in irradiated Zircaloy-2 electron beam giving rise to the so-called denuded zone possibly due to notch tip plasticity. This is in contrast to what was observed in Zr-2.5Nb pressure tube material where hydride precipitation readily occurs in areas of high stress [40]. Finally, at blunt 'U' notches, hydride reorientation was found to be more readily occurring within the high stress region at the notch tips. This was attributed by Schofield to the presence of increased numbers of preferred planes for orientation perpendicular to the direction of the applied principal stress in the enlarged high stress area.

2.12 Hydride Precipitation Models

Hydride Modelling

Finite element modelling has been used to study DHC initiation using the process zone approach which can predict the threshold stress for DHC initiation. The model reviewed here is the process zone model by Scarth and Smith [162]. Hydrided regions (process zones) ahead of SCFs were assumed to have averaged properties of hydride and Zr matrix which simulates the stress relaxation due to plasticity at a stress concentration. Cracking or DHC initiation takes place when the relative displacement across the discrete process zone at the surface or flaw root (which is related to the hydrided region thickness) reaches a critical value [5, 162]. The critical process zone displacement is calculated using Equation 2.22:

$$d_{crit} = \frac{{K_{IH}}^2}{E_0 p_{crit}} \quad where \quad E_0 = \frac{E}{1-\nu^2} \tag{2.22}$$

where p_{crit} is threshold hydride fracture stress. Note, the use of the Young's modulus E and the Poisson's ratio ν, shows that the process zone modelling do not account for any microstructural variations. Furthermore the process zone method is a practical engineering approach in that the mechanisms of hydride formation and fracture are not addressed in detail.

2.13 Summary

Zirconium alloys used in nuclear water reactors as fuel cladding, fuel assemblies and internal component materials are subjected to several types of stresses including thermal, mechanical and irradiation during reactor operation. However, zirconium alloys are prone to hydrogen ingress via (1) corrosion, (2) radiolysis of water and (3) fuel oxidation. When the concentration of hydrogen in the Zr solid solution exceeds the solvus limit for precipitation, like during reactor shut-down or post-operation storage, the phase transformation to brittle hydride precipitates occurs which can threaten the structural integrity of the component.

Hydrogen diffusion in zirconium components occurs via entropy and stress driven diffusion from areas of high to low concentrations and from low to high hydrostatic stress respectively. Hydride precipitation then occurs at microstructurally favourable precipitation sites when the hydrogen terminal solid solubility limit is reached. Hydrogen solubility in Zr can be effected by factors including (1) irradiation, (2) stress, (3) oxygen content, (4) alloying additions, (5) point defects and (6) hydrogen Gettering.

Hydride precipitation in zirconium were found to precipitate within grains, between them, or both, at sites displaying high energy such as grain boundaries. Studies have described grain boundaries between grains as interfaces between misorientated crystals along which the atomic structure is locally distorted, which suggests that grain boundaries are a localised stress-raisers which may be under either tension or compression. These studies suggest that some GBs under tension act as favorable sites for hydride precipitation, while other studies put forward the effect of crystallography of bounding grains on hydride precipitation. Studies however do not discuss the effects of grain size and GB density on the hydride precipitation distribution. Other stress-raisers, such as SPPs, have been reported to produce hydrostatic stress fields around them which may act as favorable sites for hydrogen diffusion and thereafter hydride precipitation, although experimental evidence showing hydride precipitates at or near SPPs have not been produced yet. Hydride precipitation and accumulation was also discussed in literature to be near or at stress concentration features such as notches, that can also be known as

long range stress raisers. Studies by Schofield et al. show that different notch geometries have an effect on hydrogen diffusion and hydride precipitation in an experimental DHC initiation study. Findings from literature however do not provide a link between microstructural effects on hydride precipitation and DHC. Experimental studies on hydride precipitation and reorientation are often treated at the macroscopic scale, with little regard to the effects of microstructure on the hydride precipitation distribution. Research questions that link microstructural stress raisers, that are favourable sites for hydride precipitation, and the initial stage of DHC, that involves hydride reorientation, have not been yet answered. The hydride precipitation dynamic and its effect on hydrige distribution and reorientation in stress loaded and unloaded microsctructures is not yet fully understood. A study that provides a better understanding of the hydride precipitation distribution in Zr microstructures containing different number of SPPs and different average grain sizes is useful and can also contribute to parameterising computational models that incorporate microstructural effects of zirconium to predict hydrogen diffusion and hydride precipitation.

Finite element models presented in literature, of hydrogen diffusion in zirconium components, typically compute the stress state and simulate the kinetics of stress-driven diffusion. FEM studies in literature have so far ignored atomic scale anisotropy because the FE models do not account for microstructural effects such as the anisotropic crystallography nor the anisotropic polycrystallinity of Zr. Chapter 7 describes a framework that highlights the importance of incorporating microstructural effects in hydrogen diffusion models, which have not yet been explored.

2.13.1 Research Strategy

Microstructural hydride nucleation sites, often not well understood in the DHC research field, are classified in this project as long range stress raisers (e.g. notches) and microstructurally local stress raisers (grain boundaries and SPPs). These stress raisers allow microscopic hydride needles to precipitate at their site which creates favourable conditions for another micro-hydride to precipitate in its vicinity; this autocatalytic nucleation sequence continues until macroscopic hydrides, known as macro-hydrides, are formed in loaded and unloaded conditions [40]. Current engineering DHC models do not explicitly account for favourable hydride microstructural sites in their techniques and so the need for understanding and providing a strategy that quantifies those sites is present in this field of research.

Initial experiments are conducted to quantify the macro-hydride precipitation without an externally

applied stress in the matrix of as-received and annealed grain size-enhanced Zr-4 and Zircadyne-702 (Zr-702, commercially pure zirconium). The number density, size distribution, area fraction and intra/inter-granular hydride percentage were quantified as a function of grain size and SPP content with the aim of studying the potency of inter-granular hydride precipitation sites (GBs) and intra-granular ones (SPPs). The results of these tests are presented in Chapter 5.

Similar hydride analysis, but on thermomechanically cycled Zr-4 (as-received and annealed grain-enhanced), is presented in Chapter 6, which shows quantification results of hydride precipitation due to both long range and local stress raisers after thermo-mechanical cycling of samples with two different notch geometries. The analysis was performed on notch tip and bulk hydride precipitation in conditions promoting the very early stages of hydride reorientation. Finally, a multiscale model is introduced in Chapter 7 that uses finite element modelling, sequentially parametrised by first-principles quantum mechanical calculations as well as irreversible thermodynamical analysis, to compute notch-tip hydrogen profiles with microstructural effects. This methodology unifies continuum scale stress analysis, using the finite element approach, and atomic scale stress analysis, using the elastic dipole tensor of point defects. The steady state notch-tip hydrogen profiles in mono and polycrystalline specimens are determined for different notch geometries and crystal orientations and compared with experimental observations.

Chapter 3

Experimental Methodology

3.1 Introduction and Objectives

This study examines the effects of microstructure on hydride precipitation in Zircaloy-4 (Zr-4) and commercially pure Zr (Zr-702). That is the effect of local microstructural features such a grain size, second phase particles and deformation twins, along with long range stress concentration features such as 'V' and 'U' notches. Zr-4 and Zr-702 alloys were supplied by Rolls-Royce and ATI metals respectively, in the form of hot-rolled and partially recrystallised plates with their respective chemical compositions shown in Table 3.1. Grain growth recrystallisation heat treatment, to enhance the grain size of both Zr-4 and Zr-702, was done at ∼800°C (test matrix shown in Appendix) (below the $\alpha \rightarrow \alpha+\beta$ transus temperature in Zircaloy-4) for 14 days in inert argon atmosphere at 10^{-3} Pa for 22 Zr-4 and 12 Zr-702 samples in multiple encapsulated tubes containing one sample per treatment. This heat treatment is similar to the one reported by Tong et al. and yields the formation of the blocky-α microstructures with uniform and bimodal grain sizes [64, 80].

Table 3.1: The chemical composition of Zr-4 and Zr-702. The full chemical composition of both materials is presented in Appendix A, measured by AMG Analytical ltd.

Elements	Cr (wt.%)	Fe (wt.%)	Nb (wt.%)	Sn (wt.%)	Hf (wt.%)	O (wt.%)	Zr (wt.%)
Zr-4	0.11	0.26	<0.05	1.51	<0.05	0.142	97.98
Zr-702	<0.05	0.09	<0.05	0.15	0.97	0.148	98.49

3.2 Metallographic Characterisation Techniques of As-received and Grain Size Enhanced Zircaloy-4 and Zircadyne-702

3.2.1 Optical Microscopy

Initial metallography of as-received and blocky-α microstructures was performed using polarised optical microscopy on mechanically polished samples of Zr-4 and Zr-702. The optical microscope used is an Olympus BX51 optical microscope with an attached Olympus DP70 camera. A range of magnifications from 5× to 50× was used to produce micrographs for image analysis. Sample preparation for optical imaging involves Bakelite powder mounting using a METASERV machine, followed by grinding with SiC grit papers (800-4000 grit) using a Struers TegraPol-21 grinding machine at a disk rotation speed of 300 rpm. After grinding, samples were mechanically polished using Struers Tegramin-20 automatic polishing machine for 10 hours at a force of 5 N and a 250 rpm disk rotation (to minimise grain deformation specially in blocky-α grains) using a neutralised colloidal silica, oxide polishing suspension (OPS). The OPS solution of a pH of around 9.8 was neutralised with H_2O_2 to minimise the formation of any undesired adhesive surface hydrides during polishing (H_2O:H_2O_2, 5:1). Samples were then cleaned from OPS using water and a common household detergent. After mechanical polishing and in order to reveal the grain structure, the samples were etched in a dilute acidic solution of HF:HNO_3:H_2O with a ratio of 5:45:50 followed by thorough rinsing in distilled water.

3.2.2 Scanning Electron Microscopy

Scanning electron microscopy (SEM) was used in this project to produce micrographs of hydride features with high contrast. The formation of such images lie in the fundamental penetration and interaction between electrons and the surface of the specimen. An electron beam, focused into a fine probe in the dry vacuum chamber of the microscope, dissipates its energy through several mechanisms. These will result in generated signals such as secondary electrons (SE), back-scattered electrons (BSE), diffraction backscattered electrons (BSD), used to determine crystallographic structure and orientation, and characteristic X-rays for use in elemental analysis. Secondary electrons are most commonly used to investigate a sample's morphology and topography while back-scattered electrons provide information on compositional variations according to atomic number.

SE and BSE are distinguished by their energy values with SE having energies as low as ∼50 eV

while the energies of BSE can be up to 30 keV. The low energy SE allows signal to be easily detected and collected by an area detector placed close to the probe due to their limited travel distance in order to produce a high quality image. BSE are reflected from the primary beam and interact elastically with the sample's atoms with little energy loss, allowing them to be back-scattered close to their original position. To collect as many back-scattered electrons as possible, the detector is placed underneath the probe above the specimen. BSE were used to produce micrographs containing SPPs that were analysed in as-received and blocky-α specimens. Sample preparation for SEM imaging is similar to that outlined in Section 3.1.1 but can also require additional 60 seconds electro-polishing after removing samples from Bakelite using a hacksaw. Electro-polishing was done using a mixture of 10% perchloric acid and 90% methanol at 30 V and a temperature of $\sim$ -42°C (solution cooled using $N_{2(l)}$), which potentially introduced hydrides of <5 wppm into the microstructure [7]. SE and BSE imaging were performed on samples after stub mounting using a Zeiss Sigma 300 and Auriga field emission gun (FEG) SEM instruments using an accelerating voltage of 5 keV and a 30 µm aperture at a working distance of $\sim$14 mm. SEM samples were mounted on SEM aluminium stubs using adhesive carbon tape and silver paint to reduce sample charging. As-received specimens were analysed at relatively high magnifications ($\geq$ 300×), while blocky-α specimens, containing large grains where analysed below 250×.

3.2.2.1 Electron Dispersive X-ray Spectrometry

X-rays created via the interaction of the primary electron beam with the sample surface are used to qualitatively micro-analyse the chemical composition of the Zr alloy matrix. The detector used for characterising X-rays in this project is an energy dispersive spectrometer (EDS), which is also known as energy dispersive X-ray spectrometer (EDX). EDX analysis of SPPs were done at magnifications of >10,000 at a working distance of $\sim$15 mm, an aperture of 1 µm and an acceleration voltage of 20 keV to detect small particles containing heavy atoms such as Fe and Cr, also using Zeiss Sigma 300 and Auriga field emission gun (FEG) SEM machines. Figure 3.1 shows the interaction of incoming primary electrons with a sample.

3.2.3 Electron Back-scatter Diffraction

Electron back-scatter diffraction (EBSD) is an SEM-based technique used to quantify microstructural information about the crystallographic nature the zirconium matrix. EBSD was used in this project to reveal crystallographic orientations, as well as information on grain size, grain boundary misorientation and texture. EBSD patterns are generated by electron interaction at the surface of the specimen, which

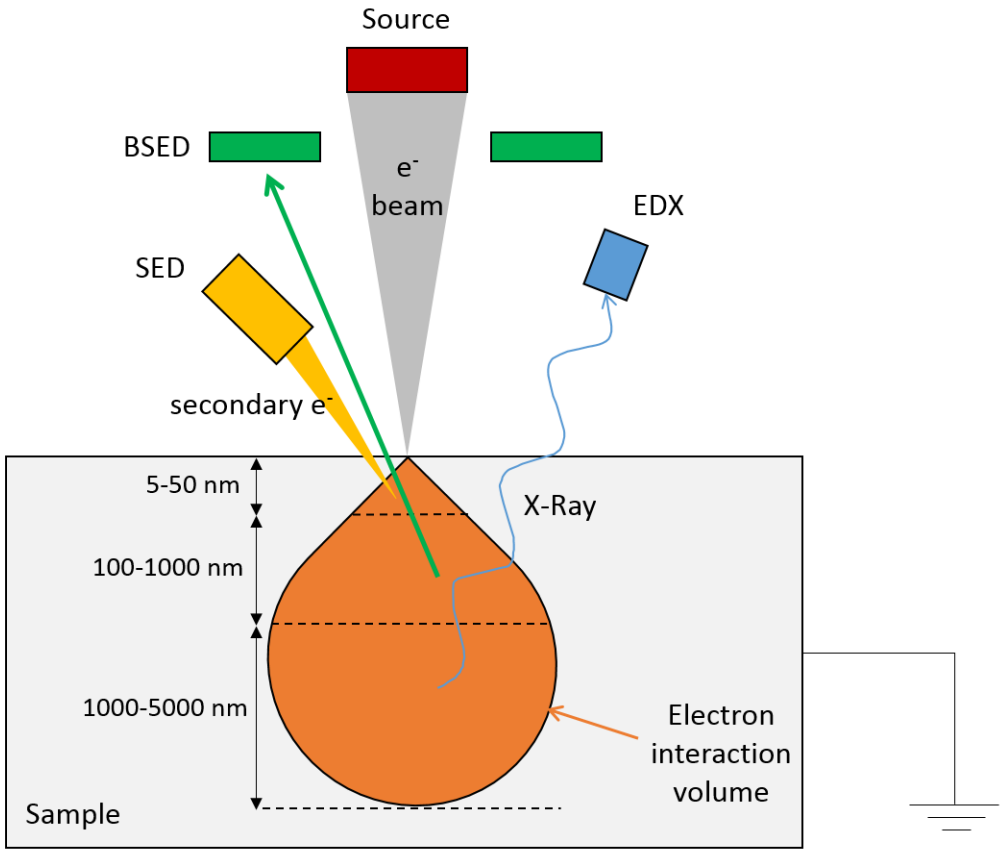


Figure 3.1: Useful SEM signals generated by electron–atom interactions. Secondary electrons (SE), back-scattered electron (BE) and X-rays are generated and detected by SE, BSE and EDX detectors. The electron volume interaction with atoms in shown in orange that reaches a depth of 5000 nm at an beam accelerating voltage of 20 keV.

is tilted to 70° to maximise the number of BSE hitting the detector. EBSD patterns are generated, known as Kikuchi bands, that correspond to an individual crystallographic plane. Each pattern is detected on a phosphor screen and is unique to the diffracting crystal structure and orientation with respect to an assigned frame of reference.

During this study, bulk as-received and grain size enhanced Zr-4 and Zr-702 samples were ground and electro-polished via methods similar to the one for SEM. Electro-polishing was also necessary to produce a defect free surface and maximise electron-atom interactions during EBSD mapping. All analyses were performed on a Zeiss Sigma FEG-SEM instrument using an accelerating voltage of 20 keV and a 120 µm aperture at a 1-1.5 µm step size. All specimens were titled at 70°, at a working distance of 15-20 mm with the EBSD detector 10-15 mm away from the sample surface.

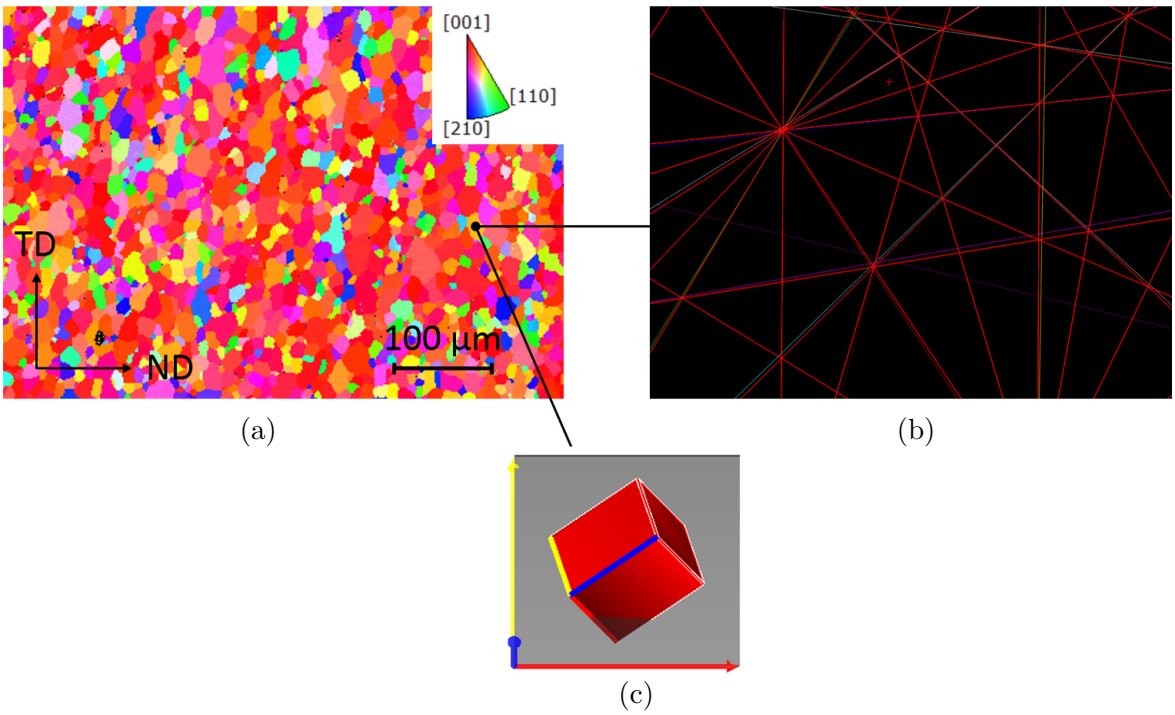


Figure 3.2: Electron back-scattered diffraction patterns (EBSPs) (a) are shown for a polycrystalline Zircaloy-4 sample at a step size of 1.5 µm, with (b) generated bands, representing crystallographic planes, from the individual grain selected from (a) along (c) the corresponding orientation of the hcp crystal in that selected -Zr grain.

Bruker ESPRIT 2 software was used for EBSD post-processing analysis to produce pattern quality maps, grain maps (for grain size measurement), phase maps, pole figures and inverse pole figures (IPF) for texture and finally grain analysis maps. The latter gives important information on misorientation distribution such as grain average misorientation (GAM), grain orientation spread (GOS) and grain boundary misorientation. GAM and GOS maps for polycrystals are plotted as a colour scale map to show regions of high and low angles from the grain average crystal orientation, corresponding to regions of high and low constrained slip, respectively [12]. GAM and GOS maps provide a qualitative measure of microstructural features with strain build-up or relief. GAM concern only neighboring measurement points and applies only to those lying in the same EBSD grain. The GOS is the GAM, but averaged over all points in one given grain to provide an estimate of the average amount of constrained slip in the grain during polycrystal deformation [163]. In general, grains with low GOS have low stored strain energy and grains with high GOS have high stored strain energy due to the high levels of plastic slip.

GOS is calculated as the average misorientation angle between each pixel size in the grain and the average grain orientation using equation 3.1 [15]:

$$GOS = \frac{1}{N}\sum_{i=1}^{N} g_i . < g >^T \tag{3.1}$$

where:

1. g_i is the orientation of pixel i in a grain,
2. $\langle g \rangle$ is the the average orientation of the grain,
3. and N is the total number of pixels

Crystal symmetry is applied to both orientations to find the minimum value. The GAM is calculated as the average misorientation angle between each point (in a grain) and its m adjacent points [15].

$$GAM = \frac{1}{Nm}\sum_{i=1}^{N}\sum_{j=1}^{m} g_i . < g >_j^T \tag{3.2}$$

3.3 Mechanical Properties Characterisation

The as-received mechanical properties of the material used in this project (Zircaloy-4 and Zircadyne-702) were characterised after a series of mechanical tests at 25°C and 350°C. Uniaxial tensile tests were carried out using the Zwick EZ-005 machine to provide an effective way to characterise the response to loading at room temperature and 350°C. Tensile tests on a total of six samples were performed at a strain rate of 0.001 mm s^{-1} to determine the yield strength (YS) and ultimate tensile strength (UTS) of the as-received Zr-4 and Zr-702 material along the plate rolling direction (RD) and transverse direction (TD). Dimensions of the tensile specimens are shown in Figure 3.3(a). Figure 3.3(b) shows the Zr-4 plate and (c) shows the vacuum chamber of Zwick EZ-005 machine used to test tensile specimens at 350°, heated using infrared (IR) bulbs and recorded using thermocouples connected to specimens.

The yield strength for specimens with blocky-α grains was calculated theoretically using the Hall-Petch equation due to the difficulty in capturing a sufficient number of grains in a tensile test specimen cross-section. Hall-Petch coefficients for pure zirconium at room temperature were reported by Armstrong et al. [73]:

$$\sigma_y = 29.42 + \frac{7.89}{\sqrt{D}} \tag{3.3}$$

where σ_y is the yield stress in MPa for an average zirconium grain diameter D in mm. The equation does not take into account the texture of the material and the alloying elements or impurities that tend to increase the tensile or yield strength of the alloy [74].

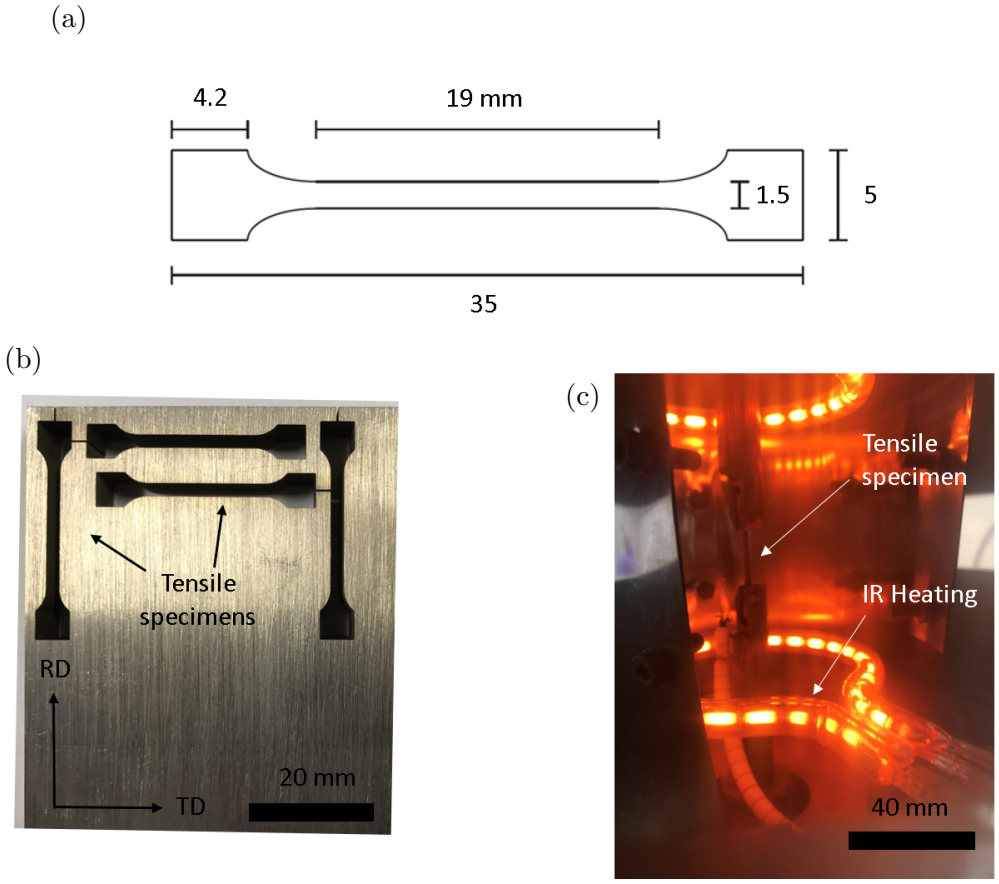


Figure 3.3: The dimensions of tensile (a) specimens used to determine the yield and tensile strength of Zr-4 and Zr-702 material. The RD and TD orientations of the tensile dogbone specimens is shown in the Zr-4 plate (b) along with the vacuum chamber (c) used for high temperature testing at 350°.

3.3.1 Hardness Testing

A macro-indenter was used to measure the room temperature Vickers hardness of as-received and grain growth annealed specimens. Hardness was measured before and after grain growth enhancment to estimate the difference in yield strength post heat treatment. Samples were indented 25 times per cm^2 on both sides of specimens. Load was applied at 10 N for 10 seconds. Vickers hardness number, the ratio of the load applied to the indenter to the surface area of the indentation, is calculated using Equation 3.4 [164]:

$$H_v = 2Psin\frac{(\theta/2)}{D^2} = \frac{1.8544P}{D^2} \tag{3.4}$$

where P is the applied load in kg, D is the mean diagonal of the indentation in mm, and θ is the angle between opposite faces of the indenter (136°) [164].

Estimating the 0.2% offset yield strength using Vickers hardness can also be done using an empirical relationship based on material flow curves. Equation 3.5 shows this relationship [165, 166]:

$$\sigma_{0.2} = \frac{H_v}{3} \times (0.1)^{n'} \tag{3.5}$$

where $\sigma_{0.2}$ is the 0.2% offset yield strength in kgf/mm^2 (= 9.81 MPa) and n is the exponent in Meyer's Law. The parameter n' is a material constant that relates to the strain hardening of Zr (= 2.5) [166].

3.4 Electro-chemical Hydrogen Charging

All hydride-containing samples used throughout this work were electro-chemically hydrogen charged. Samples with dimensions of 21 × 6 × 3 mm were cut for charging. An adapted version of the Lepage technique [27] was used and is based on the diffusion of hydrogen into the sample from an adhesive hydride layer produced using electro-chemical interactions. A simplified schematic of the charging technique is outlined in Figure 3.5. The zirconium cuboids acted as the cathode (negative sample-terminal) and a platinum mesh for the anode (positive inert-terminal) in order to limit any chemical material degradation throughout the process. Mechanical polishing, using 800 and 1200 grit silicon carbide paper at 5 N was done before hydriding in order to remove any surface oxides. The samples and mesh were spot welded to zirconium and platinum wires respectively using time parameters of five cooling and seven welding cycles with each cycle taking 0.02s. Charged at 2 kA m^{-2} in an electrolytic solution of diluted H_2SO_4 (H_2SO_4:H_2O-2:100), at a temperature of 65°C (±5°C), samples formed a uniform surface hydride layer, Figure 3.6(a). The relationship between hydriding time and hydride layer thickness before saturation at temperatures ranging between 20 to 100°C is shown in Figure 3.4 [22].

The thickness of the layer corresponded to a theoretical hydrogen concentration relative to the sample thickness. The relationship between the thickness of the hydride layer and hydrogen concentration in Zr is outlined in Equation 3.6 [27]:

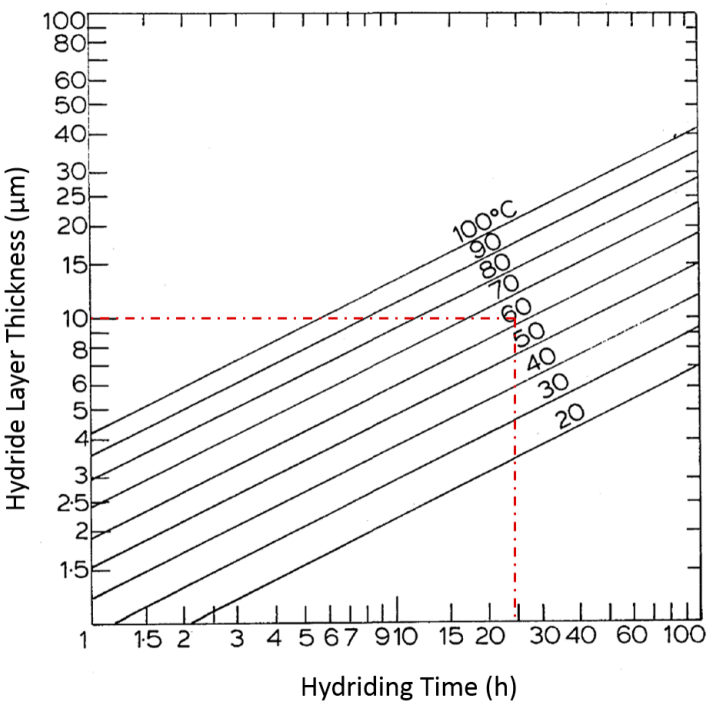


Figure 3.4: Relationship between hydriding time vs hydride layer for Zr-4 charging under a current density of 1 kA m^{-2}. The red dashed line, shows that hydriding Zr-4 for 24 hours produces a hydride layer thickness of 10 µm. Adapted from [22].

$$l_{hydride} = 7.232 \times 10^{-2}[H][l] \tag{3.6}$$

Where $l_{hydride}$ is the hydride layer thickness (µm), [H] is the hydrogen concentration (wppm) and [l] is the overall sample thickness (mm). Diffusion of the hydride layer into the bulk to form uniformly distributed hydrides was obtained via a thermal treatment with a temperature governed by the established hydrogen concentration from Equation 3.6 and determined using Equation 3.7:

$$TSS_H = [H] = A \times \frac{-Q}{RT} \tag{3.7}$$

where TSS_H is the terminal solid solubility of hydrogen in zirconium (wppm), A is a constant (1.2×10^5), Q is the activation energy for diffusion (8550 cal/mol), R is the molar gas constant and T is the temperature (K).

The hydride homogenisation temperature, correlating to the TSS_H for the estimated hydrogen concentrations, was used to determine the diffusivity constant D using Equation 3.8:

$$D = 7 \times 10^3 exp\frac{-Q}{RT} \tag{3.8}$$

The hydride homogenisation treatment time required for uniform hydrogen diffusion into the bulk, was calculated using Equation 3.9:

$$t_{annealing} = \frac{1.5 \times L^2}{D} \tag{3.9}$$

where $t_{annealing}$ is diffusion time and L is sample thickness. Figure 3.6(b) shows the Zr-4 microstructure post 4 hours homogenisation anneal at 400°C and furnace cool at a rate of 1-3°C with uniformly distributed macro-hydrides across the sample cross-section.

The EMGA-930 inert gas fusion (IGF) element analyser was used to experimentally measure the hydrogen concentration after electrolysis and hydride thermal diffusion. The method involved cutting four 0.15-0.30 g samples of Zr-4 specimens from hydrided materials at three different equidistant regions at edges and centre of the specimens. Specimens were ground after cutting using SiC 800 grit paper to remove any surface oxides. Specimens were then weighed to ±0.001 g after thorough rinsing in acetone. Specimens were later placed in a nickel crucible and inserted in the furnace electrode assembly before starting analysis, as outlined in the ASTM E1447 standard [167]. Hydrogen concentration data produced from the EMGA-930 were reported in this study.

3.4.1 Hydride and SPP Characterisation in Non-Cycled Samples

Hydride precipitation in hydrogen charged Zr-4 and Zr-702 unloaded specimens was characterised using optical and SEM imaging for 24 as-received (12 × Zr-4 and 12 × Zr-702 on the normal direction face of the hot-rolled, partially recrystallised plate) and 24 blocky-α samples (12 × Zr-4 and 12 × Zr-702), in a total area of ∼5 mm^2 per sample. Sample preparation for hydride characterisation involves mechanical polishing for 4-10 hours using a neutralised colloidal silica, followed by electro-polishing as previously described. Electro-polishing steps for SEM imaging is presented in Section 3.1.2 but instead performed for 30 seconds, to minimise chemical attack on hydride precipitates. Polarised optical microscopy was used to generate micrographs at magnifications of 5, 10 and 20×. Polarised optical micrographs, which produce high contrast between grains, particularly in the Zr anisotropic microstructure, were used to quantify the intragranular and intergranular fraction in samples. Examples of polarised optical micrographs, showing as-received and blocky-α Zr-702 microstructures containing

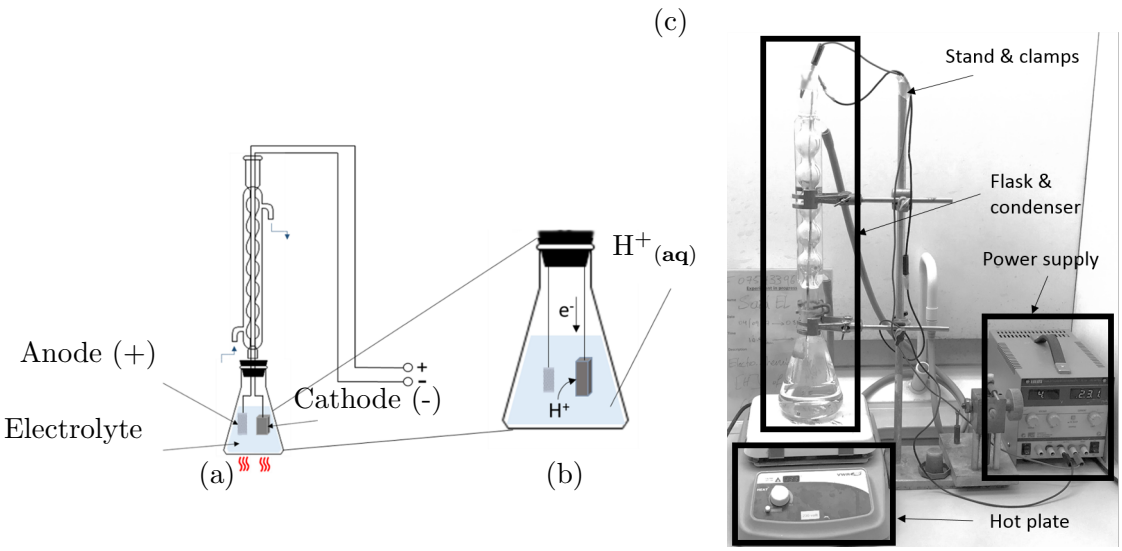


Figure 3.5: Electro-chemical hydrogen charging set-up used to introduce hydrides in zirconium specimens; (a) the anode Pt mesh and the cathode Zr sample were spot welded onto Pt and Zr wires respectively. The attraction between H^+ ions and the electrons is shown in (b) resulting in the formation of an adhesive hydride layer at the negative electrode [27].

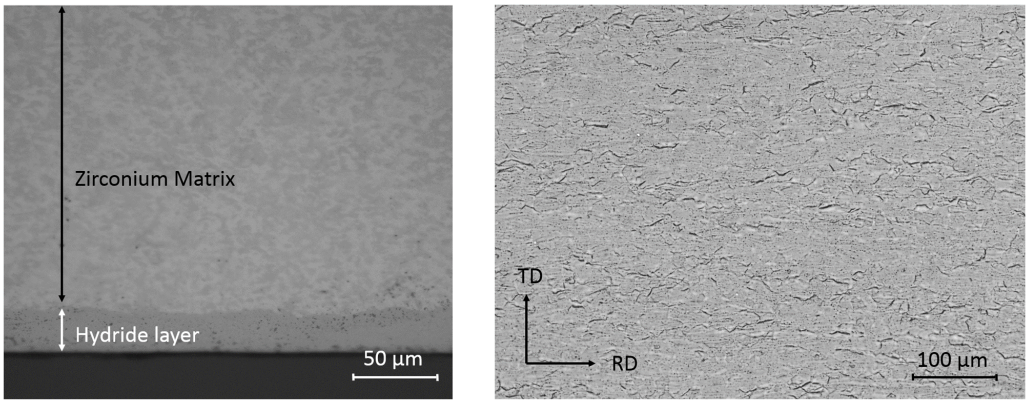


Figure 3.6: (a) Optical micrograph of a 10-20 µm hydride layer, visible along the sample cross-section. The hydride layer, produced via electro-chemical hydrogen charging, diffuses (b) throughout the sample thickness showing alignment along the sample RD.

intra and intergranular macrohydride features, are shown in Figures 3.7 and 3.8. The counting process of inter and intragranular hydrides employs the following rules: Intergranular hydrides are defined as black macro-features that form on grain boundaries only, from end-to-end. Intergranular hydrides form features that follow the same geometry as the grain boundary, and hence they are easily identified. Intragranular hydrides are defined as black macro-features that either (1) form completely inside grains (end-to-end), (2) form inside grains and propagate at grain boundaries or (3) form inside one grain,

cross a grain boundary and propagate into another (transgranular). The direction of intragranular hydrides tend to be governed by the grain crystal structure. Figures 3.7 and 3.8 show intergranular, intragranular and transgranular macro-hydrides in as-received and blocky-α microstructures.

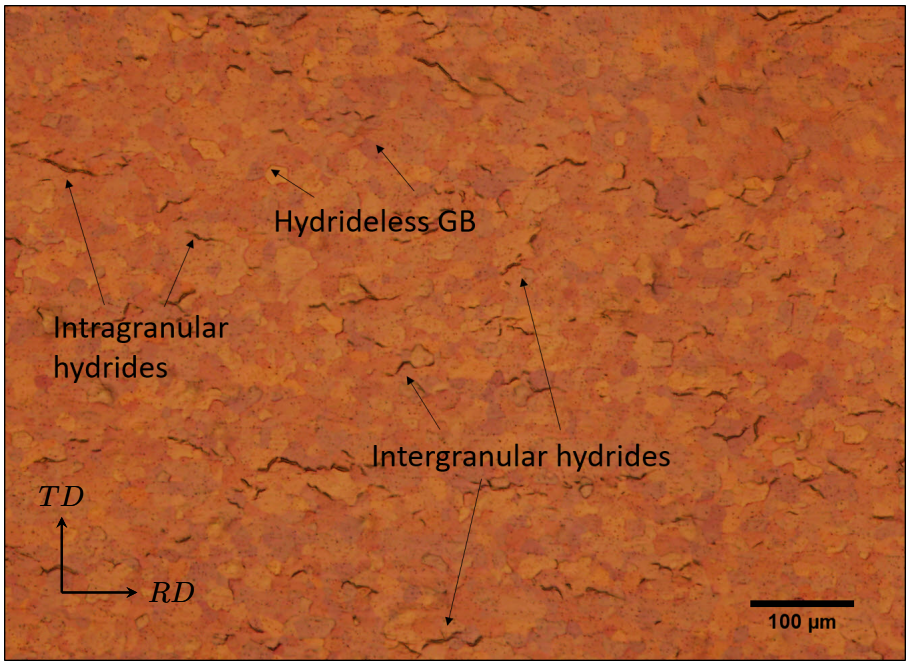


Figure 3.7: Polarised optical micrograph of as-received Zr-702 used for macro-hydride characterisation.

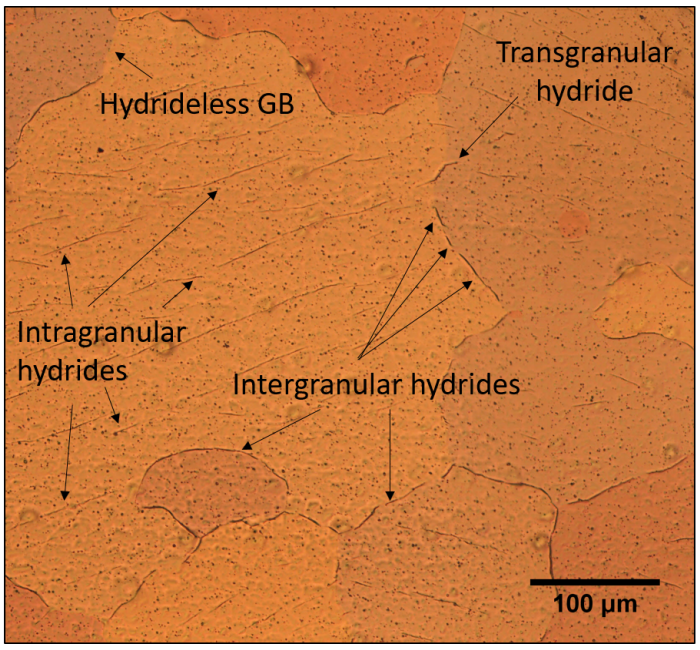


Figure 3.8: Blocky-α microstructure containing inter, intra and transgranular hydrides. The latter is considered to be in the same category as intragranular hydrides.

In order to perform quantitative analysis on macrohydride precipitates, the Fiji ImageJ software

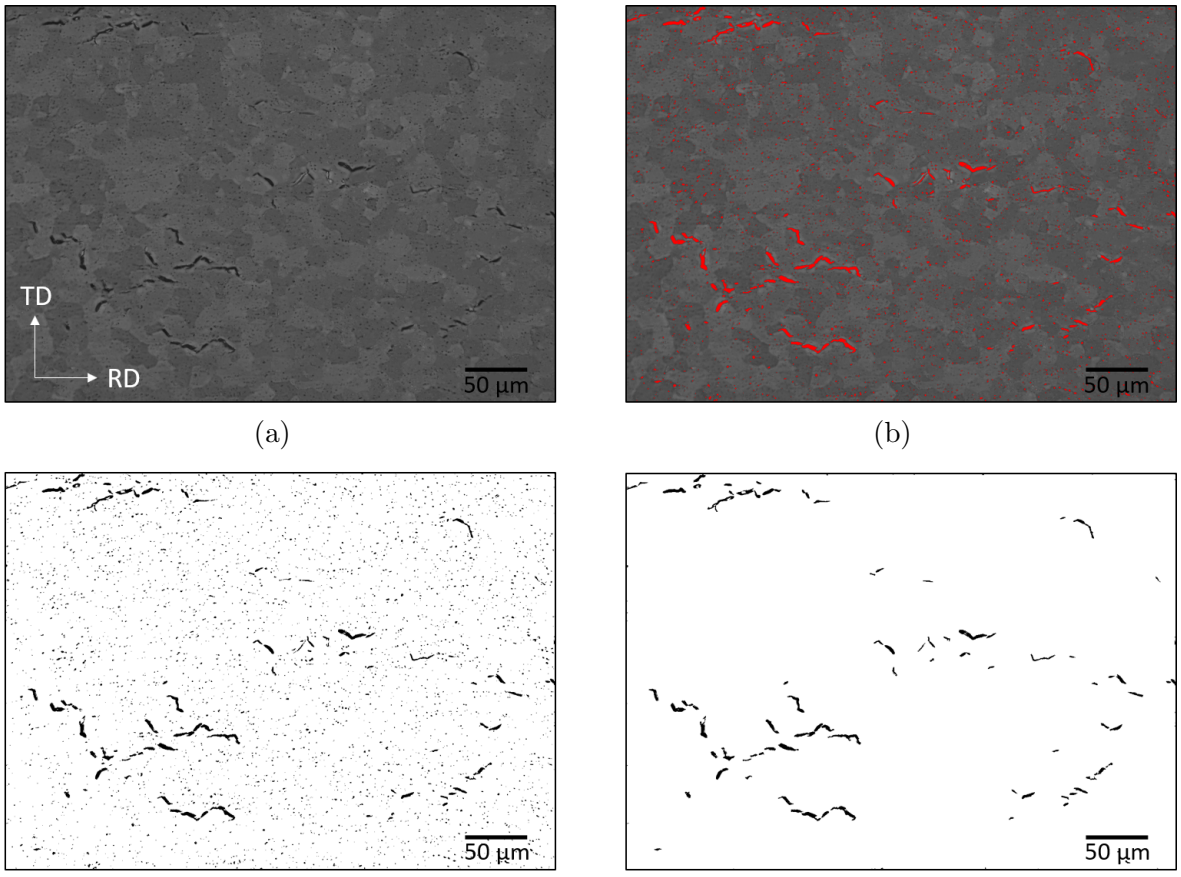


Figure 3.9: Image processing using the Fiji ImageJ software [28].

[28] was used to transform microscopy images to a digital binary format. Using the red thresholding feature on Fiji ImageJ, intra and intergranular hydrides were highlighted in red, as shown in Figure 3.9(b), followed by binary thresholding at 64/255 (where 0 is black and 255 was white) (Figure 3.9(c)). Figure 3.9(d) shows macrohydride features in black and the Zr matrix in white after noise cancellation (noise accounts for any microstructural black features below 6 µm^2). The size of macro-hydrides analysed range between 6 to 100 µm^2 for as-received microstructures and between 6 to 1000 µm^2 in blocky-α specimens with macro-hydride features at edges excluded. The Fiji ImageJ software outputs the following quantities: (1) hydride size distribution, (2) hydride number density and (3) hydride area fraction. The latter parameter is used to estimate the hydrogen concentration using the following standard weighting formula [168] that assumes the amount of hydrogen in solid solution is negligible in comparison to the amount in the hydrides and the hydrides are in the δ-phase with a molecular formula of $ZrH_{1.66}$ corresponding to a H concentration of 62.4 at.%. The formula also assumes that the hydrides are homogeneous features, that is, the stoichiometry is uniform over the microscopically

observed region defined as the hydride of which the A_{hydride} is calculated:

$$W_H = \frac{W_\delta A_{hydride} \rho_\delta}{(\rho_{Zr}(1 - A_{hydride}) + \rho_\delta A_{hydride})} \tag{3.10}$$

where, W_H is hydrogen concentration in wppm, W_δ is the hydrogen concentration in δ-hydride phase in wppm, $A_{hydride}$ is the measured area fraction, ρ_δ is the density of the δ-hydride phase (5.65 g cm^{-3}) and finally, ρ_{Zr} is the density of α-Zr phase (6.54 g cm^{-3}).

The second hydride parameter quantified using the Fiji ImageJ software is the hydride number density, which corresponds to the number of hydrides analysed in a micrograph per unit area. This parameter was used to explore the total number of hydride nucleation sites in the microstructure. This metric may be used to provide computational models with information about the number of favourable microstructural hydride nucleation sites at a given hydrogen concentration which is neglected in current models. The hydride number density was also split into percentages of inter and intragranular hydrides by simple process of counting, which gives more information about the hydride precipitation dynamic in the microstructure. The error throughout the analysis was quantified using the standard deviation.

SPP characterisation was also performed using Fiji ImageJ that aims to explore the effects of SPPs on intragranular hydride precipitation. As part of material characterisation, the number density and size distribution of SPPs in as-received and blocky-α specimens was quantified using high magnification (10,000-30,000× at a working distance of 15 mm) SEM BSE and EDX micrographs. Results from SEM and EDX mapping also provide a qualitative measure of the chemical composition found in SPPs, such as the amount of Cr and Fe. Backscatter SEM images show heavy atoms scattering more electrons back towards the detector than the lighter alloying atoms, that appear brighter in the SEM image. The size of SPPs analysed ranges between 0.1 µm and 1 µm diameter and a circularity between 0.5 and 1. The threshold limit applied is similar to that of hydride analysis and the noise cancellation or the despeckling process is done for any feature below 0.007 µm^2.

3.5 Thermo-mechanical Testing

3.5.1 Sample Preparation

The cuboid geometry of the Zr-4 specimens for thermo-mechanical cycling were cut using electro-discharge machining (EDM) from Zr plates. A grinding procedure was then used to remove EDM Cu

residue. The cuboid dimensions were chosen to be 42 mm × 10 mm × 6 mm in the orientations shown in Figure 3.10(a). The specimen dimensions were chosen after taking material availability into account. Specimens were then notched centrally using the notch grinding method by an external contractor (SJP Enginnering UK ltd), using a jig borer with specific size cutters, by introducing increments of small cuts until the required depth is achieved. Notch geometries introduced were chosen to match ones from a previous experimental study by Schofield et al. [5], and are as follow:

1. A notch having a depth of 1 mm, parallel sides and a root radius of 700 µm as shown in Figure 3.10(b). This specimen is referred to as the 'U' notch specimen.

2. A sharp notch having a depth of 1 mm, a total flank angle of 45° and a root radius 50 µm as shown in Figure 3.10(c). This specimen is referred to as the 'V' notch specimen.

The 'V' notch geometry was defined in literature following an extensive sectioning and examination programme by Schofield [5]. In the programme Schofield sectioned ∼800 samples showing different notch profiles, that were examined and analysed. For the same applied load, it was ensured that the test specimen notch would generate higher peak tensile normal stresses, calculated on an elastic-plastic basis, than any geometry observed in the actual component. Schofield described the 'V' notch geometry as the worst case idealised geometry and was used in his DHC initiation studies. The 'U' notch geometry also used by Schofield represented the minimum tolerance condition for a machined notch. The 'U' notch produces less stress triaxiality than the 'V' notch-tip, which produces higher peak tensile normal stresses. Notch geometries were also chosen as such, in order to make test results easily comparable with studies by Sagat et al. and Cui et al. [26, 169]. Both types of notch geometries were introduced along the plate normal direction on the TD and RD faces. Microstructures of Zr-4 were characterised in the bulk and notch regions using optical, SEM and EBSD with the sample preparation techniques presented in sections 3.1.2 and 3.1.3. Notch and bulk regions used for hydride analysis are defined to have areas of 1.8 × 2.8 mm^2 and 3.5 × 15 mm^2 respectively and are shown in Figure 3.10(d).

3.5.1.1 Zr-4 Grain Growth Annealing and Characterisation

For ten notched specimens the average grain size in the microstructure was increased using the heat treatment technique proposed by Tong and Britton to yield 'blocky-α' grains with size ranging between 250-1000 µm [12, 80]. The heat treatment was done, after notching the specimens, at 800°C for 336 h in quartz glass tubes containing an inert argon atmosphere at 10^{-3} Pa, followed by air cooling.

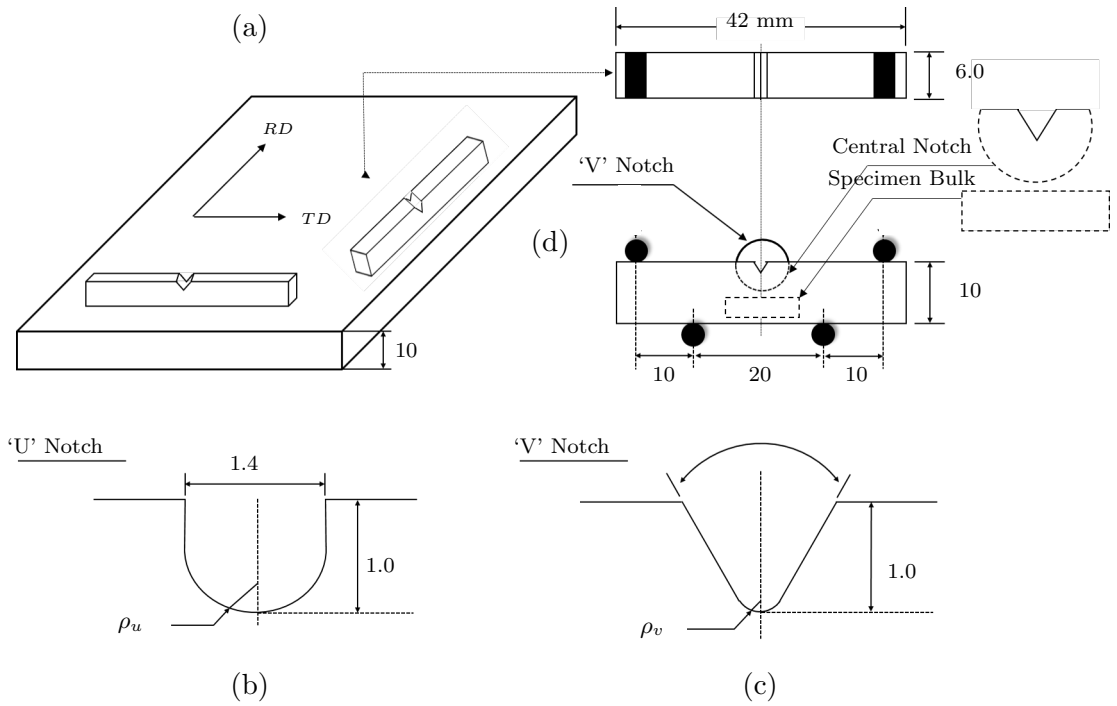


Figure 3.10: (a) Orientations of samples with respect to the plate. The 'U' and 'V' notch geometries are shown in (b) and (c) where ρ represents the notch root radius with values of 700 µm and 50 µm respectively. (d) shows the four-point bending set-up whereby the upper fixed rollers and the lower loading rollers are shown in black circles with a diameter of 3 mm.

The texture and grain size of the blocky-α microstructures were also characterised using EBSD and SEM via the same sample preparation techniques for specimens with as-received grain sizes. Table 3.2 summarises the test matrix which highlights the size of SPPs quantified in Chapter 5 in samples of different grain sizes. The full test matrix is presented in Appendix A.

Table 3.2: Test matrix highlighting notch geometries, applied stress intensity factor and microstructural variables.

Material	Notch root radius (µm)	Texture	Average Grain Size (µm)	SPP Size	Applied K (MPa$\sqrt{}$m)
Zr-4	50	$(0002)_{\alpha Zr}$	10<a<20	Fine	2, 4, 6, 8
		Random	250<a<1000	Coarse	2, 4, 6, 8
	700	$(0002)_{\alpha Zr}$	10<a<20	Fine	2, 4, 6, 8
		Random	250<a<1000	Coarse	2, 4, 6, 8

3.5.1.2 Hydrogen Charging

Thermo-mechanically cycled specimens were electrochemically hydrogen charged for 48 hours prior to hydride homogenisation to concentrations of 100-150 wppm to allow the formation of uniformly distributed macro-hydride features. Hydrogen charging was performed on notched specimens using the method described in Section 3.3. The same Pt mesh was used in the electrochemical cell for

charging these specimens as for the small non-loaded samples. The samples were also spot welded to the zirconium specimens using time parameters of 5 cooling and 10 welding cycles with each cycle taking 0.02s. The EMGA-930 inert gas fusion element analyser was also used to measure the hydrogen concentration after electrolysis and hydride thermal diffusion.

3.5.2 Mechanical Cycle

Standard four-point bending (Figure 3.11) tests were performed on the Zwick-Roell RetroLine Mayes machine at temperatures ranging between 20 and 350°C. The loading configuration of four-point bending was chosen to mimic applied load on industrial components and to provide a range of low to high tensile stress gradients concentrated at the notch-tip in bending. A maximum of three consecutive thermo-mechanical cycles were applied to allow hydrogen and hydrides to diffuse and reorientate around both notch geometries at favourable microstructural nucleation sites. Figure 3.10(d) shows the loading configuration whereby the loading span (distance between the lower rollers) is half the support span (distance between the upper rollers, L).

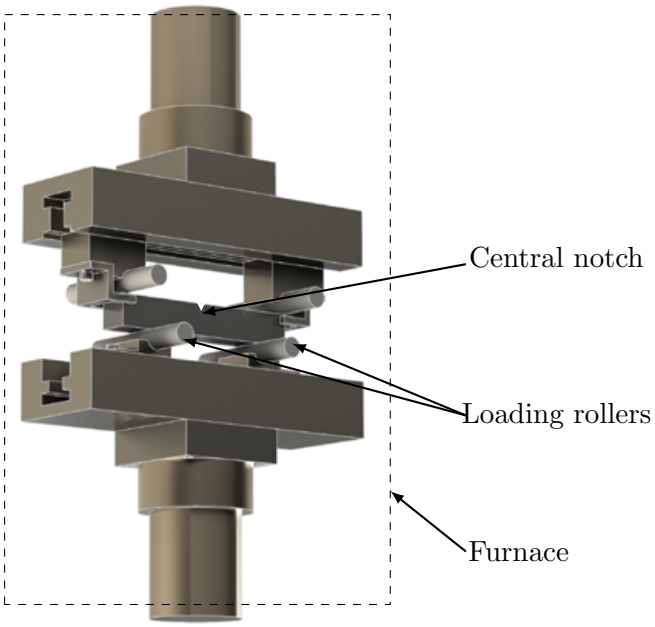


Figure 3.11: A scheme that shows the four-point bending rig whereby the distance between the loading rollers is half the distance between the upper rollers.

The nominal bending stress σ_{nom} at the midpoint of the cuboid specimen was calculated using the following equation [170]:

$$\sigma_{nom} = \frac{3}{4}\frac{FL}{bW^2} \tag{3.11}$$

where b is the width of the specimen, W is the thickness and F is the applied force by the rollers. The stress intensity factor (K) was used to characterise the applied load for specimens with both blunt and sharp notches for convenience and consistency with literature. K was calculated using the nominal bending stress using the following equation by Tada et al. [170]:

$$K = \sigma_{nom}\sqrt{\pi a} f(\frac{a}{W}) \tag{3.12}$$

a, is the notch depth (1 mm), and W is the thickness of the specimen (6 mm). $f(\frac{a}{W})$ is given by the following [169, 170]:

$$f(\frac{a}{W}) = 1.122 - \frac{1.4a}{W} + \frac{7.33.a^2}{W^2} - \frac{13.08.a^3}{W^3} + \frac{14.a^4}{W^4} \tag{3.13}$$

The stress distribution ahead of the 'V' and 'U' notch tips can thereafter be calculated using the following equation by Creager et al. [171]:

$$\sigma_{ij} = \frac{K}{\sqrt{2\pi r}} f_{ij}(\theta; \frac{\rho}{r}) \tag{3.14}$$

where σ_{ij} represents the linear elastic crack tip stress distribution, ρ is the notch root radius, r is the radial coordinate from a position $\frac{\rho}{2}$ behind the notch and f_{ij} is a non-dimensional function of angle θ and $\frac{\rho}{r}$. Directly ahead of the notch (θ= 0):

$$f_{xx} = (1 - \frac{\rho}{2r}); f_{yy} = (1 + \frac{\rho}{2r}); f_{xy} = 0 \tag{3.15}$$

3.5.3 Thermal cycle

The specimens were loaded at room temperature to a range of stress intensity factors in load control of 2, 4, 6 and 8 MPa$\sqrt{}$m for as-received and grain size enhanced materials, and then subjected to a 3 hour isothermal dwell hold at a temperature above TSS_D of 100-150 wppm (= 350°C reached at a rate of 62°C min^{-1}) [158]. This hold allows sufficient time for all the precipitated micro-hydrides and

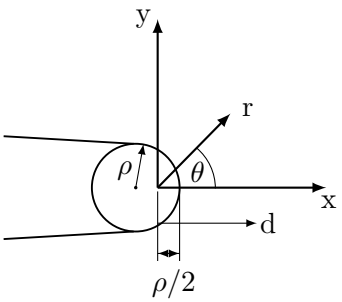


Figure 3.12: Convention used in definition of spatial coordinates for a notch where d is the distance from position $\rho/2$.

in-turn macro-hydrides in the microstructure to dissolve into the zirconium matrix and prevent hydride ratcheting. At 350°C, entropy driven diffusion of hydrogen produces a relatively uniform distribution of hydrogen in the specimen [172]. The temperature was then decreased from 350°C to 280°C at a rate of 1-2°C min^{-1}, and held for 3 hours at 280°C, the hydrogen atoms move via a stress driven diffusion process towards the notches and precipitate as new hydrides as TSS_P is reached. Hydride precipitates thereafter relieve the local stress at the precipitation site. The cycle is then finally followed by furnace cooling to room temperature when almost all remaining hydrogen atoms form hydrides. The furnace was connected to thermocouples to monitor the temperature throughout the cycles. Figure 3.13 shows the schematic profiles of the thermal and stress cycles.

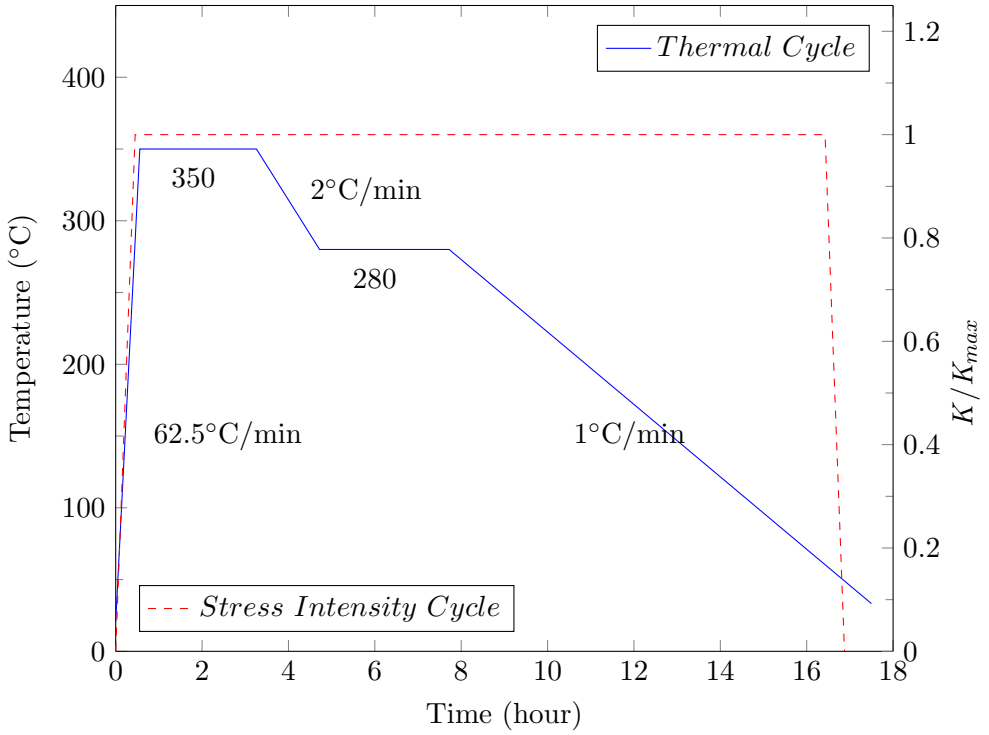


Figure 3.13: Profiles of the thermal and stress intensity cycles at a $K = 8$ MPa$\sqrt{\text{m}}$ for as-received Zr-4 specimens.

3.6 Choice of Thermo-mechanical Cycling Parameters

A large number of factors were taken into account during the planning stage of thermo-mechanical testing to study the effects of microstructure on hydride precipitation. In order to achieve some degree of hydrogen diffusion towards two distinct notch geometries, in relatively low yield stress materials, and hydride precipitation at favourable microstructural sites, the choice of load and temperature applied to specimens was very important. The long range SCFs were chosen to be in the form of 'V' and 'U' notches to primarily have two distinct generated stress profiles, upon notch loading, which enables the study of notch geometry effects on hydride precipitation. 'V' and 'U' notch geometries were also chosen to provide some degree of ease when comparing results with literature [5, 26, 169].

The thermomechanical cycling was performed to achieve the very early stages of DHC, where hydrogen diffusion towards SCFs and the first stage of hydride reorientation around loaded notches begin to occur. This is far before hydride cracking initiation that is achieved during DHC testing and requires many more number of cycles and longer peak hold temperatures below or near the TSS_D. The cycles in this study involve a heat-up, a period of sustained high-temperature hold and then cool down all during an applied constant load. The duration of the thermomechanical cycles is much less than when in-service which is usually at a sustained high-temperature hold for periods that last weeks.

3.6.1 Applied Load

The typical stress intensity factor for DHC initiation is 10-20 $MPa\sqrt{m}$. The load range applied in this study (2, 4, 6 and 8 $MPa\sqrt{m}$) was chosen to be below the one typically required for DHC initiation in order to study hydride precipitation around notch-tip geometries with stresses low enough to avoid plasticity at notch roots and to allow microstructural stress-raisers such as grain boundaries, SPPs and deformation twin boundaries to still have an effect on short range hydrogen diffusion and therefore on hydride precipitation near the notches. The load was applied and removed at rate of 1.5 $MPa\sqrt{m}$/min similar to the temperature rate applied during heat-up.

3.6.2 Applied Temperature

Peak test temperature (T_{max}) was chosen to be above the hydride TSS_D to ensure thermal ratcheting of hydrides does not occur. At temperatures near or below TSS_D, not all hydrides dissolve, adding

complexity to the study. Heat-up rate to T_{max} was chosen to be relatively high at 62.5°C min^{-1} in order to decrease the test duration. The heat up rate was found by Jackson, Schofield and Asprey [5] to have little effect on hydrides and hence it is not as important as the cool down rate that has an effect on hydrogen diffusion towards favourable microstructural sites [149]. The duration of the isothermal dwell period at T_{max} was chosen to be 3 hours, to keep creep deformation negligible and to allow sufficient time for hydrogen dissolution and diffusion. The soak temperature (T_{soak}) was chosen to be at 280°C for a 3 hour duration to allow more favourable conditions for hydride precipitation during the cool-down stage of the cycle. Finally the cool-down rate from T_{max} to T_{soak} and from T_{soak} to room temperature was chosen to be very small at 1-2°C min^{-1} to allow sufficient time for hydride precipitation at favourable sites to occur, although studies show that cooling rates below temperatures of 120°C also have little effects on hydride precipitation [5].

3.6.3 Hydrogen Concentration

A hydrogen concentration of 100-150 wppm was chosen to provide enough hydrides but allow microstructural features that act as local stress-raisers (grain boundaries and SPPs) to remain visible in micrographs. At concentrations above 150 wppm hydrides start to form very coarse macro-hydrides near the notch that cannot be easily seen at and around SPPs and also cannot be distinguished as intra or inter-granular [40]. Notch and bulk regions used for hydride analysis are defined to have areas of 1.8 × 2.8 mm^2 and 3.5 × 15 mm^2 respectively and are shown in Figure 3.10(d).

3.7 Hydride and SPP Characterization and Quantification

After thermo-mechanical testing, stressed samples were ground and mechanically polished using the methods described in Section 3.3. Optical and SE SEM images were then taken and analysed also using Fiji ImageJ software [28] using the parameters highlighted in Section 3.3.1. Micrographs were also transformed into a binary format using a grayscale threshold limit with similar processing parameters as for non-stressed specimens. Upon processing the binary micrographs, the total number density of macro-hydrides was determined as a function of the grain size. The hydride number density was further distinguished into percentages of intra-granular hydrides, using polarised optical imaging, that provides data for comparing the relative potency of GBs and SPPs in the bulk and at the notch tips. Notch and bulk regions used for hydride analysis are defined to have areas of 1.8 × 2.8 mm^2 and 3.5 × 15 mm^2 respectively and are shown in Figure 3.10(d) where the 1 mm notch is shown to be central in the

cuboid specimen and the bulk region is 4-5 mm away from the notch tip where the hydrostatic stress becomes compressive. Table 3.3 highlights and defines the SPP and hydride parameters calculated for cycled and non-cycled Zr specimens.

Table 3.3: List of parameters used for hydride and SPP quantification.

Quantity	Symbol	Definition	Unit
SPP Parameters			
SPP number density	ρ_{SPP}	A parameter that quantifies the average SPP number density per unit area of one category of hydride nucleation sites, distinguished between Zr-4 and Zr-702, as a function of alloy composition	(μm^{-2})
SPP area fraction	A_{SPP}	A parameter that quantifies the average percentage area occupied by SPPs, as a function of alloy composition	(%)
Hydride Parameters			
Hydride number density	ρ_{hydride}	A parameter that quantifies the average hydride number density per unit area of macro-hydride precipitates at all nucleation sites	(mm^{-2})
Hydride area fraction	A_{hydride}	A parameter that quantifies the average percentage area occupied by macro-hydrides at all nucleation sites	(%)
Microstructural Parameters			
Grain size	l_{G}	A parameter that quantifies the average grain size in a given area using the Bruker 2 software's EBSD map analysis and the line intercept method	(μm)

Chapter 4

Computational Methodology

4.1 Finite Element Modelling of Mechanical Loading

Four-point bending simulations were performed using the commercial finite element analysis code Abaqus Standard 2019 [173]. The models' dimensions matched the experimental geometry (i.e. 42 mm × 10 mm × 6 mm) and contained either a 'V' or a 'U' notch as described in Section 3.5. The specimens notches were parameterised by the root radius and the flank angle as shown in Figure 3.10. The 2D mesh of the 'V' and 'U' notch model are shown in Figure 4.1. For the 2D plane stress and plane strain models, continuum 4-node bilinear, reduced integration with hourglass control (CPS4R for plane stress and CPE4R for plane strain) were employed. The 'V' notch had a total of 19093 elements and 19250 nodes and the U notch 51388 nodes and 51035 elements. The element length around the notch tip was around 0.05 mm which increased to around 0.2 mm away from notch. The 3D model was generated by extruding the 2D model to give 16 elements through the thickness of the geometry such that the element width was 0.375 mm in the through thickness (z) direction. The 3D model had a total of 864000 continuum 3D 8 node elements (C3D8) and 926007 node and was used to determine the variation in stress state through the thickness of the sample. The 3D mesh of the 'V' notch model is shown in Figure 4.2.

4.1.1 Boundary Conditions

To simulate the supporting rollers, the nodes at the location of the rollers contact point with the specimen were constrained from moving in the y coordinate direction. The loading rollers were simulated by applying a concentrated force to the nodes corresponding to position of the rollers central

contact points in the y coordinate direction. To prevent rigid body motion in the 2D model, the node at the root of the V and U notch was constrained from moving in the x direction as shown in Figure 4.1. For the 3D model, the nodes at the mid length of both surfaces, at the base of the geometry were constrained in the x direction to prevent displacement in the x and rotation around the y axis, and 2 nodes at both ends of one surface (shown in Figure 4.2) were constrained from moving in the z direction to prevent rigid body displacements and rotations.

The Zr-4 FE sample was loaded to the maximum load applied in the experiments (K= 8 MPa$\sqrt{}$m). Initially, elastic-plastic material properties were employed, however it was determined that no plasticity was developed in the model at these loads, hence the models were subsequently run elastically, with an elastic modulus E = 74 GPa and Poisson's ratio 0.37, corresponding to the Zr-4 material properties at 350°C [40]. The solutions from the FE models were validated using solutions provided by the Creager field equation [171]:

$$\sigma_{ij} = \frac{K}{\sqrt{2\pi r}} f_{ij}(\theta; \frac{\rho}{r}) \tag{4.1}$$

where σ_{ij} represents the linear elastic crack tip stress distribution, ρ is the notch root radius, r is the radial coordinate from a position $\frac{\rho}{2}$ behind the notch and f_{ij} is a non-dimensional function of angle θ and $\frac{\rho}{r}$. Directly ahead of the notch (θ= 0):

$$f_{xx} = (1 - \frac{\rho}{2r}); f_{yy} = (1 + \frac{\rho}{2r}); f_{xy} = 0 \tag{4.2}$$

FEM simulations combined with a USDFLD subroutine (shown in the Appendix A) to produce contour plots of the hydrostatic stress and stress triaxiality ratio ($\sigma_{hyd}/\sigma_{Mises}$) around the 'V' and 'U' notches.

4.1.2 Stress Analysis

Figure 4.3 shows the σ_{xx} distribution maps at the surface and mid-plane of the 3D model compared with the plane stress and plane strain models. The triaxiality distribution maps in plane stress are shown in Figure 4.4(a) and (b) highlighting the difference in constraint between the 'V' and the 'U' notch tips. Triaxiality in plane strain condition is also shown in Figure 4.5 that highlights a larger

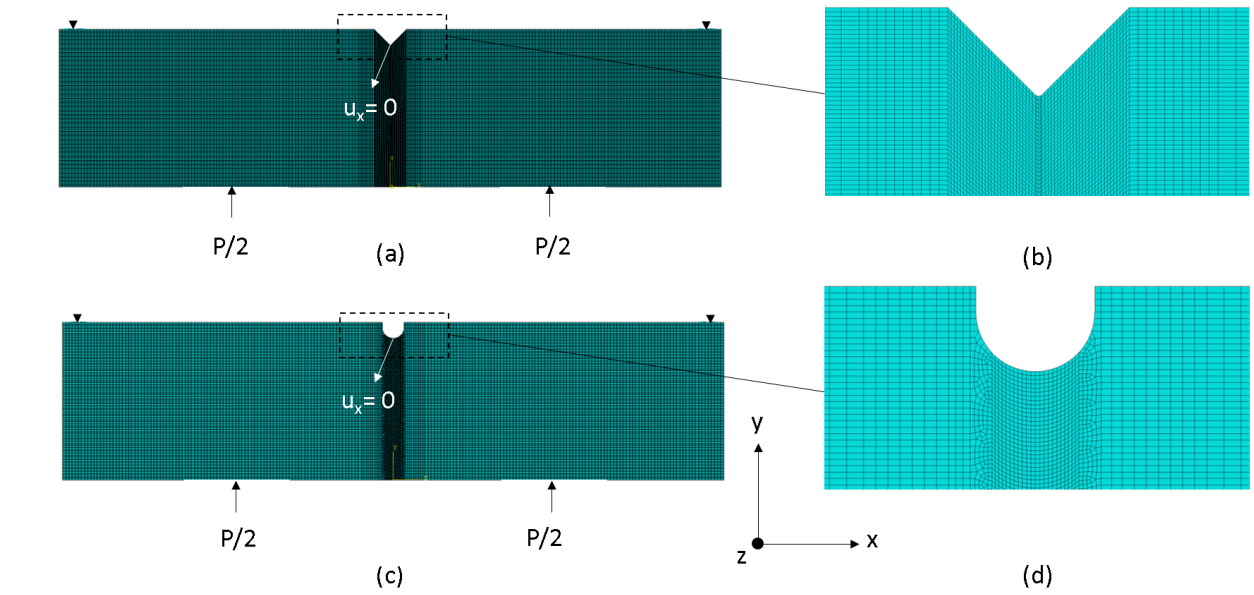


Figure 4.1: Images of the 2D mesh and boundary conditions for the (a)(b) 'V' and (c)(d) 'U' notch models. P corresponds to the applied force and u_x corresponds to the displacement in the x direction.

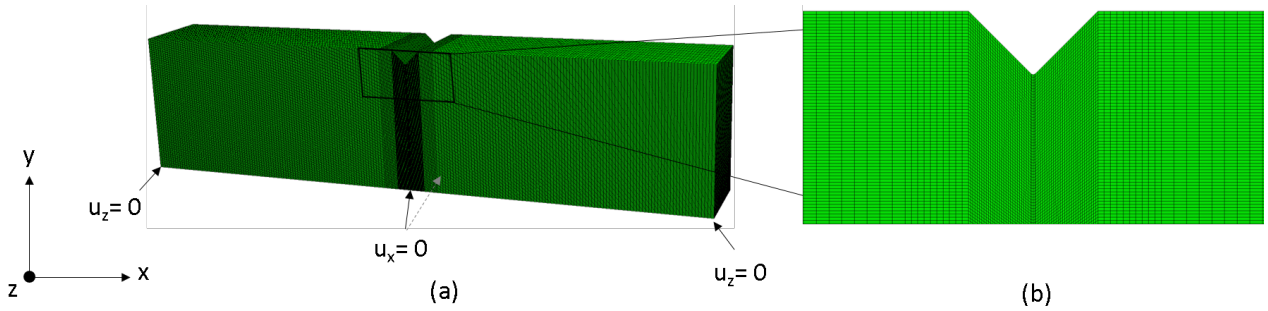


Figure 4.2: Images of (a)(b) the 3D mesh for the 'V' notch with boundary conditions.

triaxiality produced by both notches compared to plane stress conditions. Plane strain conditions have a more detrimental effect on hydrogen diffusion and hydride precipitation at notch tips, however industrial components experience biaxial loading and so the plane stress model is more representative to real components. Finally, Figure 4.6 shows the triaxiality distribution from the 3D model at the surface and at the mid-plane of the 'V' and the 'U' notch specimens and shows that the mid-plane triaxiality is closer to the one in plane stress conditions than plane strain. Figure 4.6 also highlights the difference in triaxiality between both notch geometries which has an effect on hydrogen diffusion.

Figure 4.7 shows the 'V' and 'U' notch hydrostatic stress distribution at the surface and at the

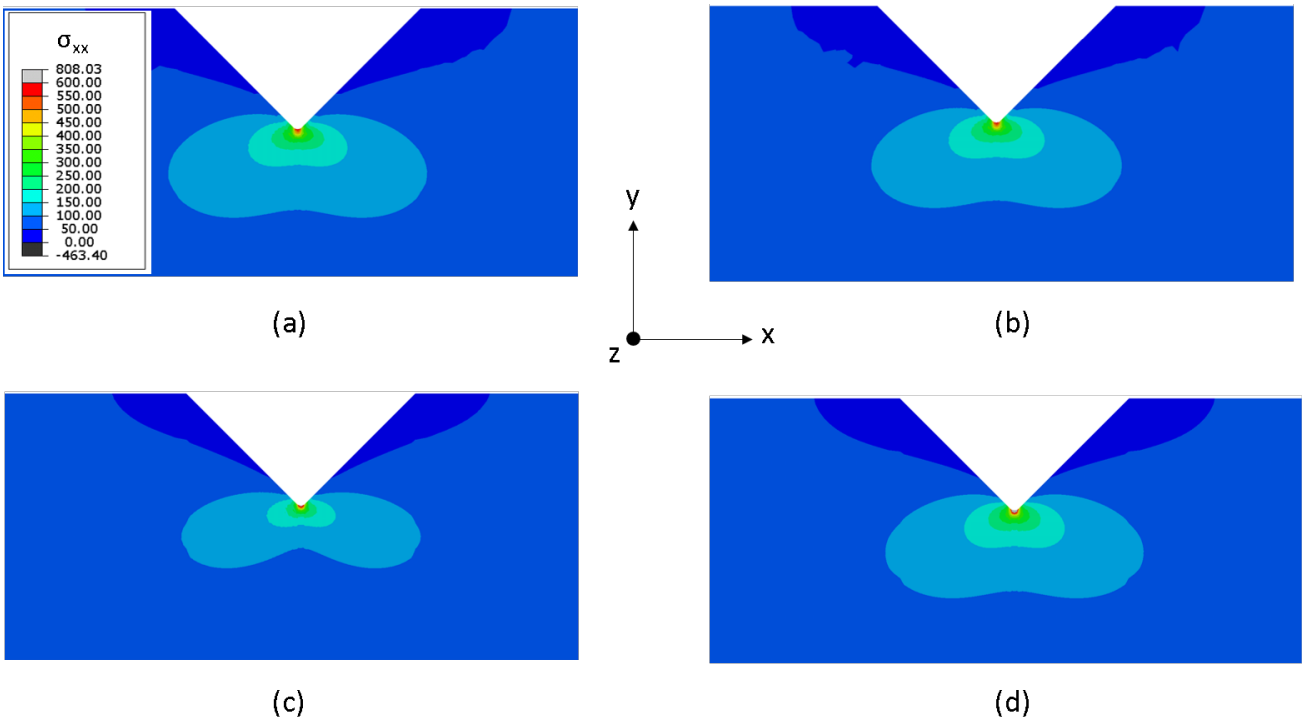


Figure 4.3: Comparison of the σ_{xx} stresses at K= 8 MPa$\sqrt{}$m at the 'V' notch tip from the 2D (a) plane stress and (b) plane strain models with the (c) surface and (d) mid-plane of the 3D model.

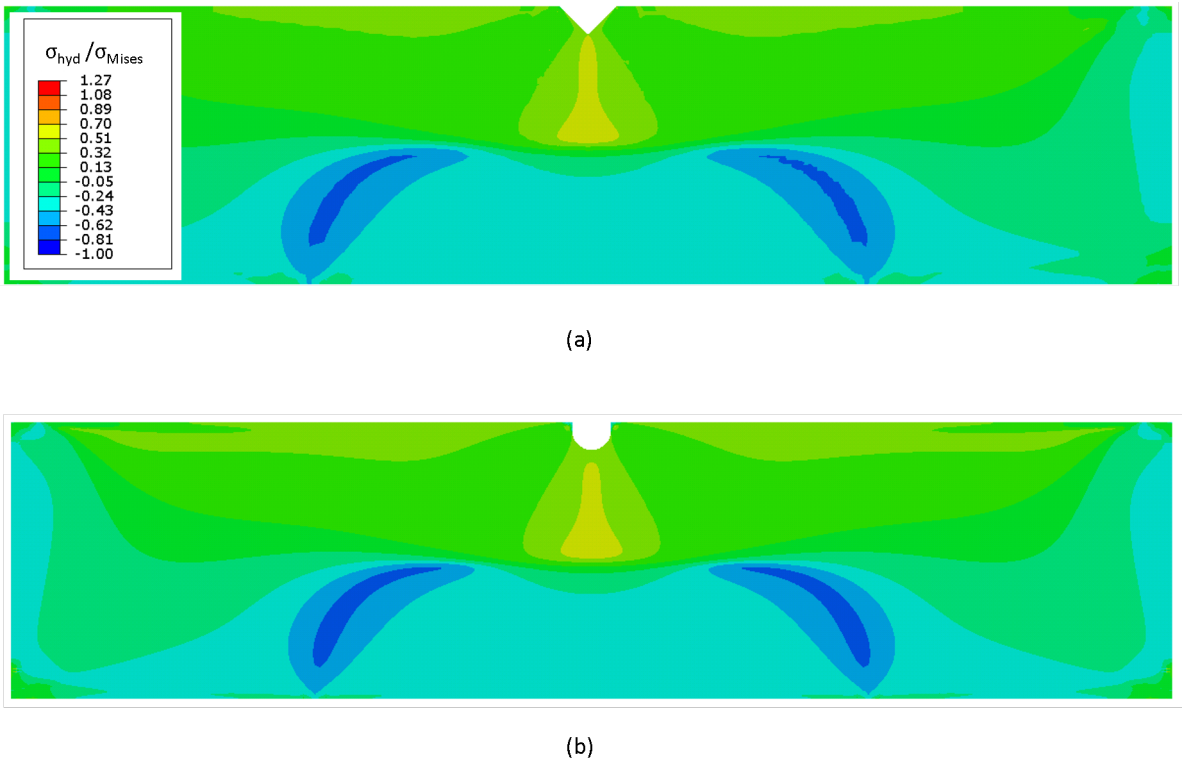
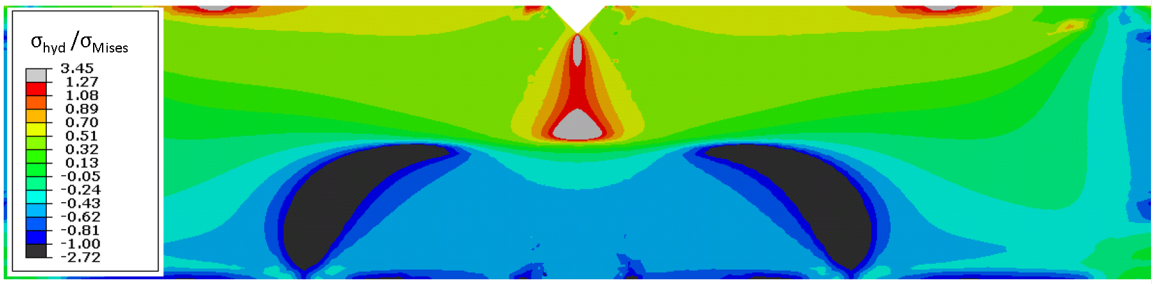
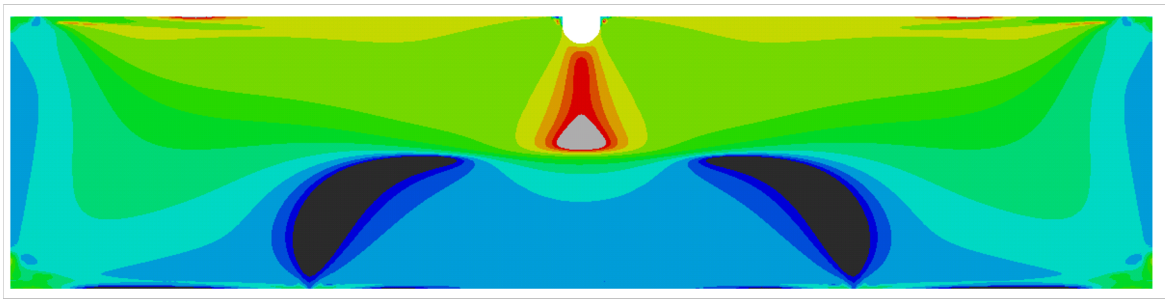


Figure 4.4: (a) 'V' notch triaxiality ($\sigma_{Mises}/\sigma_{hyd}$) in comparison to (b) the 'U' notch distribution in plane stress conditions at K= 8 MPa$\sqrt{}$m.



(a)



(b)

Figure 4.5: (a) 'V' notch triaxiality ($\sigma_{Mises}/\sigma_{hyd}$) in comparison to (b) the 'U' notch distribution in plane strain conditions at K= 8 MPa$\sqrt{}$m.

mid-plane of the 3D model. Hydrogen diffusion towards SCFs along the hydrostatic stress gradient can be said to occur from the compressive hydrostatic regions, shown in black in Figure 4.7, to the the tensile ones near both notch geometries. 'V' and 'U' notches at the surface again show a smaller stress level than at mid-plane, with 'V' notches displaying a more localised hydrostatic stress distribution at the tip than the 'U' notches that produce a more wider spread.

4.1.3 Hydrogen Diffusion Modelling

2D FE modelling, used to provide information about notch geometry effects on hydrostatic stress gradients required for hydrogen diffusion from a less tensile to a more tensile region, were also used to explore the stress and hydrogen diffusion interaction in different HCP crystallographic planes. This is presented in Chapter 7; the 2D plane stress FE models were used to build a multi-scale model which incorporated the HCP microstructural hydrogen diffusion anisotropy. Atomistic-to-continuum coupling was done using the fundamental quantum mechanical elastic dipole tensors to compute the elastic interaction energy between interstitial hydrogen atoms and the stress concentration feature in the FE model. Using a Fortran subroutine presented in Appendix A, and the plane stress FE model, the

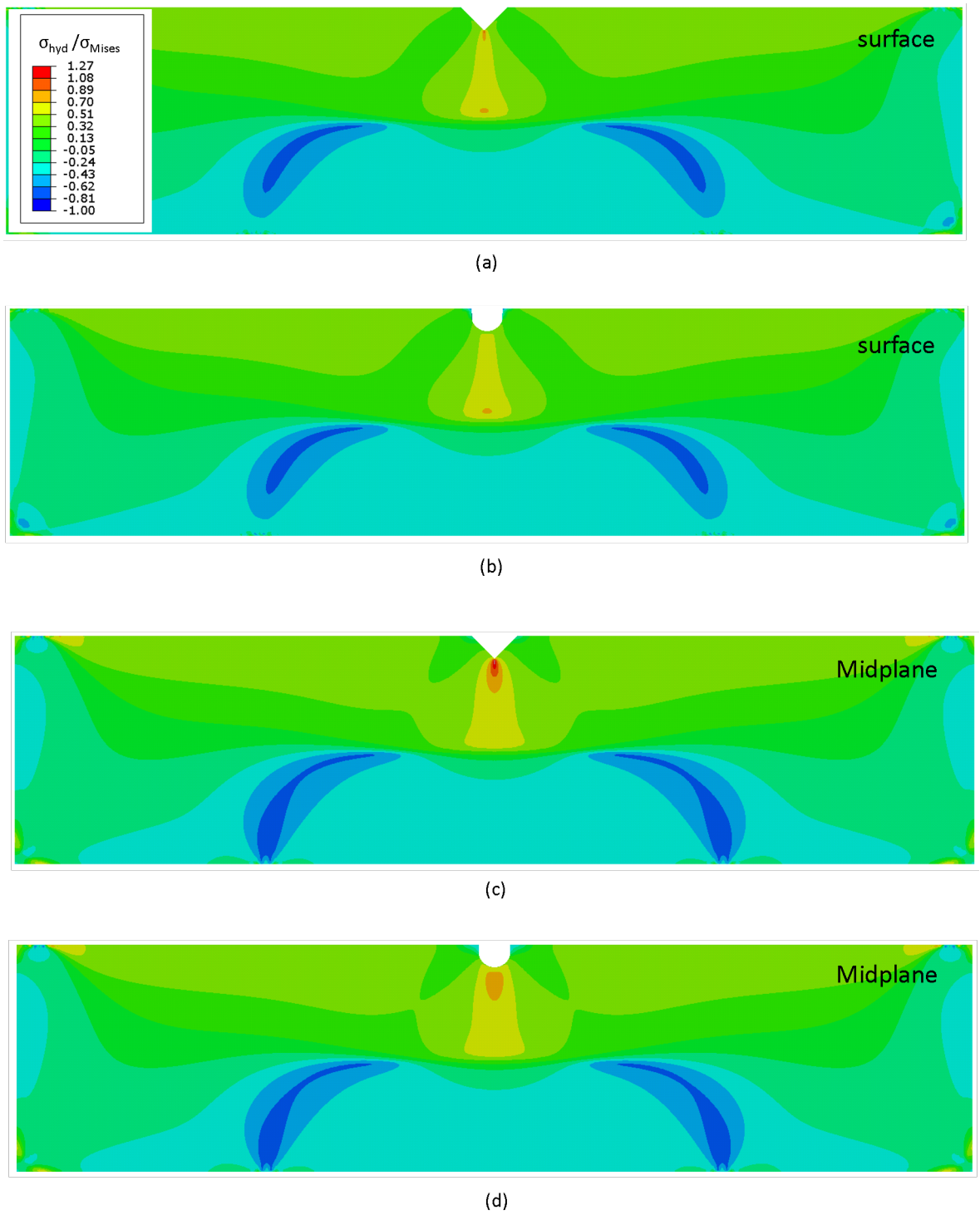


Figure 4.6: 'V' and 'U' notch triaxiality ($\sigma_{Mises}/\sigma_{hyd}$) at (a)(c) the surface and at (b)(d) the mid-plane of the 3D models at K= 8 MPa$\sqrt{}$m.

equilibrium state hydrogen concentration profiles where computed at 'V'. Further methodology details about the multiscale model is presented in Chapter 7.

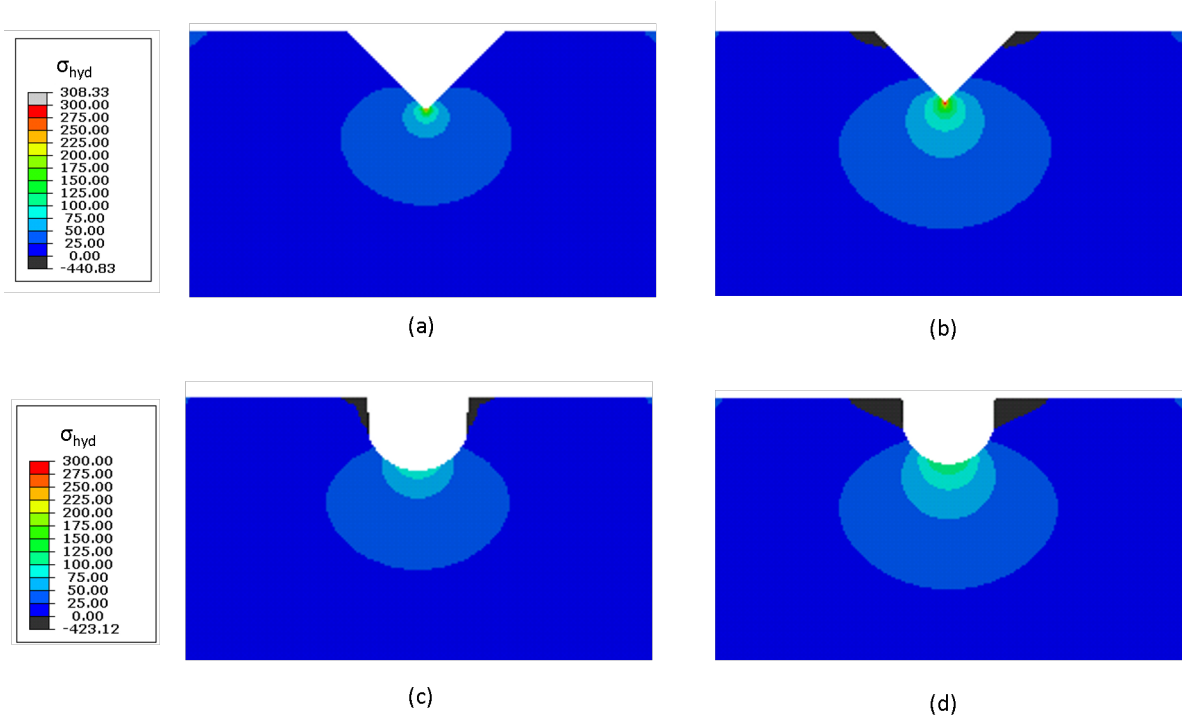


Figure 4.7: 'V' and 'U' notch hydrostatic stress distribution at (a)(c) the surface and at (b)(d) the mid-plane of the 3D models at K= 8 MPa$\sqrt{}$m.

Chapter 5

Hydride Precipitation Sites – Microstructural Hierarchy

5.1 Outline

This chapter aims to determine the effects of microstructure on hydride distribution in as-received and blocky-α Zr-4 and pure zirconium without external loading, with the aim of studying the potency of inter and intra-granular hydride precipitation sites. The chapter demonstrates a simple strategy to quantify the preferential hierarchy of hydride nucleation sites as a function of grain size and SPP content. Hydride precipitation in two different zirconium alloy samples was examined using optical and scanning electron microscopy (SEM) imaging in microstructures containing different amounts of second phase particles (SPPs) in small and blocky-α grains. This chapter begins by presenting results of microstrucural and mechanical characterisation of the as-received and grain growth annealed blocky-α specimens of Zr-4 (97.98 wt.% Zr) and commercially pure zirconium (98.49 wt.% Zr). The effect of grain growth annealing on SPPs is then analysed, followed by hydride quantification with respect to grain size and SPP content.

5.2 Introduction

Typical industry standards involve the use of empirical handbook solutions to predict hydride cracking initiation, in specific materials, as a function of macroscopic parameters, such as the elastic moduli and component geometry [40]. Although this approach is convenient, the absence of microstructural information provides a very conservative analysis which, in turn, complicates its application to the wide

variety of materials that have been manufactured to have different textures and alloy compositions. Macroscopic hydride features can be observed both at the inter-granular and intra-granular sites, suggesting that grain boundaries (GBs) and possibly SPPs are energetically-favourable nucleation sites [40]. Furthermore, hydrides were also found to precipitate at twin boundaries [150, 174], further increasing the complexity of the hierarchy of nucleation sites. Accordingly, to generate microstructural models of hydride or hydrogen distribution and hence hydride embrittlement or delayed hydride cracking (DHC), it is necessary to quantify the respective roles of microstructural features in hydride precipitation. Therefore, one aim of DHC research concerns, in part, the development of computational models that are capable of exploring statistically the space of DHC and predicting its failure criteria, which would be a cost-effective complement to the somewhat limited and expensive test programmes. One necessary step towards the development of these models is the ability to efficiently simulate micrographs of hydride distributions in various zirconium alloy microstructures [121, 175]. To this end, this chapter focuses on comparing the relative potency of GBs and SPPs as hydride nucleation sites under slow (furnace cooled) conditions. As a means of isolating the effects of SPPs, two sets of α-zirconium alloy samples were used, namely, commercially pure zirconium[1], Zircadyne-702 (Zr-702), and a standard component material Zircaloy-4 (Zr-4), the latter of which has more alloying additions than the former. The chemical composition of both alloys is shown in Table 5.1. For both sets of samples, specimens composed of various average grain sizes l_{G} were used, ranging from the typical as-received metal microstructure to the problematic 'blocky-α' systems [12]. The intermetallic SPP content is dependent on the quantity of the typical low solubility alloying elements: iron (Fe) and chromium (Cr). Zr-702 contains maximum 0.14 wt.% of Fe+Cr, while Zr-4 contains 0.37 wt.%. The specimens were characterised using optical microscopy and SEM imaging as well as electron back-scatter diffraction (EBSD) and energy dispersive x-ray (EDX) analysis.

Table 5.1: The chemical composition of Zr-4 and Zircadyne-702. (Zr: balance). The full chemical composition of both materials is presented in Appendix A, measured by AMG Analytical ltd.

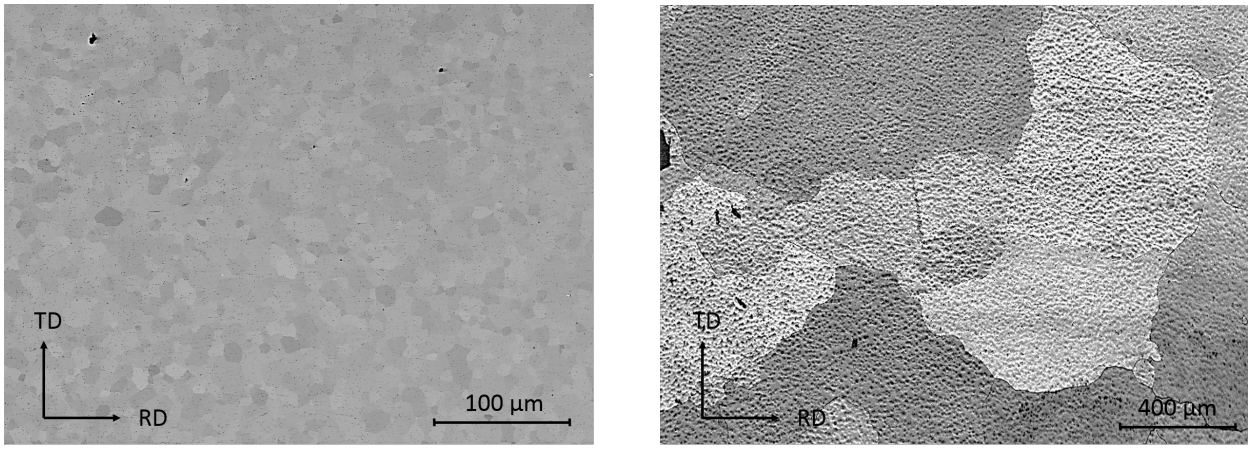
Elements	Cr (wt.%)	Fe (wt.%)	Nb (wt.%)	Sn (wt.%)	Hf (wt.%)	O (wt.%)	Zr (wt.%)
Zr-4	0.11	0.26	<0.05	1.51	<0.05	0.142	97.98
Zr-702	<0.05	0.09	<0.05	0.15	0.97	0.148	98.49

[1]NB. Commercially pure Zirconium is different (containing 0.97 wt.% Hf) to nuclear grade, where Hf must be <0.02 wt.%.

5.3 Microstructural Characterisation

5.3.1 Zr-4

The microstructure of as-received Zr-4 is shown in Figure 5.1(a) using secondary electron SEM. Figure 5.1(a) reveals the equiaxed α-Zr grain structure with an average grain size, l_G, of 14.8 µm. Annealed Zr-4 at 800-830°C for 336 h produces microstructures similar to the one shown in Figure 5.1(b) that contains blocky-α grains. The grain size of the specimen shown in Figure 5.1(b) has an average of 411 µm.



(a) (b)

Figure 5.1: Secondary electron micrographs of Zr-4 samples with (a) as-received small grains (1753 grains with an average size of ∼15 µm) and (b) annealed large grains (59 grains with an average size of 411 µm).

The pole figures for as-received Zr-4, that are a stereographic projection of the crystallographic directions present in the volume of analysed grains, are shown in Figure 5.2(c). The 0001_{Zr} pole figure displays two asymmetric peaks of basal pole density, close to the sample normal direction (ND) at the centre of the pole figure. This shows the typical texture of zirconium alloys that is produced during thermomechanical treatments within the fabrication process (such as plate rolling). The asymmetry of the basal peaks indicate microscopic fluctuation in grain orientation for the spread of grains analysed within the sample volume [60]. The texture of the Zr-4 used in this project matches the one reported in literature as the $(0002)_\alpha - Zr$ texture. This texture is caused by the c-axis of the *hcp* crystals that rotates 30-40° from the ND of the plate towards its transverse direction (TD) [10]. The corresponding inverse pole figure (IPF) maps in the RD and ND directions are shown in Figure 5.2(a) and (b), respectively.

The pole figures for a grain size enhanced specimen containing blocky-α grains is shown in Figure

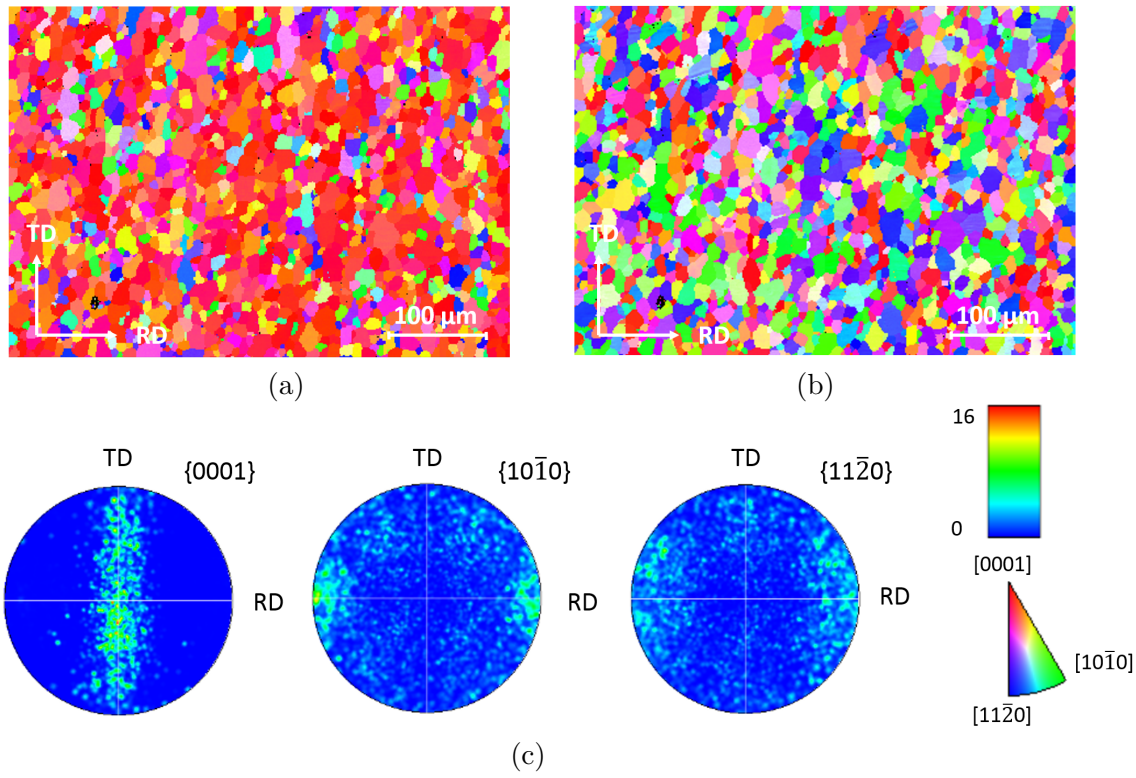


Figure 5.2: Inverse pole figure, IPF_{RD} (a) and IPF_{ND} (b) revealing the as-received Zr-4 equiaxed grain structure. Their corresponding pole figures (c) highlight the expected Zr-4 rolling texture. (step size: 1 µm, accelerating voltage: 20 keV and number of grains analysed: 1582).

5.3(c). Due to the large size of grains (l_{G}= 411±56 µm), an accurate texture of the material cannot be made with any confidence due to the limited number of grains in a map. However, it is considered that due to grains recrystallising, the texture is close to random after the annealing treatment [176]. In other words the texture of the grain growth annealed specimens may or may not be inherited from the parent texture, with or without preference for a particular orientation. Figure 5.3(a) and (b) show the IPF_{RD} and IPF_{ND} maps, respectively, of the blocky-α Zr-4 specimen containing 59 grains with a bimodal size distribution. Island grains can be observed in large grained Zr-4 samples plausibly due to the high modal SPP density within and around them that have been shown to pin grain growth [177]. Some deformation twins were formed in blocky-α grains after hot bakelite mounting and grinding at loads equal to and above 15 N. The sample preparation procedure was adjusted accordingly to prevent their formation by grinding at loads of 5 N or less.

Grain average misorientation (GAM) maps, generated after post-processing EBSD maps, are shown in Figure 5.4 for as-received and blocky-α Zr-4 microstructures. GAM maps for as-received and blocky-α Zr-4 samples show that the former has a higher energy throughout the microstructure as shown by

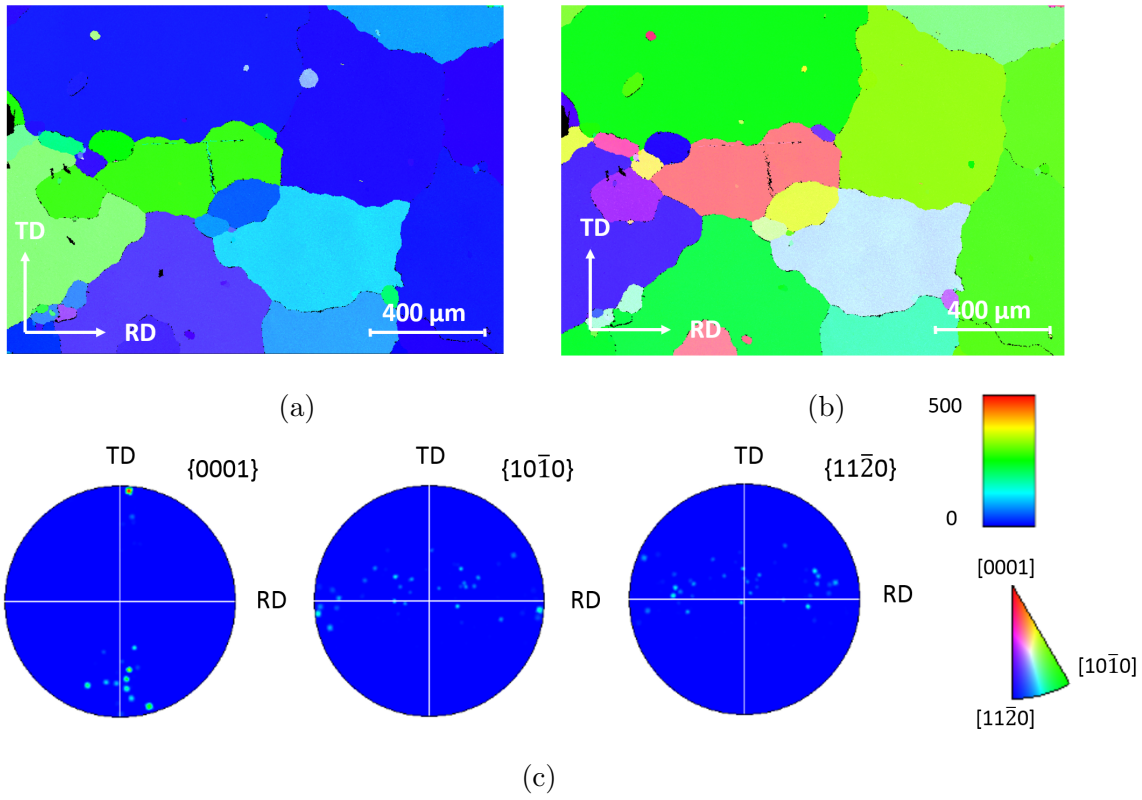
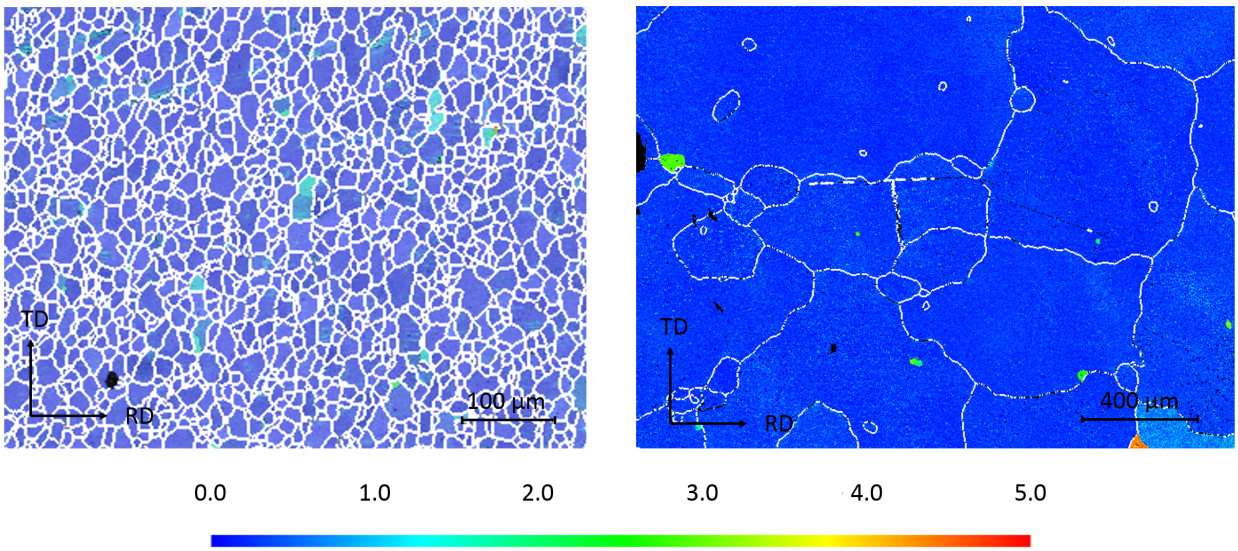


Figure 5.3: Maps of IPF_{RD} (a) and IPF_{ND} (b) revealing the blocky-α Zr-4 grain structure. Their corresponding pole figures (c) highlight the apparently textureless microstructure. (step size: 2 µm, number of grains analysed: 59).

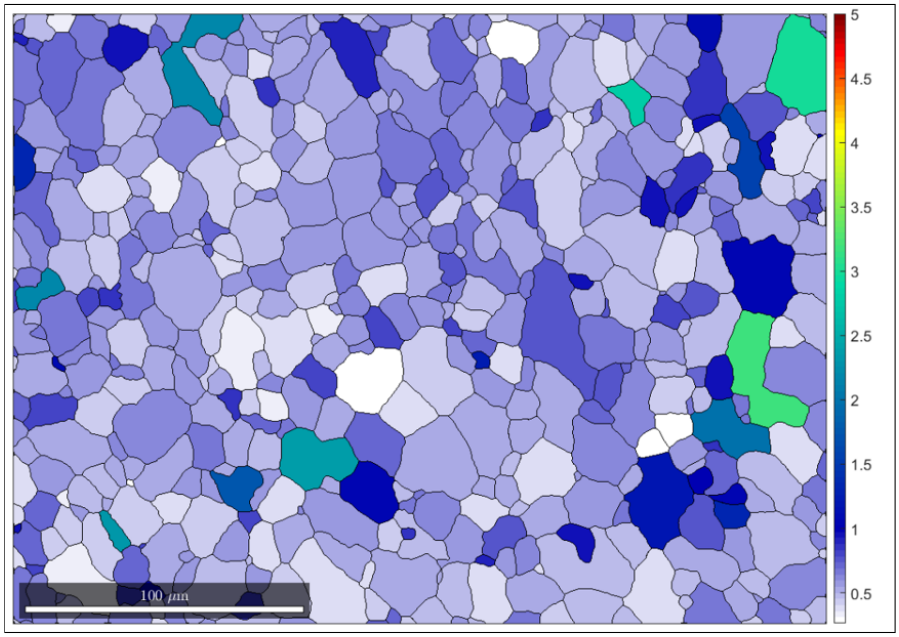
the dominance of the light blue colour. This colour indicates that the average grain misorientation is at around 1-2°. The blocky-α specimen has a lower energy level relative to the as-received specimen with a dominant dark blue colour, which indicates an average grain misorientation at around 0-1°. The percentage area of GBs, shown in white, was found in as-received specimens with an average grain size 15±4 µm to be 17%, which decreases to 3% the blocky-α specimen with an average grain size of 411±56 µm.

Figure 5.5 shows the same results as in GAM maps but as grain orientation spread maps in as-received and blocky-α specimens. Figure 5.5(a) shows an as-received Zr-4 microstructure with a relatively higher GOS misorientation average than in the blocky-α microstructure shown in Figure 5.5(b).

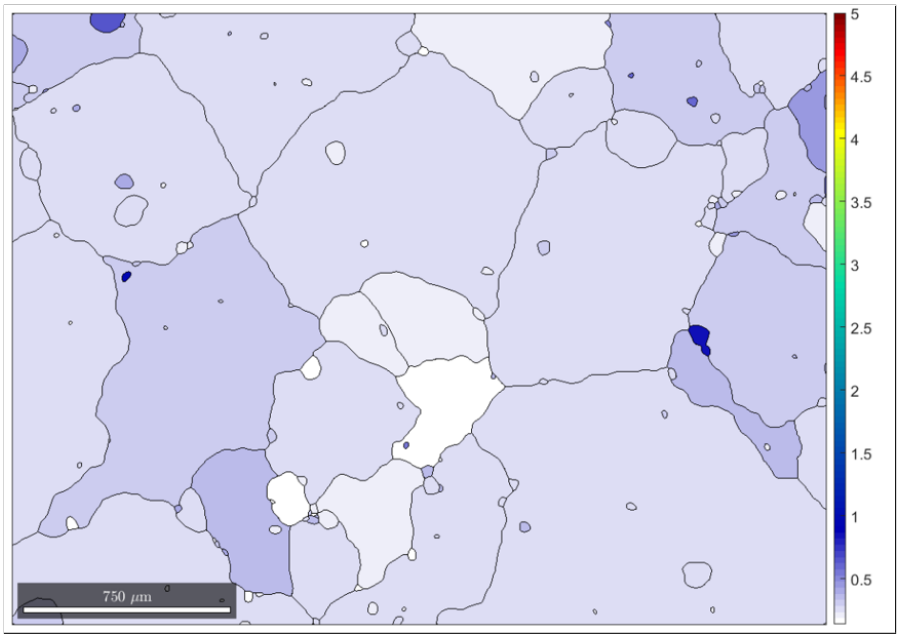


(a) (b)

Figure 5.4: Grain average misorientation (GAM) maps of (a) as-received Zr-4 sample and (b) blocky-α grains sample, whereby the misorientation angle ranges between 0.0° (blue) to 5.0° (red) as shown in the colour scale bar.



(a)



(b)

Figure 5.5: Grain orientaion spread of as-received (a) and blocky-α (b) Zr-4 specimens.

5.3.2 Zr-702

The IPF$_{RD}$ and IPF$_{ND}$ maps of as-received Zr-702 are shown in Figure 5.6(a) and (b). These reveal the equiaxed, α-Zr grain structure with an average grain size, l_G, of 28±7 µm. The IPF maps show 929 analysed grains The pole figures for as-received Zr-702 are shown in Figure 5.6(c). The 0001_{Zr} pole figure displays two asymmetric peaks of basal pole density, near the sample ND at the centre of the pole figure, the peaks are however closer to each other than in Zr-4.

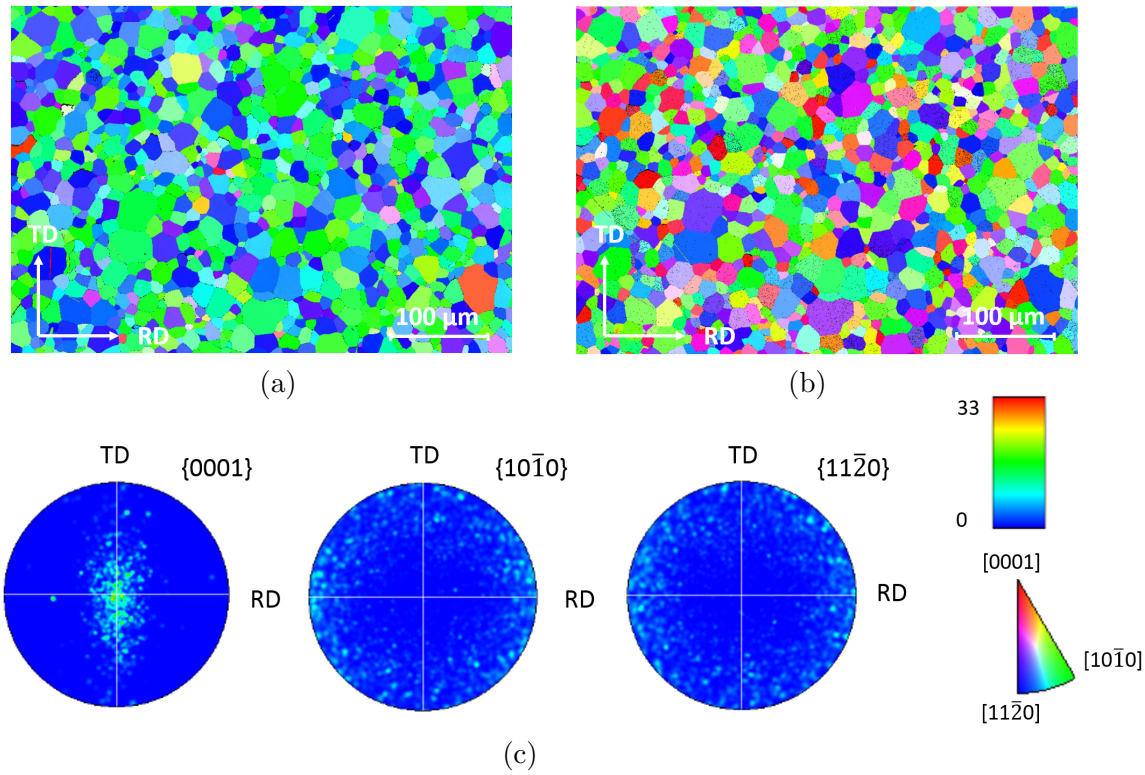


Figure 5.6: Maps of IPF$_{RD}$ (a) and IPF$_{ND}$ (b) revealing the as-received Zr-702 equiaxed grain structure. Their corresponding pole figures (c) highlight the expected Zr-4 rolling texture. (step size: 1 µm, number of grains analysed: 929).

The pole figures for a grain size enhanced specimen containing blocky-α grains is shown in Figure 5.7(c). It is also considered that due to grains recrystallising and increasing in size from ∼30 µm to ∼1000 µm, the texture tends towards random after the anneal treatment, however just like for Zr-4, the texture is difficult to quantify due to the small number of large grains. Figure 5.7(a) and (b) show the IPF$_{RD}$ and IPF$_{ND}$ maps respectively, of a blocky-α Zr-702 specimen, containing 82 grains with an average grain size of 325 ±26 µm. IPF maps shows that Zr-702 has a higher extent of bimodal grain size distribution than that in blocky-α Zr-4 specimens. This therefore means that the grain

growth anneal in Zr-702 produces more abnormal grains than in Zr-4. This was not expected as Zr-702 contains less SPPs that tend to pin grain growth. In contrast, however, island grains, associated with a local high SPP number density [177], are rarely observed in blocky-α Zr-702 specimens.

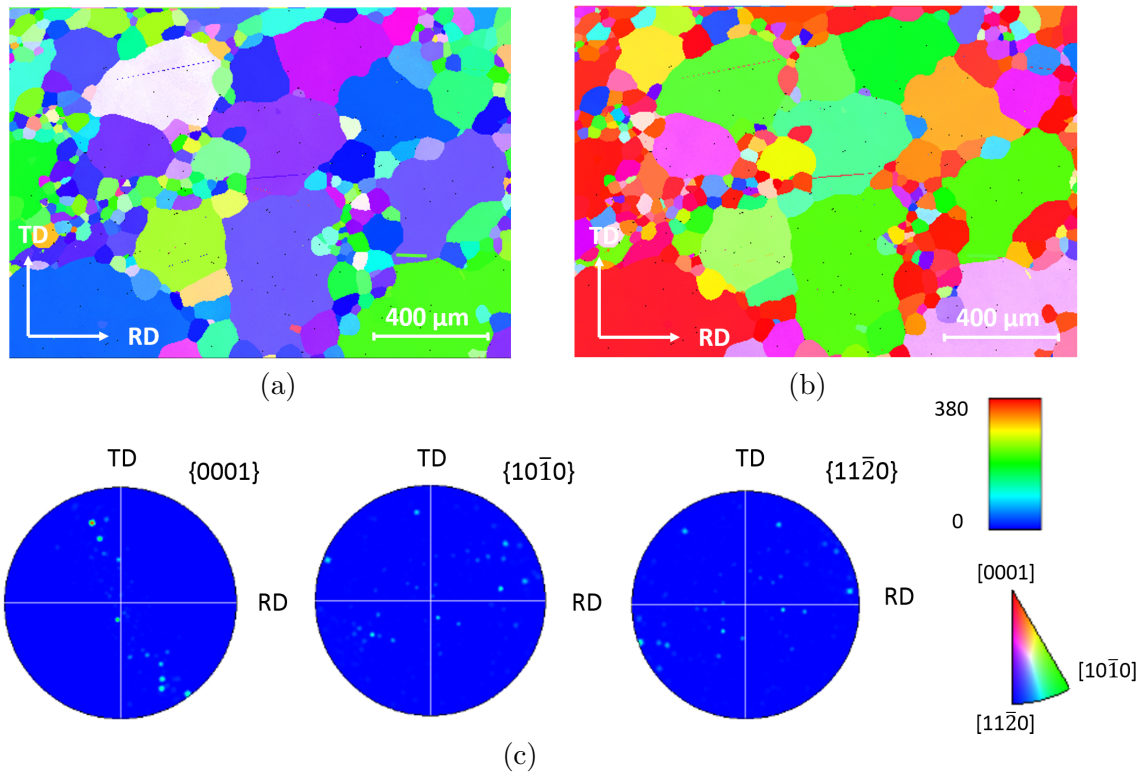
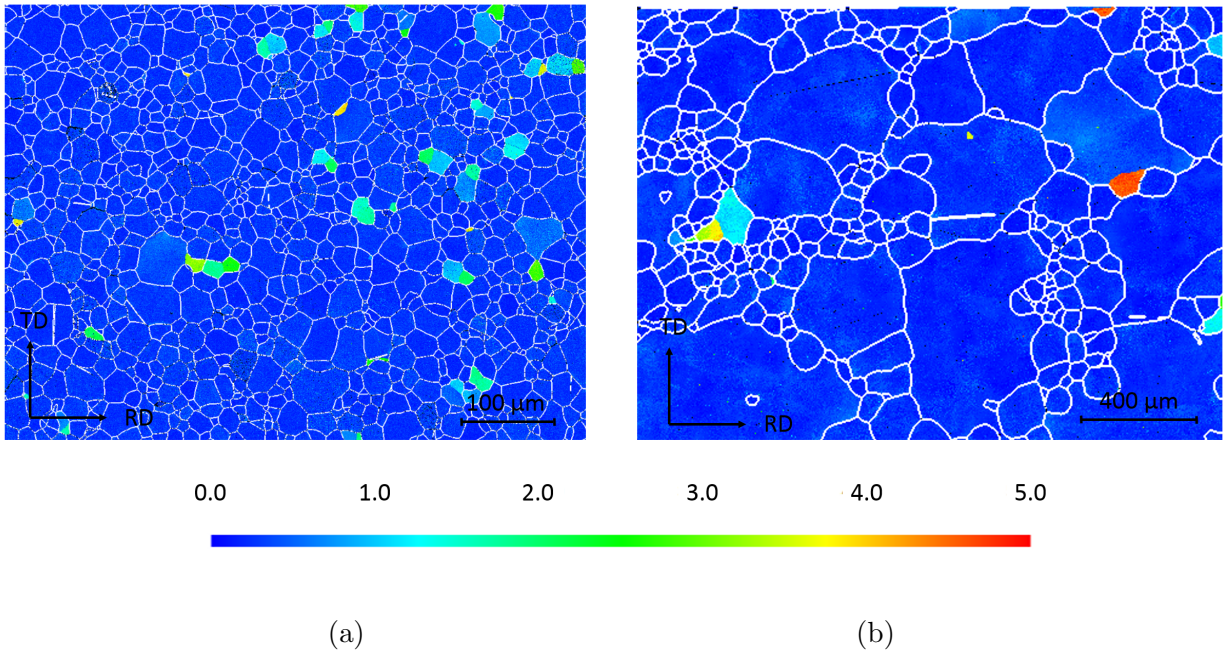


Figure 5.7: Maps of IPF$_{RD}$ (a) and IPF$_{ND}$ (b) revealing the blocky-α Zr-702 grain structure. Their corresponding pole figures (c) highlight the textureless microstructure. (step size: 2 µm, number of grains analysed: 148).

GAM maps for as-received and blocky-α Zr-702 microstructures are shown in Figure 5.8. GAM maps show that the former has a slightly larger amount of local deformation than the latter with a uniform distribution of high angle grain misorientation ranging up to 3-4°. Blocky-α specimens were found to have an overall lower energy level indicated by the dominant dark blue colour that corresponds to the low angle intra-granular misorientation of 0-1°. However, a small number of grains were found to have a very high angle intra-granular misorientation in those specimens with a misorientation of 4-5°.



(a) (b)

Figure 5.8: Grain average misorientation (GAM) maps of (a) as-received Zr-702 sample and (b) blocky-α grains Zr-702 sample, whereby the misorientation angle ranges between 0.0° (blue) to 5.0° (red) as shown in the colour scale bar.

5.4 SPP Characterisation

This study aimed to quantify the effect of SPPs on hydrides that precipitate after hydrogen diffusion takes place. As part of material characterisation the number density of SPPs (ρ_{SPP}) in Zr-4 and Zr-702 was quantified using SEM back-scatter and EDX analysis. Results from SEM+EDX mapping provide a qualitative measure of the chemical composition found in SPPs such as the amount of Cr and Fe. Back-scatter SEM images show heavy atoms scattering more electrons back towards the detector than the lighter alloying atoms, that appear brighter in the SEM image as shown in Figure 5.9(a). Figure 5.9 (b) shows three SPPs at higher magnification that appear darker than the Zr background. The binary images used to analyse SPPs, using Fiji ImageJ, are shown in Figure 5.9(c) and (d) respectively. Figure 5.10 shows, qualitatively, the effect of grain growth annealing on ρ_{SPP} and the SPP size in Zr-4. Table 5.2 and Figure 5.11 show that ρ_{SPP} reduce by 27% after recrystallisation, showing an average ρ_{SPP} of 0.034±0.009 SPP µm^{-2} in as-received Zr-4 and 0.025±0.004 SPP µm^{-2} in Zr-4 specimens with 'blocky-α' grains (l_G>250µm). The SPP number density is quantified as an average per unit area, irrespective of SPP size distribution, to give a parameter that represents the number of intra-granular nucleation sites per unit area in the microstructure. The median area of a an SPP (A_{SPP}) in as-received Zr-4 specimens was also quantified to be 0.15 µm^2 (which implies a diameter of ∼0.4 µm assuming

SPPs are perfect circles, ranging up to a maximum of 1.1 µm), a value of A_{SPP} which is 33% less than the median SPP size in recrystallised blocky-α specimens as shown in Figure 5.12. This indicates that the recrystallisation heat treatment has a coarsening effect on SPPs. The modal area was around 0.1 µm^2 in as-received and blocky-α Zr-4 specimens but their respective frequency is reduced from around 27 to 20% showing that smaller SPPs have presumably dissolved and redistributed to larger ones. This effect can be seen in Figure 5.10 that shows BS SEM images, with their corresponding binary maps, of the SPP distribution in as-received and in blocky-α Zr-4 with a near random distribution in both microstructures.

Finally, ρ_{SPP} in Zr-702 was quantified to be 0.019±0.005 SPP mm^{-2} in as-received Zr-702 and 0.017±0.004 SPP mm^{-2} in specimens with 'blocky-α' Zr-702 grains. This decrease of 11% is 2.5× smaller than the decrease in ρ_{SPP} observed in Zr-4 after the blocky-α heat treatment. The median A_{SPP} in as-received Zr-702 was found to be 0.14 µm^2, which is less than the median SPP size in recrystallised blocky-α Zr-702 specimens at 0.29 µm^2, as shown in Figure 5.13. The reduction in ρ_{SPP} and the increase in A_{SPP} also shows that SPPs dissolve and coarsen after the grain size enhancement heat treatment in Zr-702.

The theoretical relationship between ρ_{SPP} and A_{SPP} in as-received materials, before the grain growth heat treatment, and after the treatment is shown in equation 5.1:

$$I_{\rho_{SPP}} \times I_{A_{SPP}} = F_{\rho_{SPP}} \times F_{A_{SPP}} \tag{5.1}$$

where I and F correspond to the initial (before treatment) and final (after treatment) ρ_{SPP} and A_{SPP} in Zr-4 and Zr-702. Experimental results show that there a 8.7% difference between initial and final quantities in Zr-4 and 17.7% in Zr-702 and even though the averages after the treatment are taken over a range of grain sizes, the difference between theory and experiments maybe due to a statistical sampling effect, but may also be due to the following microstructural phenomena:

1. Dissolved Fe and Cr atoms trapped at dislocations in a similar mechanism to the Cotrell atmosphere. Dissolved alloying elements then get released after the heat treatment.

2. Segregation of Fe at GBs that may diffuse to SPPs as GB density reduce after the grain growth treatment.

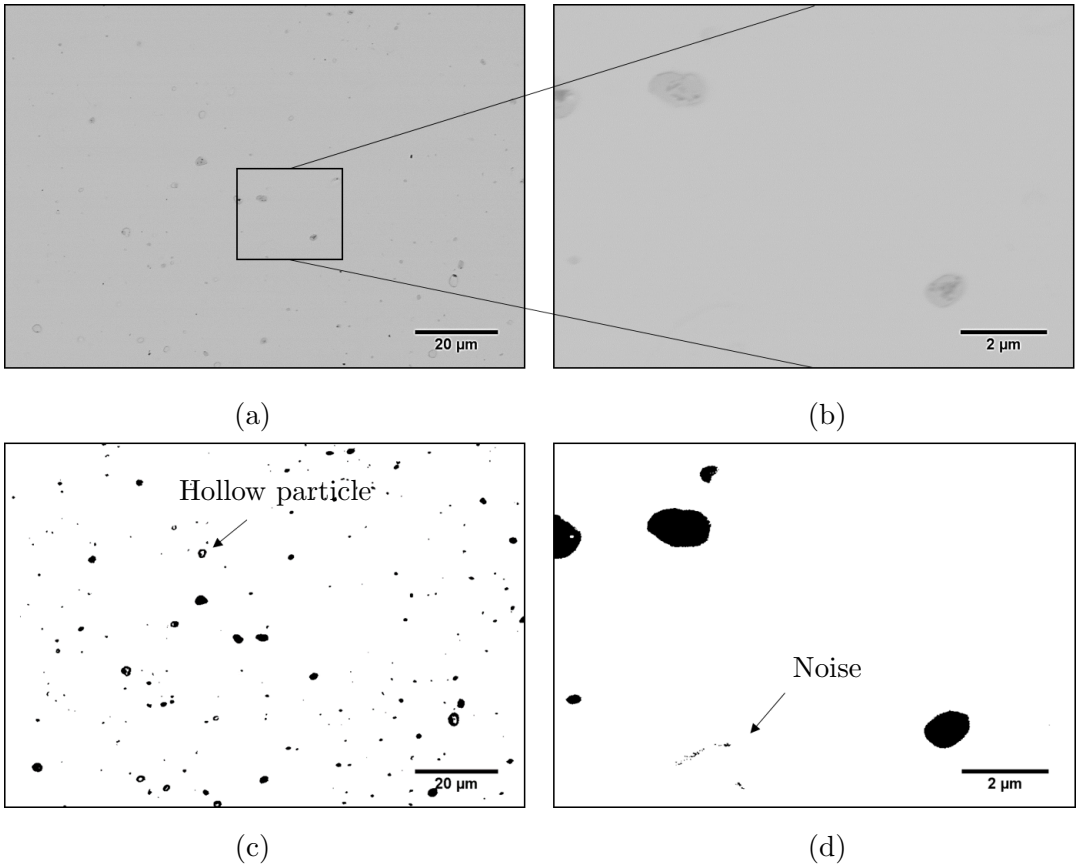


Figure 5.9: (a) Back-scattered SEM image of as-received Zr-4 specimen taken at ×2.5k magnification showing the bright zirconium background and the relatively dark particles. A small region from (a) was magnified to ×12.5k to show the substructure of the particles that were found to have small darker regions within. Binary images of (a) and (b) used for SPP number density and size distribution analysis are shown in (c) and (d), respectively. The arrow in (c) highlights a hollow particle that is taken into account during analysis while the noise in (d) is not considered in the analysis.

Table 5.2: The SPP number density (ρ_{SPP}) in Zr-4 and Zr-702 samples with as-received grain sizes (l_G<30µm). The standard deviation (SD) is also presented.

Alloy	SPP Number Density, ρ_{SPP} ($\times 10^{-2}$ µm^{-2})	SD ρ_{SPP}	Average Grain Size, l_G (µm)	SD l_G
Zr-4 as-received	3.4	0.9	15	3
Zr-4 recrystallised	2.5	0.4	790	57
Zr-702 as-received	1.9	0.5	32	5
Zr-702 recrystallised	1.7	0.4	770	34

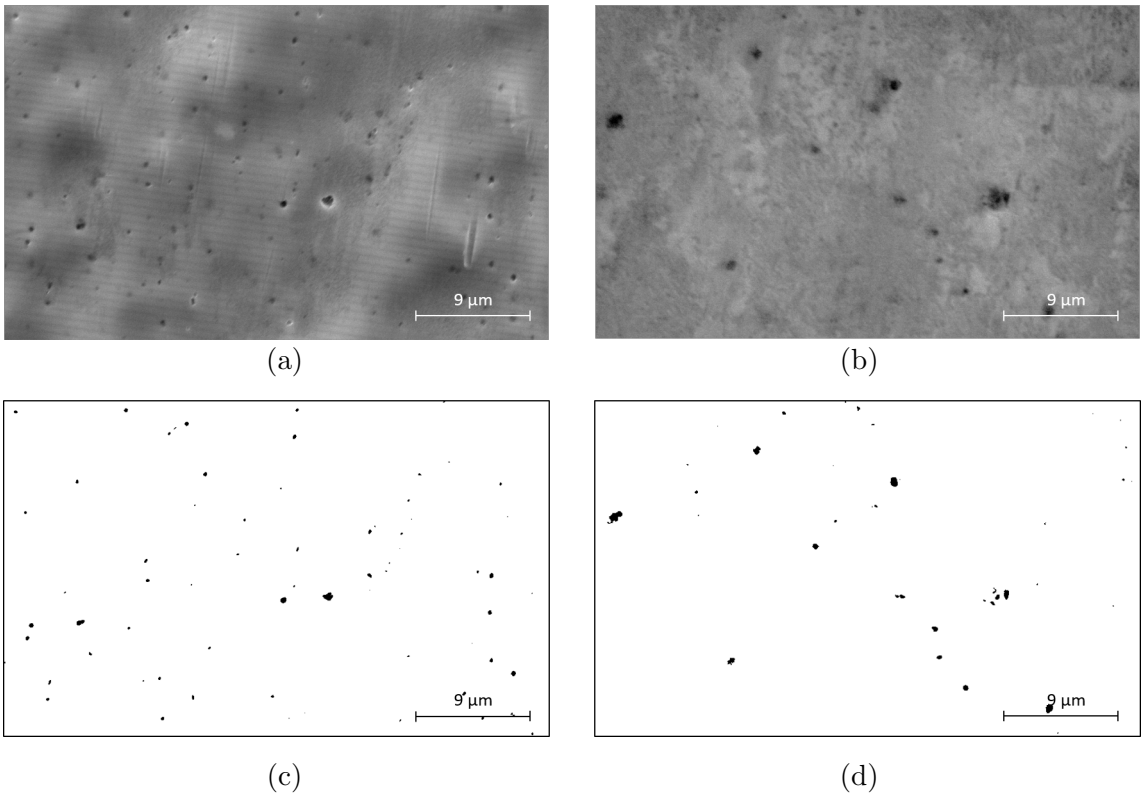


Figure 5.10: BS SEM images at a magnification of 10,000× of (a) as-received Zr-4 (b) grain growth annealed Zr-4. Their corresponding thresholded binary images are shown in (c) and (d) that highlight the size and number density reduction of SPPs from as-received to blocky-α microstructures.

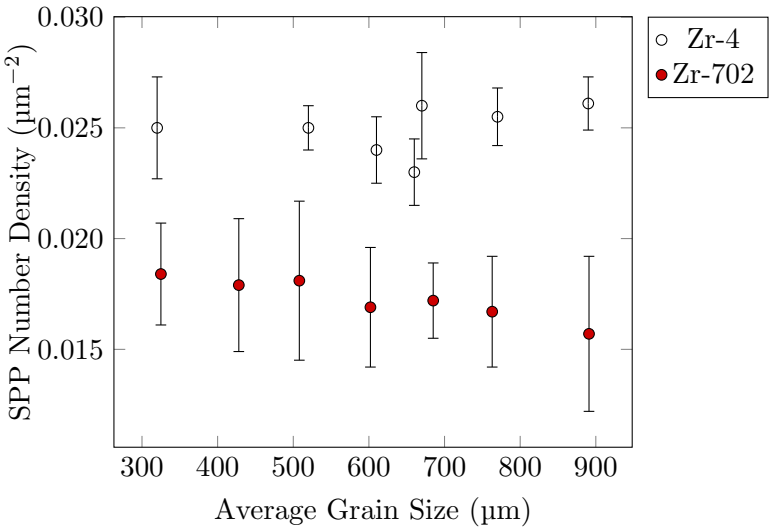


Figure 5.11: The number of second phase particles (SPPs) per µm^2 in blocky-α grain specimens of grain sizes >250 µm. Error bars show the standard deviation (SD) of SPP number density (ρ_{SPP}).

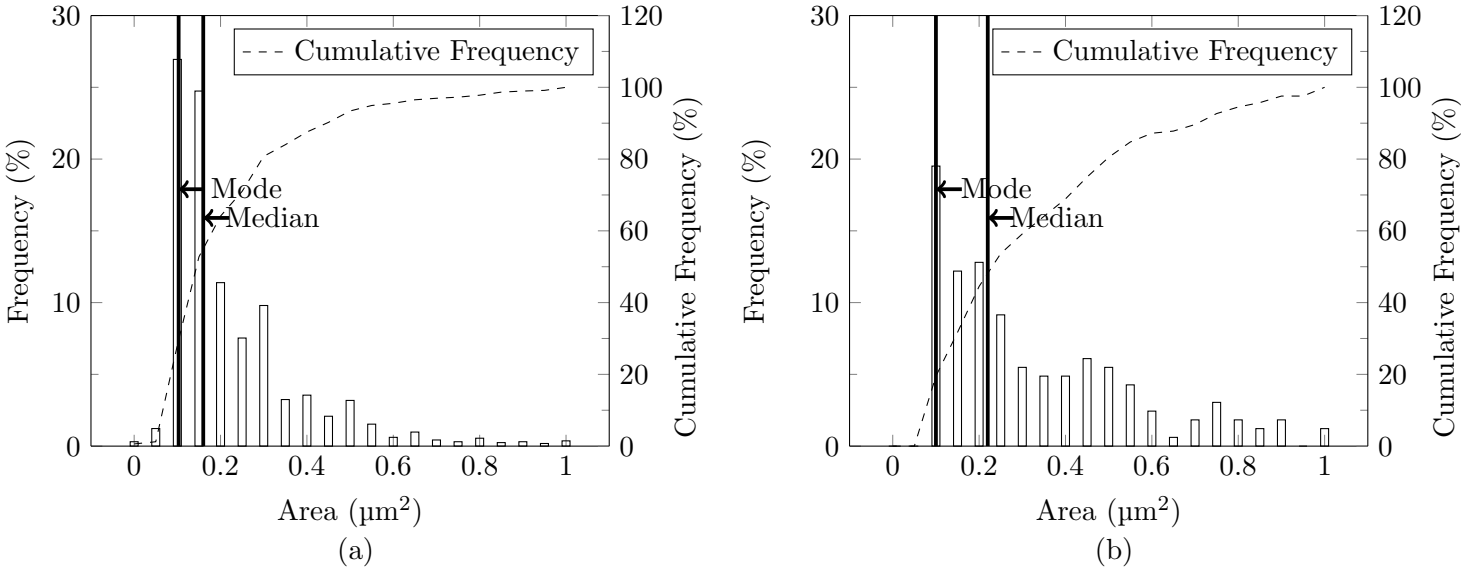


Figure 5.12: The SPP area distribution in (a) as-received Zr-4 with l_G= 15 µm and (b) blocky-α specimen with l_G= 770 µm. The median SPP area in as-received samples was found to be 0.15 µm^2 and 0.22 µm^2 in recrystallised ones.

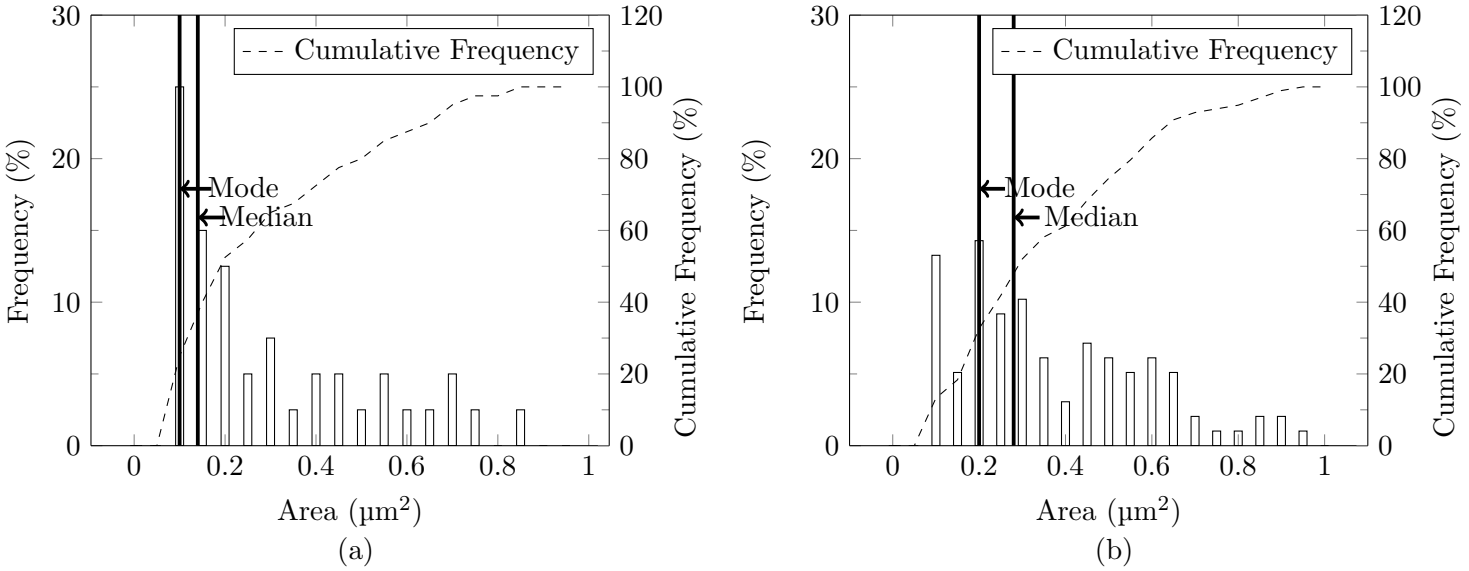


Figure 5.13: The SPP area distribution in (a) as-received Zr-702 with l_G= 32 µm and (b) blocky-α specimen with l_G= 602 µm. The median SPP area in as-received samples was found to be 0.14 µm^2 and 0.29 µm^2 in blocky-α microstructures.

5.5 Mechanical Characterisation

5.5.1 Zr-4 and Zr-702 Mechanical Properties

The 0.2% proof stress, ultimate tensile stress and the ductility of Zr-4 and Zr-702 (20°C and 350°C) are presented in Table 5.3. Figure 5.14 shows the stress-plastic-strain curves for as-received Zr-4 and Zr-702 samples, at 20 and 350°C in the RD and TD directions of the plate, which highlights the reduction in yield strength and the increase in ductility as temperature increases from 25 to 350°C. The specimens in RD (specimen's gauge longitudinal direction is in the rolling direction of the plate) do not show a visible yield point at which macroscopic plasticity start to occur, whereas TD specimens tend to have a more defined yield point. This is due to the textured nature of zirconium whereby the hcp crystals align <30°C from the ND towards the plate's TD and slip is more likely in RD due to its higher Schmid factor than TD.

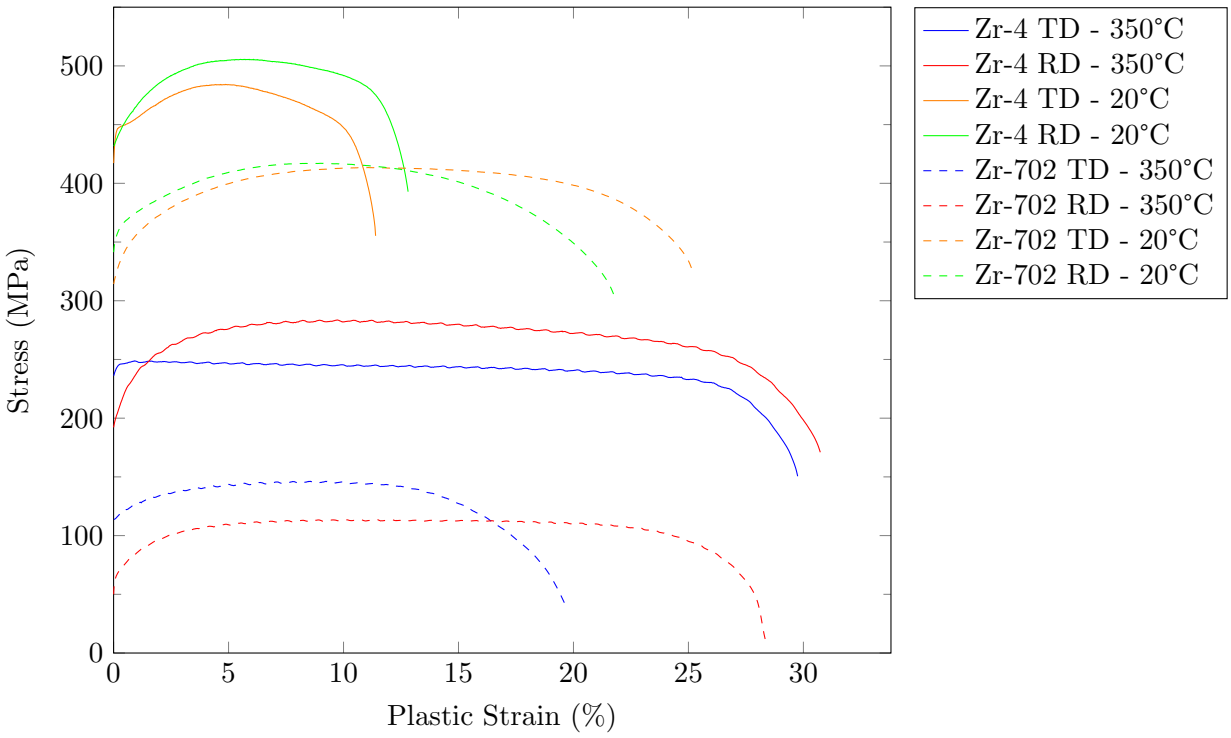


Figure 5.14: Tensile testing stress-plastic-strain curves for Zr-4 and Zr-702 as-received grain size at two different temperatures for the rolling direction (RD) and transverse direction (TD) of plate.

5.5.1.1 Hardness Testing

Vickers hardness results are shown in Figure 5.15 with a Vickers hardness number (VHN) values for as-received Zr-4 and Zr-702 of 210 and 193.5 VHN respectively. One possible reason for the difference

Table 5.3: Tensile properties of Zr-4 and Zr-702 in the RD and TD, as-received grain size, at 20°C and 350°C.

Specimen	Tensile Properties		
	Yield Strength at 0.2% Offset (MPa)	Tensile Strength (MPa)	% Elongation
Zr-4 RD at 20°C	419	505	12.8
Zr-4 TD at 20°C	417	484	11.4
Zr-4 RD at 350°C	192	283	30.7
Zr-4 TD at 350°C	236	248	29.8
Zr-702 RD at 20°C	341	417	21.8
Zr-702 TD at 20°C	341	413	25.1
Zr-702 RD at 350°C	50	113	28.4
Zr-702 TD at 350°C	114	146	19.7

Standard deviation is at ∼5%.

in hardness between as-received Zr-4 and Zr-702 is the larger average grain size in the latter at 28 µm versus 15 µm in Zr-4, as well as the difference in alloying elements content between Zr-4 and Zr-702 at maximum 0.29 wt.% of Fe+Cr+Sn in Zr-702, while Zr-4 contains 1.88 wt.% Fe+Cr+Sn. The room temperature 0.2% proof stress for as-received Zr-4 and Zr-702, obtained from tensile test results shown in Tables 5.3, are also shown in Figure 5.15. These show that the 0.2% proof stress decreases from 414 to 341 MPa from as-received Zr-4 to Zr-702 respectively, a bigger percentage decrease than the one observed in hardness.

Grain growth annealing causes a small reduction in VHN from as-received to blocky-α Zr-4 and Zr-702. In Zr-4 the hardness decreases from 210 to 165 VHN highlighting the effect of increase in grain size. In Zr-702 specimens the hardness also decreases after grain growth annealing but to a smaller extent than in Zr-4 as shown in Figure 5.15.

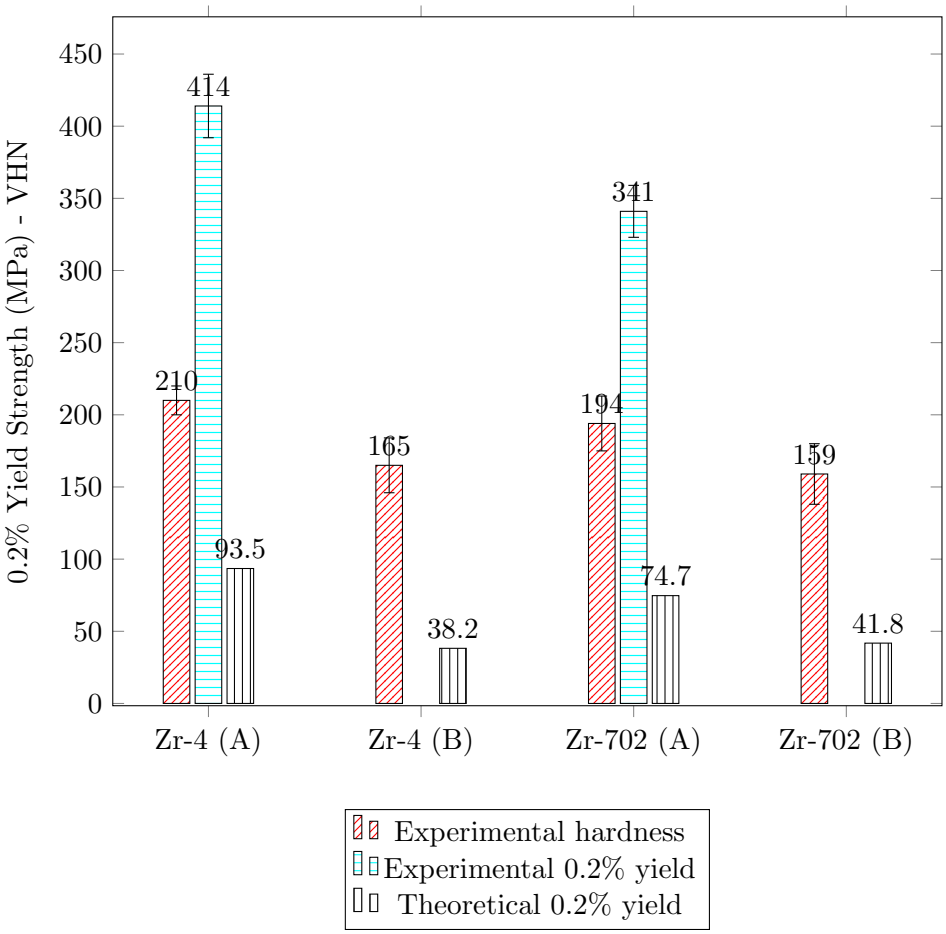


Figure 5.15: The experimental Vickers hardness number (VHN) for (A) as-received and (B) blocky-α grained (B) Zr-4 and Zr-702 is shown in blue columns. The experimental 0.2% yield strength is shown for as-received materials while a theoretical yield based on the Hall-Petch equation is shown for all specimens. NB the 0.2% yield strength for blocky-α specimens was not experimentally produced.

5.6 Hydride Quantification and Discussion

Figure 5.16(a) shows a secondary electron micrograph of as-received Zr-4, containing a hydrogen concentration of 100±18.4 wppm which corresponds to a theoretical hydride area fraction of 1.7% and an experimental value pre-cycling of 1.4±0.2%. $\rho_{hydride}$ of macro-hydride precipitates was quantified to be 374±70.5 and 103±17.5 macro-hydrides mm^{-2} for Zr-4 small (∼15 µm) and large grains (250-900 µm), respectively. This was marginally lower for Zr-702 where $\rho_{hydride}$ was quantified to be 246±60.7 and 99±11.34 macro-hydrides mm^{-2} for small l_G (∼30 µm) and large l_G (250 – 900 µm), respectively. Figure 5.17 shows that around 45% of hydrides precipitated within the small grains of the Zr-4 samples compared to 12% for the small grained Zr-702 samples. However, the difference in as-received grain size between Zr-4 and Zr-702 (∼15 µm and ∼30 µm respectively) and the scatter in the data of hydride number density in these alloys, the difference in intragranular precipitation cannot be attributed to the

difference in SPP content.

As l_G was increased from 15 – 50 µm to 250 – 1000 µm, for both alloys, the percentage of hydrides that precipitated within grains (different types shown in Figure 5.18) increased in both Zr-4 (from 45% to 87%) and in Zr-702 (from 12% to 74%), the intra-granular precipitation in Zr-4 was again higher at 87% compared to 74% in Zr-702, however the scatter in data does not confirm the inference of larger SPP number density causing a larger intra-granular precipitation. Finally, some experimental SEM+EDX images of hydride precipitation at or around SPPs in as-received and blocky-α specimens can be seen at high magnification as shown in Figures 5.19, 5.20 and 5.21. Such microstructural hydride areas (showing hydrides precipitating near or at SPPs) are not easily found in Zr-702. Figures also show binary maps of the hydrides and SPPs along with EDX maps of Fe and Cr SPPs.

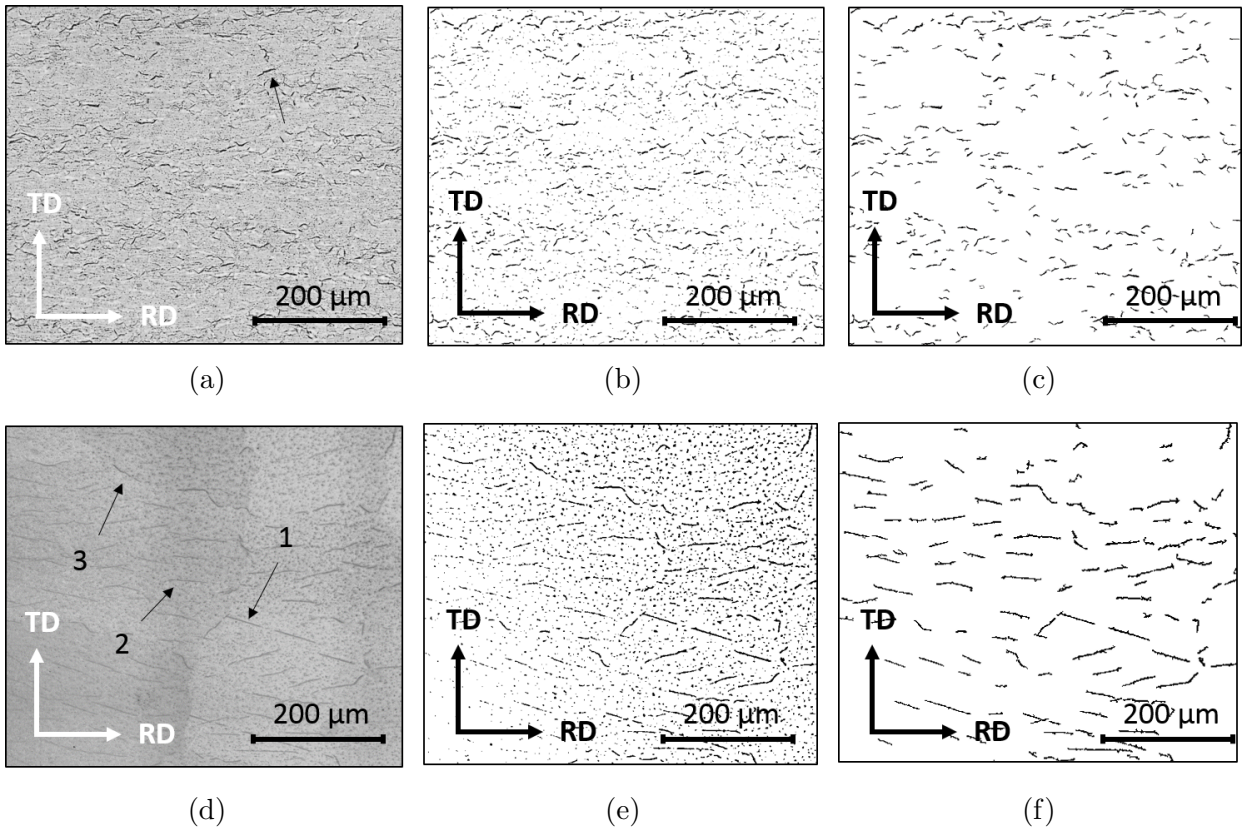


Figure 5.16: (a) Secondary electron micrographs of Zr-4 in the RD-TD plane (average grain size ∼15 µm). Blocky-α grains containing hydrides in Zr-4 are shown in (d). Binary images of the micrographs used for hydride analysis are respectively shown (b) and (e) with noise and (c) and (f) without noise, revealing the black macro-hydride features. The arrow in (a) shows an inta-granular hydride in as-received Zr-4 while arrows 1, 2 and 3 in (d) show twin boundary hydrides (twins produced during grinding above 15 N), intra-granular hydrides and inter-granular hydrides respectively.

The hydride size distribution in Zr-4 and Zr-702, characterised by the area of each macro-hydride

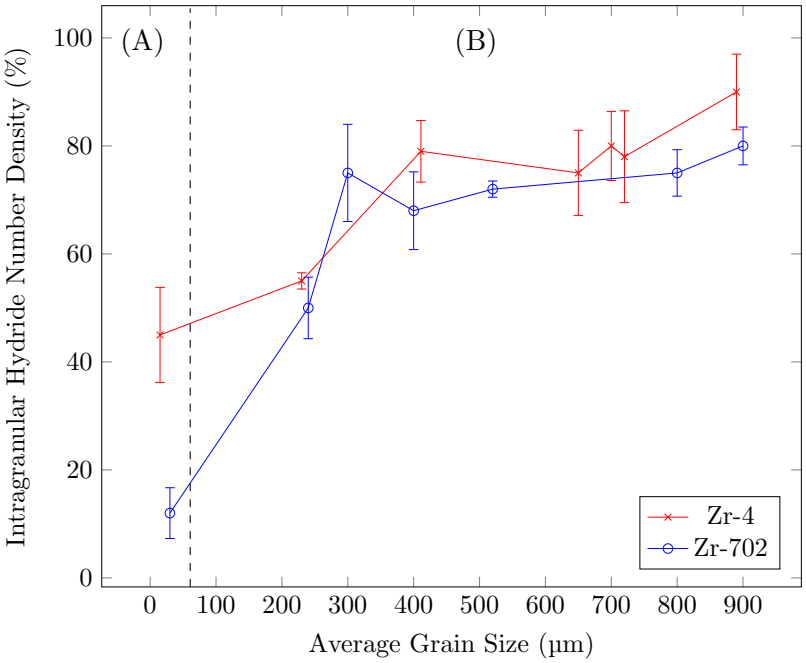


Figure 5.17: Hydride distributions parameterised by grain size and SPP content, as represented by the proportion of intra-granular hydrides for Zr-702 and Zr-4 specimens of differing average grain sizes. Vertical error bars show the standard deviation of the proportion of intra-granular hydrides. The graph shows two regions split by a vertical dashed line, whereby region (A) is for as-received grain sizes and (B) for specimens containing blocky-α grains.

packet is shown in Figures 5.22 and 5.23. In the small grained Zr-4 samples around 14% of hydrides were found to have a modal area between 6–10 µm^2. The area of hydrides in as-received Zr-4 ranges up to 70 µm^2 ($\leq$1%). This area distribution was found to be significantly different in samples with blocky-α grains, where 5% of hydrides were found to have areas between 6–100 µm^2 and ranging up to $\sim$1000 µm^2 ($\leq$1%) with a modal hydride area of 230 µm^2. In the small grained Zr-702 samples the trend was similar where around 3% of hydrides were found to have an area between 6–10 µm^2 ranging up to 70 µm^2 ($\leq$2%). This area distribution was also found to be different in samples with blocky-α grains, where 3% of hydrides were found to have areas between 6–100 µm^2 and ranging up to $\sim$950 µm^2 ($\leq$1%) with a modal hydride area of 100 µm^2.

Discussion

It is evident that GBs are potent nucleation sites for hydrides. Referring to Figure 5.16(a), this can be seen for the small-grain Zr-702 samples, which can contain higher proportions of inter-granular hydrides than their larger grain counterparts shown in Figure 5.16(d), however any clear trend in Zr-4 and Zr-702 specimens is somewhat masked by the scatter in the hydride number density data. Theoretically, zirconium hydrides are distinct thermodynamic phases defined by their stoichiometric

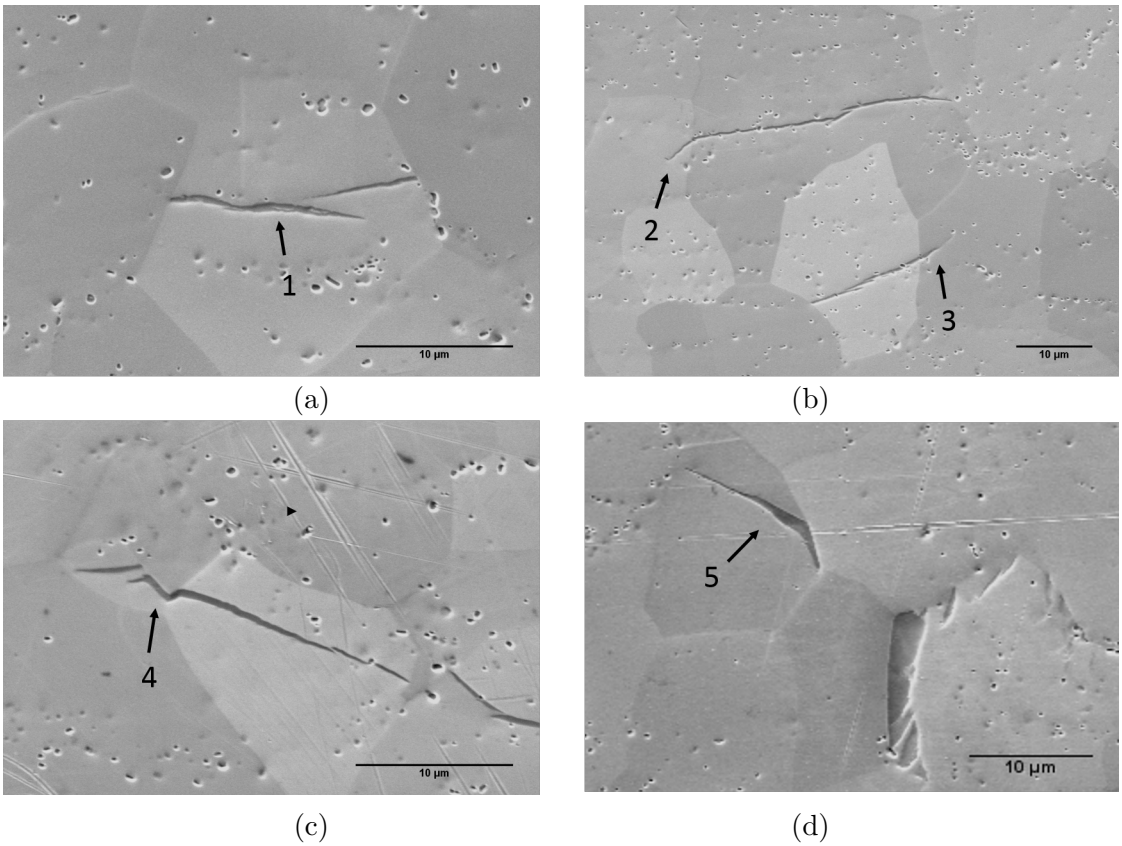


Figure 5.18: Types of intra-granular hydrides; Arrow (1) shows two macro-hydrides precipitating fully inside a grain and decorating crystal planes. (2) and (3) show macro-hydrides precipitating intragranually in one grain and crossing the GB into another. In the case of (2) there is a clear change of hydride orientation as the hydride crosses the GB from one grain to another. Arrow (4) shows a similar hydride behaviour but with a small degree of intergranular precipitation when crossing grains, also with a change of hydride orientation after crossing. And finally, arrow (5) shows an intra-granular hydride that does not cross into another grain, instead continues to precipitate at the GB.

and crystallographic properties, the high intergranular hydride percentage in commercially pure Zr may fundamentally be attributed to the hierarchy of heterogeneous nucleation sites in metals [148]. Generally, nucleation sites are stress-raisers with favourable defect structures that provide desirable conditions for precipitation; in this formalism, GBs are presumed to be the most favourable [40, 148]. Therefore, small-grain samples may have a high fraction of inter-granular hydrides as they contain a high density of GBs specially in as-received commercially pure Zr. The formation of hydrides at GBs is also linked to the slow cooling rate following the hydrogen homogenisation treatment, which allows hydrogen diffusion to remain fast for a longer period of time before hydrogen is trapped at nucleation sites. This ensures that the hydride distribution pattern has sufficient time to attain the most optimal free energy configuration, which is reflected in the activation of the GB nucleation sites that are most energetically favourable. The formation of hydrides at faster cooling rates (air cooling)

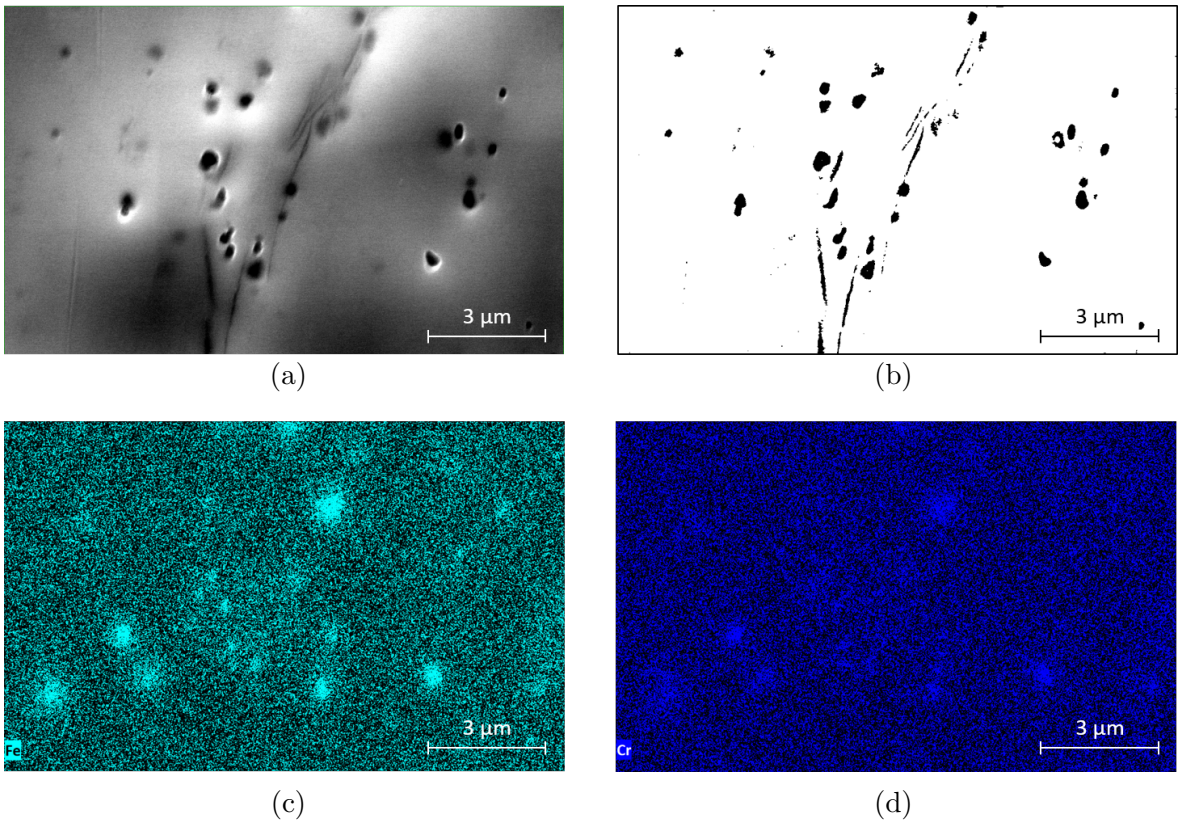


Figure 5.19: Micro-hydride precipitates at and around SPPs (a) in as-received Zr-4. The corresponding binary image (b) shows circular black SPPs surrounding lenticular micro-hydrides that appear to stack on top of each other. EDX maps of Fe (c) and Cr (d) atoms give a good indication of the SPP location.

was found by Birch et al. to produce more intra-granular hydrides, which is likely due the relative tendency for hydrogen to diffuse towards existing hydride structures and promote hydride growth [149]. Intra/intergranular percentage results for Zr-4 however do not support the theory with certainty, due to the scatter in data for their as-received specimens.

It is also worthwhile to note that not all GBs have equal hydride precipitation potency. GBs themselves can also have a hierarchy for hydride precipitation which is controlled by crystallography and misorientaion between grains. GBs that have hydride precipitates are most likely crystallographically well aligned and optimally-misorientated for hydride precipitation [178]. Furthermore GBs control the morphological growth of inter-granular hydride features, as shown in Figure 5.16(c)(f). Again, this can be traced fundamentally to the geometry of GBs as planar defects, whose local compatibility mismatch stresses are most pronounced along the length of the interface between highly-misorientated adjacent grains [179]. Therefore, given the potency of GBs, the texture will most likely have a significant effect on both the nucleation and growth of hydrides. Moreover, it appears that GBs also affect the size

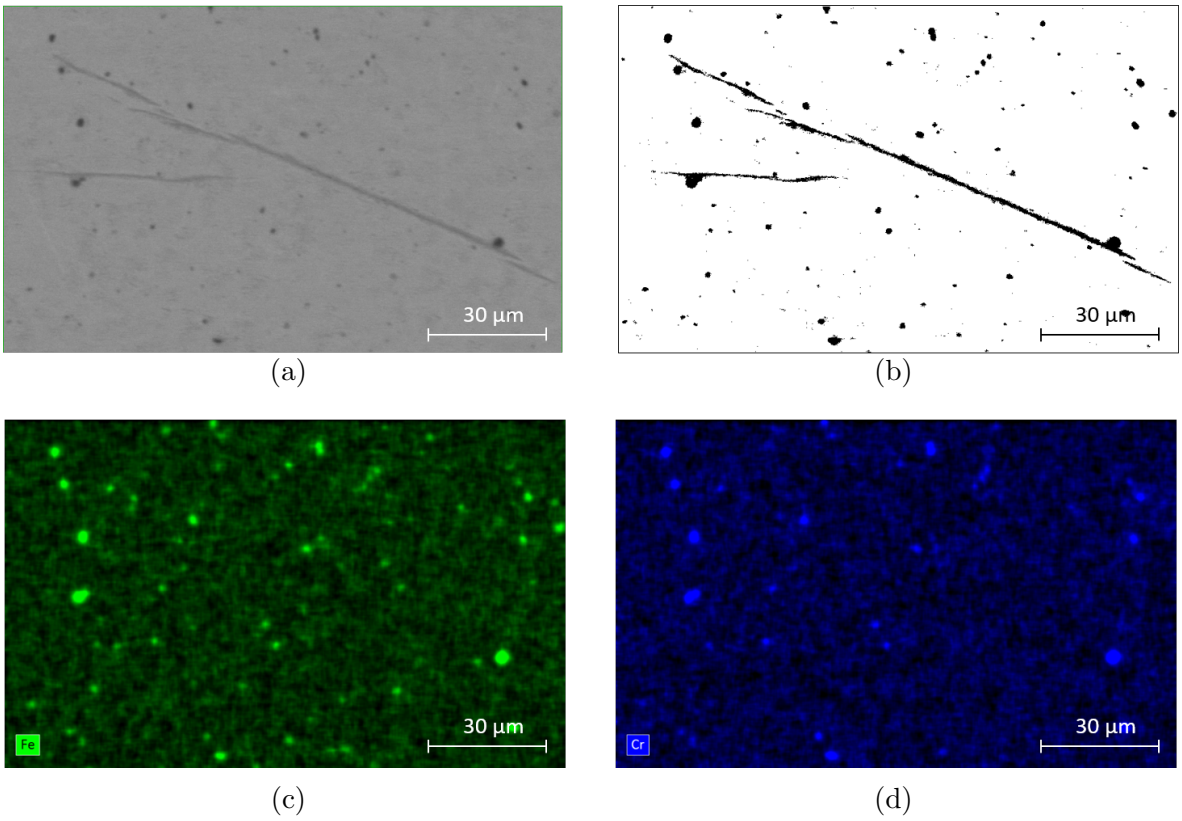


Figure 5.20: Macro-hydride precipitates at and around SPPs (a) in blocky-α Zr-4. The corresponding binary image (b) shows circular black SPPs surrounding large macro-hydrides. EDX maps of Fe (c) and Cr (d) atoms give a good indication of the SPP location.

of the hydrides, considering Figures 5.22 and 5.23. Here, the hydride size corresponds to the area of a macroscopic hydride feature that is, upon closer inspection, a stack structure of microscopic hydride phase platelets [40, 180]. In the smaller grain samples, the high density of GBs can disrupt the regularity of the micro-hydride stacking, leading to the formation of smaller macro-hydrides [181, 182]. These results indicate the importance of GBs as nucleation sites; therefore, computational models of hydride precipitation or hydrogen distribution should aim to incorporate the effects of GBs explicitly.

In contrast to GBs, the role of SPPs in influencing hydride precipitation cannot be seen in Figure 5.17 due to the scatter in the intra-granular hydride percentage in small and large grained specimens of both alloys. Figure 5.17 does however show that there are more intra-granular hydrides in large-grain samples than small ones. From the theoretical standpoint, the interface between the intermetallic inclusions and the parent matrix may be thought of as a more localized variant of a GB-like defect. Accordingly, the effect of SPPs as nucleation sites is analogous to GBs; however, if SPPs are less potent stress-raisers than GBs, the role of SPPs as nucleation sites only becomes more influential as

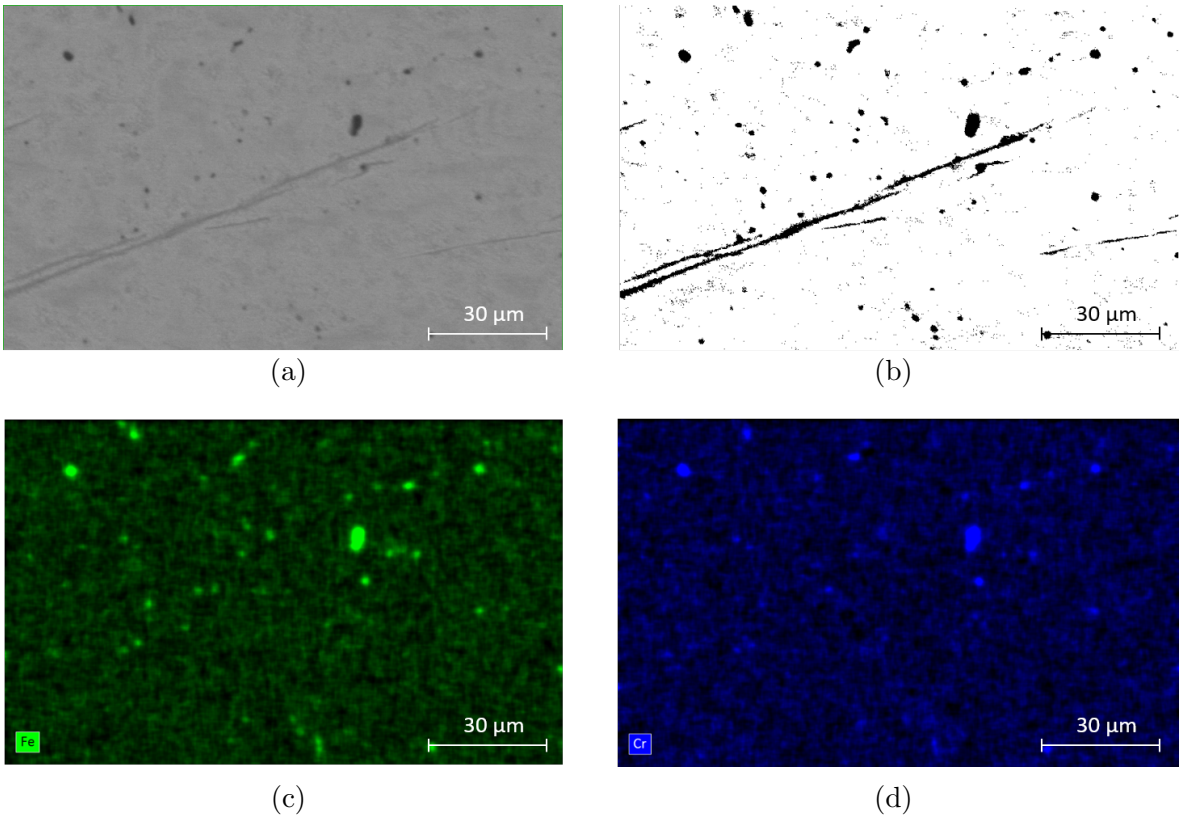


Figure 5.21: Macro-hydride precipitates at and around SPPs (a) in blocky-α Zr-4. The corresponding binary image (b) shows circular black SPPs surrounding macro-hydrides. EDX maps of Fe (c) and Cr (d) atoms give a good indication of the SPP location.

the density of favourable GBs decreases (i.e in specimens of large grain size). Figure 5.17, shows more intra-granular hydrides in Zr-4 as opposed to Zr-702 however due to the scatter in data, the uncertainty in mean and median values hinders any clear conclusions on the effect of SPPs on intra-granular precipitation.

Finally, it is worth noting that Zr-702 has a percentage of Hf (0.97 wt.%) present in the solid solution which makes its chemistry slightly different to Zr-4 and because it has little Sn content (0.15 wt.% in Zr-702 vs 1.51 wt.% in Zr-4), it makes it much less hard than Zr-4. One hypothesis might be that the thermodynamic driving force required for nucleation of hydrides will be greater for a harder matrix. A larger temperature drop will be required to develop the driving force required for nucleation and so in a harder lattice hydride nucleation should occur at a lower temperature. At lower temperature, diffusion is slower and more hydrides will form inside the grains because the distances that H can diffuse will be smaller. This therefore implies that more intra-granular precipitation of hydrides in a harder lattice (Zr-4) might occur although again this hypothesis cannot be proven due to the uncertainties in the means.

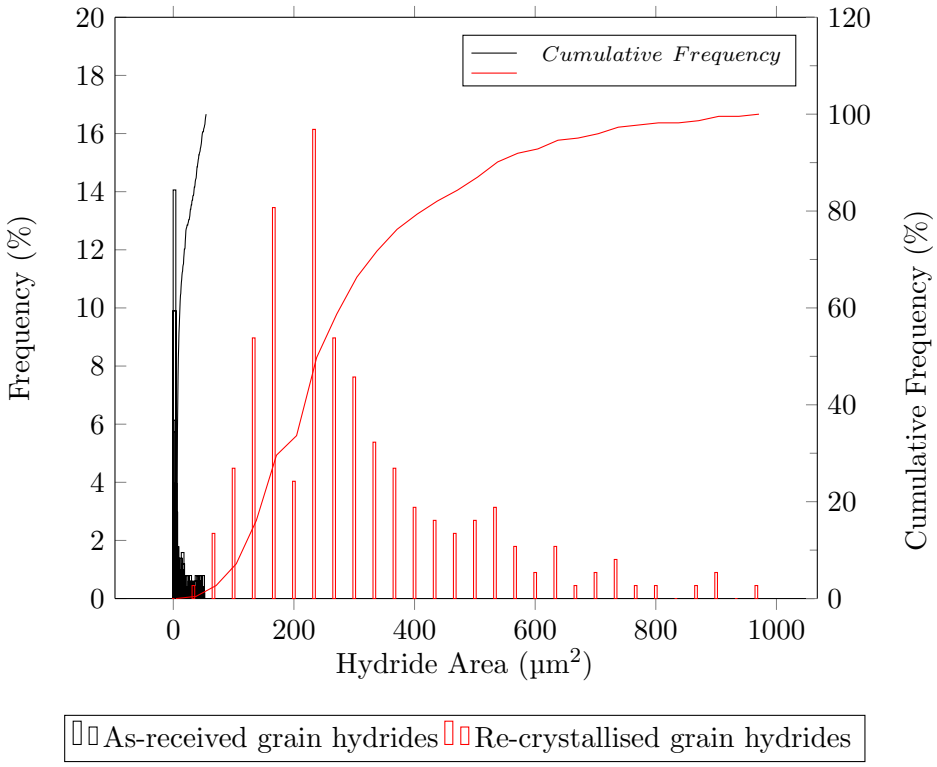


Figure 5.22: The macro-hydride area distribution in Zr-4 for an as-received sample with $l_G \simeq 15$ µm and an enhanced grain size sample with $l_G \simeq 720$ µm. The modal area of hydrides in as-received Zr-4 is 8 µm^2 and 230 µm^2 in blocky-α specimen.

In addition, Breen et al. [183] has shown that Sn forms cluster or regions of high concentration between inter-granular deuterides and the α-Zr reaction front which may show that deuteride growth rate is controlled by the partition of Sn to the α-Zr matrix. This suggests that Sn in Zr-4 has the higher destabilizing effect than all other alloying additions on hydride phases and that Sn is relatively more stable in pure Zr than in any zirconium hydride, as shown by a recent density functional theory study by Christensen et al. [184]. In Zr-4 the Sn content of 1.51 wt.% will therefore act to make hydride precipitation more sluggish rather than provide a nucleation site for precipitation as Fe and Cr particles do [16]. Sn is in the solid solution of the α-Zr matrix, meaning that it will not likely have an effect of hydrogen diffusion, other that having a binding effect on hydrogen in solution, unlike SPPs that may act as localised stress-raising features for hydrogen to diffuse towards [16].

Even though experimental data does not provide certainty about whether SPPs have an effect on the larger intra-granular percentage in Zr-4 relative to Zr-702, computational models of hydride precipitation or hydrogen distribution, should distinguished by SPP content to provide a more realistic picture of the microstructure; for example, this can be achieved by invoking microstructural parameters such as ρ_{SPP} and A_{SPP} that quantify the density and size of intra-granular nucleation sites that

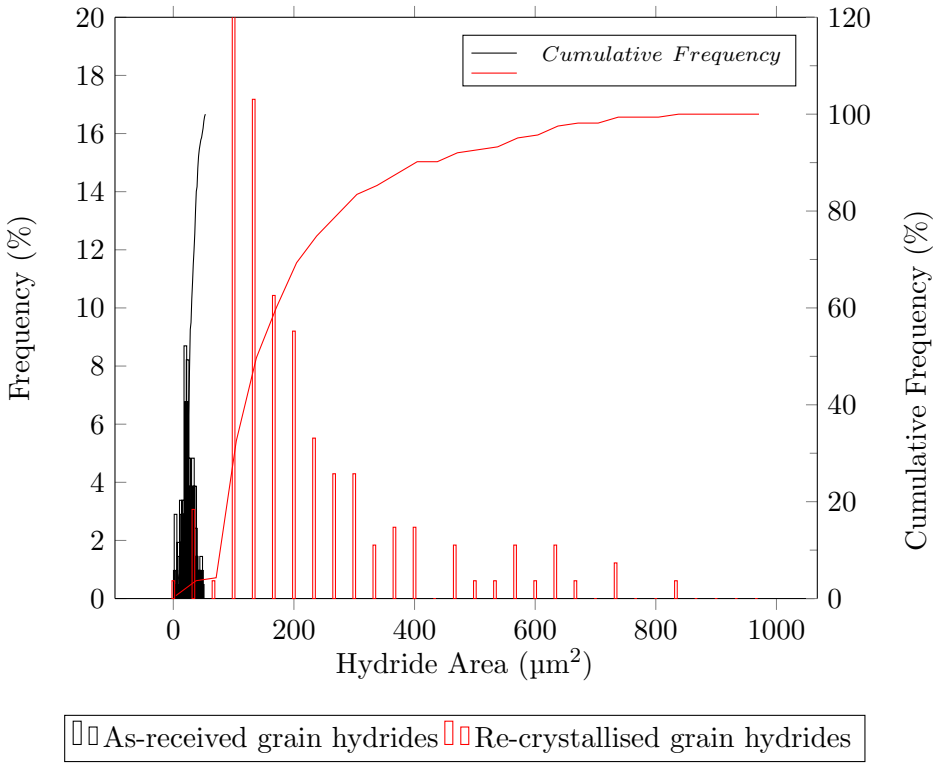


Figure 5.23: The macro-hydride area distribution in Zircadyne-702 for an as-received sample with l_G ≃30 µm and an enhanced grain size sample with l_G ≃800 µm. The modal area of hydrides in as-received Zr-702 is 28 µm^2 and 100 µm^2 in blocky-α specimen.

represent the random SPP population of stress-raisers within grains.

In summary, the experimental results presented in this chapter provide a valuable insight into the parameter space associated with GBs and SPPs as two important classes of nucleation sites under slow furnace cooling conditions. In particular, it is essential that models of hydrogen diffusion and hydride precipitation should include the microstructural information that characterises the texture and alloy composition through inter- and intragranular nucleation sites. Such information can be implemented to some extent by explicitly treating GBs and SPPs.

5.7 Conclusions

Hydride precipitation in zirconium was quantified for materials with different grain sizes and alloy compositions to attempt to compare GBs and SPPs as inter and intragranular hydride nucleation sites respectively. This provides a strategy to quantify the preferential hierarchy of micro-hydride nucleation sites that lead, via autocatalytic nucleation, to the detrimental macro-hydride features. It was found that for smaller grain (as-received) Zr-702 specimens, there was a higher proportion of inter-granular hydrides, relative to intra-granular hydrides, however there is some uncertainty in the trend found in

found in Zr-4 alloys due to overlap in the error bars. Finally, even though hydrides can be seen to precipitate at and around SPPs in using BS SEM + EDX imaging, as the grains were grown in size, the scatter in data of hydride number densities and the overlap in their standard deviation between both alloys, masks off any clear trend about the effects of reduced GB density and SPP content on the preference of hydride precipitation in Zr-4 and Zr-702.

Results of hydride distribution can be used to parametrise microstructural models of hydride precipitation or hydrogen distribution as grain boundaries and SPPs can be regarded as significant features in the Zr microstructure that may alter hydride distribution.

In summary it was observed that:

1. Hydrides were found to precipitate at and around SPPs in both Zr-4 and Zr-702 as-received and blocky-α microstructures using BS SEM + EDX imaging.

2. A clear trend of the effect of SPPs on intra-granular macro-hydride precipitation in Zr-4 and Zr-702, the latter with less SPP content that the former, cannot be found in both alloys.

Chapter 6

Quantification of Stress-driven Hydride Precipitation in As-received and 'Blocky-α' Zr-4 Microstructures

6.1 Outline

The effects of notch acuity on hydride distribution at grain boundaries (GB) and intragranular sites in as-received and blocky-α Zr-4 were investigated after thermo-mechanical loading. The chapter also considers the effects of material texture, grain size and SPP distribution. The test material was chosen to be Zr-4 due its relatively high yield strength that provides a reasonable hydrostatic tensile stress gradient for hydrogen diffusion and because it is representative of material used in industrial components.

6.2 Introduction

Hydride distribution and orientation plays an important role in the embrittlement of industrial Zr components such as fuel cladding; radially oriented hydrides have been shown to be much more detrimental to mechanical properties than circumferentially oriented hydrides and so understanding the effects of microstructure on stress driven hydride reorientation is important. Hydride reorientation in Zr components becomes particularly important during the transition of nuclear fuel rods between wet and dry storage; during this transition, many of the hydrides are dissolved into the matrix as the temperature rises above the dissolution temperature and then precipitate again upon cooling [185].

The process of reorientation starts with hydrogen interstitials, that are driven by a hydrostatic stress gradient, diffusing through the matrix to accumulate ahead of tensile stress concentrating features (SCFs) such as notches [169]. At temperatures above the terminal solid solubility for dissolution (TSS_D), hydrogen sits in solid solution until a critical solvus for phase transformation is exceeded, whereupon zirconium hydride precipitates are nucleated. Hydride precipitates are formed at temperatures below the terminal solid solution for precipitation (TSS_P) [20]. After hydrogen stress-driven diffusion and below TSS_P hydrides precipitate ahead of such dominant SCFs and thereafter threaten the structural integrity of the component [5]. Such SCFs produce a tensile stress region ahead of them, that is found to contain many macroscopic hydrides, each composed of many microscopic hydride needles of the order of microns. When one of these microscopic hydride needles is precipitated at a favourable microstructural nucleation sites, it creates favourable conditions for another microscopic needle to precipitate in its vicinity; this sequence of stacking continues until macroscopic hydrides are formed, leading to a mechanism known as autocatalytic nucleation. Favourable localised hydride microstructural nucleation sites, explored in Chapter 5, include GBs [60, 151] and SPPs [16, 179].

Hydride precipitation in mechanically stressed zirconium samples has been studied extensively for the past 50 years for highly textured Zr-4 cladding materials with small average grain sizes of 10-20 µm, with less work done on microstructures containing larger grain sizes [40]. Thin tube zirconium cladding under certain manufacturing conditions, may develop blocky-α grains that can potentially occupy the entire wall thickness [64]. Chapter 5 shows that blocky-α grains reduce the GB density, which was found to alter the heterogeneuous hydride nucleation behaviour. Chapter 5 also shows that large blocky-α grains could also potentially allow intra-granular hydride precipitates to reach lengths of the order of millimeters. Blocky-α grains lead to less interruption to the autocatalytic nucleation process beginning at an intragranular nucleation site; the microhydride stacking would likely continue until a grain boundary was reached and this would go on if the grains were larger and hence the grain boundaries were on average further away. This chapter now explores the blocky-α effects (grain size and texture) on hydrogen stress driven diffusion and hydride precipitation but after thermomechanical cycling.

Other than GBs as hydride nucleation sites, SPPs have also been found to act as favourable nucleation sites [179, 186]. This was experimentally demonstrated in Chapter 5 where it was found that as grain sizes were increased, the proportion of intra-granular hydrides increased to a higher extent

in specimens with a higher SPP content (Zr-4). The intermetallic SPP number density (3×10^{-2} µm^{-2} in Zr-4 and 2×10^{-2} µm^{-2} in Zr-702) are defined by the quantity of the low solubility alloying elements, such as iron (Fe) and chromium (Cr), that were often found associated with hydrides [187]. Chapter 5 has shown that intragranular sites are generally less potent hydride nucleation sites than GBs in as-received materials, but the role of intragranular sites becomes more influential as the density of GBs decreases such as in the blocky-α microstructures or potentially, as shown in literature, when the cooling rates are high [149].

After showing that SPPs and GBs act as hydride nucleation sites in zirconium specimens that do not have an external stress applied to them in Chapter 5, this chapter focuses on understanding the effects of an externally applied stress on the relative potency of inter/intragranular precipitation sites after hydride reorientation around long range stress concentration features in the form of 'V' and 'U' notches. Like in Chapter 5, this was also done under slow cooling conditions. Experiments use specimens containing various average grain sizes (l_{G}) ranging from the as-received (l_{G}= 10-50 µm) to the blocky-α systems (l_{G}= 500-1000 µm) that were produced and subjected to three thermal cycles whilst under load using four-point bending. Some of the parameters chosen for testing in this chapter are similar to the values required for DHC except for the number of cycles, which generally needs to be more to induce DHC. Optical microscopy and scanning electron microscopy (SEM) via secondary electron (SE) imaging, were used to produce microstructural images that were then analysed to quantify hydride precipitation at inter and intragranular sites around (1) 'V' notches with geometries of 1 mm depth, 45° flank angle and a root radius of 50 µm and (2) 'U' notches of 1 mm depth and root radius of 700 µm. To study the effects of microstructure and loading on hydride nucleation and precipitation the applied experimental conditions are summarised below:

1. Maximum test temperature of 623 K. This is shown in Figure 6.1 at point (a).

2. A hydrogen concentration (C_H) of 100-130 wppm that is fully in solution at 623 K. Hydrogen in solid solution will mainly diffuse via entropy driven diffusion to uniformly occupy tetrahedral sites in the Zr matrix. As the temperature decreases towards the TSSp (point (b) in Figure 6.1), hydrogen atoms either diffuse to new favourable microstructural sites or towards sites that have (or had, before dissolution) hydrides at them [20, 21, 118].

3. A range of applied stress intensity factors (2-8 MPa$\sqrt{\mathrm{m}}$), in the notionally elastic regime, below the range required for DHC initiation (10-20 MPa$\sqrt{\mathrm{m}}$).

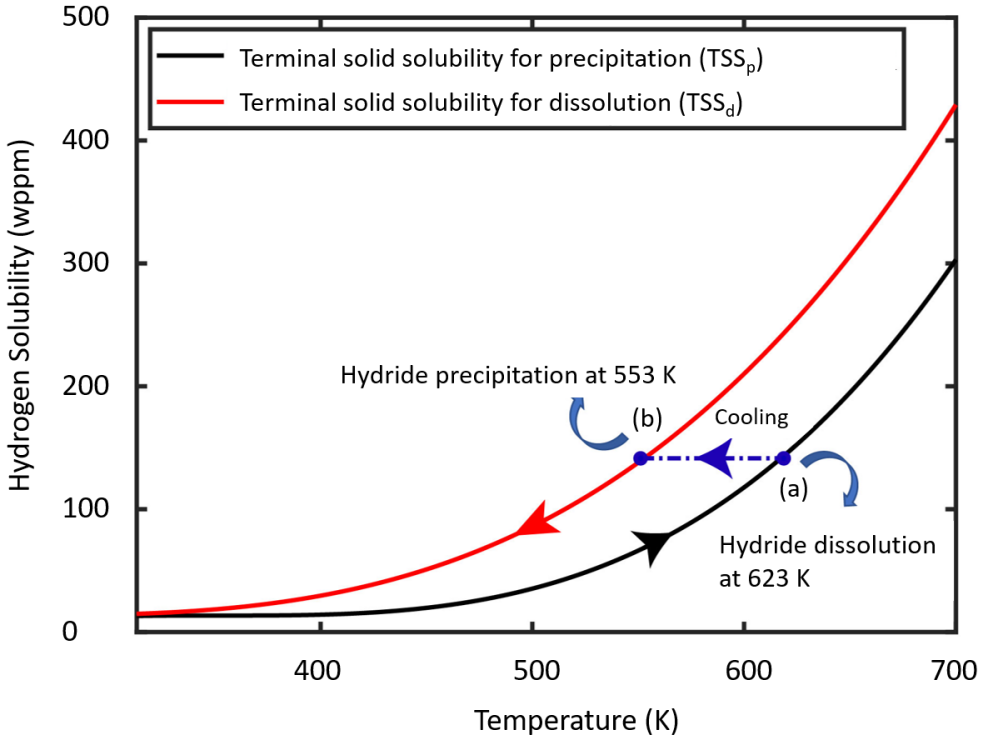
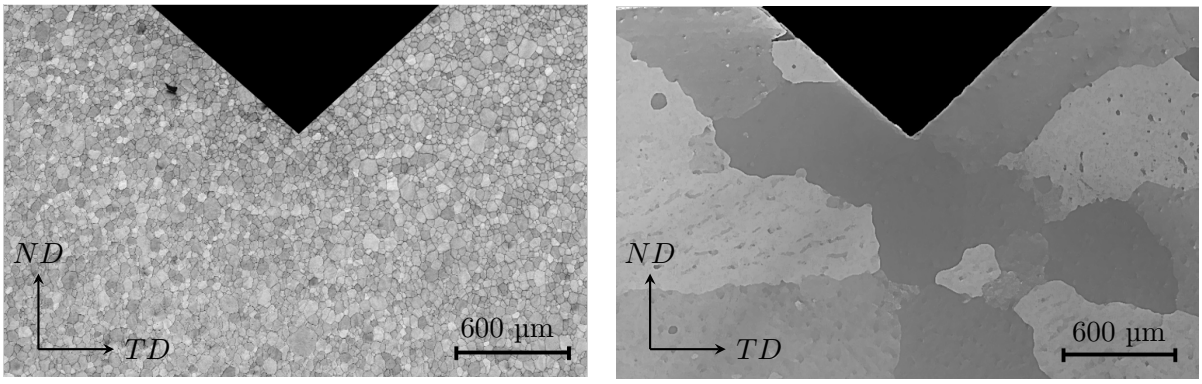


Figure 6.1: A schematic showing the terminal solid solubility of precipitation and dissolution of hydrogen in Zr versus temperature in K.

6.3 Results and Discussion

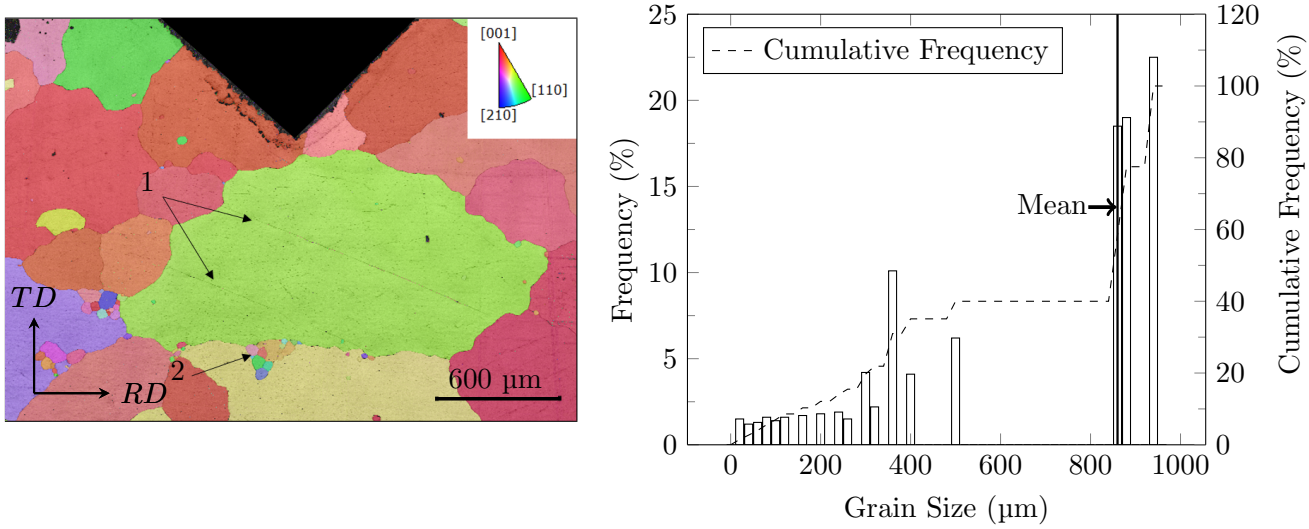
6.3.1 Microstructure

The microstructure of an as-received Zr-4 specimen with a central ground 'V' notch is shown in Figure 6.2(a), which can be characterised as equiaxed grains with average size of 15±4 µm. Figure 6.2(b) shows a grain growth annealed (blocky-α) Zr-4 specimen also with a central ground 'V' notch with l_G of 685±27 µm. As in Chapter 5, the texture of as-received Zr-4 was found to be the basal texture of $(0002)_{\alpha Zr}$. Although, it was not possible to capture a sufficient number of grains in an EBSD map, the macro-texture of blocky-α specimens appeared to be random. Blocky-α specimens also yielded abnormal grain growth in some specimens as shown in Figure 6.3(a). Figure 6.3(b) shows the bimodal grain size distribution in a blocky-α Zr-4 specimen with an average grain size of 880±44 µm. Such bimodal distribution is characteristic of the blocky-α specimens. Figure 6.3(a) also shows a couple of T1 type mechanical twins, in a notch-tip blocky-α grain, formed after three thermo-mechanical cycles at K= 8 MPa$\sqrt{}$m. T1 twins were characterised using EBSD as shown in Figure 6.4.



(a) (b)

Figure 6.2: Secondary electron micrograph of V-notch region of electro-polished, non-hydrided Zr-4 (a) as-received specimen and (b) recrystallised specimen containing 'blocky-α' grains.



(a) (b)

Figure 6.3: Map of IPF_{RD} of a V-notched recrystallised Zr-4 specimen after thermo-mechanical cycling (a) containing 82 grains, whereby arrows labelled (1) show T1 mechanical twins and arrow (2) shows small grains due to abnormal grain growth. The grain size distribution (b) is shown for the recrystallised specimen shown in (a) that contains 'blocky-α' and some abnormal grains.

6.3.2 Hydride Distribution

The hydrogen content of specimens was measured using inert gas fusion (IGF) to be 126±19 wppm, which corresponds to a theoretical hydride area fraction of 2.1% and an experimental value pre-cycling of 1.9±0.3%. Figure 6.5 shows the hydride precipitation in a bulk region of as-received and blocky-α Zr-4 pre-cycling. The hydrides appear to precipitate predominantly along the TD in Zr-4 (Figure 6.5(a)) and in blocky-α Zr-4 they can be clearly distinguished between intra-granular and inter-granular hydrides at lower magnification than in the as-received microstructure, as shown in Figure 6.5(b). The

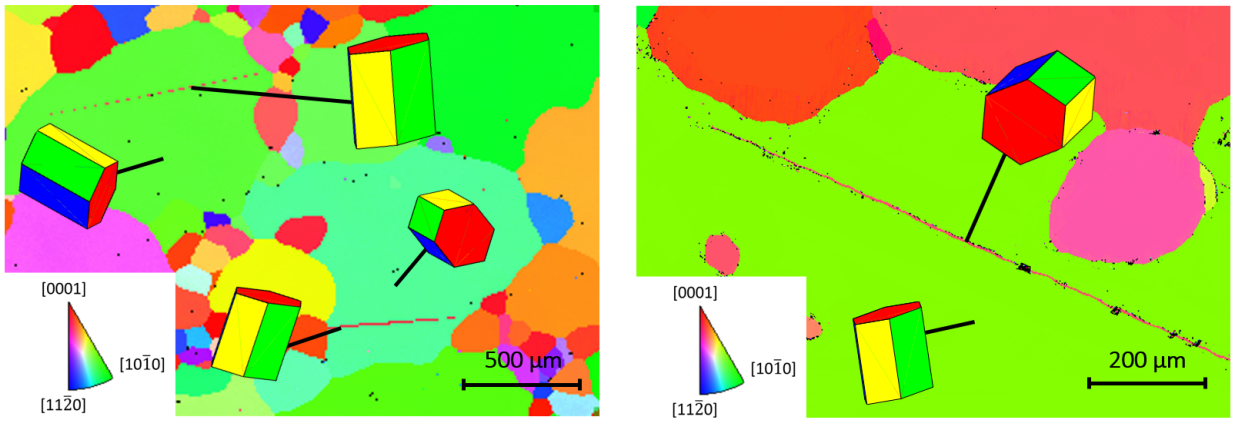


Figure 6.4: T1 twins in Zr grains with 85° misorientation between the <c> axes of the parent grain and the twin.

grain boundary density reduces considerably after grain growth annealing that results in an increase of intra-granular hydride precipitation, even when considering that the number density of SPPs has reduced and their single average size has coarsened. Figure 6.6 shows hydride reorientation at the left flank of the 'V' and 'U' notches in as-received l_G after 3 thermo-mechanical cycles at a peak K of 8 MPa$\sqrt{}$m, at lower magnification in Figure 6.7. Hydrides appear to precipitate within the expected notch stress profile at K equal to 8 MPa$\sqrt{}$m delineating the isostress contours. This simply means that the direction of individual macroscopic hydrides mirrors the stress field, a behaviour that has been reported extensively in literature [5, 30, 169]. This pattern was not observed at stress intensity factors below 8 MPa$\sqrt{}$m. Furthermore, hydrides delineating the isostress contours were only observed in as-received Zr-4 specimens and not in the blocky-α ones. However, the latter specimens may have shown a sign of hydrogen diffusion towards notches, as the number densities, at room temperature, were found to increase from the bulk to the notch regions of their specimens as shown in Table 6.1 but the scatter in the data masks any clear trend in the hydride distribution in the bulk and at both notch geometries.

6.3.3 Hydride Quantification: As a function of K

Notched specimens ('V' and 'U') with as-received grain sizes and between 700 to 900 µm were thermo-mechanically cycled at K= 2, 4, 6 and 8 MPa$\sqrt{}$m in order to study the effects applied stress intensity, at different notch acuities, on inter and intragranular hydride precipitation sites. The hydride number density (ρ_{hydride}) provides an insight into the number pertaining to nucleation sites per unit area in the matrix and when split between intra and inter-granular hydride percentage, it provides a potency

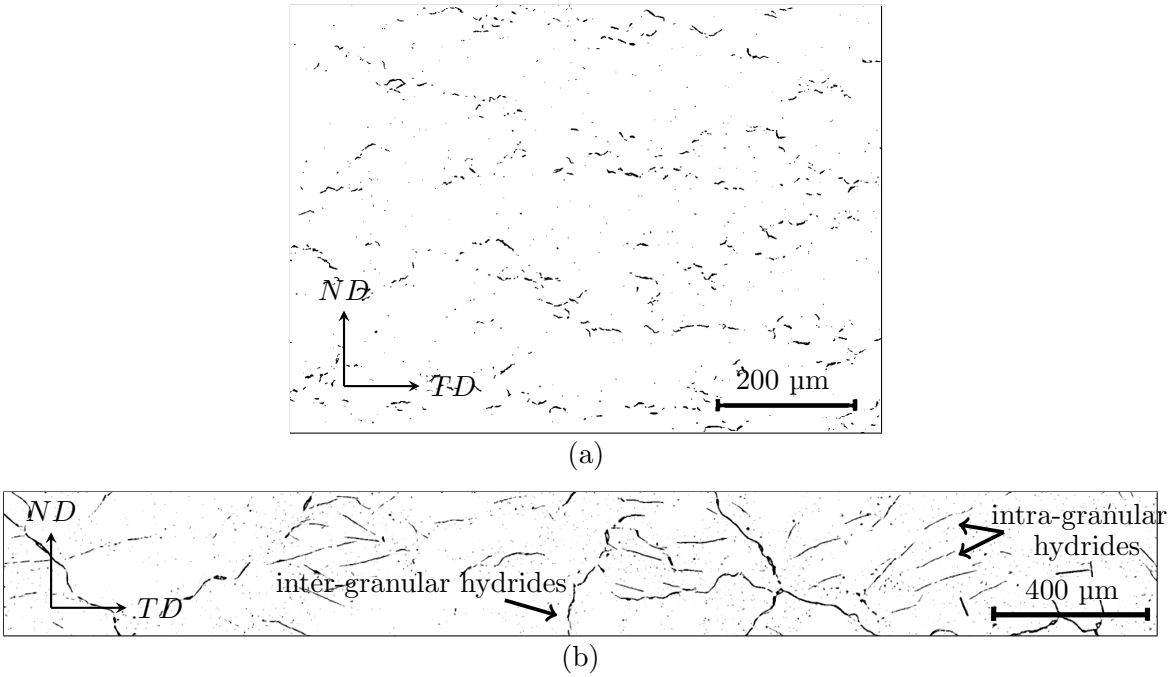


Figure 6.5: Thresholded optical images showing hydride precipitation in the bulk of (a) as-received and (b) blocky-α microstructure of a Zr-4 specimen on the ND-TD plane.

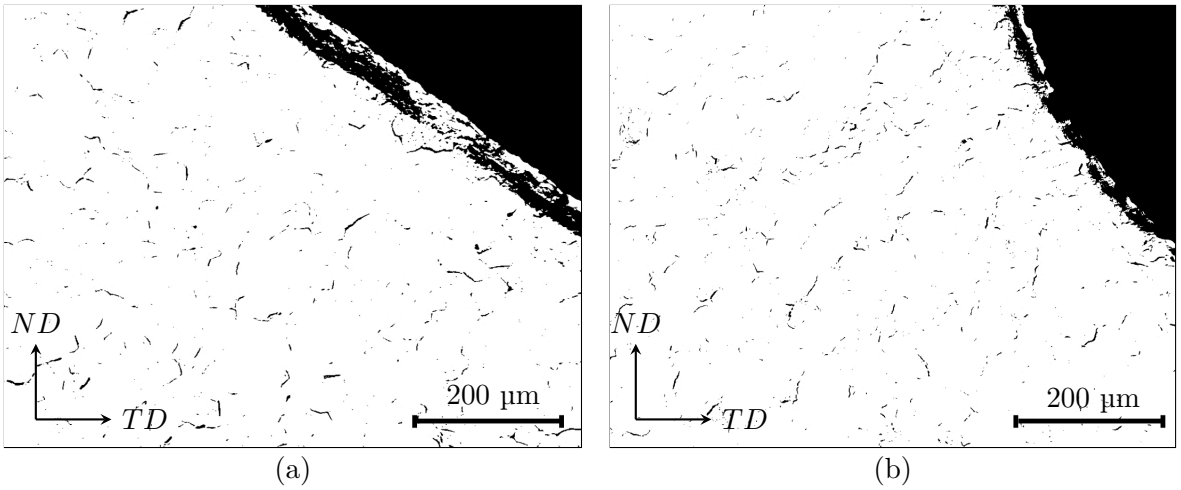


Figure 6.6: Thresholded images showing Zr-4 specimens in the TD-ND plane of the plate on the left flank of (a) the 'V' notch and (b) the 'U' notch specimen after 3 thermo-mechanical cycles at $K = 8$ MPa$\sqrt{}$m.

measure for intra-granular sites, such as SPPs, and GB hydride nucleation and precipitation assuming all hydrides precipitate at favourable sites.

6.3.3.1 Effect of K on hydride number density in as-received Zr-4:

Results for specimens with as-received grain sizes are shown in Figure 6.8. Hydride number densities were found to be slightly higher in TD oriented specimens in the bulk and at the notch tips but the

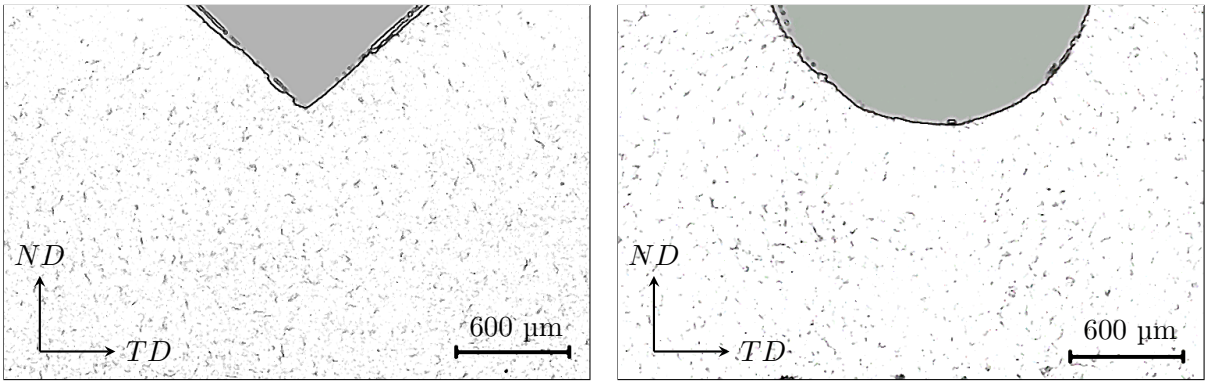


Figure 6.7: Thresholded images showing Zr-4 specimens in the TD-ND plane of the plate with (a) 'V' notch and (b) 'U' notch after 3 thermo-mechanical cycles at K= 8 MPa$\sqrt{}$m.

discrepancy in the TD and RD specimens was found to be minimal (<2%), and hence the data for both were combined. Figure 6.8 that shows that at K= 2 and 4 MPa$\sqrt{}$m the hydride number density remains similar between the notch area and the bulk. However, at K= 6 and 8 MPa$\sqrt{}$m the scattered data of hydride number density increases by at least 20%, which may highlight the effect of a threshold stress gradient on hydrogen diffusion and therefore hydride precipitation at new nucleation sites [40, 169].

The macro-hydride number density around 'V' notches were found to be higher than in 'U' notched ones. This is especially the case at 8 MPa$\sqrt{}$m with an increase of 177 hydrides mm^{-2} over that observed at 6 MPa$\sqrt{}$m versus an increase of only 49 hydrides mm^{-2} around 'U' notches. This results is attributed to the larger hydrostatic stress gradients generated by 'V' notch tips in these small grain size specimens at 8 MPa$\sqrt{}$m that seem to increase the amount of hydrogen diffusing towards new nucleation sites around the sharper SCF, as shown in Figure 6.9. The hydrostatic stress profiles, generated by the elastic FE 2D plane stress model (described in Chapter 4), for 'V' and 'U' notches are shown in Figures 6.10 and 6.11 respectively.

6.3.3.2 Effect of K on hydride number density in blocky-α Zr-4:

Specimens with blocky-α grain sizes did not show any clear evidence on the whether an applied K from 2 to 8 MPa$\sqrt{}$m has an effect on the hydride number density in the bulk and at both notch geometries as shown in Figure 6.12. It is noted however that the overall hydride number density is much lower in blocky-α specimens than for small grain specimens which is attributed in Chapter 5 to the low density of GBs that cause less disruption of the regularity of the micro-hydride stacking, leading to the formation of longer and continuous macro-hydride features. Figure 6.13 shows SE SEM micrographs of a 'V' notch blocky-α specimen after thermo-mechanical cycling at 8 MPa$\sqrt{}$m in the bulk (a) and

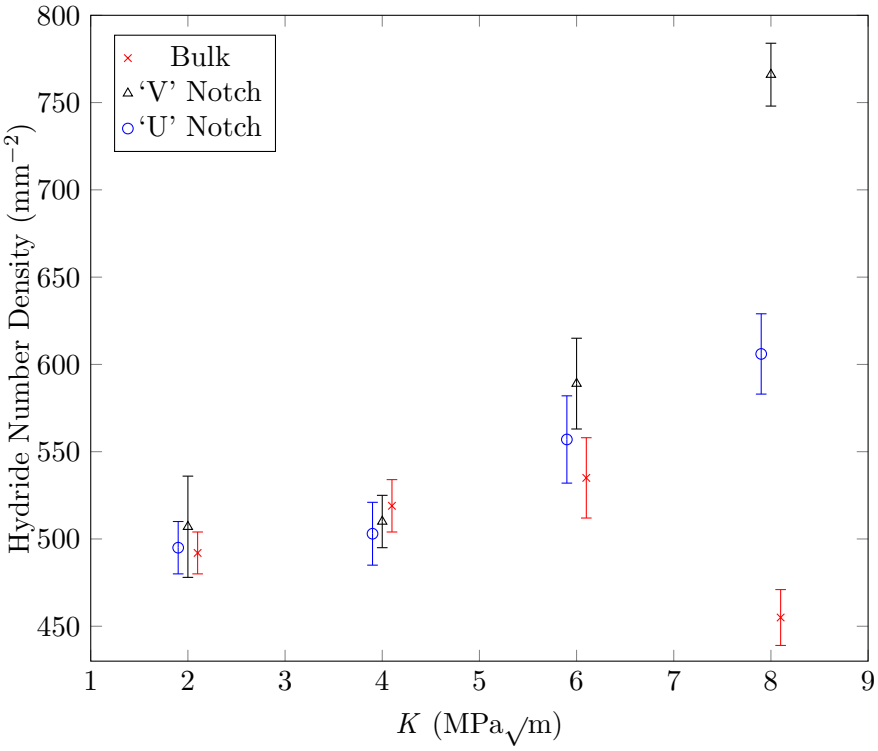


Figure 6.8: The macro-hydride number density after three thermo-mechanical cycles with K ranging from 2 to 8 MPa$\sqrt{}$m in as-received Zr-4 in the bulk, around 'V' and around 'U' notched specimens. Error bars show the standard deviation in hydride number density.

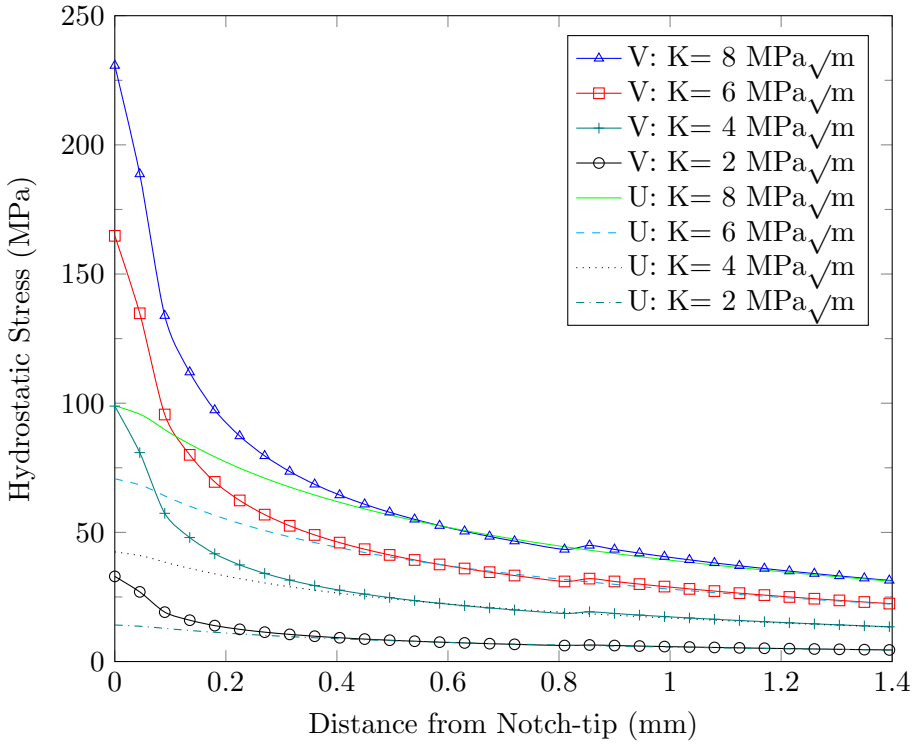


Figure 6.9: FE prediction of hydrostatic stress profiles below 'V' and 'U' notch-tips for as-received Zr-4 at 350°C.

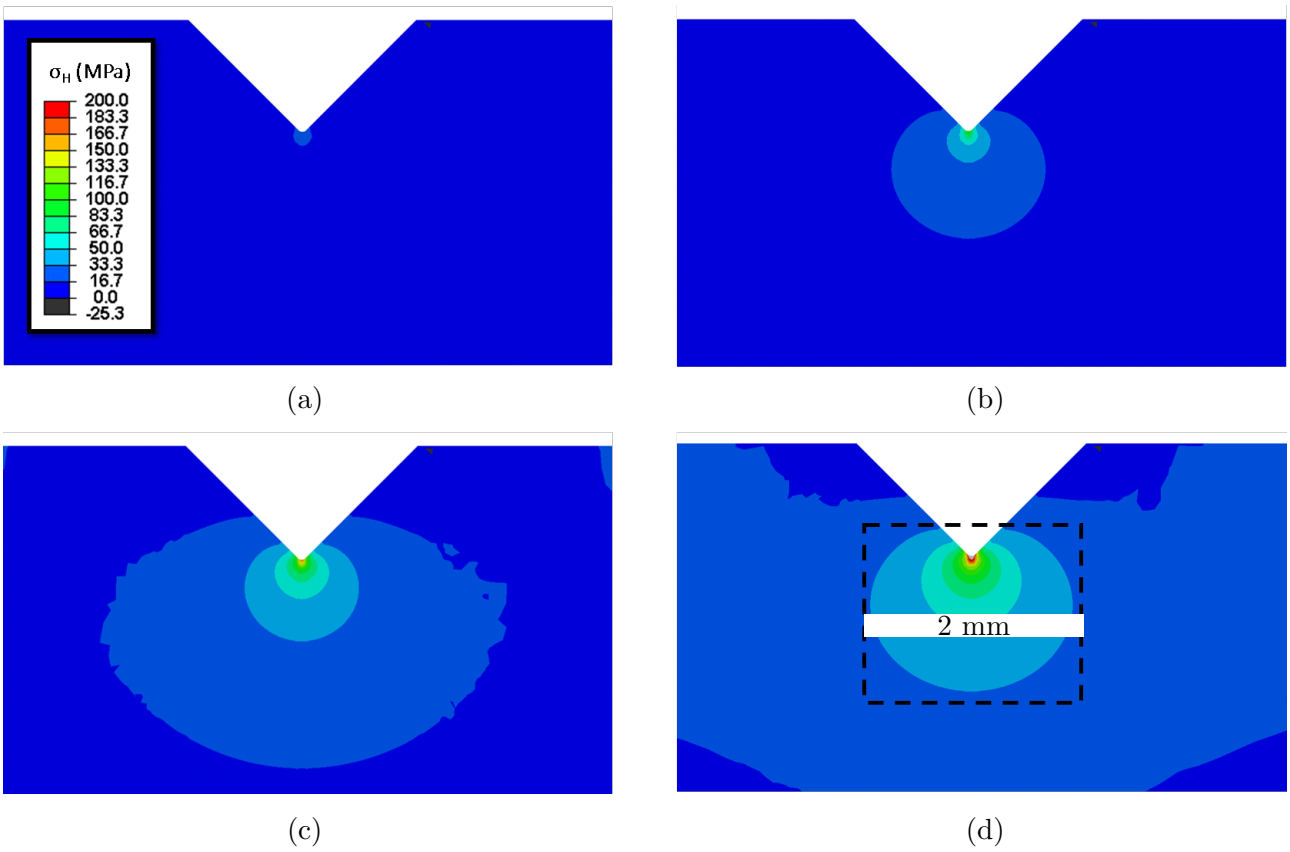


Figure 6.10: Hydrostatic stress profile around 'V' notches at (a) K= 2, (b) K= 4, (c) K= 6 and (d) K= 8 MPa$\sqrt{}$m. The box in (d) highlights the size of the enhanced hydrostatic stress notch tip region.

around the notch tip (b).

6.3.3.3 The effect of K on intragranular hydride precipitation in as-received and blocky-α Zr-4:

The intra-granular hydride percentages as a function of K, in as-received and blocky-α specimens, are shown in Figure 6.14(a) and (b) respectively. Results show that any clear trend on the effect of K on intragranular hydride precipitation in both grain size, cannot be found due to the large scatter in data points. In as-received and blocky-α specimens, an increase in K from 2 to 8 causes an increase in intra-granular hydrides around 'V' and 'U' notches, however the increase in both microstructures is scattered in data which masks any clear trend.

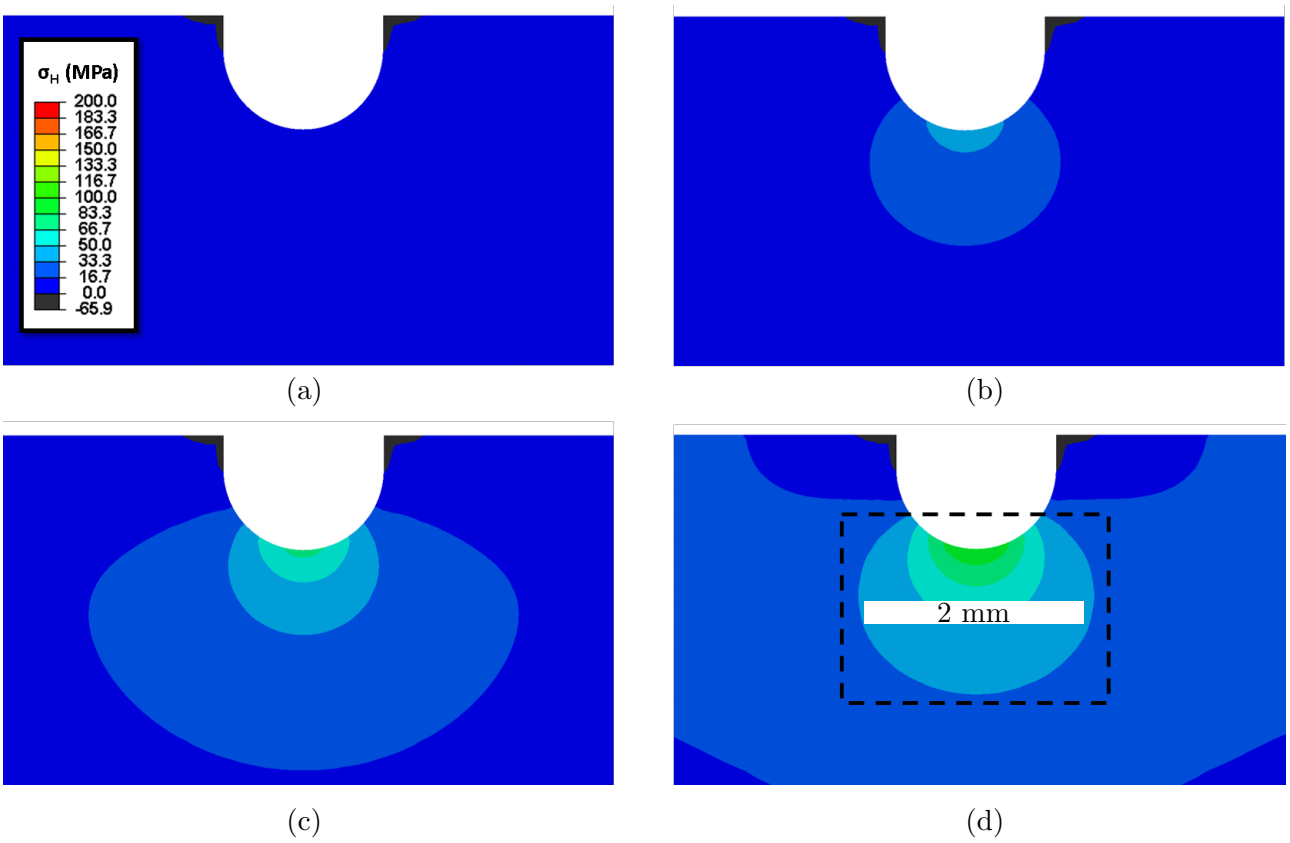


Figure 6.11: Hydrostatic stress profile around 'U' notches at (a) K= 2, (b) K= 4, (c) K= 6 and (d) K= 8 MPa$\sqrt{}$m. The box in (d) highlights the size of the enhanced hydrostatic stress notch tip region.

6.3.3.4 The effect of *K* on hydride area fraction in as-received and blocky-α Zr-4:

The area fraction of hydrides (A_{hydride}) at K= 2, 4, 6 and 8 MPa$\sqrt{}$m in the bulk and around notches was quantified. Unlike ρ_{hydride} and intra/inter-granular hydride %, that give a measure or insight into the potency of SPPs and GB for hydride precipitation, the A_{hydride} provides information about hydrogen concentration difference between the bulk and the notches. The hydrogen concentration or fraction in wppm can be calculated using the following standard weighting formula [168] that assumes the amount of hydrogen in solid solution is negligible in comparison to the amount in the hydrides and the hydrides are in the δ-phase with a molecular formula of $ZrH_{1.66}$ corresponding to a H concentration of 62.4 at.%. The formula also assumes that the hydrides are homogeneous features, that is, the stoichiometry is uniform over the microscopically observed region defined as the hydride of which the A_{hydride} is calculated:

$$W_H = \frac{W_\delta A_{hydride} \rho_\delta}{(\rho_{Zr}(1 - A_{hydride}) + \rho_\delta A_{hydride})} \tag{6.1}$$

where, W_H is hydrogen concentration in wppm, W_δ is the hydrogen concentration in δ-hydride phase in wppm, $A_{hydride}$ is the measured area fraction, ρ_δ is the density of the δ-hydride phase (5.65 g cm^{-3})

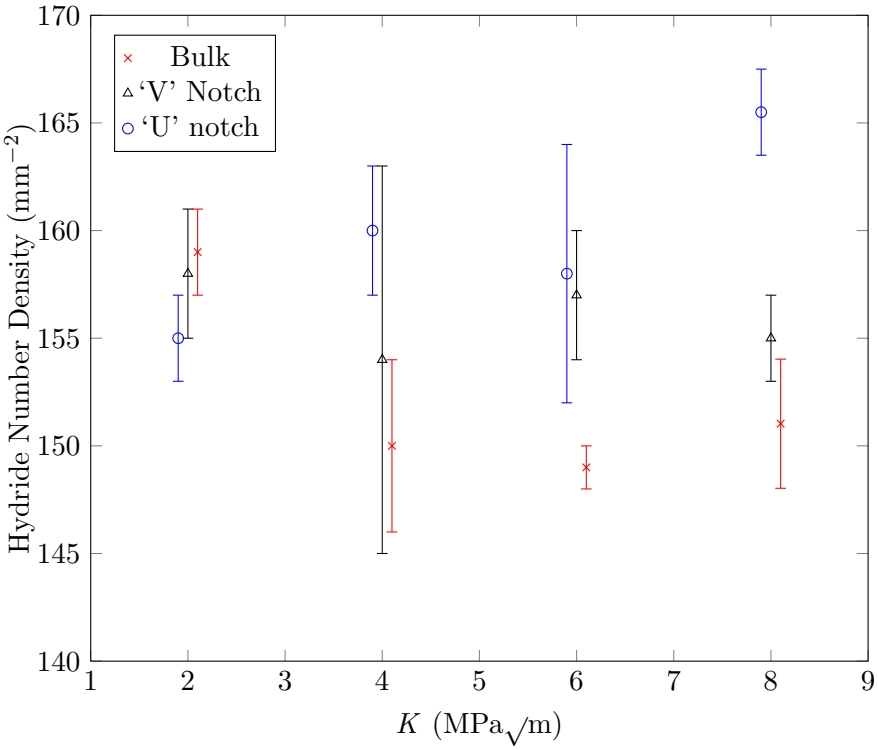
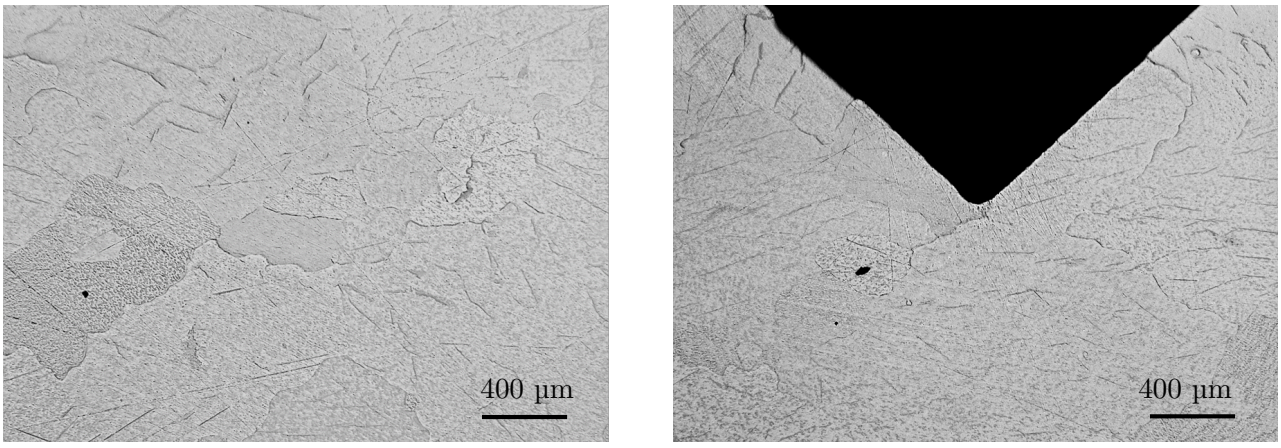


Figure 6.12: The macro-hydride number density after three thermo-mechanical cycles with K ranging from 2 to 8 MPa$\sqrt{}$m in blocky-α (l_G= 700-900 µm) Zr-4 in the bulk, around 'V' and around 'U' notched specimens. Error bars show the standard deviation in hydride number density.



(a) (b)

Figure 6.13: SE SEM micrographs of a blocky-α specimen in the bulk (a) and at the notch-tip (b).

and finally, ρ_{Zr} is the density of α-Zr phase (6.54 g cm^{-3}). Figure 6.15(a) and (b) show the hydrogen concentration calculated using the experimentally quantified A_{hydride} for as-received and grain growth enhanced specimens respectively.

Figure 6.15(a) shows that for as-received Zr-4 the hydrogen concentration was found to be higher around both notch geometries than in the bulk at K= 6 and 8 MPa$\sqrt{}$m although the scatter in the

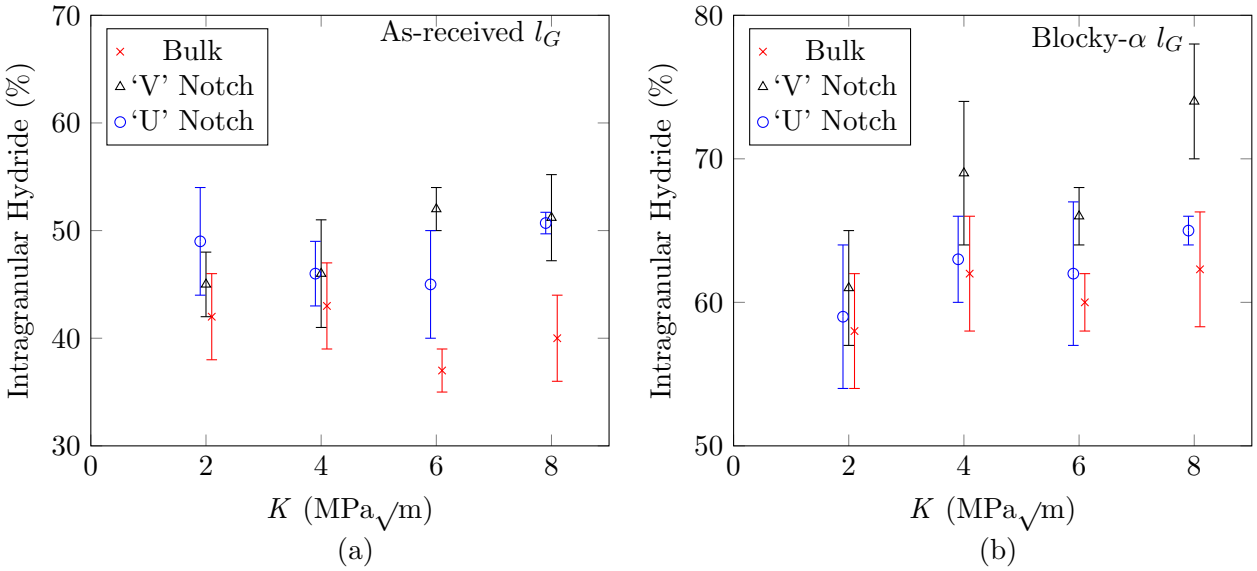


Figure 6.14: The intra-granular hydride number density (%) after three thermo-mechanical cycles with loads ranging from 2 to 8 MPa$\sqrt{}$m in (a) as-received (b) recrystallised (l_G= 700-900 µm) Zr-4 in the bulk, around 'V' and around 'U' notched specimens. Error bars show the standard deviation in intra-granular hydride fraction.

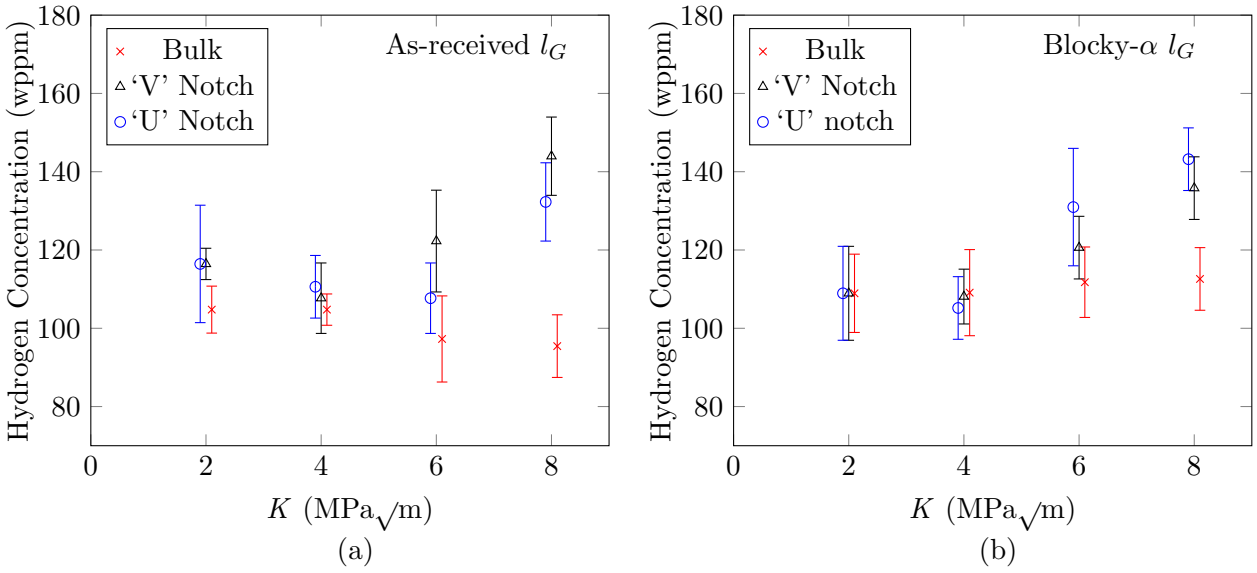


Figure 6.15: The hydride area fraction (%) after three thermo-mechanical cycles with loads ranging from 2 to 8 MPa$\sqrt{}$m in (a) as-received (b) recrystallised (l_G= 700-900 µm) Zr-4 in the bulk, around 'V' and around 'U' notched specimens.

data may also mask any certainty in the effect of a dominant SCF on hydrogen concentration. At 8 MPa$\sqrt{}$m, the difference in hydrogen concentration was found to be the largest between the notches and the bulk. The 'V' notch specimens showed the marginally larger hydrogen concentration at the notch-tip than 'U' notch specimens at 6 and 8 MPa$\sqrt{}$m, again, due to the larger hydrostatic tensile stress gradient they produce in as-received grain sizes. The decrease in hydrogen concentration in the

bulk can be also seen at an applied stress of 6 and 8 MPa$\sqrt{}$m. This shows that the bulk acts as a lower hydrostatic tensile region of which hydrogen diffuse away from, towards one with high stress.

Figure 6.15(b) shows hydrogen concentration as a function K for grain growth enhanced Zr-4. The data hydrogen concentration in blocky-α specimens was also scattered and was found to be larger around both notch geometries relative to the bulk at an applied stress of 6 and 8 MPa$\sqrt{}$m. Unlike as-received specimens, hydrogen concentration at 6 and 8 MPa$\sqrt{}$m was found to be higher around 'U' notches than around 'V' ones for reasons discussed in Section 6.3.6.

6.3.4 Hydride Quantification at K= 8 MPa$\sqrt{}$m: As a function of grain boundary and SPP density

To study the influence of inter and intragranular hydride precipitation sites on macro-hydride precipitation in thermally cycled Zr-4 specimens, ρ_{hydride} and intra-granular hydride percentage were quantified at various grain sizes at a fixed K of 8 MPa$\sqrt{}$m. ρ_{hydride} was quantified for the bulk and at the notch tip areas, after 3 thermo-mechanical cycles, in the as-received (l_{G}= 10-20 µm) and grain size enhanced specimens (l_{G}= 500-1000 µm). The hydride number density is quantified as an average per unit area, irrespective of hydride size distribution, to give a parameter that represents the number of intragranular and intergranular macro-hydride precipitates per unit area in the microstructure. Results for ρ_{hydride} are summarised in Table 6.1 for as-received and grain size enhanced specimens at a load of K= 8 MPa$\sqrt{}$m.

Table 6.1: Macro-hydride number density and intra-granular hydride fraction after 3 thermo-mechanical cycles at K= 8 MPa$\sqrt{}$m in as-received and blocky-α Zr-4 in the bulk and around the 'V' and 'U' notches.

l_{G} (µm)	Parameter	Bulk	SD	'V' Notch	SD	'U' Notch	SD
15	Hydride Number Density (mm^{-2})	455	26	766	14	606	15
	Intra-granular Hydride Fraction (%)	39.7	5.9	51.2	7.0	50.7	5.0
500-1000	Hydride Number Density (mm^{-2})	151	13	162	5	165.5	12
	Intra-granular Hydride Fraction (%)	61	16	74	2.0	65	2.5

The intra-granular hydride percentage and the macro-hydride number density results (Table 6.1) show the following trends in as-received Zr-4 thermomechanically cycled at K= 8 MPa$\sqrt{}$m:

The intra-granular hydride fraction was found to be around 51% around both notch types versus 40% in the bulk (Table 6.1). This shows that the intra-granular hydride precipitation around notches

becomes more favourable than in the bulk in the presence of a larger tensile stress field.

The bulk contains 40% less macro-hydrides compared to around 'V' notches at $K = 8$ MPa$\sqrt{\text{m}}$ highlighting the hydrogen stress-driven diffusion effect [156, 188, 189].

The increase in macro-hydride number density at notch regions from bulk in as-received material was found to be consistently higher around 'V' notches (by 58%) than around 'U' ones (by 33%). This is attributed to the higher peak hydrostatic tensile stress gradient, towards new microstructural sites, generated by 'V' notches in as-received material as shown in Figure 6.9.

Results for grain size enhanced Zr-4 specimens containing blocky-α grains, thermomechanically cycled at $K = 8$ MPa$\sqrt{\text{m}}$, are also presented as an average over all grain sizes in Table 6.1 and for individual grain size in Figure 6.16 and are summarised below:

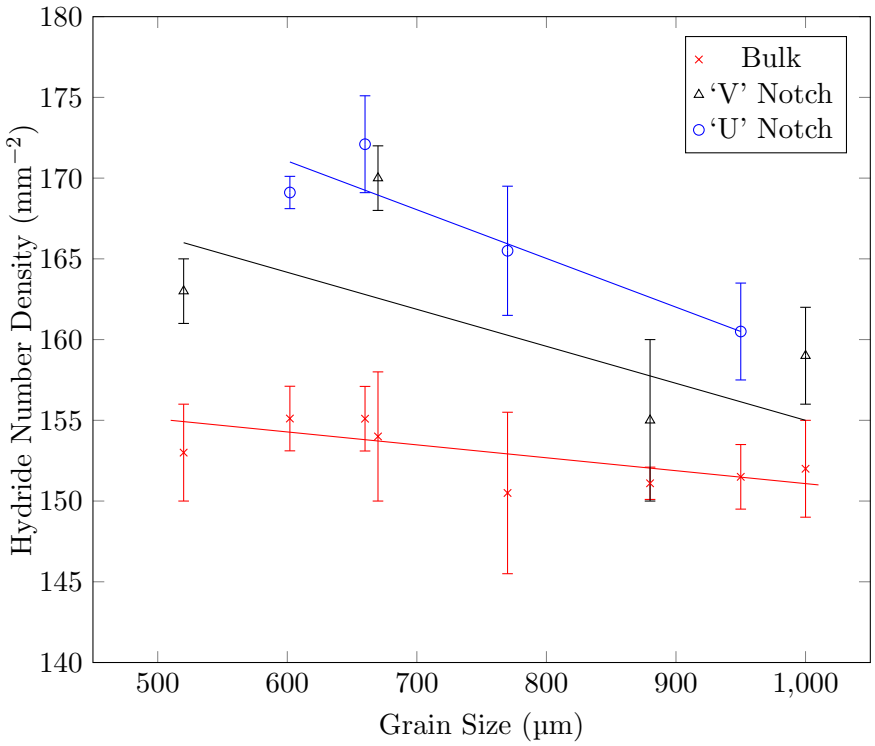


Figure 6.16: The macro-hydride number density after three thermo-mechanical cycles $K = 8$ MPa$\sqrt{\text{m}}$ in blocky-α Zr-4 in the bulk, around 'V' and around 'U' notched specimens.

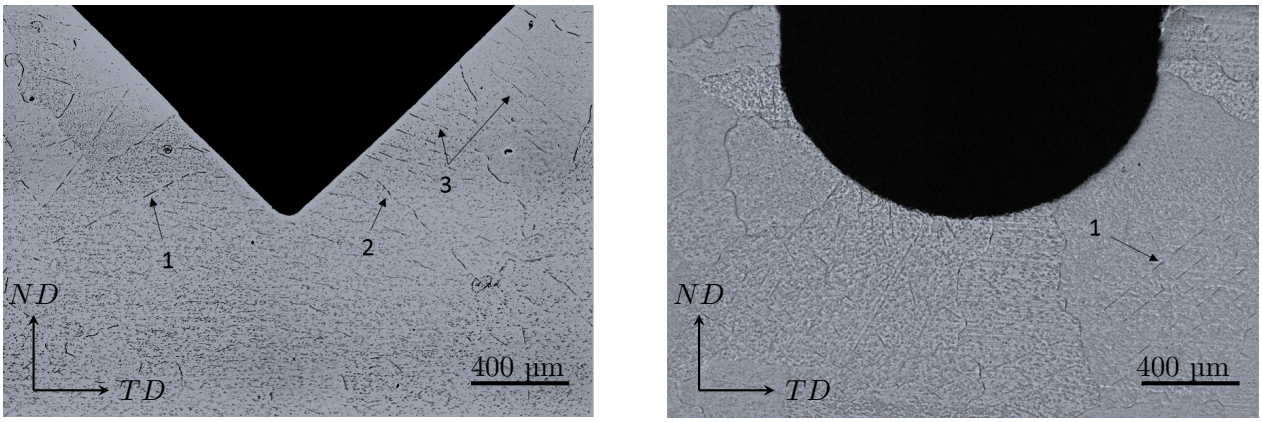
The hydride number density in blocky-α specimens with grain sizes ranging from 500 to 1000 µm was found to increase by an average over all grain sizes of 8% from the bulk towards both notch geometries. The increase was however small and uncertain due to the scatter in data. The lower hydride density at SCFs in blocky-α specimens in comparison to as-received specimens, could be due

to the lower yield strength of blocky-α microstructures relative to as-received Zr-4 that limits the generation of a large hydrostatic tensile stress gradient towards new hydride nucleation sites and also microstructurally due to the large hydrogen diffusion distances in blocky-α grains that may cause an increase in hydride stacking rather than nucleations at new microstructural sites. A best fit trend line using least square method is shown in Figure 6.16 to show the increase from the bulk (red) to around 'V' notches (black) and around 'U' ones (blue) as a function of grain size. Although the data for the hydride number density is consistent in the bulk with some degree of scatter, the data for hydride number density at both notch geometries contains a larger degree of scatter with some outliers that do not fit the trend like at ∼700 µm 'V' notch region. The difference in the hydride number density around both notch geometries, albeit uncertain due to the scatter in data, was expected to show the hydride number density to be consistently higher around 'V' notches than around 'U' ones as observed in as-received specimens. Considering the large grain size of the bocky-α microstructure, this could be attributed to the formation of plastic zones at the 'V' notch tip that tend to limit and flatten the hydrostatic stress gradient [190–192]. Further reasons are discussed in Section 6.3.6.

Finally, Figure 6.17 shows that re-orientation of hydrides at $K = 8$ MPa$\sqrt{}$m is not visible in blocky-α grains. This mean that hydrides do not appear to precipitate within the notch stress profile like in as-received specimens where the direction of individual macroscopic hydrides mirrors the stress distribution predicted for this geometry. This phenomenon can be again attributed to the relatively low yield stress that limits the formation of a hydrostatic tensile stress gradient in soft blocky-α microstructures. Microstructurally, the absence of hydride re-orientation in blocky-α specimens may also indicate that either a high GB density plays a significant role the in the re-orientation of individual hydrides (as observed in as-received specimens), or the SPPs, that are both coarser and have a lower number density in blocky-α specimens, influence hydride stress re-orientation. The absence of re-orientation was observed in all blocky-α specimens with grain sizes ranging between 500-1000 µm.

6.3.5 Hydride Quantification at Twins

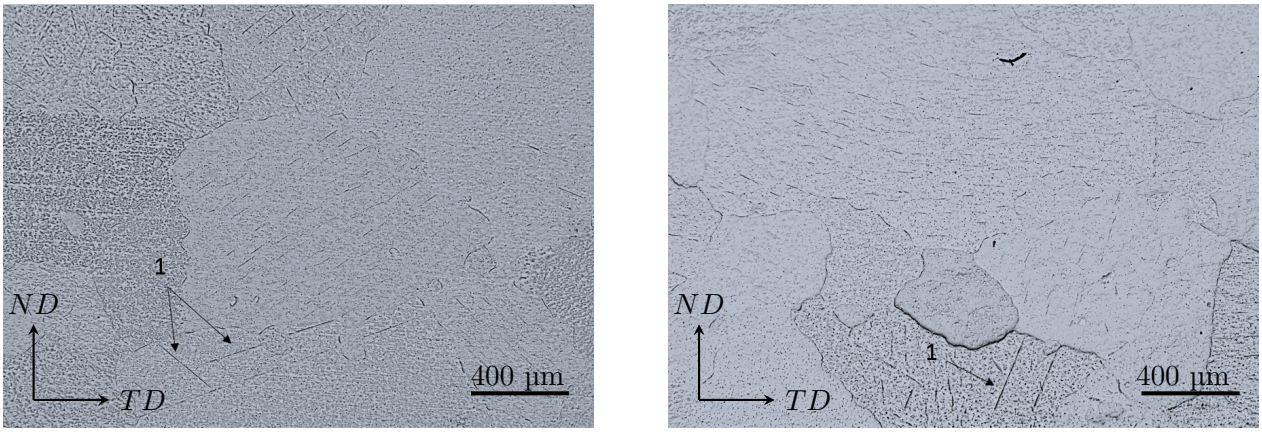
Mechanical twins were clearly observed in blocky-α specimens, at the notch regions and at in the bulk of both types of notched specimens. The percentage of grains containing deformation twins in the bulk is at ∼7%, a value lower than that around notches (∼12%). Twins can be easily seen in the microstructure using optical imaging as shown in Figure 6.18, and were found to have hydride precipitates at their boundaries, within them or both, appearing in dark black in Figure 6.18. Twins in blocky-α grains were found to be of T1 type ($\{10\bar{1}2\}$ $<10\bar{1}1>$) with an 85° misorientation between the <c> axes of the



(a) (b)

Figure 6.17: Optical images showing blocky-α Zr-4 specimens with an average grain size (l_G) of 700-900 µm, containing 100-130 wppm, in the TD-ND plane of the plate with (a) 'V' notch and (b) 'U' notch after 3 thermo-mechanical cycles at K= 8 MPa$\sqrt{}$m. Arrows labelled (1) show twins containing macro-hydride precipitates within blocky-α grains. Arrows (2) and (3) show inter and intra-granular hydrides respectively at percentages of ∼30% and ∼70% respectively around the notches after cycling in comparison to a ratio of ∼40% and ∼60% respectively in the bulk.

parent grain and the twin (Figure 6.4) [193]. Figure 6.19(a) shows a binary optical image of a blocky-α 'U' notch sample with an average grain size of 830 µm after three thermo-mechanical cycles containing T1 twins containing macro-hydrides. Twins were found to have a grain size dependent length and a very small width of <5 µm. Figure 6.19(b) shows the area distribution of the twins that were found to have a number density of 8±4 mm^{-2} and an average area of 522 µm^2. T1 twins were often found to form in grains with l_G>600 µm.



(a) (b)

Figure 6.18: Optical images showing blocky-α Zr-4 specimens with a grain size (l_G) of 700-900 µm, containing 100-130 wppm, in the TD-ND plane of the plate showing (a) bulk region of a 'V' notch specimen and (b) bulk region of a 'U' notch, after 3 thermo-mechanical cycles at K= 8 MPa$\sqrt{}$m. Arrows labelled (1) show twins containing macro-hydride precipitates within blocky-α grains.

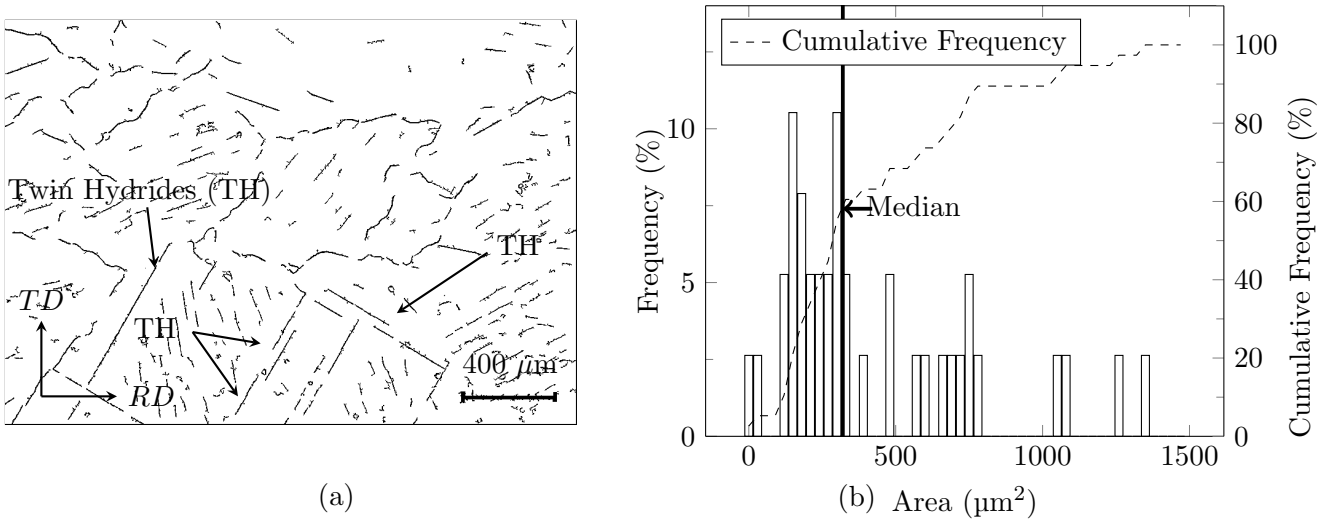


Figure 6.19: (a) Thresholded optical image of a blocky-α thermo-mechanically cycled ($\times$3) 'U' notch specimen. Mechanical T1 type twins shown were found to contain macro-hydride features. The area distribution of twin hydrides (b) shows the median at 270-300 µm^2, a value that is dependent on grain size.

6.3.6 Discussion of Hydride Nucleation Sites Hierarchy

Referring to Table 6.1, the increase in ρ_{hydride} from the bulk towards notches, was found to be different around both notch geometries. Although the scatter in data hinders any clear trend, the difference can be attributed to the degree of notch acuity. Stress driven hydrogen diffusion in the specimens, occurs along a stress gradient that influences the movement or hopping of hydrogen atoms from one site to another. As previously explained in the literature review (Chapter 2), this biased hopping mechanism occurs due to the misfit strain energy, caused by a hydrogen in the interstitial site of a Zr HCP crystal, that leads to hydrogen atoms avoiding compressive regions and migrate towards tensile regions [40]. In theory, the higher the tensile stress field (such as around 'V' notches or cracks), the higher the accumulation of hydrogen and in turn hydride area fraction and density. The larger hydride density and area fraction were only the case, however, in as-received grain size specimens that have a relatively high yield strength of 414 MPa and 213 MPa at room temperature and 350°C respectively. In blocky-α specimens, that are softer than as-received specimens, the scatter in data masks any clear trend in hydride distribution at both notch geometries. This can possibly be attributed to the notch tip plasticity produced in blocky-α 'V' notch tip grain, that limit the formation of a hydrostatic stress gradient due to limited hardening in the material. There are however other factors to discuss here, which are as important as the plasticity effect. Firstly, consider Figures 6.10(d) and 6.11(d), the hydrostatic stress enhanced region inside the dashed boxes highlights a difference in stress

distribution at the two different notch geometries, 'V' and 'U'. The two major differences are (1) the higher peak hydrostatic stress at the 'V' notch tip, and (2) the larger zone that hydrostatic stress enhanced region occupies at the 'U' notch tip as indicated by the scale bar ahead of notches at $K=$ 8 MPa$\sqrt{}$m. These differences in hydrostatic stress distribution between the two notch geometries, may have an effect on hydrogen diffusion and activation of microstructural sites. Considering again Table 6.1 and Figure 6.16, the higher peak hydrostrostic stress at 'V' notch tips, seem to have a larger effect in as-received specimens on hydrogen diffusion than in 'V' notch blocky-α ones, by creating a large short range hydrostatic stress gradient, in a microstructure that contains very small grains and is more textured. On the other hand, the large zone the hydrostatic stress enhanced region occupies at 'U' notch tips, seem to be the dominant factor in increased hydrogen diffusion in blocky-α microstructures that contain very large grains with a random texture. This interaction between the hydrostatic stress distribution and the microstructure, can be experimentally shown by the scatter in data of ρ_{hydride} and A_{hydride}, whereby the number of activated microstructural nucleation sites (such as GBs and SPPs), in as-received and blocky-α specimen may change with respect to stress distribution. Notch tip plasticity is of course a factor to consider in blocky-α microstructures, but it is highly dependent on the blocky-α notch tip grain, which spreads a constant crystal structure over a large notch region, and one or two blocky-α grains can solely determine the amount and size of plasticity produced depending on their orientation to slip. Experimentally, Chapter 6 does not produce enough statistics to study the notch tip crystallography effect, and so this observation lead to a computational study presented in Chapter 7 Part II, that studies more accurately the effect of notch tip plasticity and crystal structures in blocky-α grains around 'U' and 'V' notch geometries.

Considering the effects of SPPs on hydride precipitation, the percentage of inter-to-intra-granular hydride precipitation in as-received Zr-4 from the bulk towards notches, were found to be 60% intergranular and 40% intragranular in the bulk to 50:50 in the notch region. This means that there is an increase in intra-granular hydride precipitation around notch geometries, although the scatter in data masks any clear trend. In therory, after three thermo-mechanical cycles, hydrogen atoms diffuse towards the high hydrostatic tensile stress region near the notch tip and first occupy favourable intergranular localised stress concentration features such as GBs that are perpendicular to the applied load and are crystallographically well aligned for hydride precipitation (or optimally-misorientated for hydride precipitation). These are GB planes that are parallel to the basal plane of one bounding Zr grain and have high energy due to grain misorientation [178] (more on GB effects below). Once

these sites around the notch saturate, hydrogen atoms may either diffuse towards other GBs that are less favourable sites for intergranular hydride nucleation, or towards intragranular localised stress raisers that may produce local hydrostatic tensile stress, such as intragranular SPPs [178]. Recent modelling using 2D discrete dislocation plasticity shows that SPPs likely provide local hydrostatic tensile stress [16]. Around loaded notches, such SPPs would be present in a region under a globally dominant applied hydrostatic tensile stress which may interact with the local SPP hydrostatic stress and therefore effect the notch stress profile produced. Although grain size at the notch region might be the dominant factor, which either causes a significant increase or reduction in GB density which alters the fraction of intergranular precipitation.

Considering now the effect of GBs on hydride precipitation. The potency of GBs as hydride nucleation sites, with externally applied stress, is noticeable in the bulk and around the stress concentrated notches. The intergranular precipitation in the bulk of as-received Zr-4 samples was found to be 11% higher than around the notches, although there is uncertainty due to data scatter, this may suggest that the potency of GBs as hydride nucleation sites decreases due to competition with stress factors around the notches where the tensile stresses are high. To explain this finding, we can start by considering specimens that have no external applied stress; inter-granular hydrides prefer to sit at GBs that have large misorientation angles (high energy) [178], i.e larger than the general misorientation limit for low angle boundaries ($\theta > \theta^* = 15°$) in the Read–Shockley model [194]. The crystallographic orientation relationships between hydrides and unloaded Zr matrix, determined by using pole figures, is $(0001)_{\alpha-Zr}//111_{\delta-Zr_{1.66}}$ at all nucleation sites for inter and intra-granular hydrides [60, 195]. For inter-granular hydrides however, this relationship only exists between hydrides and one bounding basal Zr grain [23, 60, 145, 146, 196]. This shows that hydride nucleation energy and nucleation rate at GBs in an unloaded Zr specimen is dependent on the GB type and hence energy level, determined by the misorientation angle between two grains, and on the crystallography on one bounding grain to have a basal orientation. When specimens are subjected to an external stress, of 8 $\text{MPa}\sqrt{\text{m}}$ in this work, higher tensile stresses at the notch tip region are generated in comparison to the bulk, can increase (at the notch region) and decrease (in the bulk) the local strain in the GBs and therefore change the GB energy [178]. Furthermore, previous studies have shown that the GB energy under applied tensile stress increases as the grain boundary plane approaches 90° to the direction of applied tensile stress i.e hydrides prefer to precipitate at GBs that are perpendicular to the tensile stress axis [40, 60]. Results from Table 6.1 show that for the same type of microstructure (as-received Zr-4) the inter-granular precipitation in the bulk (lower tensile stress) albeit scattered was higher than around the notches,

with both regions containing a very similar number of GBs that are perpendicular to the applied stress axis. However, due to hydrogen stress driven diffusion, hydrogen at the notches likely saturate GBs that are perpendicular to the tensile axis and satisfy the criterion of having high energy and have one bounding basal grain orientation. This suggests that the number of favourable GBs near the notch tip may be less common, which then may drive the H to diffuse towards the other nucleation sites inside the grains such as SPPs or other defects.

6.4 Conclusions

Precipitation of hydrides at energetically favorable nucleation sites was observed in experiments at long range and localised stress-raisers.

Conclusions are summarised below:

1. Reorientation of hydrides in as-received specimens was observed at K= 8 MPa$\sqrt{}$m and was found to be more prominent around 'V' notches. These notches provide a large hydrostatic stress gradient which causes a larger number density of hydrides to precipitate in their vicinity relative to 'U' notches.

2. Large grained Zircaloy-4 specimens showed no hydride reorientation or stress contour hydride precipitation at all stress intensity factors of 2-8 MPa$\sqrt{}$m. This is probably due to the relatively low yield stress that limits the formation of a hydrostatic tensile stress gradient.

3. Results show that there is an increase in intra-granular hydride percentage from the bulk to the surroundings of both notch geometries but the scatter in data causes uncertainty in the trend in the effect of SPPs on intragranular hydride precipitation near both notch geometries.

4. T1 type twins in blocky-α grains were also found to act as hydride precipitation sites and were found containing hydrides in grains with l_G>600 µm.

Chapter 7

Computational Stress Analysis of Notch-Tip Hydrogen Profiles in Zr-4

7.1 Outline

In this chapter a modelling framework, split into two parts, aims to establish a modelling strategy for incorporating the microstructural hexagonal close-packed (HCP) anisotropy and polycrystallinity that produces a biased path for hydrogen diffusion towards long range stress concentration features (SCFs) in the form of loaded notches. The multiscale methodology that is put forward in Part I, incorporates and studies the isolated effects of the HCP anisotropy on hydrogen diffusion in Zr. The second part of this chapter puts forward a model that acts as a proof of concept to the anisotropy incorporation in Part I, and in addition studies the effects of plasticity and polycrystallinity on hydrogen distribution. Part I features a 2D plane stress finite element model (developed by myself in collaboration with Patel et al. [30]), coupled with atomic scale density functional theory (DFT) parameters from literature [197]. Part II features another model developed and used by Dr Liu [29] which not only acts as a proof of concept to the hydrogen diffusion anisotropy incorporation from Part I, but also uses crystal plasticity finite element theory in quasi-2D plane stress conditions to study the effects of plasticity, at SCFs, on hydrogen diffusion in monocrystals. Furthermore, Dr Liu's model was supplied, from my experiments, with electron back-scattered diffraction (EBSD) data from blocky-α 'V' notch specimens which allowed the model to also incorporate experimental polycrystalline microstructures and study the effects of grain boundaries (GBs) on hydrogen distribution.

Part I

7.2 Introduction

Hydride precipitation in Zr can be seen in experimental results, in Chapters 5 and 6, to be dependent on microstructure. Macro-hydrides were found to either precipitate at grain boundaries or inside the grains in as-received and blocky-α microstructures. In Chapter 5 it was clear that hydrides in as-received un-loaded Zr specimens prefer intergranular precipitation and to a smaller extent in blocky-α microstructures where the GB density is reduced. This preferential intergranular macro-hydride precipitation highlights the potency of grain boundary nucleation, which was then studied in Chapter 6 for the same microstructures, but under applied load, near SCFs in the form of 'V' and 'U' notches. Results from Chapter 6 show that the preference of hydride precipitation sites changes in loaded Zr specimens in the bulk and around the SCFs. Notch acuities were found to effect the hydride number density in the notch regions. In addition the percentage of intergranular hydride precipitation was found to reduce near the notch-tips from the bulk in both microstructures, while intragranular precipitation increases. The change in the hydride precipitation distribution in loaded Zr-4 specimens in the notch regions was attributed to (1) the different level and range of hydrostatic stress gradients produced by 'V' and 'U' notches, (2) grain crystallography and GB misorientation near SCFs and (3) GB orientation with respect to the applied load.

Current models in the literature of hydrogen diffusion in a notched zirconium specimen typically employ the finite element method (FEM) to compute the temperature dependent stress state and simulate the kinetics of stress-driven diffusion [132, 133]. In these studies, the hydrogen interstitial is usually modelled as a misfiting sphere, an assumption that does not account for the atomistic scale anisotropy associated with the hydrogen interstitial. Considering Figure 7.1, this atomistic scale anisotropy is exhibited in the hydrogen diffusivity, which varies along the different crystallographic directions. As zirconium alloy reactor components have a polycrystalline microstructure, hydrogen diffusion can be affected by the texture of many misorientated HCP crystals or grains. Therefore, the hydrogen diffusivity may vary depending on the zirconium alloy microstructure [40, 134]. Currently there exists a variety of commercial zirconium alloy materials, each of which has different microstructural properties [135]. Accordingly, it is essential to establish a framework for continuum stress-driven hydrogen concentration profiles that incorporate the atomistic scale anisotropy so that microstructural

effects can be simulated.

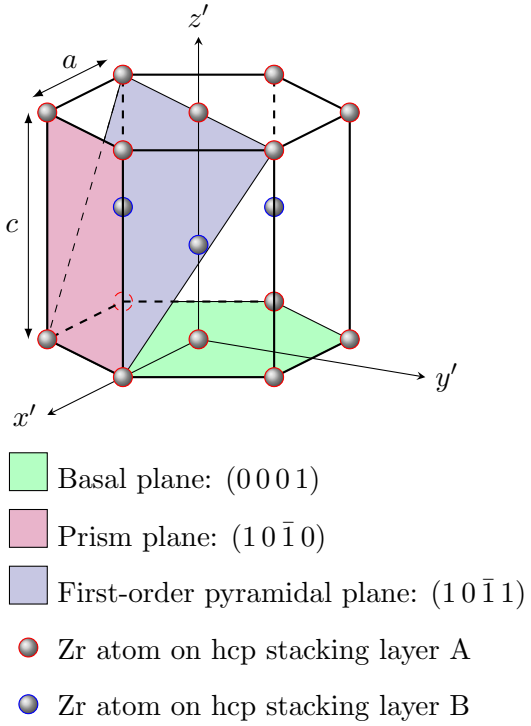


Figure 7.1: The unit cell of hexagonal α-zirconium showing the distinct crystallographic planes. The anistropic properties of α-zirconium are attributed to its non-ideal c/a ratio of 1.593, which itself is fundamentally a consequence of its electronic structure.

This chapter aims to formulate a multiscale framework that couples the atomistic scale description of hydrogen in zirconium with the continuum thermodynamic theory of stress-driven diffusion. Stress-driven diffusion involves the computation of the elastic interaction energy between the distortions caused by diffusing species and all other stress sources in the matrix [6]. Embedded within this concept of the elastic interaction energy is the atomistic-to-continuum scale coupling. As each hydrogen atom is a point defect occupying a tetrahedral interstitial site in the zirconium crystal, it exerts defect forces on its neighbouring zirconium atoms. These point defect forces can be translated to a property of the point defect known as the elastic dipole tensor. According to Nazarov et al. the elastic dipole tensor characterises the long-range stresses generated by the point defect [197]. Using the elastic dipole tensor, it is possible to construct a formula for the elastic interaction energy that captures the interstitial symmetry. This approach accounts for the crystal orientation relative to the stresses or strains produced by a SCF within the elastic interaction energy. This is not possible in the standard isotropic methodologies that employ the misfitting sphere model. Incorporating the elastic dipole tensor is, therefore, a necessary first step towards a generalised framework for stress analysis in polycrystalline materials.

In this part of the chapter, a preliminary methodology for multiscale stress analysis of hydrogen in a notched Zr specimen is outlined. The simulated specimen dimensions were chosen to be 42 mm × 10 mm × 6 mm similar to the experimental specimens used for Chapter 5. Four-point bend tests are simulated using `Abaqus CAE` FEM analysis. Additionally, notch geometry variations were considered in this model to account for the SCF geometry effect on hydrogen distribution. Hence, for this part, various V-notch geometries were chosen for comparison. The FEM analysis in this part of the chapter is based on an isotropic elastic model but the proposed methodology in Part II accounts for the continuum scale anisotropy. Continuum scale isotropy is suitable for Part I in order to demonstrate the isolated effects of atomic scale anisotropy using the elastic dipole tensors. The anisotropic elastic dipole tensor is introduced to evaluate the elastic interaction energy between hydrogen interstitials and the stresses generated by loaded notches. Furthermore, this chapter studies hydrogen equilibrium profiles and not hydride precipitation, so a temperature of 623 K is chosen. At these temperatures the typical hydrogen diffusion velocities in zirconium are on the order of ~ 1 mm/hour and so, for now, the kinetics of diffusion need not be modelled explicitly. Considering the model specimen dimensions, the time scale for the hydrogen profile to equilibrate is relatively small in comparison to that of typical loading cycles in reactors. For practical purposes, this high diffusion rate justifies modelling steady state hydrogen profiles in the elastic fields of the SCF, that is, thermodynamic equilibrium is established instantaneously. Finally, this model assumes relatively low concentrations of hydrogen at a background concentration of 130 ppm, so that hydrogen-hydrogen interactions may be neglected. This assumption agrees with first-principles electronic structure simulations which suggested that hydrogen anions repel each other in solid solution in α-zirconium [129]. Noting these assumptions, the present work unifies continuum scale and atomistic scale stress analysis to compute notch-tip hydrogen profiles under steady state conditions using linear irreversible thermodynamics.

7.3 Modelling Approach and Setup

In the following sections, the three distinct stages of the proposed multiscale stress analysis are established.

The first stage is the continuum scale stress analysis of a notched homogeneous Zr specimen. The specimen stress state σ_{ij} is computed using a two-dimensional plane stress FEM model. The second stage is the atomistic scale stress analysis using the elastic dipole tensor ρ_{ij} for hydrogen in α-zirconium, calculated via density functional theory Zr-H system simulations by Nazarov et al. [197].

The third stage is the equilibrium stress analysis using linear irreversible thermodynamics that begins by computing the elastic interaction energy field E_{int}. A generic variant of this three-stage methodology is depicted in Figure 7.2. The parameters used in this study are listed in Table 7.1 and explained further in the text.

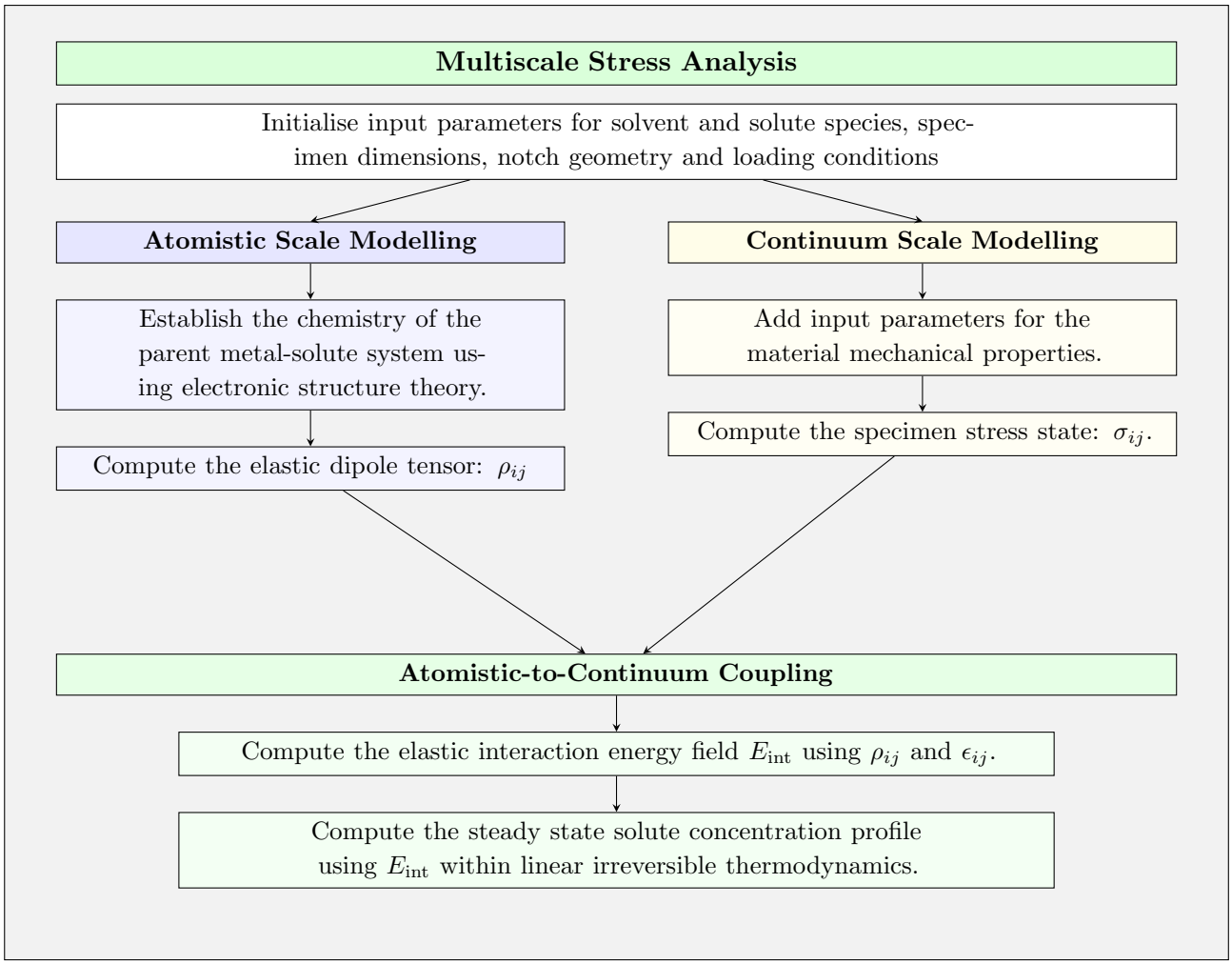


Figure 7.2: Schematic breakdown of the multiscale stress analysis. Adapted from [6].

7.3.1 Stress State of Notched Zirconium

Specimens were meshed by part using the plane stress 4-node bilinear, reduced integration with hourglass control (CPS4R) linear quadrilateral element type. The model was chosen to be in plane stress conditions that give three strain components, which enable future analysis on hydrogen diffusion in all directions of the HCP crystal (this is explained in later sections). The elements in the model range from 0.05 mm at the notch-tip and 0.2 mm around the notch to 0.2 mm for the remainder of the sample geometry. The mechanical properties of the model were chosen to be isotropic, define by

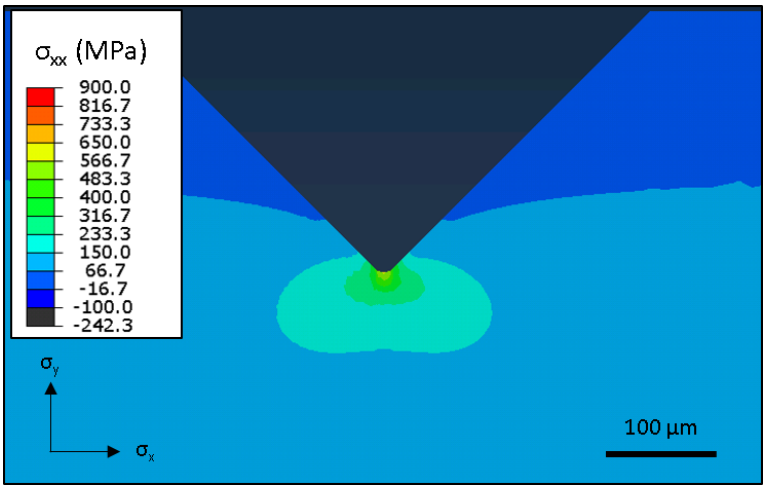
Table 7.1: List of parameters and variables required for this multiscale stress analysis. Adapted from [6].

Quantity	Symbol	Value	Ref.
MECHANICAL			
Elastic interaction energy	E_{int}	—	(−)
Notch flank angle	ϕ	$\{45°, 30°, 20°\}$	(∗)
Notch root radius	R	50 µm	(∗)
Poisson's ratio	ν	0.34	[4]
Strain tensor	ϵ_{ij}	—	(∗)
Stress tensor	σ_{ij}	—	(∗)
Young's modulus of Zr-4 at 623 K	$\mathcal{E}$	74 GPa	[4]
THERMODYNAMIC			
Boltzmann constant	k_{B}	86.2 µK/eV	
Background concentration	c_0	130 wppm	[1]
Chemical potential	μ	—	
Temperature	T	623 K	[1]
ELECTRONIC STRUCTURE			
Elastic dipole tensor	ρ_{xx}	1.74 eV	[12]
	ρ_{yy}	1.74 eV	[12]
	ρ_{zz}	2.36 eV	[12]

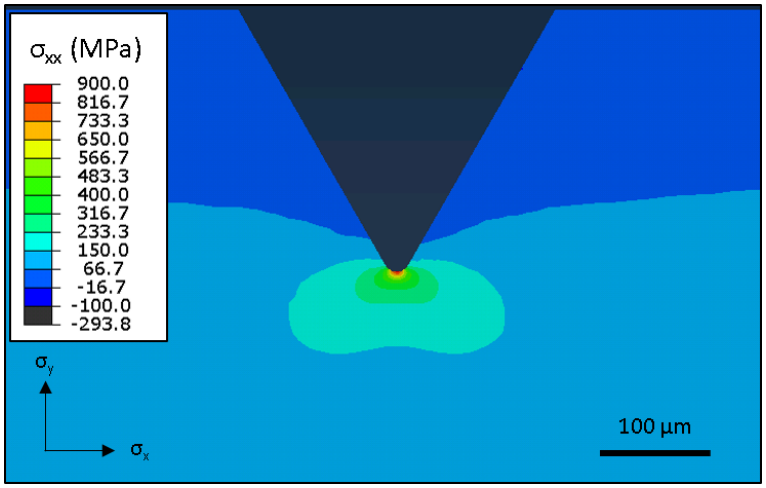
the Young's modulus and Poisson's ratio presented in Table 7.1. The specimens have 'V' notches parameterised by the root radius R and the flank angle ϕ, which are quasi-statically loaded to 1.6 kN within the elastic regime using `Abaqus CAE` implicit solver. The stress output of the simulations is shown using σ_{xx} maps in Figure 7.3 for three V-notches of $R = 50\,\mu\text{m}$ but with different flank angles $\phi \in \{45°, 30°, 20°\}$, and the ϵ_{xx} and ϵ_{yy} output used in the atomistic-to-continuum couplings in shown in Figure 7.4. Chapter 4 fully describes the FE model used as part of the multi-scale modelling in this part of the chapter.

7.3.2 Stress Analysis

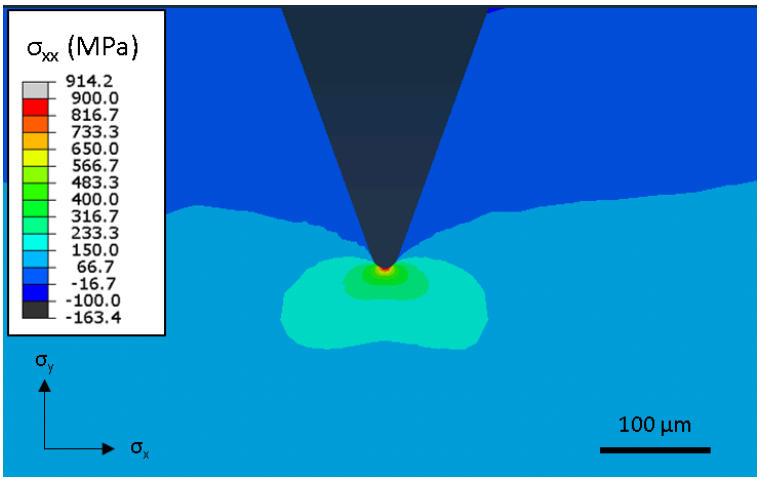
After obtaining the stress state of the notched specimens which can be used to compute strain tensors, it is important to discuss how this elastic distortion can drive hydrogen diffusion. Hydrogen diffusion in Zr has been discussed in previous chapters to be entropy-driven along a concentration gradient driven by a chemical potential, and stress-driven along a positive hydrostatic gradient. Entropy driven diffusion of hydrogen is controlled by its chemical diffusion potential (μ), and in a non stress-free continuum, μ competes with the energy of interaction between the stresses from SCFs and the stresses of the hydrogen interstitials at a distance r and angle θ from the notch tip. Accordingly there is another diffusion potential generated by the energy of interaction between these two stress sources, denoted $E_{\text{int}}(r, \theta)$, which is a scalar field with an intensity that varies with the relative distance between the hydrogen interstitial and the SCF [30, 198]. The elastic interaction energy, $E_{\text{int}}(r, \theta)$, can be defined



(a)



(b)



(c)

Figure 7.3: σ_{xx} (MPa) distribution maps at notch-tips in Zircaloy-4 specimens at K= 8 MPa$\sqrt{}$m. All three notches have the same root radius $R = 50\,\mu$m but different flank angles (ϕ). (a) $\phi = 45°$. (b) $\phi = 30°$. $\phi = 20°$.

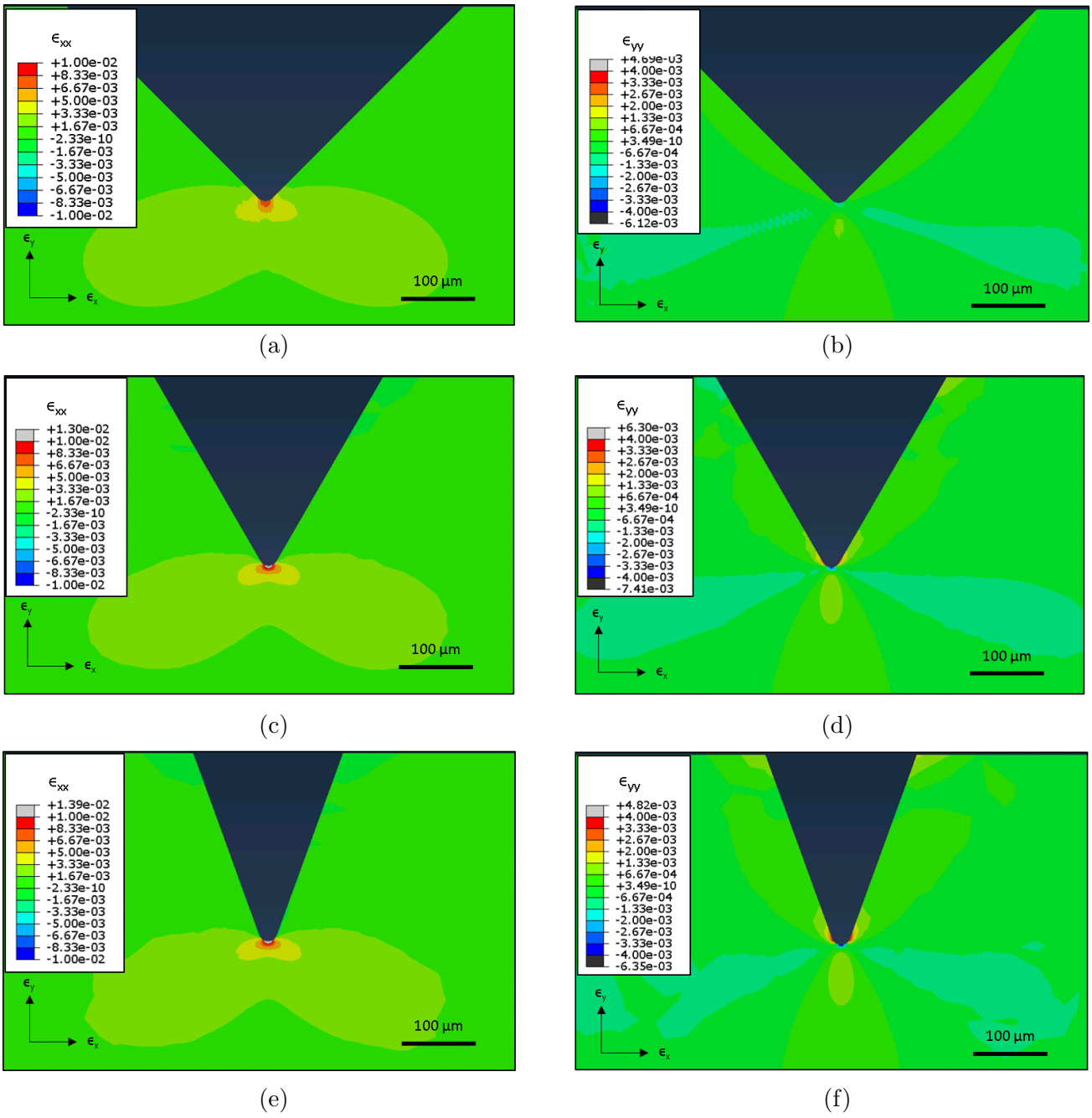


Figure 7.4: ϵ_{xx} (a)(c)(e) and ϵ_{yy} (b)(d)(f) distribution maps at notch-tips in Zircaloy-4 specimen at K= 8 MPa$\sqrt{}$m. (a, b) $\phi = 45°$. (c, d) $\phi = 30°$. (e, f) $\phi = 20°$.

as the volume integral over the volume of the continuum, as reported by the work of Eshelby [198].

The competing effects of the entropy and the elastic interaction energy on hydrogen diffusion can be treated by a linear combination of the two diffusion potentials, chemical and elastic. The equilibrium hydrogen concentration profile is defined in the limit that elastochemical diffusion potential is zero as

$$c(r, \theta; T) = c_0(T) \exp\left[-\frac{E_{\text{int}}(r, \theta)}{k_B T}\right], \tag{7.1}$$

where the temperature-dependent constant $c_0(T)$ is the uniform background concentration which is assumed to be the concentration of hydrogen in solid solution of 130 wppm at a uniform temperature T [30].

7.3.3 Atomistic-to-Continuum Coupling

In order to unify the atomistic and continuum length scales, a strategy to calculate the $E_{\text{int}}(r, \theta)$ is required. In an isotropic continuum where interstitial hydrogen atoms are treated as misfitting spheres, the elastic interaction energy is approximated by calculating the product of the hydrogen spherical misfit volume of transport and the hydrostatic pressure at a distance r and angle θ from the notch tip. It is worth noting that the spherical misfit volume of transport is a scalar quantity that cannot capture the symmetry of hydrogen tetrahedral interstitial site. This means that any analysis conducted using this product to compute $E_{\text{int}}(r, \theta)$ cannot truly account for crystalline anisotropy.

Contrary to the assumption of spherical isotropy, experimental work suggests that hydrogen interstitials do not resemble perfect spheres [128]. Hydrogen interstitials are reported to resemble the trigonal symmetry of the tetrahedral interstitial site which give rise to anisotropy in hydrogen diffusion. The trigonal symmetry associated with tetraheral hydrogen interstitials is shown in Figure 7.5. Unlike the misfitting sphere model, it is possible to capture the interstitial symmetry using the more general elastic model of point defects. This model defines a parameter that replaces hydrogen spherical misfit volume of transport in order to account for the atomistic scale hydrogen diffusion anisotropy [30, 197]. The parameter is called the elastic dipole tensor

$$\rho_{ij} \equiv \sum_{\alpha} f_i^{\text{H}}(\mathbf{p}^{\alpha}) p_j^{\alpha}, \tag{7.2}$$

whose components only depend on the atomic positions p_j^{α} and inter-atomic forces between the hydrogen interstitial and neighbouring zirconium atoms $f_i^{\text{H}}(\mathbf{p}^{\alpha})$. The components of ρ_{ij} used in this study for the crystallographic coordinate system shown in Figure 7.5 were calculated using density functional theory by Nazarov *et al.* [197]. ρ_{ij} for a tetrahedral interstitial is diagonal and the component relationships $\rho_{xx} = \rho_{yy}$ and $\rho_{zz} > \rho_{xx}$ reflect the trigonal symmetry of the interstitial site.

Now, using ρ_{ij}, it is possible to evaluate the expression for $E_{\text{int}}(r, \theta)$ used to calculate the equilibrium hydrogen concentration. The SCFs in the model, in the form of loaded notches, produce an elastic strain ($\epsilon_{ij}^{\text{SCF}}(r, \theta)$) computed using the FE model. Approximating the stresses exerted by hydrogen

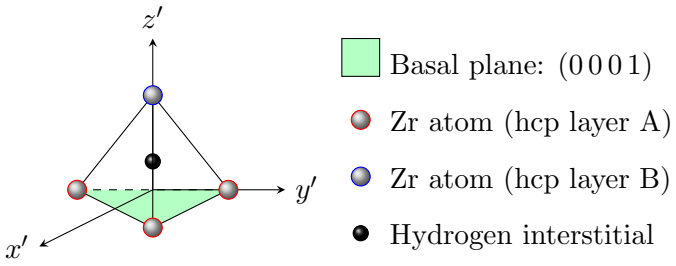


Figure 7.5: A hydrogen interstitial occupying a tetrahedral site in hexagonal α-zirconium. The hydrogen anion forms three equivalent bonds with the zirconium atoms on the basal plane and a fourth nonequivalent bond with a zirconium atom along the transverse c-direction; the tetrahedral interstitial possesses a trigonal symmetry. Adapted from [6].

interstitials using ρ_{ij}, it is possible to write

$$E_{\text{int}}(r,\,\theta) \simeq -\rho_{ij}\epsilon_{ij}(r,\,\theta). \tag{7.3}$$

$E_{\text{int}}(r,\,\theta)$ is in units of eV, same as the unit of ρ_{ij}, and ϵ_{ij} is dimensionless. Note that ρ_{ij} and ϵ_{ij} must be expressed in the same coordinate systems and considering Figure 7.1, when the basal plane (0 0 0 1) and the the prism plane (0 0 $\bar{1}$ 0) of the HCP unit cell are on the same plane of the 2D specimen surface, Eq. (7.3) reduces to the simpler expressions [30]:

$$E_{\text{int}}(r,\theta) = \begin{cases} -\left[\rho'_{x'x'}\epsilon_{xx}(r,\theta) + \rho'_{y'y'}\epsilon_{yy}(r,\theta)\right] & \text{on} \quad (0\,0\,0\,1) \\ \\ -\left[\rho'_{x'x'}\epsilon_{xx}(r,\theta) + \rho'_{z'z'}\epsilon_{yy}(r,\theta)\right] & \text{on} \quad (1\,0\,\bar{1}\,0) \end{cases} \tag{7.4}$$

The respective expressions for $E_{\text{int}}(r,\theta)$ on the basal plane and prism plane are different because of the rotational asymmetry of ρ_{ij}, that is, ρ_{ij} varies with the crystallographic plane on which ϵ_{ij} is computed. The expressions for $E_{\text{int}}(r,\theta)$ would be more complicated on other HCP planes, such as the pyramidal planes, in comparison to those given in Eq. (7.4), but the FE model enables their calculation as it produces all strain components. The explicit regard to anisotropy is characteristic of the elastic dipole model of point defects, whereas the isotropic counterpart for $E_{\text{int}}(r,\theta)$ as determined using the misfitting sphere modelling is the same irrespective of crystallographic orientation.

Finally the steady state hydrogen concentration scalar field $c(r,\,\theta)$ can be calculated ahead of the notch tip using Eq. (7.4) within Eq. (7.1) using a sub-routine code presented in the Appendix. Using simple test parameters, it is straightforward to show that in a tensile region where $\epsilon_{ij}(r,\,\theta)$ is positive, $E_{\text{int}}(r,\,\theta)$ is positive and hence $c(r,\,\theta)/c_0 > 1$, suggesting that hydrogen is drawn to tensile regions.

Conversely, hydrogen is depleted from compressive regions.

7.4 Results

Simulations of the notch-tip hydrogen profiles using the two expressions for $E_{\text{int}}(r, \theta)$ in Eq. (7.4) are shown in Figure 7.6 and Figure 7.7 respectively. In the former case, the simulation map shows the basal plane, whereas in the latter case, the simulation map shows the prism plane. For both cases, the three notch geometries chosen are used for comparison.

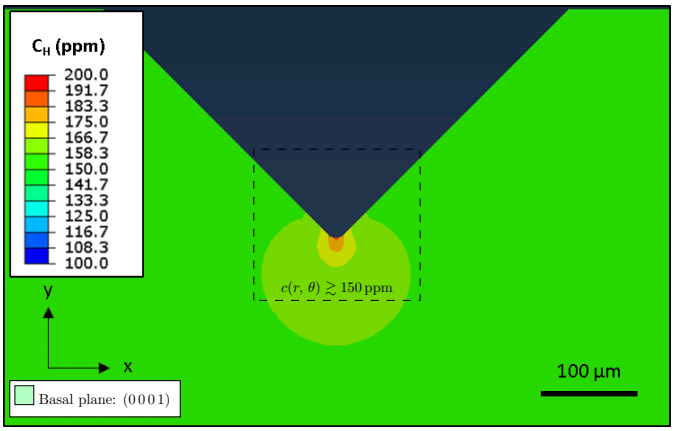
Firstly, the effect of notch geometry on the equilibrium hydrogen concentration profile is considered. Figure 7.6 shows that there is at least 20% increase of hydrogen concentration at the notch tip from the background value for all three notch geometries. This increase correlates to the higher stress values at the notch-tips. Furthermore, it can be seen in Figures 7.6 and 7.7, that the maximum value of notch-tip hydrogen concentration increases as the notch flank angles decrease from 45° to 20°.

Considering the microstructural effect on hydrogen distribution. Comparing a given notch geometry from Figure 7.6 and Figure 7.7, it is evident that hydrogen accumulation is greater if the notch is loaded on the prism plane as opposed to the basal plane. This effect is more noticeable for sharper notches with smaller flank angles. This is a direct consequence of the trigonal symmetries embedded within ρ_{ij} and, more specifically, the inequality $(\rho_{xx} + \rho_{yy}) > (\rho_{xx} + \rho_{zz})$ that reflects the transverse isotropy.

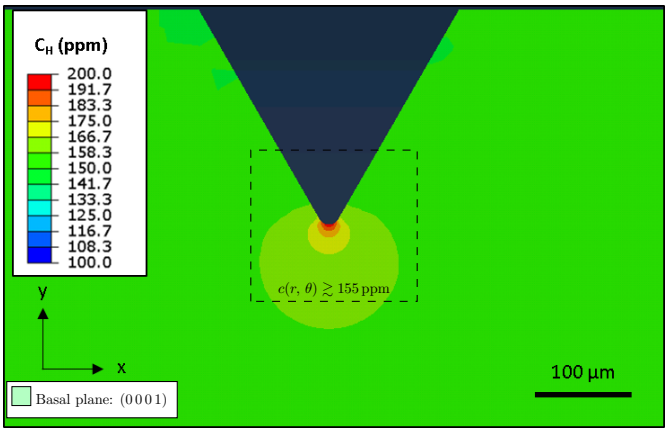
7.5 Discussion

The simulated notch-tip hydrogen profiles, determined in this investigation, can be related to an experimental observation of notch-tip hydride distribution. FE simulations coupled with DFT derived dipole tensor show that hydrogen will diffuse from the bulk of specimens towards a dominant or long range SCF in the form of loaded notches. Chapter 5 shows this behaviour via an increase in hydride number density at the notch tip regions in comparison with the bulk. Hydrides precipitate at regions with enhanced hydrogen concentrations and so hydrogen concentration maps provide information about preferable hydride precipitation regions around notch geometries.

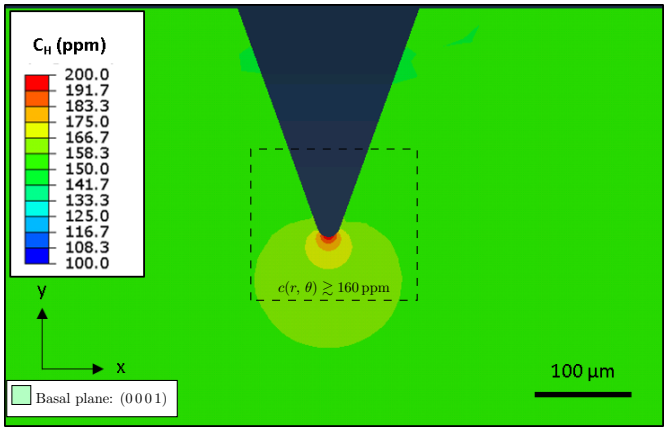
Considering the effect of notch geometry on hydrogen concentration profiles (Figures 7.6 and 7.7). The hydrogen-enhanced regions at notch tips increases in concentration as the notch flank angle decrease, highlighting the effect of elastic hydrostatic stress gradients on hydrogen diffusion. Stress



(a)



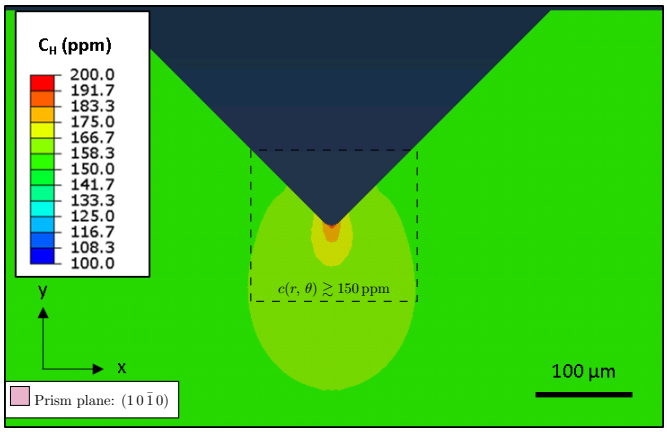
(b)



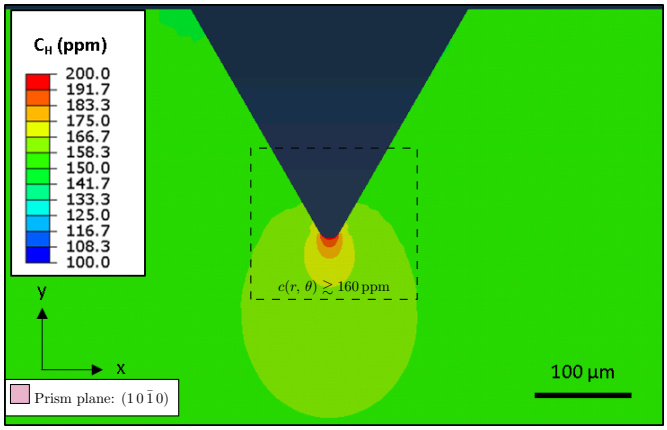
(c)

Figure 7.6: The hydrogen concentration profile at the tip of a V-notch of root radius $R = 50\,\mu$m with flank angles of (a) 45° (b) 30° and (c) 20°, all at $K = 8$ MPa$\sqrt{}$m. The (x, y)-plane of the simulation cell is the basal plane. The dashed square highlights the notch-tip hydrogen enhanced region.

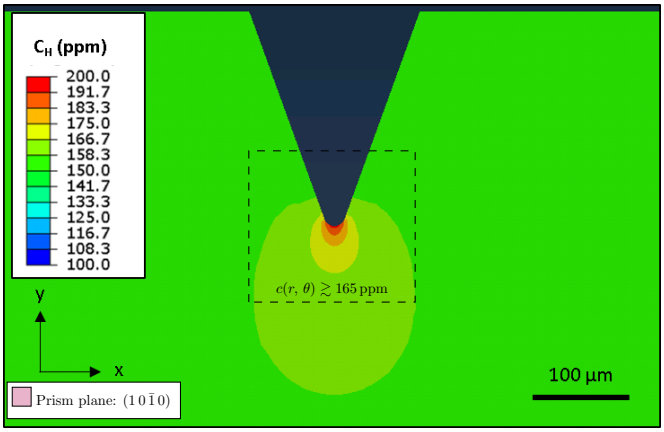
maps in Figure 7.3 show that the notch with the smallest notch flank angle (20°), produces the largest peak stress, σ_{xx}, right ahead of the notch tip while the stress localisation appears to be similar to all the other notch geometries due to notch root radius that is kept constant in all geometries. This



(a)



(b)



(c)

Figure 7.7: The hydrogen concentration profile at the tip of a V-notch of root radius $R = 50\,\mu$m with flank angles of (a) 45° (b) 30° and (c) 20° all at $K = 8$ MPa$\sqrt{}$m. The (x, y)-plane of the simulation cell is the prism plane.

simple stress effect enhances the hydrogen concentration levels at notches with small flank angles, such as one shown in Figure 7.6(c), whilst having the same size of a hydrogen enhanced zone as in the other larger flank angled notches with similar notch root radii.

Considering now the effect of the atomic scale anisotropy defined by the elastic dipole tensor. It is evident, that hydrogen concentration is higher at notch tip regions loaded on the prism planes than basal planes. This effect can be seen by considering the different expressions for $E_{\text{int}}(r, \theta)$ on the basal and prism planes, and by comparing hydrogen distribution maps in Figure 7.6 and Figure 7.7. In the former case, the isotropy of the basal plane leads to an analysis that is very to similar to the purely isotropic misfitting sphere analysis, which seems to underestimate the notch tip hydrogen concentration. Figure 7.6 shows a more localised hydrogen enhanced notch tip region, while Figure 7.7 shows a larger hydrogen enhanced region (mainly in the y direction) which is the more realistic case on the prism plane.

Exploring the isolated effects of the elastic dipole tensors and their contribution in incorporating the atomic scale anisotropy, highlights the importance of microstructural effects on hydrogen diffusion and hydride precipitation. Part II of this chapter, extends this study to another multiscale model by Liu et al. [29], that acts as a proof of concept to the atomic scale anisotropy incorporation as well as incorporating the continuum scale anisotropy and polycrystallinity.

7.6 Conclusions

This investigation focused on modelling hydrogen distribution profiles in Zr-4. The standard continuum scale methodology for stress-driven hydrogen concentration profiles was generalised to incorporate the effects of anisotropy at the atomistic scale. Incorporating the atomic scale anisotropy was done via elastic dipole tensors of hydrogen interstitials in α-zirconium, a fundamental property of the point defect. This multiscale stress-diffusion analysis was proposed to evaluate notch-tip equilibrium hydrogen profiles in 2D plane stress specimens of Zr-4 under a four-point bending. Preliminary results for various notch flank angles agree with experimental work. It was also shown how the notch-tip hydrogen enhancement is affected by atomic scale anisotropy, an effect that is not present in traditional isotropic analyses.

The multiscale framework can be extended to more realistic cases and possible future work include: Incorporating the continuum scale stiffness matrix for prism and basal planes instead of a simple elastic isotropic continuum. This continuum scale anisotropy will allow the study of elastic dipole tensors in basal and prism monocrystals in an inexpensive model. Part II extends this framework to proof its concept via another model which in addition incorporates continuum scale anisotropy and polycrystallinity.

Part II

7.7 Analysis of Anisotropic Stress-Driven Hydrogen Equilibrium Profiles using a Crystal Plasticity Model

In this part of the chapter, the concept of using the elastic dipole tensors to account for atomic scale hydrogen diffusion anisotropy, associated with tetrahedral interstitial symmetry, is put to demonstration. A crystal plasticity finite element (CPFE) model was chosen to act as a proof of concept, which was developed and ran by Liu et al. [29], and parameterised by my experimental data. This establishes a multiscale framework for hydrogen stress-concentration profile analysis which combines the atomistic scale anisotropy and microscale crystal-based plasticity.

The model in part I simply focuses on an elastic isotropic Zr specimen, and it was clear that the elastic dipole incorporation at the atomic scale allows us to couple anisotropy with the continuum scale. Now, we can explore the anisotropy at the microscale, intermediate to the atomic and continuum scale, by explicitly considering polycrystalline texture. Coupling of crystal plasticity and atomistic hydrogen diffusion anisotropy is also applied to predict the quasi-steady-state hydrogen concentration profiles at GBs near notch tips for specimens with thermomechanical loading conditions taken from experimental studies of Chapter 5.

7.8 Crystal Plasticity Modelling Incorporating Atomistic Analysis

The CPFE model captures large plastic deformation near the notches, by the application of the finite strain theory that uses the elastic, plastic and thermal deformation gradients. The thermal deformation gradient is defined by a diagonal tensor in the reference crystallographic coordinate system describing the anisotropic thermal expansion of Zr-4. The plastic deformation gradient is defined by the dislocation slips among all slip systems, i.e it takes the rate of resolved shear strain into account, along with the slip directions and the normal of the slip systems.

The atomic scale anisotropy is also accounted for in this part via the elastic dipole tensors to calculate the elastic interaction energy from Equation 7.4. The energy of interaction between the lattice strain, generated by stresses of a loaded SCF, and the stresses, generated by hydrogen interstitials, is coupled with the CPFE model using the same methodology put forward in Part I to compute the

notch-tip steady-state hydrogen concentration profiles.

7.8.1 CPFE Model Setup

Figure 7.8 shows the balancing process between the model computational efficiency, model accuracy and the load validation with the elastic 3D four-point bend model. A full elasto-plastic 3D FE model, shown in Figure 7.8(a), with dimensions similar to experimental specimens of Chapter 6 (42 mm × 10 mm × 6 mm), was used to provide a validation of tensile stress distribution with a truncated quasi-2D model shown in Figure 7.8(b). The truncated quasi-2D model has a non-uniform stress loading at both edges, to mimic the four-point bending, in quasi-plane stress conditions. The truncated model has a full elasto-plastic FE model (shown in blue) which is constructed using a simple bilinear yielding behaviour (yielding at 420 MPa and strain hardening to 500 MPa at 0.016 plastic strain) with displacement boundary conditions also shown in Figure 7.8(b). A reduced area of the truncated model shown in Figure 7.8(b), was modelled to contain either a monocrystal or multiple blocky-α grains (shown in green) at the notch region, with material properties defined by the CPFE theory.

Simulations for polycrystalline blocky-α microstructures, have materials properties defined for each grain, parameterised by experimental EBSD data from Chapter 6 for grain crystal orientations and geometry. Two blocky-α 'V' notch Zr-4 samples were experimentally tested under thermo-mechanical four-point bending conditions and their surface crystal orientations were obtained via EBSD mapping. Using an in-house `python` code, their grain geometry and corresponding crystallography were then individually reconstructed inside `ABAQUS` [173].

The full 3D model shown in Figure 7.8(a) has 28,020 elements with a mesh size of 20-100 µm. The reduction models have 36756 elements for the 'V' notch sample and 37050 for the 'U' notch sample with 20 µm mesh size and four elements through the thickness (80 µm). The C3D20R mesh type was chosen in the truncated models with 20 integration nodes that capture the quadrilateral curvature necessary for the CPFE subroutine. From the elasto-plastic response of the 3D model in Figure 7.8(c), the stress responses along the edge path of the cutting geometry is consistent with the linear-gradient stress distribution applied at the edge of truncated model. Furthermore, the stress response along path C-C' was consistent between the original and truncated model during elastic loading period as shown in Figure 7.8(d).

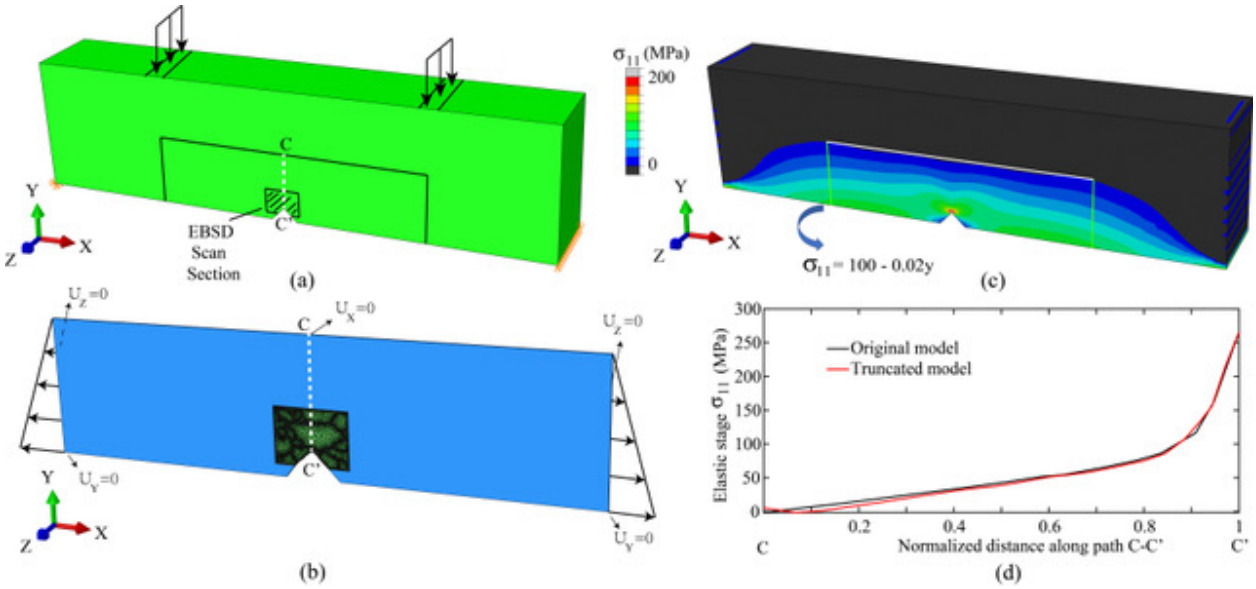


Figure 7.8: A 3D FE model (a), highlighting the displacement and loading boundary conditions, with a simplified loading configuration of four-point bending. A truncated quasi-2D plane stress model (b) which has a reduced microstructure embedded at the notch tip. The full model tensile stress distribution (c) on the bottom half sample is compared with the truncated model along path C-C' (d) [29].

7.9 Results

7.9.1 Hydrogen Profiles in Monocrystalline Structures

The first study that was employed via CPFE and atomistic scale coupling was done in the absence of polycrystals. In order to understand the effects of plasticity on hydrogen distribution in different i.e. most extreme 'hard' and 'soft' grain orientations and notch acuities, mono-crystalline simulations were set up. Samples were loaded to a 133 MPa nominal stress at 623 K (force boundary conditions are shown in Figure 7.8(b)). Figure 7.9 shows results for 'V' and 'U' notch geometries, with similar notch geometries to experimental specimens from Chapter 6, modelled on the prismatic plane and therefore correspond to a relatively hard mono-crystal. When these hard grains are loaded, the 1^{nd} order pyramidal ⟨c+a⟩ slip system is activated. The critical resolved shear stress (CRSS) values for the 1^{nd} order pyramidal ⟨c+a⟩ and the prismatic ⟨a⟩ slip are 532 MPa and 153 MPa respectively. Figure 7.10 shows the same notch geometries, but modelled on the basal plane corresponding to a soft grain, and when loaded the easy slip prismatic systems get activated.

Firstly, notch geometry effects show that the plastic zone in Figure 7.9(a.1) is less constrained at the 'U' notch tip than at the 'V' notch tip, shown in Figure 7.9(a.2). However the peak plastic strain is higher in the latter, which is an expected effect of the high acuity 'V' notch geometry. This effect was

also seen in the softer single grains in Figures 7.10(a.1) and 7.10(a.2) where the notches open on the basal plane. Considering the effect of plasticity on hydrostatic stress (σ_{hyd}) and hydrogen concentration (C_H), hard mono crystals show a depletion in σ_{hyd} and C_H directly ahead of both notch geometries indicated by arrows shown in Figures 7.9(b) and 7.9(c). At the 'V' notch tips on the primatic plane, σ_{hyd} depletes to nil while at 'U' notch tips σ_{hyd} depletes to a smaller degree, but over a larger zone. C_H showed a similar depletion behaviour in both notch geometries, which is a result of plasticity.

The effect of plasticity on σ_{hyd} and C_H was found to be negligible at notch tips on the basal plane. The single grain in Figure 7.10 is softer than the one in Figure 7.9 due to the lower CRSS required to slip a prismatic plane than pyramidal. Since the load applied in this model is in stress control, the plasticity generated at basal plane notch tips, shown in Figures 7.10(a.1) and (a.2) is much smaller than in the hard monocrystal (effective plastic strain of 0.4 vs 0.8), with same notch geometry. Figures 7.10(b) and (c) show that, as a result of less plasticity, soft monocrystals produce near to zero depletion in σ_{hyd} and C_H at the notch tips.

Finally, monocrystalline simulations show again the effect of anisotropy in hydrogen steady state solution. Hydrogen concentration zones at 200 wppm, are much larger in hard monocrystals than soft ones, and the hydrogen notch tip distribution profile appears to be significantly different between the two types of crystal orientations, highlighting the importance of incorporating crystal structures and atomic scale anisotropy when computing hydrogen concentration profiles.

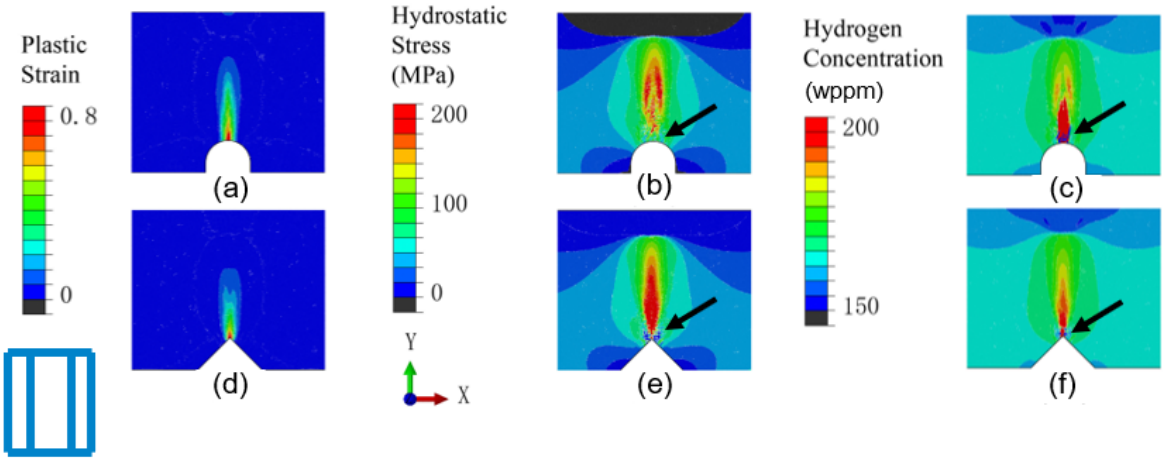


Figure 7.9: Effective plastic strain (a)(d), on a relatively hard monocrystal plane (prism), and its effect on hydrostatic stress (b)(e) and hydrogen concentration distribution (c)(f) at 'U' and 'V' notch tips at K= 8 MPa$\sqrt{}$m. The arrows in black highlight the depletion in σ_{hyd} and C_H ahead of notch tips due to plasticity.

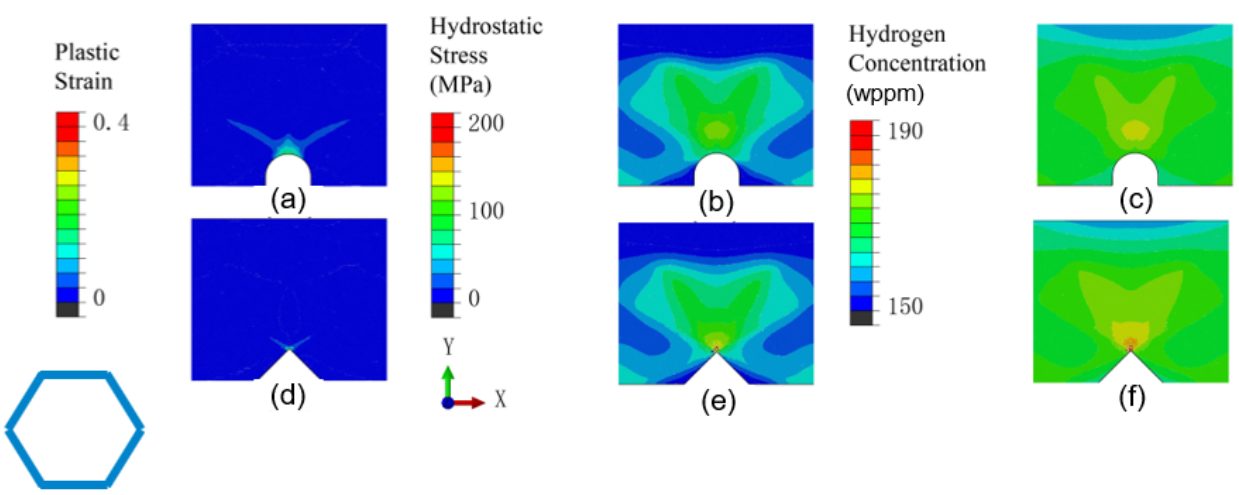


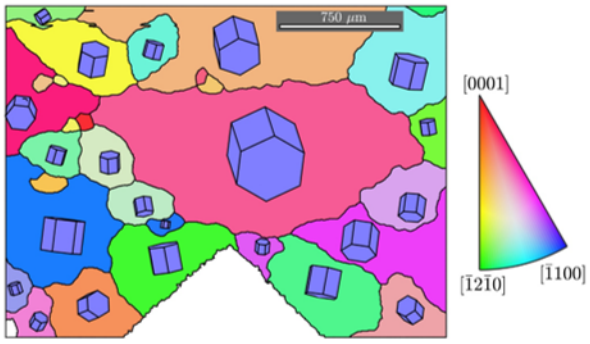
Figure 7.10: Effective plastic strain (a)(d), on a soft monocrystal plane (basal), and its effect on hydrostatic stress (b)(e) and hydrogen concentration distribution (c)(f) at 'U' and 'V' notch tips at K= 8 MPa$\sqrt{}$m.

7.9.2 Hydrogen Profiles in Polycrystalline Structures

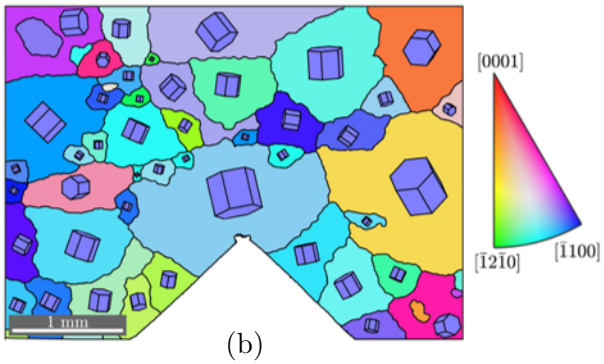
Plasticity induced by local grain interaction in the microstructure must have an important effect on local hydrogen concentration and stress redistribution and hence hydride precipitation locations. Two blocky-α Samples 1 and 2 (Figures 7.11(a) and 7.11(b) respectively) were scanned using EBSD to parameterise the CPFE model with crystal orientations and geometry of each grain in a region around the specimen notch tip. The effects of plastic flow in polycrystalline microstructures, during the load-up stage of the cycle taken from experiments, are shown in Figures 7.12 and 7.13, for samples 1 and 2 respectively.

In sample 1, at a time within the elastic stage (t_e) at 410 K, the total strain (ϵ_{11}) map shows a non-uniform distribution due to polycrystallinity (Figure 7.12(a)). No effective plastic strain ($\tilde{\epsilon}^p$) can be observed at the notch tip of the sample (Figure 7.12(c)), while σ_{hyd} and C_H appear to be in agreement (Figures 7.12(e)(g)). At a time of the plastic onset (t_p) at 468 K, the maximum ϵ_{11} significantly increases at the 'V' notch tip as $\tilde{\epsilon}^p$ is produced (Figures 7.12(b)(d)). $\tilde{\epsilon}^p$ dominates the local notch tip strain and causes the σ_{hyd} and C_H to be effectively washed out at the notch tip (Figures 7.12(f)(h)).

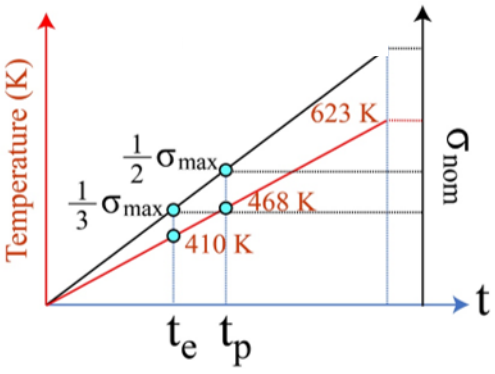
Sample 2 has a different polycrystalline arrangement at the 'V' notch tip than in Sample 1, as shown by the single dominant grain directly at the notch-tip in Figure 7.13(i). The crystallography of this notch tip blocky-α grain controls the elasto-plastic behaviour to more of an extent than in Sample 1. This is because Sample 1 has GBs nearer the notch-tip, which effect the local stress/strain



(a)



(b)



(c)

Figure 7.11: Blocky-α Sample 1 (a) and Sample 2 (b) loaded to the elastic stage t_e and plastic onset t_p (c).

distribution to a greater extent than Sample 2. ϵ_{11} distribution at t_e, shown in Figure 7.13(a), also has a non-uniform distribution, as in Sample 1, due to the compatibility effect of polycrystallinity. $\tilde{\epsilon}^p$ is also zero at t_e and so σ_{hyd} and C_H distributions are only effected by elastic strain at this time

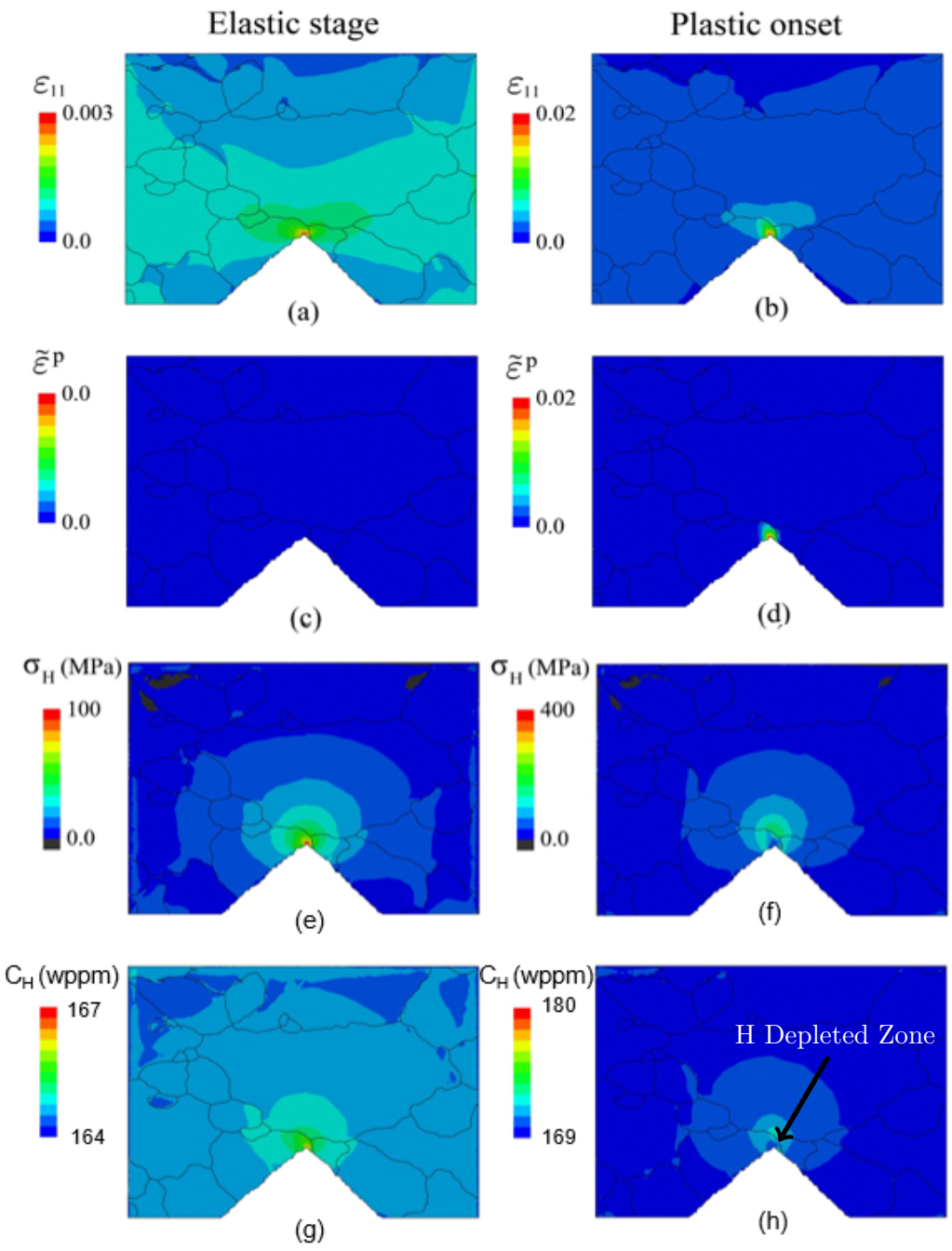


Figure 7.12: The distribution profiles of the total strain component, ϵ_{11}, (a, b), the effective plastic strain, $\tilde{\epsilon}^p$, (c, d), the hydrostatic stress σ_{hyd} (e, f) and the hydrogen equilibrium hydrogen concentration (C_H), in notch tip blocky-α Sample 1 at the elastic stage t_e and plastic onset t_p.

with no influence of plasticity on the stress state. The negative hydrostatic stress shown in Figure 7.13(e) is caused by a computational artefact at the boundary between the elasto-plastic region of the truncated model and the notch tip regions that has the CPFE theory applied to. The C_H distribution map in Figure 7.13(g) shows a higher concentration at one side of the notch than the other, due to the larger ϵ_{11} generated at the grains to the right of the notch. At t_p, the total strain ϵ_{11} is significantly

larger than at t_e, due to the presence of notch tip plasticity shown in Figure 7.13(d). A similar effect is observed in this sample, σ_{hyd} and C_H deplete right ahead of the notch tip, but to a smaller extent than in Sample 1, as shown in Figures 7.13(f) and (h).

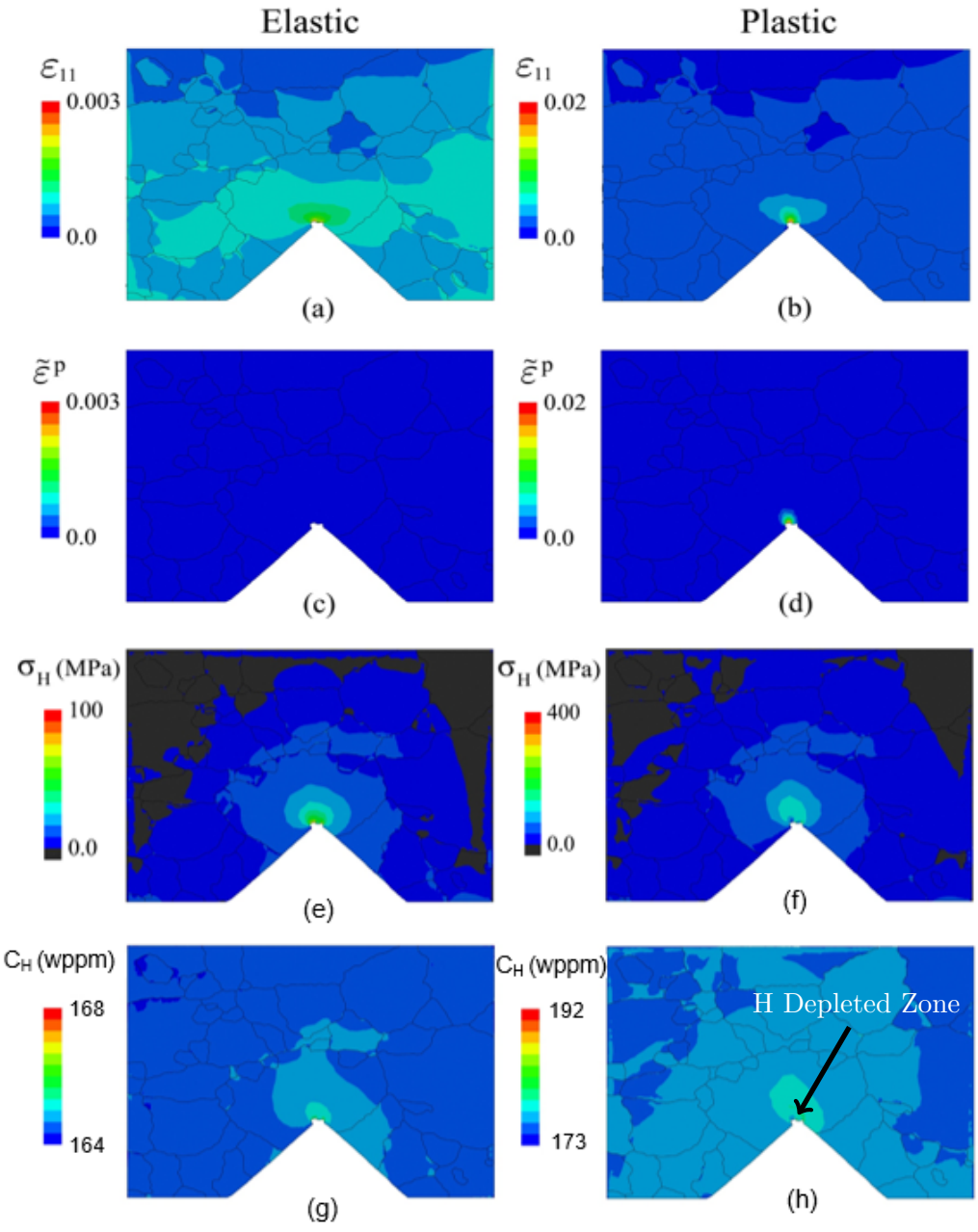


Figure 7.13: The distribution profiles of the total strain component, ϵ_{11}, (a, b), the effective plastic strain, $\tilde{\epsilon}^p$, (c, d), the hydrostatic stress σ_{hyd} (e, f) and the hydrogen equilibrium hydrogen concentration (C_H), in notch tip blocky-α Sample 2 at the elastic stage t_e and plastic onset t_p.

7.10 Thermomechanical Cycling Effect on Hydrogen Concentration

7.10.1 Computational Results versus Experimental Hydride Distribution

Taking the strain rate sensitive crystal plasticity method into account, creep effects during the high temperature stress hold, for three thermal cycles, can be accounted for. Figure 7.14 compares the C_H map and its σ_{hyd} distribution with an SEM hydride micrograph of Sample 1, which was experimentally thermomechanically cycled 3 times at a peak nominal stress of 133 MPa. C_H and σ_{hyd} are obtained at t_{top} of the last cycle (Figure 7.14(d)), where hydrogen atoms are precipitating as zirconium hydrides at SCFs (553 K). The SEM image (Figure 7.14(b)) shows that not all the GBs are occupied by hydrides near the notch tip and indeed not all grains contain intragranular hydrides. When comparing the SEM micrograph with simulations, it is evident that GBs that contain hydride precipitates, match the ones from the CPFE model that have a high C_H as shown by the black circles in Figure 7.14(a). A relatively low hydrogen concentration is observed in the white-circled GBs in Figure 7.14(a) where no intergranular hydrides are observed in the SEM image. Figure 7.14 (c) shows the σ_{hyd} distribution also matches the hydride micrographs, whereby positive σ_{hyd} corresponds to having hydride precipitates and vice versa; the negative σ_{hyd} regions corresponds to the low hydrogen concentration level, caused by hydrostatic compression. For the grain boundaries near the notch tip, a white line is drawn along the side of the grain that has a positive σ_{hyd} (>100 MPa). The SEM micrograph shows that these GBs have intragranular hydrides precipitating at them, along with depletion of intragranular hydrides inside the adjacent grains of those white lines.

7.11 Discussion

Considering firstly the effect of local crystallography on the notch tip equilibrium hydrogen concentration, it is clear from monocrystalline results that the plasticity produced in hard grains (Figure 7.9) cause the σ_{hyd} and C_H to deplete at the notch tip to a higher degree than in the softer grains (Figure 7.10). Secondly, notch geometry effects in monocrystals show that 'V' notches produce a larger peak notch tip plastic strain than 'U' notches but over a smaller zone. Relating these two results to experimental observations, notch tip crystallography, which has a more dominant effect in blocky-α microstructures than in as-received ones, would have a significant impact on hydride number density parameters, calculated in Chapter 5. The crystal orientation of a notch tip blocky-α grain not only determines the peak plastic strain generated at the notch tip (at a given load), but also the size of the plastic zone.

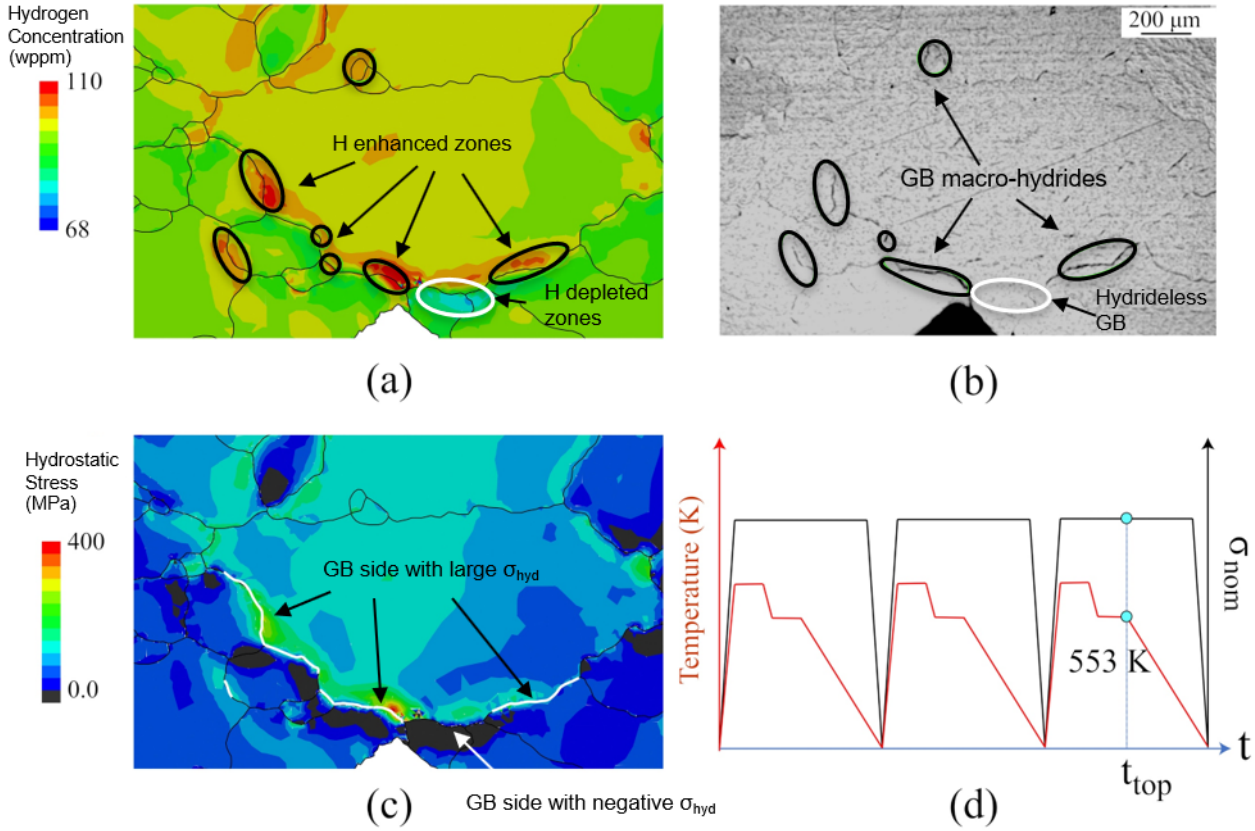


Figure 7.14: Simulated hydrogen concentration (C_H) map (a) after three thermo-mechanical cycles of Sample 1, compared with its SEM micrograph (b). The hydrostatic stress (σ_{hyd}) distribution highlights the tensile and compressive regions that interact with hydrogen diffusion (c). The white line highlight the tensile GBs. The cycling profile and the time of which simulation parameters are chosen is shown in sub-figure (d).

This means that crystallography has a direct impact on the hydrostatic stress gradient required for hydrogen diffusion from the bulk, and in turn hydride number density. Furthermore, the size of the plastic zone may also effect the number of locally activated notch tip microstructural nucleation sites such as SPPs, which may either drive hydride number density to increase or decrease.

The depletion of the equilibrium hydrogen concentration in monocrystals at notch tips, has been experimentally observed and reported in literature by Schofield et al. [5]. The depletion of hydrides at notch tips, which were described by Schofield as the denuded zones, was observed after testing in both unirradiated and irradiated Zircaloy-2 'V' notch specimens containing electron beam welds (random texture so same level homogeneity as in blocky-α microstructures), that were loaded in four-point bending to a range of stress intensity factors of 12-20 MPa$\sqrt{}$m at temperatures between 290°C and 60°C. CPFE methodology and simulation results presented in this part, may provide a mechanistic reasoning

to this phenomenon. The denuded zone phenomena was also observed in polycrystalline simulations presented in Figures 7.12 and 7.13; a similar effect of plastic strain on the depletion (washing out) of notch tip hydrostatic stress and hence hydrogen concentration can be seen in Figures 7.12 and 7.13, (f) and (h).

Polycrystalline results show that GBs have a significant effect on hydrogen distribution. Sample 1, that contains multiple GBs near the notch tip, produces a non-uniform hydrogen distribution at both the elastic and plastic stages of the load-up. GBs with high or low energies can cause an increase or decrease in the elastic interaction energy at those GBs. GBs can be different by either their orientation with respect to the applied load or by the misorienation between the bounding grains due to crystallography. These two factors have been reported in literature to effect hydride precipitation [30, 40], and can be demonstrated by the non-uniform ϵ_{11} and C_H distribution maps. GBs, as described in Chapter 5, can be thought of as local stress raisers, which have a local effect on H transport and distribution.

The effects produced by the crystallography of notch tip blocky-α grains can also be captured from the polycrystalline results in Figures 7.12 and 7.13. Sample 1, shows a hard grain directly ahead of the notch tip, which is also very near a much larger grain with a softer orientation. This difference in crystallography and grain geometry, produces a distorted total strain distribution map at the notch tip region, which in turn alters the hydrogen distribution that effects the number of activated nucleation sites in grains near the notch tip.

Sample 2 further demonstrates the effects of plasticity and polycrystallinity on the equilibrium hydrogen distribution. Sample 2 has one large blocky-α soft grain at the notch tip, and so the σ_{hyd} and ϵ_{11} produced cannot be accommodated by neighbouring grains, and so the crystallography of that sole soft grain determines how hydrogen distributes at the notch tip and therefore how many intragranular hydride nucleation sites are activated. The CPFE simulations can predict the potency of intergranular hydride precipitation sites. This prediction can be explained by also considering Sample 2 in Figures 7.13(g) and (h), where the equilibrium hydrogen concentration can be seen to be higher at certain GBs compared to other. This is again due to the two factors mentioned above that effect the GB energy. Overall, although only two blocky-α microstructures are presented for comparison from experimental data, they provide a convincing picture that hydrogen distribution and hence hydride precipitation can be predicted by the combination of a CPFE model coupled with the atomic dipole tensor for hydrogen in zirconium.

7.12 Conclusions

Polycrystalline CPFE modelling provides a method to indirectly predict intergranular and intragranular hydride precipitation sites based on the equilibrium hydrogen distribution maps. CPFE simulations not only showed the feasibility of incorporating the atomic scale elastic dipole tensor, but also provided a computational insight into the effects of cystallography and polycrystallinity on hydrogen distribution.

Results from Part II show that the equilibrium hydrogen distribution, at the load-up stage of the experimental thermo-mechanical cycle from Chapter 5, is effected by the crystallography of notch-tip mono and polycrystals.

Results also show that plasticity generated during the load-up stage, at an applied stress of 67 MPa at 468 K, causes a depletion in notch tip σ_{hyd} and therefore reduced C_H. This phenomenon has been observed in experimental studies from literature but has not been computationally studied previously [5].

The findings from this part show the importance of incorporating polycrystalline microstructural anisotropy effects in delayed hydride cracking (DHC) models. Future work that builds on these findings, can aim to account for intragranular heterogeneity with experimental data from Chapters 4 and 5. The model would then be able to predict the ideal microstructures required to minimise the initiation of DHC failure or assess the worst case microstructures for DHC. Localised intragranular stress raisers such as SPPs could be incorporated in the model via information generated by discreet dislocation plasticity methods.

Chapter 8

Overall Discussion

This project provides a quantitative link between hydride precipitation and microstructural features, thus enabling parameterisation of predictive models of hydrided microstructures for safety assessments. Current analytical and numerical models that are used to predict hydride precipitation and hydrogen concentration distribution do not account for (1) intra/intergranular heterogeneity in hydride precipitation, (2) microstructural polycrystallinity (grain boundaries and grain crystallographies) and (3) hydrogen diffusion anisotropy due HCP zirconium crystals [30, 199]. Therefore this project set out to experimentally determine the effects of GB and SPP density on microstructural hydride distribution along with the effects of notch acuity on hydride reorientation considering microstructural effects. The project also puts forward a continuum based finite element numerical model to compute notch-tip hydrogen concentration profiles in polycrystalline structures, with anisotropic hydrogen diffusion atomic scale consideration, to predict the hydrogen stress-driven distribution around notches, a sub-process of hydride reorientation and delayed hydride cracking.

8.1 Hydride Precipitation Sites in Zr-4 and Commercially Pure Zr

Most industrial research on hydride precipitation in Zr alloy components does not tend to distinguish between intergranular and intragranular hydrides and DHC predictive models do not account for the effect of grain boundaries on the hydride precipitation distribution [30, 178, 199]. Quantitative and qualitative data in this project agrees with literature regarding GBs being the preferred sites for hydride precipitation in as-received microstructures at slow cooling rates, but further highlights the degree of intragranular hydride precipitation sites in blocky-α microstructures [179]. The findings

show that the density of GBs and intragranular sites affect the resulting hydride microstructures and hence also change the conditions for DHC initiation, which is a main industrial concern [30, 185]. Results from Chapter 5, using a simple experimental methodology of quantifying hydride precipitation in specimens of varied SPP and GB density content, show that intra/intergranular localised stress raisers may change the picture of hydrogen diffusion and hydride precipitation sites at slow cooling conditions. At high temperatures, hydrogen diffusion occurs mainly via the standard entropy-driven diffusion to produce a uniform interstitial hydrogen distribution in the Zr lattice. As temperatures decrease slowly, hydrogen may begin to locally diffuse towards favourable intragranular defects such as SPPs and GBs that provide favourable conditions for heterogeneous micro-hydride nucleation. As micro-hydrides nucleate at the favourable local stress raisers, they create more favourable conditions for micro-hydride stacking that yields macro-hydrides, which were quantified in this study. Chapter 5 shows that intergranular macro-hydride precipitation may be more favourable than intragranular one, although the scatter in data may mask any clear conclusion specially in microstructures containing a high GB and SPP density such as Zr-4. However, intra-granular macro-hydride precipitation was found to be insignificantly higher in Zr-4, in both as-received and large grain sizes, when compared to commercially pure Zr with a lower SPP content. The latter finding shows that SPPs may change the hydride nucleation sites potency considering that the cooling rate is kept constant between the two materials, although the scatter in data hinders any clear effect of SPPs on intragranular hydrides. The formation of hydrides at favourable nucleation sites is linked to the slow cooling rate following the hydrogen homogenisation treatment, which allows hydrogen diffusion to remain fast for a longer period of time before hydrogen is trapped at nucleation sites [146]. This ensures that the hydride distribution pattern has sufficient time to attain the most optimal free energy configuration, which is reflected in the activation of the GB nucleation sites that are most energetically favourable [40]. The formation of hydrides at faster cooling rates (air cooling) was found by Birch et al. to produce more intra-granular hydrides, which is likely due the relative tendency for hydrogen to diffuse towards existing hydride structures and promote hydride growth or nucleating on less favourable sites [149]. Chapter 5 also showed that not all GBs are favourable sites for hydride precipitation, an observation attributed to the different energy at GBs between grains of different crystallographic orientations; in as-received Zr-4 microstructures, the intergranular hydride percentage was found to be 40% higher than in blocky-α microstructures. This was related in Chapter 5 to the low grain boundary density, but it is also worth mentioning that blocky-α microstructures are fully recrystallised and textureless therefore have a different average grain boundary misorientation angle than as-received specimens

which may cause a second order effect [12, 64]. This means that texture may also have an effect on the low intergranular precipitation percentage but more importantly shows that GBs themselves can also have a hierarchy for hydride precipitation (which can also be applied to DHC models) which is caused by both crystallography and misorientaion of grains. This agrees with previous research by Qin et al. which suggests that GBs that have hydride precipitates are most likely crystallographically well aligned and optimally-misorientated for hydride precipitation [178]. Qin et al. suggests that the combined effects of GB structure and grain orientation simultaneously govern hydride formation at GB, a viewpoint which was supported experimentally by an EBSD study that evidently showed hydrides preferring GBs lying close to the basal plane of one bounding Zr grain and having a high energy due to high misorientation between adjacent grains [178].

Finally, results from Chapter 5 highlight the effect of SPPs on hydride precipitation distribution when the GB density of Zr-4 and Zr-702 was decreased. Results from large grained blocky-α Zr specimens ($>$ 300 µm) showed that SPPs may become more favourable as hydride precipitation sites, although due to a scatter in the data, a conclusive understanding of the effect of SPPs on intragranular hydrides cannot be drawn. It is worth noting here that Zr-702 has a percentage of Hf (0.97 wt.%) present in the solid solution which makes its chemistry slightly different to Zr-4 and because it has little Sn content (0.15 wt.% in Zr-702 vs 1.51 wt.% in Zr-4), it makes it much less hard than Zr-4. The difference in solid solution strengtheners content may cause the thermodynamic driving force required for nucleation of hydrides to be greater for a harder matrix. A larger temperature drop will be required to develop the driving force required for nucleation and so in a harder lattice hydride nucleation should occur at a lower temperature. At lower temperature, diffusion is slower and more hydrides will form inside the grains because the distances that hydrogen can diffuse will be smaller. This therefore implies that more intra-granular hydride precipitates might be trapped inside grains of a harder Zr lattice. However, hardness results in Figure 5.15 disagree with this argument; hardness results show that the VHN for as-received and blocky-α Zr-4 and Zr-702 is not distinct. In addition, Breen et al. [183] has shown that Sn forms cluster or regions of high concentration between inter-granular deuterides and the α-Zr reaction front which may show that deuteride growth rate is controlled by the partition of Sn to the α-Zr matrix. This suggests that Sn in Zr-4 has the higher destabilizing effect than all other alloying additions on hydride phases and that Sn is relatively more stable in pure Zr than in any zirconium hydride, as shown by a recent density functional theory study by Christensen et al. [184]. In Zr-4 the Sn content of 1.51 wt.% will therefore act to make hydride precipitation more sluggish rather than

provide a nucleation site for precipitation as Fe and Cr particles do [16]. Sn is in the solid solution of the α-Zr matrix, meaning that it will not likely have an effect of hydrogen diffusion, other that having a binding effect on hydrogen in solution, unlike SPPs that may act as localised stress-raising features for hydrogen to diffuse towards [16].

8.2 Hydride Precipitation Sites in Loaded Zr-4

Previous studies have shown that the potency of hydride precipitation sites are influenced by an externally applied stress [169, 178]. Chapter 6, shows that a hydrostatic stress gradient produced by long range SCFs in the form of 'V' and 'U' notches, reduces the hydride number density in the less tensile bulk, and increases it in the high tensile notch tip region, although scatter in the data may mask any clear trend. The increase in hydride number density near the notches in blocky-α Zr-4, was however found to be lower than that in as-received Zr-4 specimens. The latter also produced some degree of hydride reorientation near both the 'V' and the 'U' notch tips while it is difficult to get reorientation in the former. The more interesting results however, correspond to how the distribution of the microstructural hydride precipitation sites changes after hydrogen influx occurs at the stressed notch tip regions. Firstly considering the hydrogen influx towards notches at K= 8 MPa$\sqrt{m}$ in as-received Zr-4; in these highly textured samples, the hydride number density near 'V' notches, was found to be higher than that around 'U' notched ones. This is attributed to the larger peak hydrostatic stress produced by the 'V' notches (200 MPa), that seem to produce a stress gradient which activates more microstructural precipitation sites in the notch tip region. Considering now blocky-α grain structures; the hydride number density may be higher around 'U' notches, which may suggest that the area of the hydrostatic stress field (which is larger around 'U' notches) has a greater effect on the activation of hydride precipitation sites than the peak stress (in these textureless and soft microstructures) as the peak hydrostatic stress attained was ~90 MPa lower than at 'V' notch-tips at same external load. Although the scatter in data may hinder any clear trend in hydride distribution at both notch geometries. The possible formation of plasticity may also add some degree of complexity to the problem in blocky-α grains near 'V' notch tips, even under notionally elastic loading regimes, which limits the hydrostatic stress gradient, resulting in an insignificantly lower hydride number density. The plastic zone and the maximum effective plastic strain in blocky-α grains was found in Chapter 7 using a CPFE model to be highly dependent on the crystallography of the notch tip grain. Plasticity was found to have a higher effect on hydrostatic stress (σ_{hyd}) and hydrogen concentration (C_H) in hard

mono crystals that show a depletion in σ_{hyd} and C_H ahead of 'V' and 'U' notch geometries indicated by arrows shown in Figures 7.9(b) and 7.9(c). At the 'V' notch tips on the prismatic plane, σ_{hyd} reduces to zero while at 'U' notch tips σ_{hyd} was reduced to a smaller degree, but over a larger plastic zone. C_H showed a similar depletion behaviour to σ_{hyd} in both notch geometries, which is a result of the different levels and constraint of plasticity. The effect of plasticity on σ_{hyd} and C_H was found to be negligible at notch tips of soft grains highlighting the importance of the notch-tip blocky-α grain crystal orientation on hydrogen diffusion and hydride precipitation.

In the context of hydride-induced failures and starting with Zr fuel cladding, the hydride precipitation and reorientation processes studied in this project highlight importance of microstructural features in such components. Hydride precipitation and reorientation from the circumferential to the radial direction is known to be detrimental to the structural integrity of the Zr fuel cladding components that happens after several thermomechanical cycles [40, 169, 185]. Considering that tests reported in this thesis were all carried out using three thermomechanical cycles that are arguably not representative compared to ones in reactor operation [5], discussions that relate to hydride reorientation may still be drawn out. Firstly, intergranular hydride precipitation sites that are more potent than intragranular ones in unloaded as-received grain sizes are also known to be more prone to cracking than the latter [178]. Intergranular hydrides have a higher tendency to cracking because the slip system of the intergranular hydrides and the adjacent grains do not coincide; this situation induces higher stress and incompatible strain into intergranular hydrides [150, 178]. Although results from Chapter 6 show that after 3 thermomechanical cycles intragranular precipitation percentage increases around SCFs, the trend may be expected to change when the number of thermomechanical cycles increase further, due to a potential increase in hydride precipitation at unfavourable GB sites after all intragranular ones are occupied [30]. This means that in Zr cladding components, significant hydride reorientation, after several thermomechanical cycles, from the circumferential to the radial direction near highly tensile stress regions, happens when circumferential hydrides deplete and radial intergranular ones start to increase in fraction.

8.3 Microstructural Incorporation in Hydrogen Models

Chapters 5 and 6 show experimentally that hydride precipitation is affected by microstructural features such as SPPs and GBs in loaded and unloaded microstructures, and therefore their effect on hydrogen diffusion and hydride precipitation should be considered in current engineering models [6].

As an attempt to incorporate microstructure in a hydrogen diffusion model, Chapter 7 puts forward a methodology using a simple FEM model of a notched bar in bending coupled with DFT derived parameters for the dipole tensor of H in Zr, to account for the HCP hydrogen diffusion anisotropy [30, 132, 197]. This methodology is the very early stage of incorporating microstructural effects, which starts by the fundamental effect of crystallography on hydrogen diffusion, showed that the steady-state notch-tip hydrogen concentrations are affected by atomic scale anisotropy, an effect that is not present in traditional isotropic analyses. The methodology was also trialled in a separate polycrystalline CPFE model in Chapter 7 Part II which proved its feasibility. Chapter 7 Part II further demonstrates the importance of incorporating the HCP anisotropy in a hydrogen diffusion model by comparing notch tip hydrogen distribution profiles with experimental results from a blocky-α specimen. The comparison shows that there is a good agreement between the polycrystalline CPFE model simulations and the experimental blocky-α micrograph, where hydride precipitates can be seen at GBs of large hydrostatic stress from the model and vice versa as shown by arrows and the highlighted GB in Figure 7.14.

Finally, the depletion of the equilibrium hydrogen concentration observed using CPFE model, in monocrystals and polycrystals at notch tips, has been experimentally observed in as-received Zr-2 samples and reported in literature by Schofield et al. [5]. Schofield tested irradiated textureless Zircaloy-2 “V” notch specimens containing electron beam welds, that were loaded in four-point bending at temperatures between 290°C and 60°C. Results show that after 10 thermal ratcheting cycles, extensive hydride reorientation was observed throughout the tensile region. The formation of a well-defined hydride depletion zone or denuded zone was also observed in all Schofield’s tests. CPFE methodology and simulation results presented in Chapter 7, may provide a mechanistic reasoning for this phenomenon. The denuded zone phenomenon, observed in polycrystalline simulations, is presented in Figures 7.12 and 7.13; a similar effect of plastic strain on the depletion of notch tip hydrostatic stress and hydrogen concentration can be seen in Figures 7.12 7.13(f) and (h).

Chapter 9

Overall Conclusions and Future Work

The project provides a better understanding of the hydride precipitation behaviour in Zr-4 compared to commercially pure zirconium containing as-received and blocky-α microstructures. Hydride distribution and reorientation at stress concentration features in zirconium alloys is not yet fully understood especially in soft blocky-α microstructures. The development of an improved understanding of hydride precipitation at the micro-scale helps to improve the understanding of hydride reorientation and DHC initiation by relating in a quantitative manner, microstructural hydride precipitation sites such as SPPs and grain boundaries to various thermo-mechanical loading parameters. In addition, this project provides a simple framework that introduces a method of incorporating microstructural effects in a numerical model which was also put to test in a CPFE model that proved its feasibility. The following conclusions can be drawn from the work:

1. Hydrides were found to precipitate at and around SPPs in both Zr-4 and Zr-702 as-received and blocky-α microstructures using BS SEM + EDX imaging.

2. A clear trend in the effect of SPPs on intra-granular macro-hydride precipitation in Zr-4 and Zr-702, the latter with less SPP content that the former, cannot be found in both alloys.

3. Reorientation of hydrides in loaded and as-received specimens was observed at K= 8 MPa$\sqrt{}$m and was found to be more prominent around 'V' notches, that produce a larger hydrostatic stress gradients, shown by the number density of hydrides that was higher relative to 'U' notch specimens.

4. Blocky-α Zircaloy-4 specimens showed no hydride reorientation or stress contour hydride precipitation at all stress intensity factors of 2-8 MPa$\sqrt{}$m. This is probably due to the relatively low

yield stress (60% lower yield than in as-received Zr-4) that limits the formation of a hydrostatic tensile stress gradient in the blocky-α soft microstructures.

5. The continuum scale FE model for hydrogen stress-diffusion analysis in Zr can be generalised to incorporate the effects of anisotropy at the atomistic scale. Using the elastic dipole tensor of hydrogen interstitials in α-zirconium, the notch-tip hydrogen enhancement was found to be affected by crystal orientation.

6. The equilibrium hydrogen distribution, at the load-up stage of the experimental thermomechanical cycle, was found to be effected by the crystallography of notch-tip mono and polycrystals using a CPFE model. The model also predicts that plasticity generated during the load-up stage to $K=$ 8 MPa$\sqrt{}$m of 67 MPa nominal stress at 468 K, causes a lowering of notch tip σ_{hyd} and therefore depletion of hydrogen concentration. This phenomenon has been observed in experimental studies from literature and is known to cause a hydride denuded region.

9.1 Future Work

9.1.1 Quantification of Hydride Precipitation Sites

Future experiments may include:

- Perform tests on two sets of the same base alloy (Zr-4 or Zr-702) but change the yield stress/hardness (by increasing oxygen content) of one set to study the extent of the thermodynamic driving force that is required for nucleating hydrides.

- Perform studies and tests on SPP redistribution due to irradiation, which has not been thoroughly explored yet in literature, to study the effects of SPP number density and size distribution on hydride precipitation in one as-received Zr base alloy.

9.1.2 Hydride Precipitation Sites in Thermomechanically Cycled Zr-4 Specimens

- Study the effects of microstructure on hydride precipitation due to temperature gradient-driven diffusion of hydrogen as opposed to stress-driven hydrogen diffusion. This can be done on as-received and blocky-α samples with temperature gradients to further our understanding of favourable microstructural hydride nucleation sites.

- Study the effects of thermal creep on hydride reorientation and redistribution at a SCF after stress relaxation. This testing, performed at very long high temperature stress hold, can also be performed on Zr-4 specimens with different grain sizes and different notch acuities for different extent of stress relaxation.
- Use techniques such as high-resolution EBSD to identify and quantify hydride precipitates after thermo-mechanical cycling at GBs, inside the grains or both.
- Study hydride precipitation and reorientation after thermomechanical cycling in samples containing welds that produce three distinct microstructural regions (as-received, heat effected and weld pool) in one specimen.

9.1.3 Hydrogen Stress Driven Diffusion Modelling Incorperating Microstructural hcp Anisotropy

9.1.3.1 Part I

- Extend model to 3D to study the hydrogen diffusion through the thickness from different crystallographic planes.
- Extend to hydride precipitation at regions of high hydrogen concentrations or once the terminal solid solubility for hydride precipitation is reached.

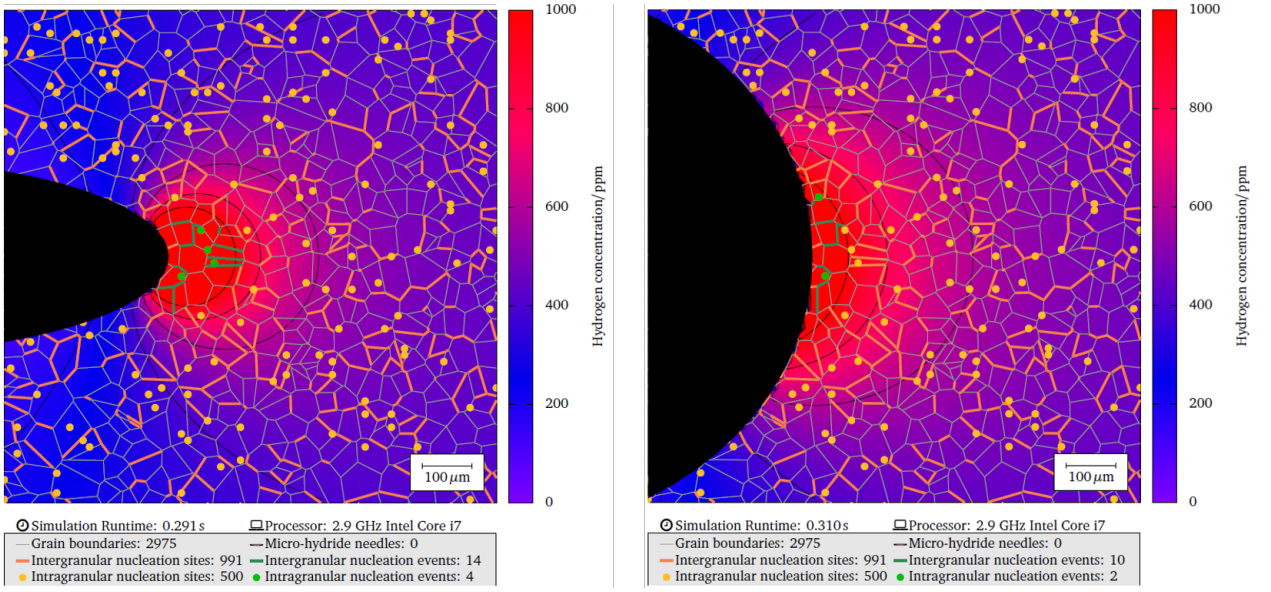
9.1.3.2 Part II

- Account for intragranular hydride precipitation heterogeneity using ρ_{SPP} and A_{SPP} data from Chapters 4 and 5. The CPFE model would then be able to predict the wosrt case microstructure for DHC. Localised intragranular stress raisers such as SPPs can be incorporated with a quantified stress field in the model via parameters derived from discreet dislocation plasticity methods [16].

Analytical models should aim to classify hydride precipitation sites according to a hierarchy of potency. A set of microstructural qualities and quantities, that can be used in future models to achieve a hierarchy of potency in microstructural sites, is given here: Firstly, in unloaded as-received grain size specimens, the most favourable GBs that are crystallographically well aligned for hydride precipitation are parallel to the basal plane of one bounding Zr grain and have high energy due to grain misorientation [178]. Intergranular hydride number density was quantified in Chapter 5 after furnace cooling to be 2.06 $\mathrm{mm}^{-2}.\mathrm{wppm}^{-1}$ (55% of ρ_{hydride} in as-received Zr-4), 22% higher than

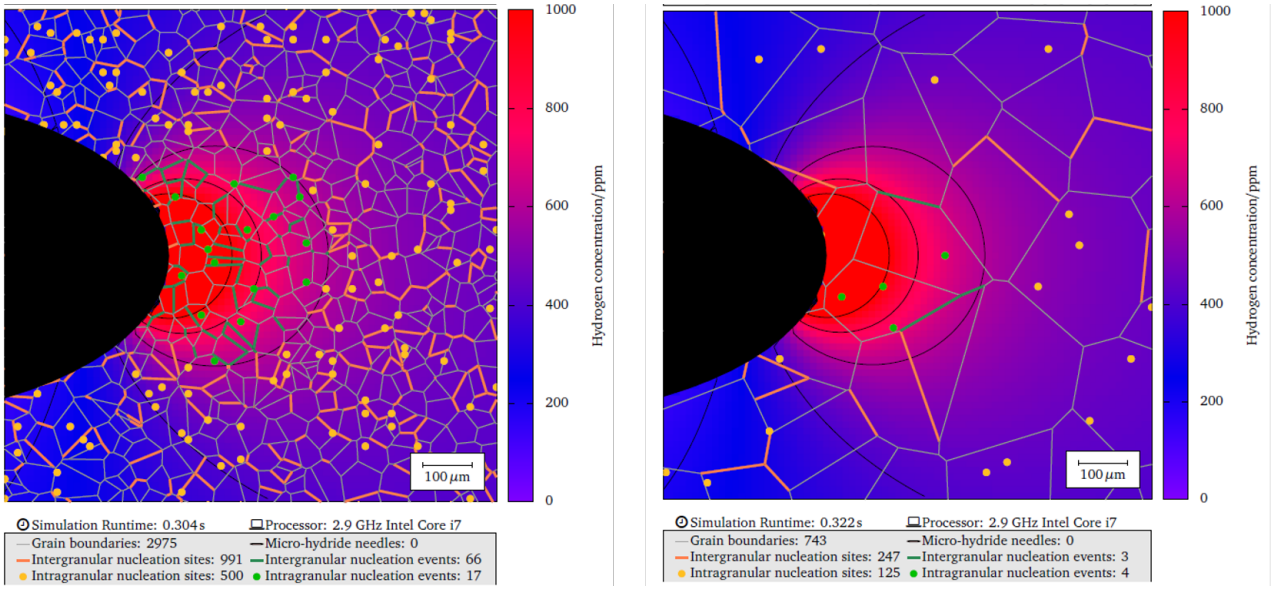
at intragranular sites. Such aforementioned values can be explicitly added to analytical models to represent as-received well crystallographically-aligned GBs with high energy for hydride precipitation. Hydride precipitation at intragranular sites such as SPPs can be considered to be the second favourable precipitation sites and can be represented using the 1.68 $mm^{-2}.wppm^{-1}$ parameter. This means that models simulating 1 mm × 1 mm maps with as-received grain size (15 µm) can explicitly add one intragranular nucleation site in every 8-9 grains assuming a bulk concentration of 100 wppm. As grain size increase the percentage of intra/intergranular precipitation changes, which can be adjusted in a model accordingly using quantities in Figure 5.17. In the presence of an applied load, the distribution of hydride precipitation changes. The GB alignment with respect to the applied load comes into play to either reduce or increase the favourability of GB precipitation; grain boundary planes that are perpendicular to the applied load direction are most favourable [7]. These GBs in as-received Zr-4 near SCFs can be represented in a model using the 2.67 $mm^{-2}.wppm^{-1}$ parameter, which is an average for 'V' and 'U' notch geometries loaded at 8 $MPa\sqrt{m}$. Intragranular sites are also effected near a SCF; intragranular hydrides can be expected to increase in number density after 3 thermomechanical cycles at tensile stress regions and their sites can be computationally represented inside grains using the 2.78 $mm^{-2}.wppm^{-1}$ parameter. Again, as grain size and load intensity change these parameters change as shown in Table 6.1, Figure 6.16 and Figure 6.12.

Considering the effects of notch acuity on microstructural nucleation site activation, analytical models can also use parameters in Table 6.1 to account for the change in inter/intragranular hydride precipitation for a constant applied load, grain size and hydrogen concentration, but at different notch geometries. Figure 9.1 shows an example of simulated micrographs by Patel et al. that are currently qualitatively informed by experimental findings from this project, but are yet to be quantitatively parameterised. Patel's analytical+numerical model [30] alters the number of activated intra/intergranular hydride nucleation sites as the notch acuity changes. In Figure 9.1(a) a 'V' notch geometry produces a larger peak tensile stress over a smaller zone near the tip than the 'U' notch geometry shown in the map in Figure 9.1(b), and in turn more intra/intergranular sites are activated over a smaller region. Finally considering the effects of grain boundary density, simulations by Patel et al. can also use parameters from Table 6.1 to model the effects of grain size on hydride precipitation for the a constant applied load, hydrogen concentration and notch acuity. Figure 9.2 shows simulated micrographs where the grain size is changed from 50 to 200 µm in Figures 9.2(a) and (b) respectively. Simulations that are qualitatively informed by experiments in this project, show that as grain size increases, intragranular precipitation also increase due to mainly a reduction in GB density.



(a) (b)

Figure 9.1: Simulated micrographs of the notch-tip hydrogen profile as a function of the notch acuity. (a) corresponds to a 'V' notch geometry and (b) 'U' notch one [30].



(a) (b)

Figure 9.2: Simulated micrographs of notch-tip hydrogen profiles as a function grain size. (a) l_G= 50 µm and (b) l_G= 200 µm [30].

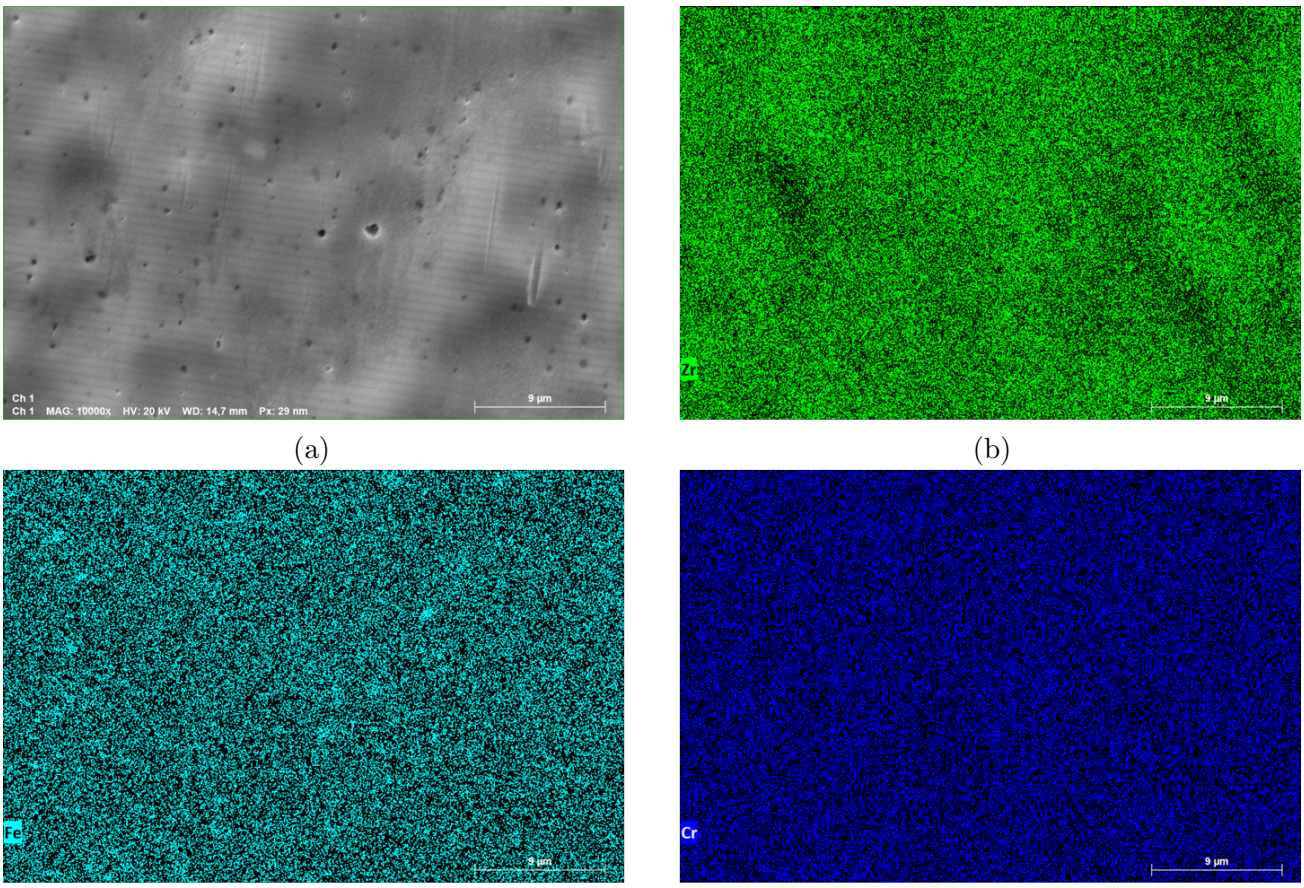
Developing microstructurally-sensitive models similar to the numerical model in this project, should pave the way towards producing more realistic engineering DHC models with high computational efficiency. An analytical model that is currently in development by Patel et al. [30] is not only capable

of realistically predicting DHC initiation for safety assessments, but also capable of predicting the ideal microstructures required to minimise unfavourable hydride precipitation especially in untextured Zr components.

Chapter 10

Appendix A

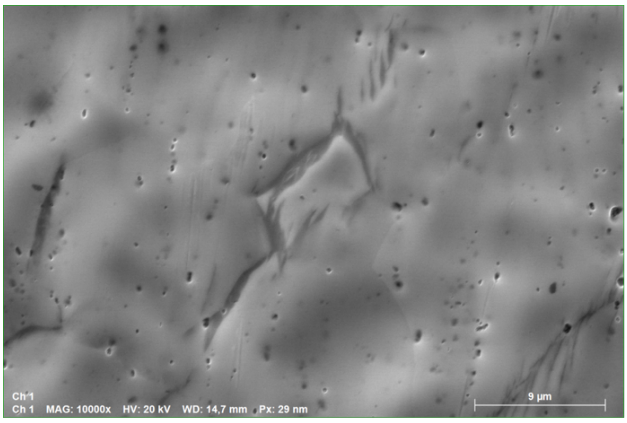
10.1 Hydride Precipitation near Second Phase Particles; SEM + EDX analysis



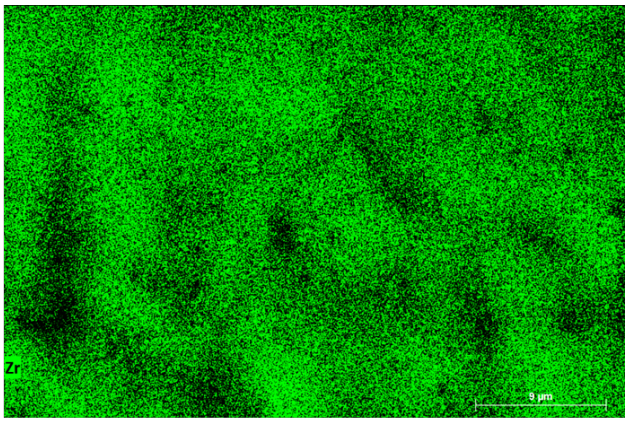
(a) (b)

(c) (d)

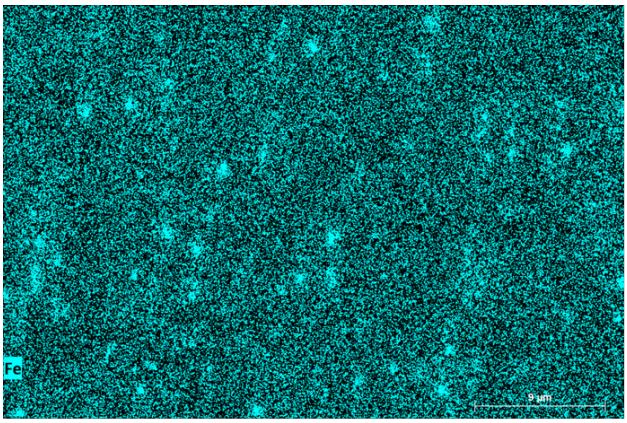
Figure 10.1: SPPs in as-received Zr-4 (a) with EDX analysis of Zr (b), Fe(c) and Cr (d).



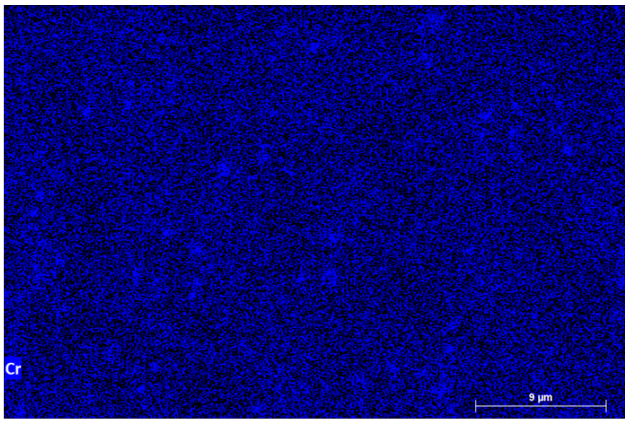
(a)



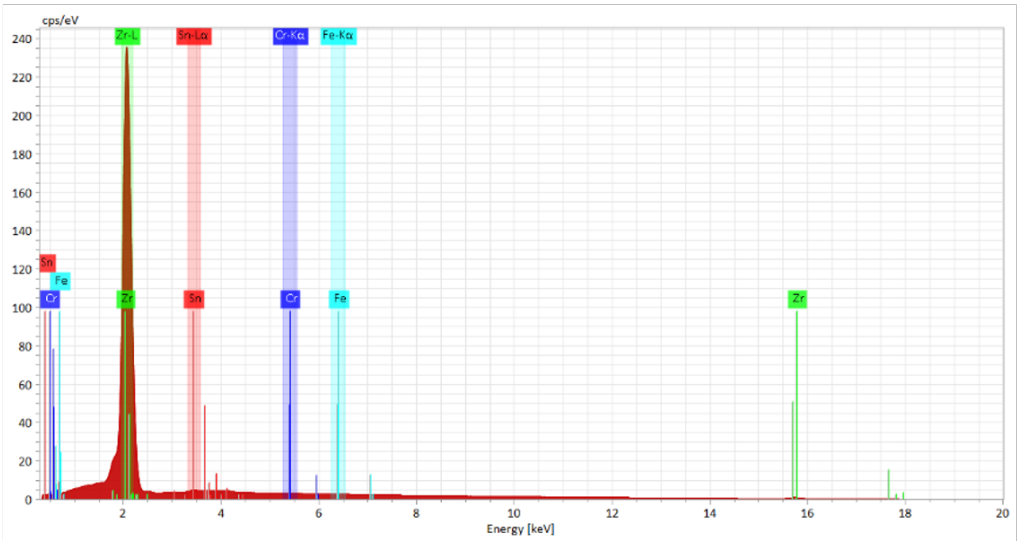
(b)



(c)

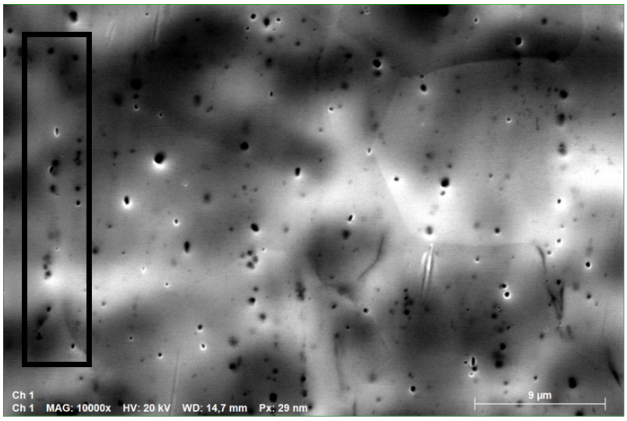


(d)

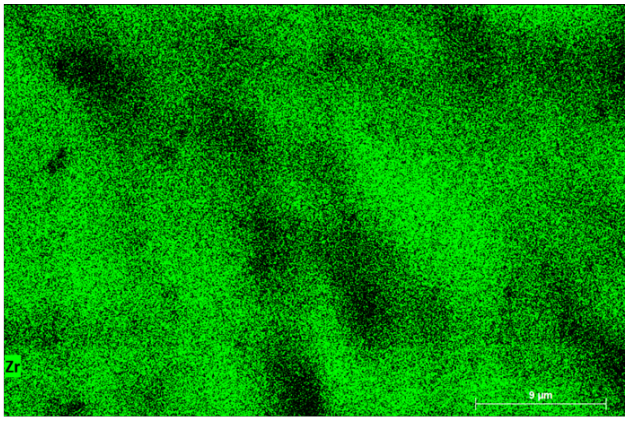


(e)

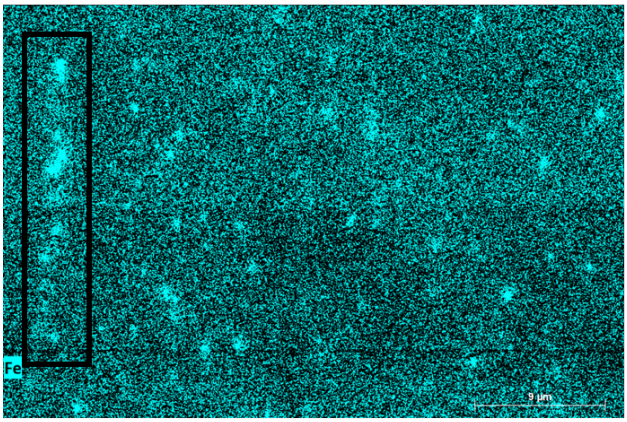
Figure 10.2: SPPs in hydrided as-received Zr-4 (a) with EDX analysis of Zr (b), Fe(c) and Cr (d) with its corresponding spectrum.



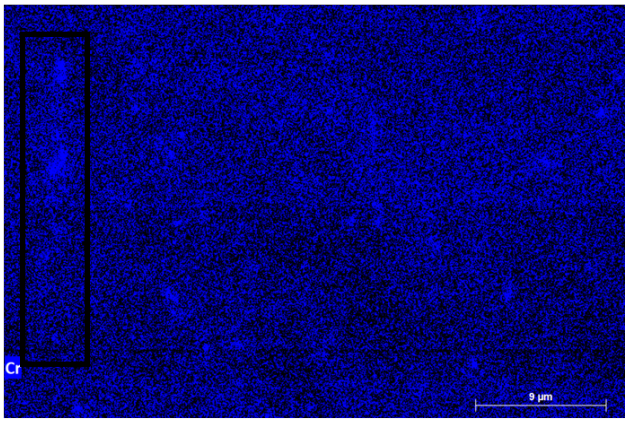
(a)



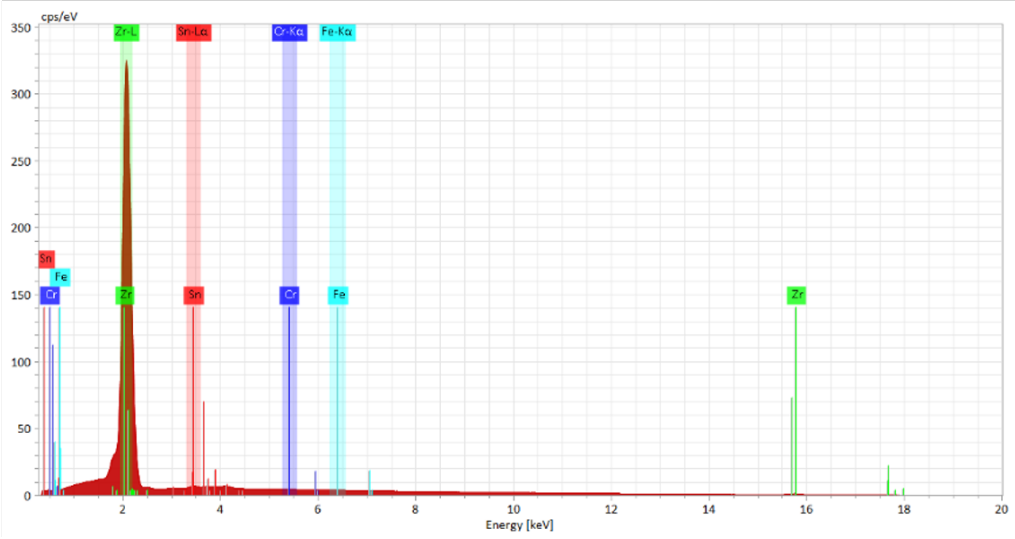
(b)



(c)

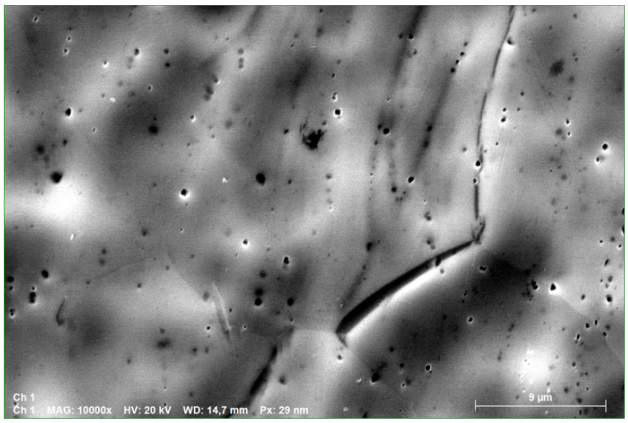


(d)

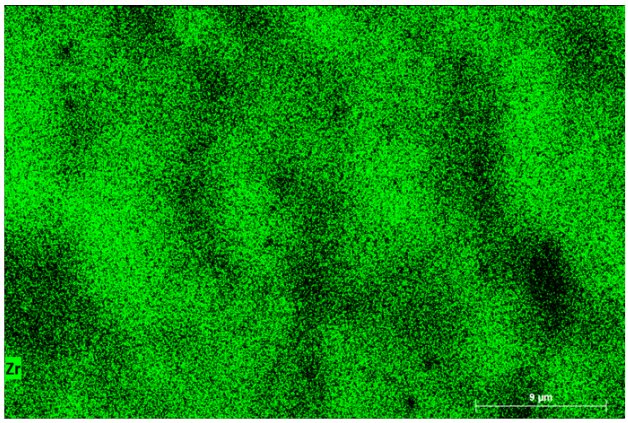


(e)

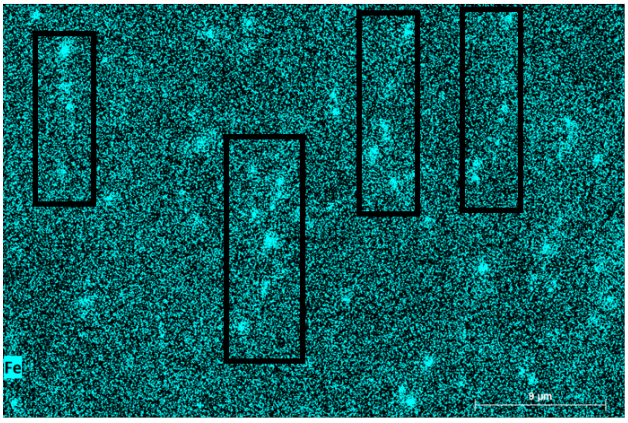
Figure 10.3: SPPs in as-received Zr-4 highlighting a vertical SPP precipitation RD pattern (a) with EDX analysis of Zr (b), Fe(c) and Cr (d) with its corresponding spectrum.



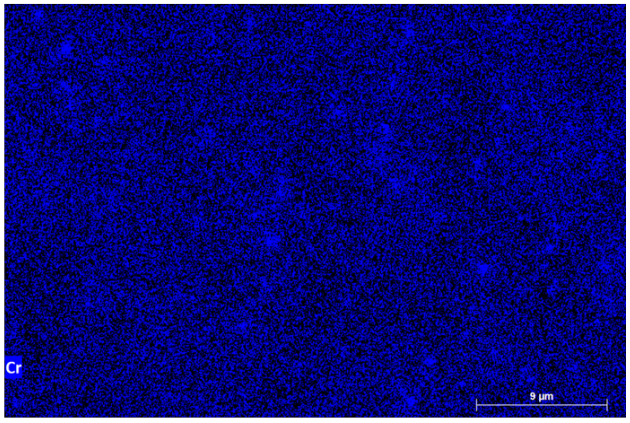
(a)



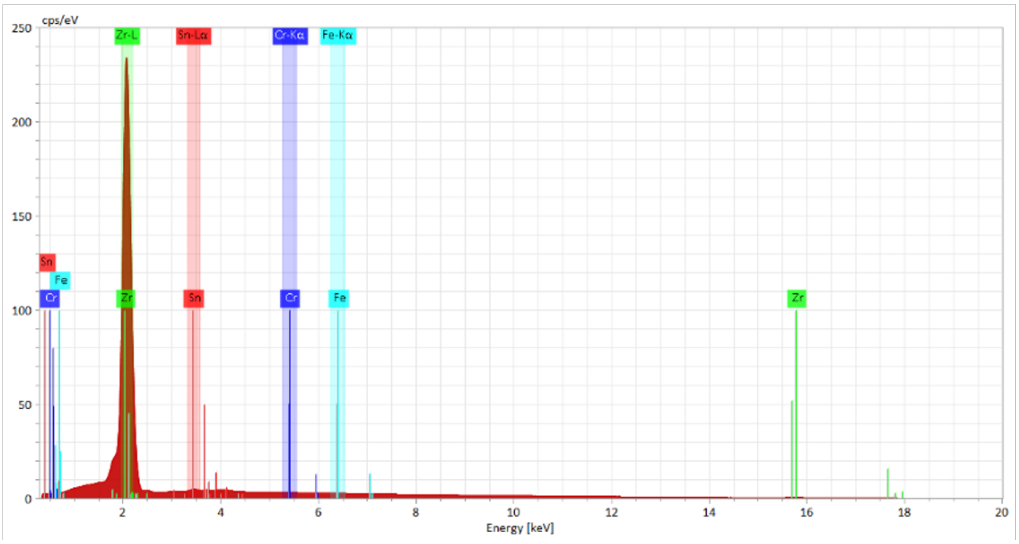
(b)



(c)

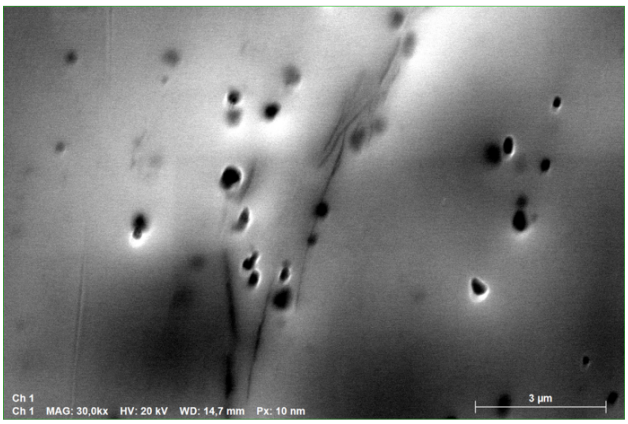


(d)

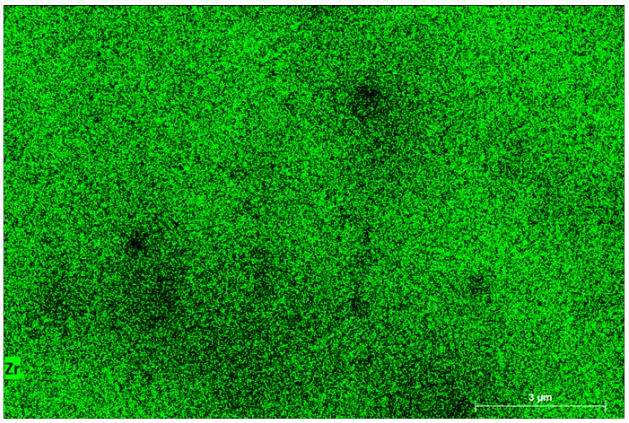


(e)

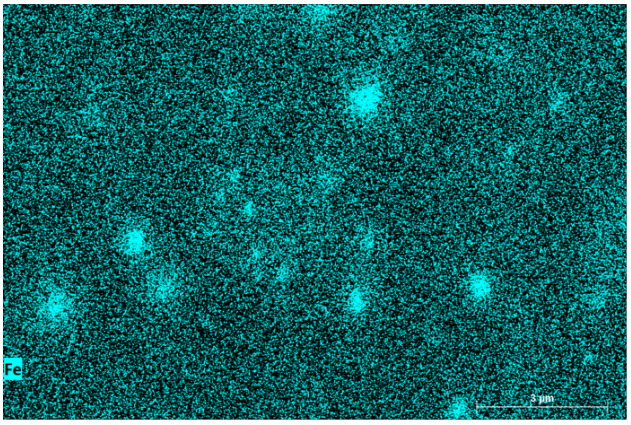
Figure 10.4: SPPs in hydrided as-received Zr-4 highlighting several vertical SPP precipitation RD pattern (a) with EDX analysis of Zr (b), Fe(c) and Cr (d) with its corresponding spectrum.



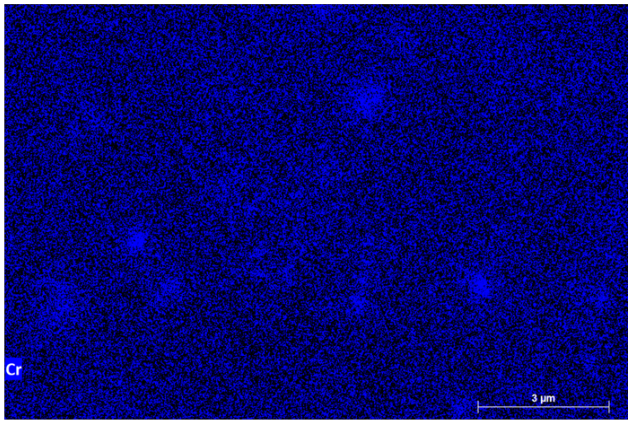
(a)



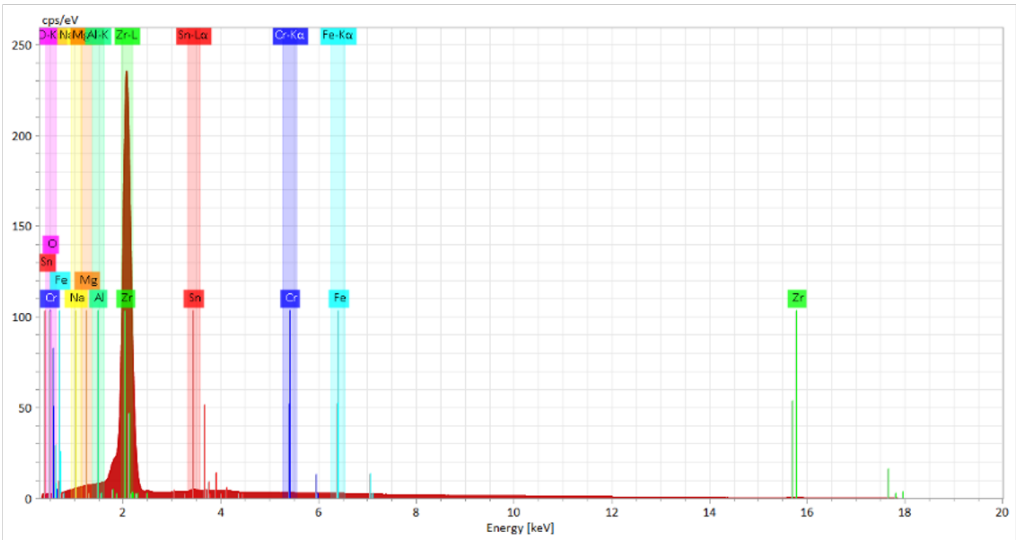
(b)



(c)

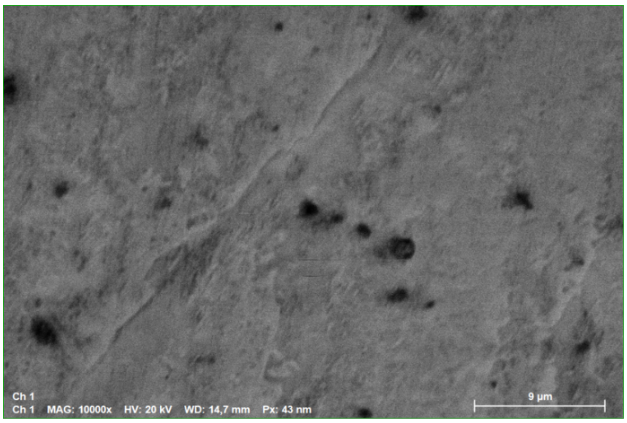


(d)

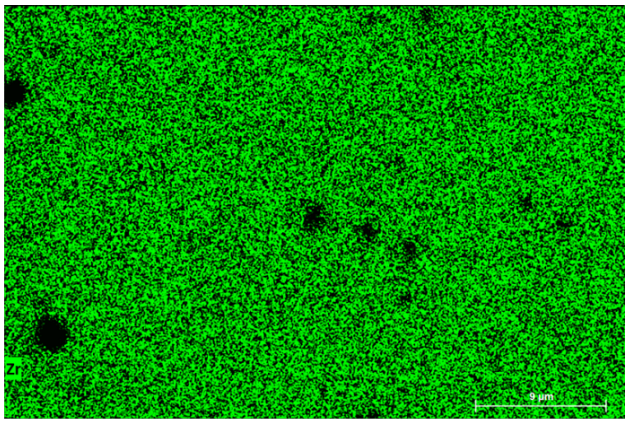


(e)

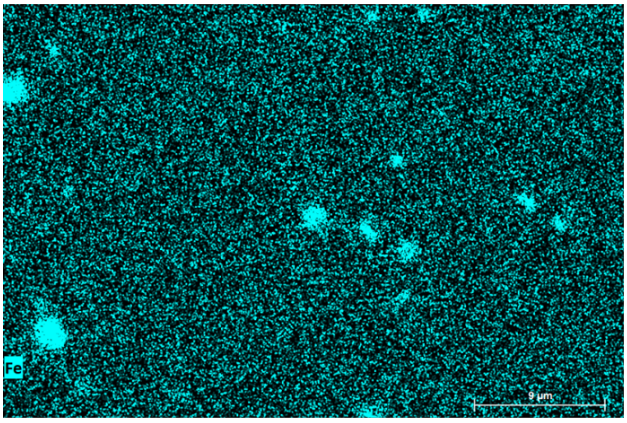
Figure 10.5: SPPs in blocky-α Zr-4 highlighting micro-hydride precipitation near SPPs (a) with EDX analysis of Zr (b), Fe(c) and Cr (d) with its corresponding spectrum.



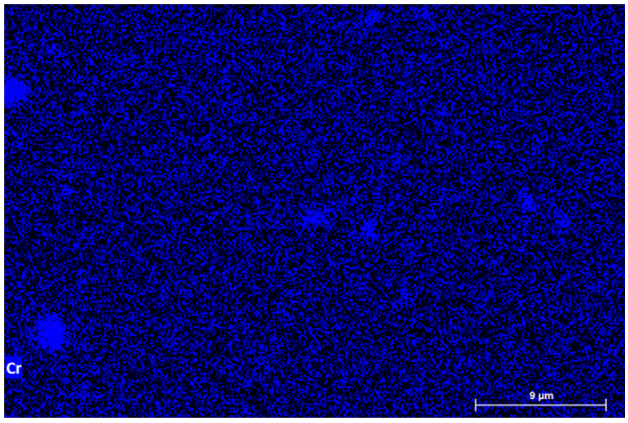
(a)



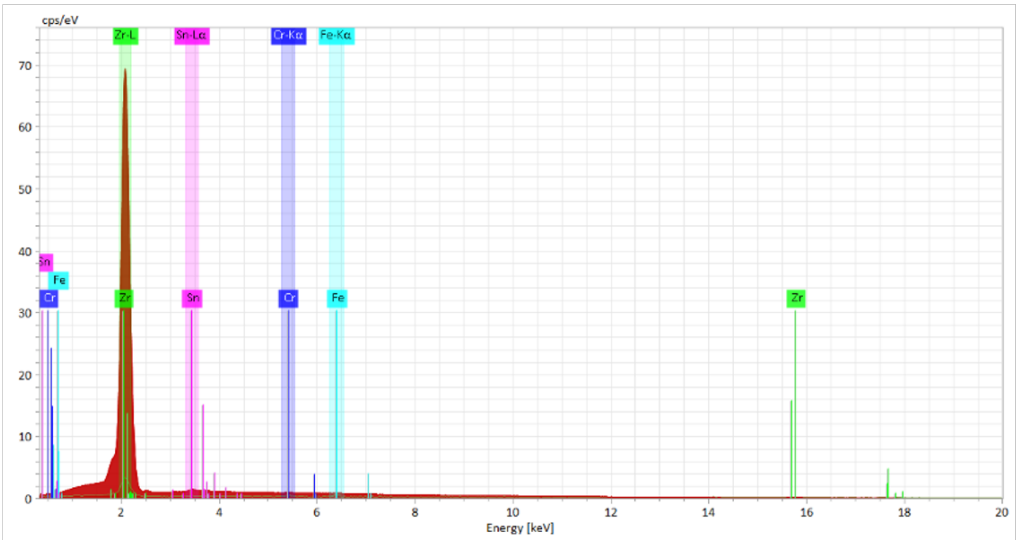
(b)



(c)

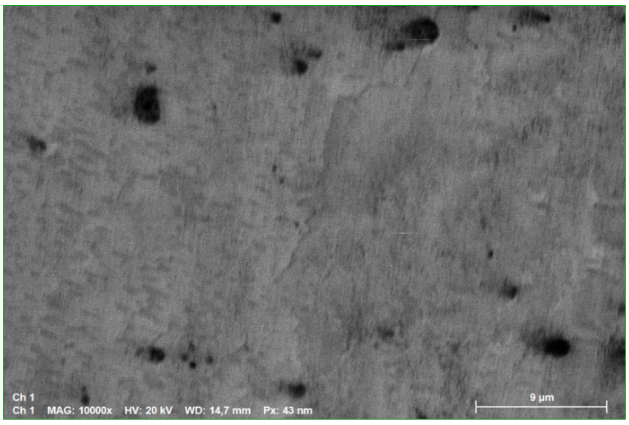


(d)

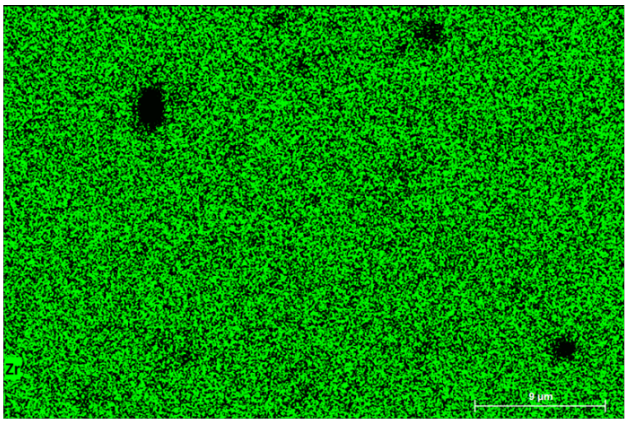


(e)

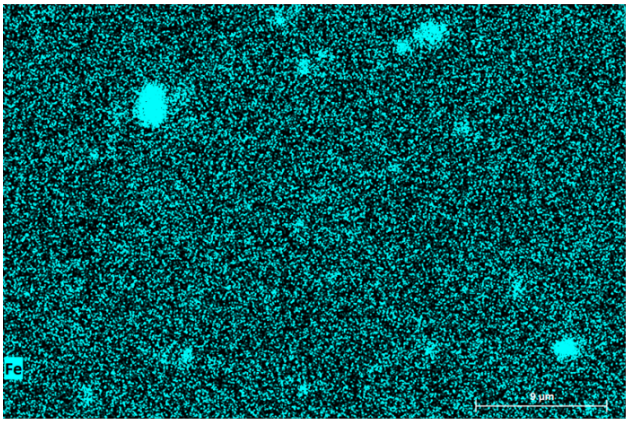
Figure 10.6: SPPs in hydrided blocky-α Zr-4 highlighting micro-hydride precipitation near SPPs (a) with EDX analysis of Zr (b), Fe(c) and Cr (d) with its corresponding spectrum.



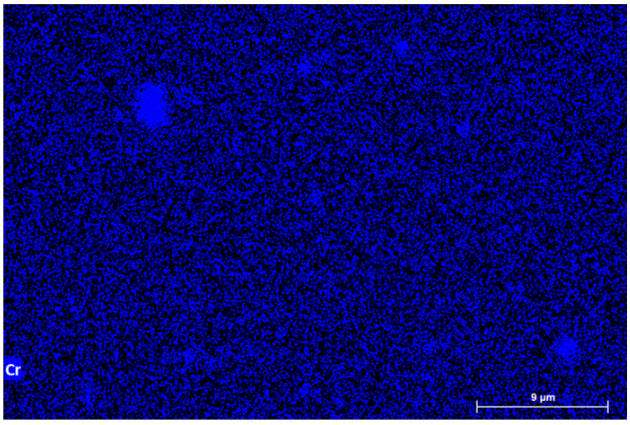
(a)



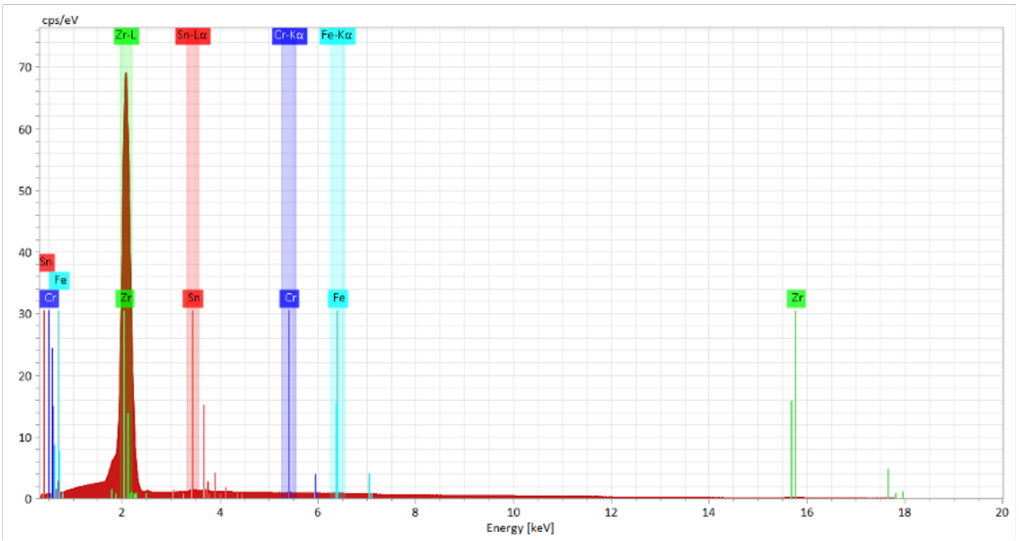
(b)



(c)

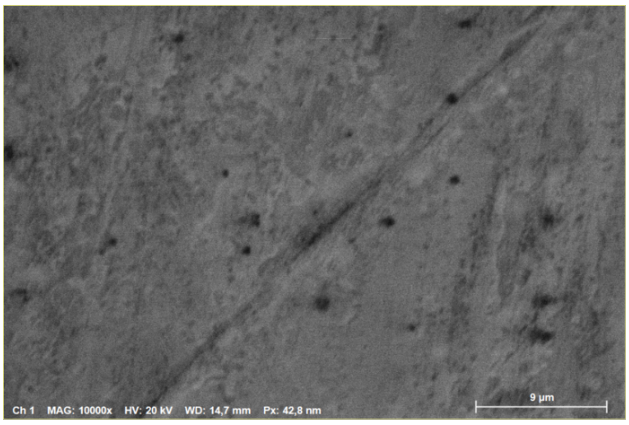


(d)

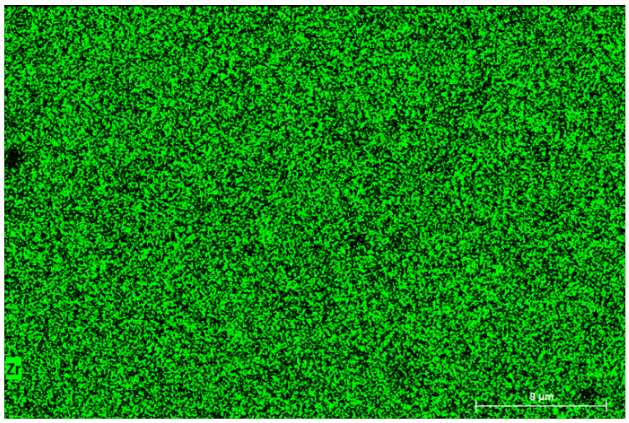


(e)

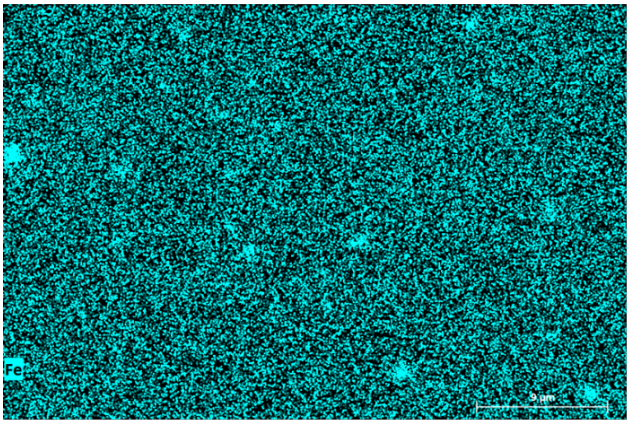
Figure 10.7: SPPs in blocky-α Zr-4 highlighting micro-hydride precipitation near SPPs (a) with EDX analysis of Zr (b), Fe(c) and Cr (d) with its corresponding spectrum.



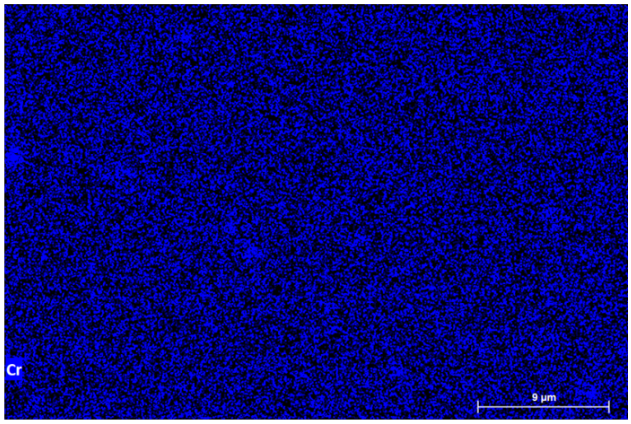
(a)



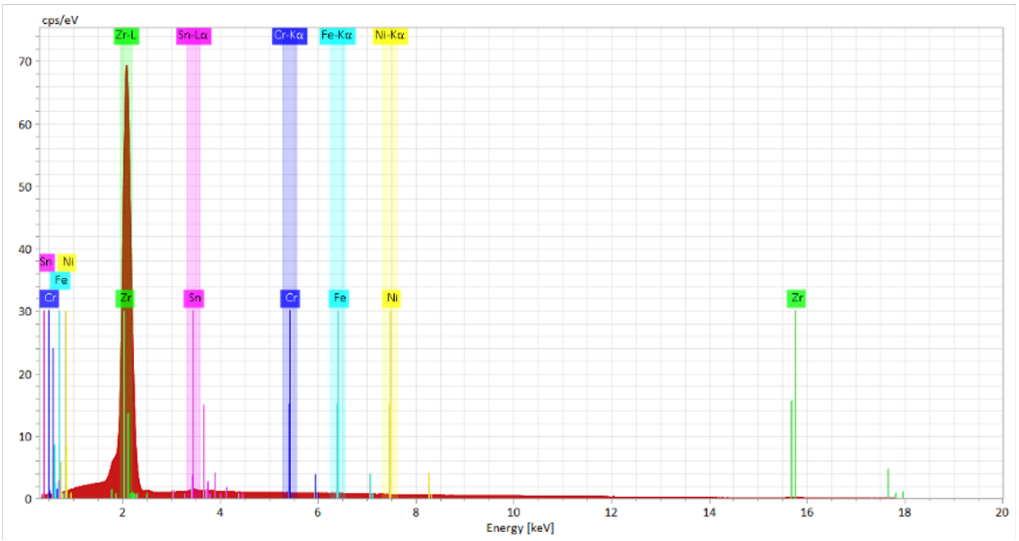
(b)



(c)

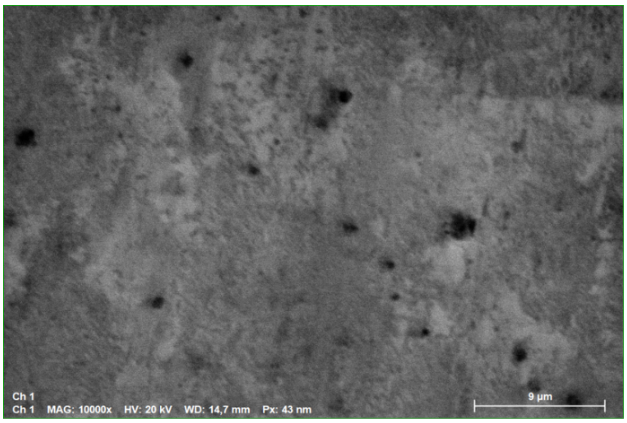


(d)

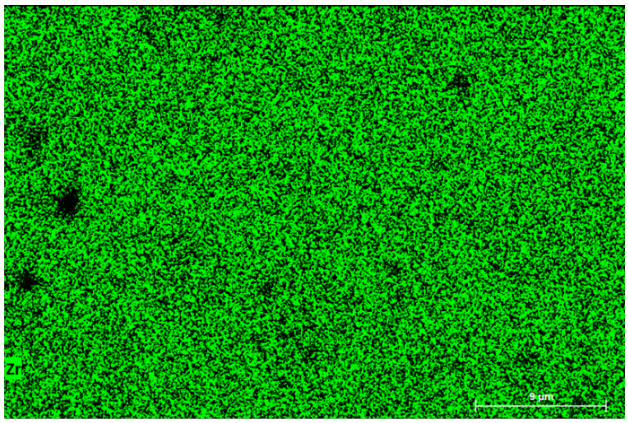


(e)

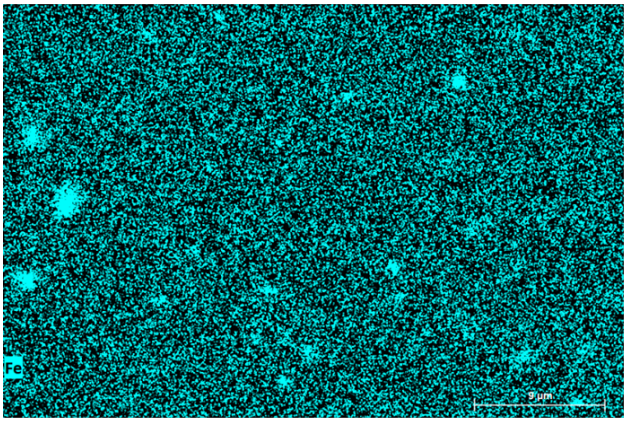
Figure 10.8: SPPs in hydrided blocky-α Zr-702 highlighting micro-hydride precipitation near SPPs (a) with EDX analysis of Zr (b), Fe(c) and Cr (d) with its corresponding spectrum.



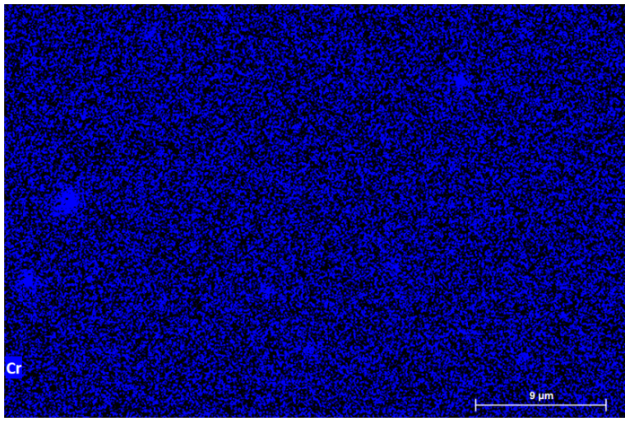
(a)



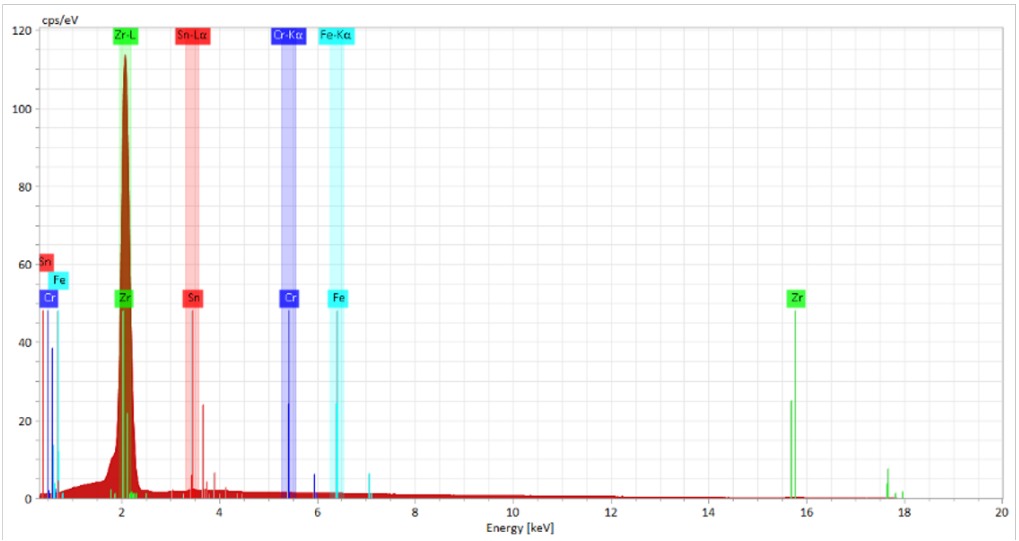
(b)



(c)



(d)



(e)

Figure 10.9: SPPs in blocky-α Zr-702 highlighting micro-hydride precipitation near SPPs (a) with EDX analysis of Zr (b), Fe(c) and Cr (d) with its corresponding spectrum.

10.2 Full Test Matrix

Table 10.1: Test matrix for specimens with C_H of ∼120 wppm, thermomechanically cycled 3 times.

Sample ID	K (MPa$\sqrt{m}$)	Grain Size (µm)	Notch Geometry
Zr-4_Textured_ar_1	8	15-20	V
Zr-4_Textured_ar_2	8	15-20	V
Zr-4_Textured_ar_3	8	15-20	U
Zr-4_Textured_ar_4	8	15-20	U
Zr-4_Rnd_1	8	500-600	V
Zr-4_Rnd_2	8	600-700	V
Zr-4_Rnd_3	8	800-900	V
Zr-4_Rnd_4	8	900-1000	V
Zr-4_Rnd_5	8	600-700	U
Zr-4_Rnd_6	8	600-700	U
Zr-4_Rnd_7	8	700-800	U
Zr-4_Rnd_8	8	900-1000	U

Table 10.2: Test matrix for specimens with C_H of ∼120 wppm, thermomechanically cycled 3 times. Specimens cycled at K= 2 where recycled at K= 4 and 6

Sample ID	K (MPa$\sqrt{m}$)	Grain Size (µm)	Notch Geometry
Zr-4_Textured_ar_k	2, 4, 6	15-20	V
Zr-4_Textured_ar_l	2, 4, 6	15-20	U
Zr-4_Rnd_m	2, 4, 6	700-800	V
Zr-4_Rnd_n	2, 4, 6	700-800	U

10.3 Fortran Codes Used For Atomistic to Continuum Scale Coupling

10.3.1 Anisotropic - Prismatic

```
SUBROUTINE USDFLD(FIELD,STATEV,PNEWDT,DIRECT,T,CELENT,
1 TIME,DTIME,CMNAME,ORNAME,NFIELD,NSTATV,NOEL,NPT,LAYER,
2 KSPT,KSTEP,KINC,NDI,NSHR,COORD,JMAC,JMATYP,MATLAYO,LACCFLA)
INCLUDE 'ABA_PARAM.INC'
CHARACTER*80 CMNAME,ORNAME
CHARACTER*3 FLGRAY(15)
DIMENSION FIELD(NFIELD),STATEV(NSTATV),DIRECT(3,3),
1 T(3,3),TIME(2)
DIMENSION ARRAY(15),JARRAY(15),JMAC(*),JMATYP(*),COORD(*)
REAL XC0, XROWX, XROWY, XKB, XT
REAL XEINT, XCONCN
XROWX = 1.74
XROWY = 2.36
XKB = 8.61733035E-5
XT = 673.15
XC0 = 130
STATEV(1) : CONCENTRATION
SUBROUTINE IS ONLY DEFINED FOR 2D
IF (TIME(2).LT.DTIME) RETURN
GET TOTAL STRAIN
CALL GETVRM('E',ARRAY,JARRAY,FLGRAY,JRCD,JMAC,JMATYP,MATLAYO,
1 LACCFLA)
EXX = ARRAY(1)
EYY = ARRAY(2)
XEINT = -(XROWX*EXX+XROWY*EYY)
XCONCN = XC0*EXP(-XEINT/(XKB*XT))
STATEV(1)= XCONCN
```

RETURN END

10.3.2 Anisotropic - Basal

SUBROUTINE USDFLD(FIELD,STATEV,PNEWDT,DIRECT,T,CELENT,

1 TIME,DTIME,CMNAME,ORNAME,NFIELD,NSTATV,NOEL,NPT,LAYER,

2 KSPT,KSTEP,KINC,NDI,NSHR,COORD,JMAC,JMATYP,MATLAYO,LACCFLA)

INCLUDE 'ABA_PARAM.INC'

CHARACTER*80 CMNAME,ORNAME

CHARACTER*3 FLGRAY(15)

DIMENSION FIELD(NFIELD),STATEV(NSTATV),DIRECT(3,3),

1 T(3,3),TIME(2)

DIMENSION ARRAY(15),JARRAY(15),JMAC(*),JMATYP(*),COORD(*)

REAL XC0, XROWX, XROWY, XKB, XT

REAL XEINT, XCONCN

XROWX = 1.74

XROWY = 1.74

XKB = 8.61733035E-5

XT = 673.15

XC0 = 130

STATEV(1) : CONCENTRATION

SUBROUTINE IS ONLY DEFINED FOR 2D

IF (TIME(2).LT.DTIME) RETURN

GET TOTAL STRAIN

CALL GETVRM('E',ARRAY,JARRAY,FLGRAY,JRCD,JMAC,JMATYP,MATLAYO,

1 LACCFLA)

EXX = ARRAY(1)

EYY = ARRAY(2)

XEINT = -(XROWX*EXX+XROWY*EYY)

XCONCN = XC0*EXP(-XEINT/(XKB*XT))

STATEV(1)= XCONCN

RETURN END

10.4 Chemical Analysis Certificates of Zr-4 and Zr-702

AMG Superalloys UK Limited
Fullerton Road, Rotherham, South Yorkshire S60 1DL, England

ANALYTICAL SERVICES

Tel. 01709-833763
Fax. 01709-830391

UKAS TESTING 1091

CERTIFICATE OF ANALYSIS

Material analysed has been supplied to AMG Analytical Services for 3rd party analysis
Results only relate to items tested

To
Materials Department
Imperial College London
Royal School of Mines
Prince Consort Road
London
SW7 2BP

FAO
Said El-Chamaa

Certificate Date	03/03/2020	Certificate No.	Lab Request No.
Date of Receipt	18/02/2020	4001115	4001114
Analysis Start Date	03/03/2020	Your Ref. / Order No.	
Analysis End Date	03/03/2020	ME/4157158	

Sample Details
No. of Samples Submitted : 2

Analysis Results

	4003798
	Zr-4
Al	<0.05 %
Si	<0.05 %
Ti	<0.05 %
V	<0.05 %
Cr	0.11 %
Mn	<0.05 %
Fe	0.26 %
Co	<0.05 %
Ni	<0.05 %
Cu	<0.05 %
Nb	<0.05 %
Mo	<0.05 %
Sn	1.51 %
W	<0.05 %
P	<0.005 %
Mg	<0.05 %
Ca	<0.05 %
Zn	<0.05 %
Zr	97.98 BY DIFF %
Hf	<0.05 %
Ta	<0.05 %
Pb	<0.05 %
O	0.142 %

END OF REPORT

Analysis on 'As Received' Basis
Material: Metallic

Comments / Remarks
Analysed using in - house documented procedures for technique(s) :
Leco XRF

Leco Nitrogen - Thermal Conductivity Leco Carbon, Sulphur, Oxygen, Hydrogen - Infra-Red

Certificate Signed by
☑ **P. W. Hurditch** Chief Chemist
☐ **S. L. Temple** Office Manager
☐ **I. Hyde** Assistant Chief Chemist

Signed

The report shall not be reproduced except in full without approval of the laboratory
Please refer to http://www.amg-s.com for our Conditions of Assay
Registered Office as above. Registered in England No. 345279 V.A.T. No. GB 789 6326 65.

AMG ANALYTICAL

AMG Superalloys UK Limited
Fullerton Road, Rotherham, South Yorkshire S60 1DL, England

Tel. 01709-833763
Fax. 01709-830391

ANALYTICAL SERVICES

UKAS TESTING 1091

CERTIFICATE OF ANALYSIS

Page No. 1 of 2

Material analysed has been supplied to AMG Analytical Services for 3rd party analysis
Results only relate to items tested

To
Materials Department
Imperial College London
Royal School of Mines
Prince Consort Road
London
SW7 2BP

FAO
Said El-Chamaa

Certificate Date	03/03/2020	Certificate No.	Lab Request No.
Date of Receipt	18/02/2020	4001115	4001114
Analysis Start Date	03/03/2020	Your Ref. / Order No.	
Analysis End Date	03/03/2020	ME/4157158	

Sample Details
No. of Samples Submitted : 2

Analysis Results

	4003797	
	Zr-702	
Al	<0.05	%
Si	<0.05	%
Ti	0.15	%
V	<0.05	%
Cr	<0.05	%
Mn	<0.05	%
Fe	0.09	%
Co	<0.05	%
Ni	<0.05	%
Cu	<0.05	%
Nb	<0.05	%
Mo	<0.05	%
Sn	0.15	%
W	<0.05	%
P	<0.005	%
Mg	<0.05	%
Ca	<0.05	%
Zn	<0.05	%
Zr	98.49 BY DIFF	%
Hf	0.97	%
Ta	<0.05	%
Pb	<0.05	%
O	0.148	%

Analysis on 'As Received' Basis
Material: Metallic

Comments / Remarks
Analysed using in - house documented procedures for technique(s) :
Leco XRF

Leco Nitrogen - Thermal Conductivity Leco Carbon, Sulphur, Oxygen, Hydrogen - Infra-Red

Certificate Signed by
☑ **P. W. Hurditch** Chief Chemist
☐ **S. L. Temple** Office Manager
☐ **I. Hyde** Assistant Chief Chemist

Signed

The report shall not be reproduced except in full without approval of the laboratory
Please refer to http://www.amg-s.com for our Conditions of Assay
Registered Office as above. Registered in England No. 345279 V.A.T. No. GB 789 6326 65.

10.5 Polycrystal Plasticity Modeling

10.5.1 Crystal Plasticity Method

To capture the large plastic deformation near the notch, finite strain method is applied with multiplicative decomposition of deformation gradient F, instead of small strain theory.

$$\mathbf{F} = \mathbf{F}^e\mathbf{F}^p\mathbf{F}^\theta \tag{10.1}$$

where $\mathbf{F}^e$, $\mathbf{F}^p$ and $\mathbf{F}^\theta$ are the elastic, plastic and thermal deformation gradient. For equations written in this study, bold symbols represent the matrix multiplications. The evolution of F is defined as,

$$\dot{\mathbf{F}}^\theta = \dot{T}\alpha\mathbf{F}^\theta \tag{10.2}$$

where T is the Kelvin temperature and α is a diagonal tensor in the reference crystallographic coordinate system describing the anisotropic thermal expansion of this zirconium alloy. In addition to material derivative of $\mathbf{F}^p$, the plastic deformation gradient $\mathbf{L}^p$ could also be defined by the dislocation slips among all slip systems, which are given by,

$$\mathbf{L}^p = \dot{\mathbf{F}}^p(\mathbf{F}^p)^{-1} = \Sigma_\kappa\dot{\gamma}^\kappa S^\kappa \bigotimes n^\kappa \tag{10.3}$$

where, $\dot{\gamma}^\kappa$ is the rate of resolved shear strain, and s^κ and n^κ are the slip direction and normal of slip system . Inside each slip system, the physical based strain rate sensitive equation of resolved shear strain is deduced from Orowan equation, which considers the planar slip occurring through dislocation glide, pinning and thermally-activated release.

$$\dot{\gamma}^\kappa = \Sigma_\kappa\rho_m(b^\kappa)^2\nu_d exp(-\frac{\Delta F}{kT})sinh(\frac{(\tau^\kappa - \tau_c^\kappa)\Delta V}{kT} \tag{10.4}$$

The resolved shear strain rate $\dot{\gamma}^\kappa$ is only activated when resolved shear stress τ^κ exceeds the critical resolved shear stress (CRSS) τ_c^κ, that is, $—\tau^\kappa— \geq \tau_c^\kappa$. Otherwise,$\dot{\gamma}^\kappa$ remains inactivated. Here, ρ_m is the mobile dislocation density, b^κ the Burgers vector, ν_d the Debye frequency, k the Boltzmann constant. Temperature here ranges from 293K to 693K consistent with the thermal tensile test and covering the temperature range during thermo-mechanical load in four-point bending. The intrinsic slip strain rate sensitivity is determined by the activation energy F and an associated activation volume

$\Delta V = \gamma_0 \ (b^\kappa)^2/\sqrt{\rho_0}$, where γ_0 is the reference shear strain level and ρ_0 is the initial pinned dislocation density.

References

[1] B Verlinden, J Driver, I Samajdar, and R D Doherty. *Thermo-mechanical processing of metallic materials*, volume 11. Elsevier, 2007.

[2] M Steinbrück and M Böttcher. Air oxidation of Zircaloy-4, M5® and ZIRLO™ cladding alloys at high temperatures. *Journal of Nuclear Materials*, 414(2):276–285, 2011.

[3] V S Saji and R M Cook. *Corrosion protection and control using nanomaterials*. Elsevier, 2012.

[4] Z L Pan, N Wang, and Z He. Measurements of elastic modulus in Zr alloys For CANDU applications. In *Proceedings of 11th International Conference on CANada Deuterium Uranium Fuel, Niagara Falls, ON, Canada*, pages 17–20, 2010.

[5] J Schofield. The initiation of delayed hydride cracking at a notch in coarse grained, random textured zircaloy weld metal, 2002.

[6] S E Chamaa, M Patel, Mark R Wenman, and Catrin M Davies. Multiscale Stress-Diffusion Analysis of Notch-Tip Hydrogen Profiles in Zircaloy-4. In *ASME 2018 Pressure Vessels and Piping Conference*, pages V06BT06A013–V06BT06A013. American Society of Mechanical Engineers, 2018.

[7] H Weekes. *Synchrotron X-ray Di raction Investigations into the Micromechanics of Hydrides in Zircaloy-4*. PhD thesis, Imperial College London, 2015.

[8] G Faccanoni. https://texample.net/tikz/examples/author/gloria-faccanoni/, 2008.

[9] P Burr. Ab-initio modelling of Zr and Be alloys for nuclear applications. 2015.

[10] B A Cheadle, C E Ells, and W Evans. The development of texture in zirconium alloy tubes. *Journal of Nuclear Materials*, 23(2):199–208, 1967.

[11] E Tenckhoff. Review of deformation mechanisms, texture, and mechanical anisotropy in zirconium and zirconium base alloys. *Journal of ASTM International*, 2(4):1–26, 2005.

[12] V S Tong and T B Britton. Formation of very large 'blocky alpha'grains in Zircaloy-4. *Acta Materialia*, 129:510–520, 2017.

[13] A Akhtar. Compression of zirconium single crystals parallel to the c-axis. *Journal of Nuclear Materials*, 47(1):79–86, 1973.

[14] H C Chu, S K Wu, and R C Kuo. Hydride reorientation in Zircaloy-4 cladding. *Journal of nuclear materials*, 373(1-3):319–327, 2008.

[15] T A Bennett, P N Kalu, and A D Rollett. Strain-Induced Selective Growth in 1.5% Temper-Rolled Fe 1% Si. *Microscopy and Microanalysis*, 17(3):362–367, 2011.

[16] L Reali, M R Wenman, and D S Balint. Modelling Time Evolution of Second Phase Particle Hydrostatic Stress during Precipitation Using 2D Discrete Dislocation Plasticity. 2020.

[17] M E Flanagan. The effect of hydrogen on the deformation behaviour of Zircaloy-4, 2008.

[18] A Garner, A Gholinia, P Frankel, M Gass, I MacLaren, and M Preuss. The microstructure and microtexture of zirconium oxide films studied by transmission electron backscatter diffraction and automated crystal orientation mapping with transmission electron microscopy. *Acta Materialia*, 80:159–171, 2014.

[19] J J Kearns. Diffusion coefficient of hydrogen in alpha zirconium, Zircaloy-2 and Zircaloy-4. *Journal of Nuclear Materials*, 43(3):330–338, 1972.

[20] J.J. Kearns. Terminal solubility and partitioning of hydrogen in the alpha phase of zirconium, Zircaloy-2 and Zircaloy-4. *Journal of Nuclear Materials*, 22(3):292–303, 1967.

[21] A McMinn, E C Darby, and J S Schofield. The terminal solid solubility of hydrogen in zirconium alloys. In *Zirconium in the Nuclear Industry: Twelfth International Symposium*. ASTM International, 2000.

[22] D O Northwood and U Kosasih. Hydrides and delayed hydrogen cracking in zirconium and its alloys. *International metals reviews*, 28(1):92–121, 1983.

[23] V Perovic, G C Weatherly, and C J Simpson. Hydride precipitation in α/β zirconium alloys. *Acta Metallurgica*, 31(9):1381–1391, 1983.

[24] K G Barraclough and C J Beevers. Some observations on the deformation characteristics of bulk polycrystalline zirconium hydrides. *Journal of Materials Science*, 4(6):518–525, 1969.

[25] L A Simpson and C D Cann. Fracture toughness of zirconium hydride and its influence on the crack resistance of zirconium alloys. *Journal of nuclear materials*, 87(2-3):303–316, 1979.

[26] S Sagat, S Q Shi, and M P Puls. Crack initiation criterion at notches in Zr-2.5 Nb alloys. *Materials Science and Engineering: A*, 176(1-2):237–247, 1994.

[27] A D Lepage, W A Ferris, and G A Ledoux. Procedure for adding hydrogen to small sections of zirconium alloys. *Materials and Mechanics Branch, Chalk River Laboratories, Chalk River, Ontario*, pages 12–13, 1998.

[28] C A Schneider, W S Rasband, and K W Eliceiri. NIH Image to ImageJ: 25 years of image analysis. *Nature methods*, 9(7):671–675, 2012.

[29] Y Liu and F P E Dunne. Hydrogen concentration model near notch tips during thermal creep of Zircaloy-4, 2020.

[30] M Patel. *MULTISCALE MODELLING OF DELAYED HYDRIDE CRACKING*. PhD thesis, Imperial College London, 2020.

[31] D MacKay. *Sustainable Energy-without the hot air*. UIT Cambridge, 2008.

[32] C N Hill. *An atomic empire: a technical history of the rise and fall of the British Atomic Energy Programme*. World Scientific, 2013.

[33] D Bodansky. *Nuclear energy: principles, practices, and prospects*. Springer Science & Business Media, 2007.

[34] N Robert and B Jerry. Oklo: Ancient African Nuclear Reactors, 2002.

[35] G Choppin, J Liljenzin, and J Rydberg. *Radiochemistry and nuclear chemistry*. Butterworth-Heinemann, 2002.

[36] World Nuclear Association. Nuclear-Powered Ships, 0.

[37] H G Rickover, L D Geiger, and B Lustman. History of the development of zirconium alloys for use in nuclear reactors. Technical report, 1975.

[38] S Glasstone and A Sesonske. *Nuclear reactor engineering: reactor systems engineering*. Springer Science & Business Media, 2012.

[39] Admiral H G Rickover. *The Decision to Use Zirconium in Nuclear Reactors*. ASTM International, 2010.

[40] M P Puls. *The effect of hydrogen and hydrides on the integrity of zirconium alloy components: delayed hydride cracking*. Springer Science & Business Media, 2012.

[41] K Linga Murty and Indrajit Charit. Texture development and anisotropic deformation of zircaloys. *Progress in nuclear energy*, 48(4):325–359, 2006.

[42] W Yeniscavich, R A Wolfe, and R M Lieberman. Hydrogen absorption by nickel enriched zircaloy-2. *Journal of Nuclear Materials*, 1(3):271–280, 1959.

[43] G P Sabol. ZIRLO™—an alloy development success. In *Zirconium in the Nuclear Industry: Fourteenth International Symposium*. ASTM International, 2005.

[44] R M K A Krishnan and M K Asundi. Zirconium alloys in nuclear technology. *Proceedings of the Indian Academy of Sciences Section C: Engineering Sciences*, 4(1):41–56, 1981.

[45] F Garzarolli, R Schumann, and E Steinberg. Corrosion optimized Zircaloy for boiling water reactor (BWR) fuel elements. In *Zirconium in the Nuclear Industry: Tenth International Symposium*. ASTM International, 1994.

[46] A S Zaimovskii. Zirconium alloys in nuclear power. *Atomic Energy*, 45(6):1165–1168, 1978.

[47] G P Sabol, P Rudling, and B Kammenzind. Zirconium in the Nuclear Industry: Fourteenth International Symposium. *ASTM STP*, 1467(3), 2005.

[48] P Barberis, D Charquet, and V Rebeyrolle. Ternary Zr–Nb–Fe (O) system: phase diagram at 853 K and corrosion behaviour in the domain Nb¡ 0.8%. *Journal of nuclear materials*, 326(2-3):163–174, 2004.

[49] P Barberis, N Dupin, C Lemaignan, A Pasturel, and J M Grange. Microstructure and phase control in Zr-Fe-Cr-Ni alloys: Thermodynamic and kinetic aspects. In *Zirconium in the Nuclear Industry: Fourteenth International Symposium*. ASTM International, 2005.

[50] J B Vander Sande and A L Bement. An investigation of second phase particles in Zircaloy-4 alloys. Technical report, 1974.

[51] N R V Bangaru. An investigation of the microstructures of heat-treated zircaloy-4. *Journal of Nuclear Materials*, 131(2-3):280–290, 1985.

[52] J P Gros and J F Wadier. Precipitate growth kinetics in Zircaloy-4. *Journal of Nuclear Materials*, 172(1):85–96, 1990.

[53] J S Bryner. The cyclic nature of corrosion of Zircaloy-4 in 633 K water. *Journal of Nuclear materials*, 82(1):84–101, 1979.

[54] A T Motta, A Yilmazbayhan, R J Comstock, J Partezana, G P Sabol, B Lai, and Z Cai. Microstructure and growth mechanism of oxide layers formed on Zr alloys studied with micro-beam synchrotron radiation. In *Zirconium in the Nuclear Industry: Fourteenth International Symposium*. ASTM International, 2005.

[55] A Motta, M G da Silva, A Yilmazbayhan, R Comstock, Z Cai, and B Lai. Microstructural characterization of oxides formed on model Zr alloys using synchrotron radiation. In *Zirconium in the Nuclear Industry: 15th International Symposium*. ASTM International, 2009.

[56] J Goldak, L T Lloyd, and C S Barrett. Lattice parameters, thermal expansions, and Grüneisen coefficients of Zirconium, 4.2 to 1130 K. *Physical Review*, 144(2):478, 1966.

[57] I L Dillamore and W T Roberts. Preferred orientation in wrought and annealed metals. *Metallurgical Reviews*, 10(1):271–380, 1965.

[58] K V M Krishna, S K Sahoo, I Samajdar, S Neogy, R Tewari, D Srivastava, G K Dey, G H Das, N Saibaba, and S Banarjee. Microstructural and textural developments during Zircaloy-4 fuel tube fabrication. *Journal of Nuclear Materials*, 383(1-2):78–85, 2008.

[59] R G Ballinger, G E Lucas, and R M Pelloux. The effect of plastic strain on the evolution of crystallographic texture in Zircaloy-2. *Journal of Nuclear Materials*, 126(1):53–69, 1984.

[60] K Une, K Nogita, S Ishimoto, and K Ogata. Crystallography of zirconium hydrides in recrystallized zircaloy-2 fuel cladding by electron backscatter diffraction. *Journal of nuclear science and technology*, 41(7):731–740, 2004.

[61] N Marchal, C Campos, and C Garnier. Finite element simulation of Pellet-Cladding Interaction (PCI) in nuclear fuel rods. *Computational Materials Science*, 45(3):821–826, 2009.

[62] E S Fisher and C J Renken. Single-crystal elastic moduli and the hcp→ bcc transformation in Ti, Zr, and Hf. *Physical Review*, 135(2A):A482, 1964.

[63] D O Northwood, I M London, and L E Bähen. Elastic constants of zirconium alloys. *Journal of nuclear materials*, 55(3):299–310, 1975.

[64] V S Tong. *EBSD Characterisation of Heterogeneous Microstructures in Zirconium Alloys*. PhD thesis, Imperial College London, 2016.

[65] P G Partridge. The crystallography and deformation modes of hexagonal close-packed metals. *Metallurgical reviews*, 12(1):169–194, 1967.

[66] A Girshick, D G Pettifor, and V Vitek. Atomistic simulation of titanium. II. Structure of 1 2 1 0 screw dislocations and slip systems in titanium. *Philosophical Magazine A*, 77(4):999–1012, 1998.

[67] N Tarrat, M Benoit, D Caillard, L Ventelon, N Combe, and J Morillo. Screw dislocation in hcp Ti: DFT dislocation excess energies and metastable core structures. *Modelling and Simulation in Materials Science and Engineering*, 22(5):55016, 2014.

[68] B J Lee, S Ahzi, and R J Asaro. On the plasticity of low symmetry crystals lacking five independent slip systems. *Mechanics of Materials*, 20(1):1–8, 1995.

[69] Y N Wang and J C Huang. Texture analysis in hexagonal materials. *Materials Chemistry and Physics*, 81(1):11–26, 2003.

[70] G C Kaschner and G T Gray. The influence of crystallographic texture and interstitial impurities on the mechanical behavior of zirconium. *Metallurgical and Materials Transactions A*, 31(8):1997–2003, 2000.

[71] L Capolungo, P E Marshall, R J McCabe, I J Beyerlein, and C N Tomé. Nucleation and growth of twins in Zr: a statistical study. *Acta Materialia*, 57(20):6047–6056, 2009.

[72] S G Song and G T Gray. Influence of temperature and strain rate on slip and twinning behavior of Zr. *Metallurgical and materials Transactions A*, 26(10):2665–2675, 1995.

[73] R W Armstrong, I Codd, R M Douthwaite, and N J Petch. The plastic deformation of polycrystalline aggregates. *The Philosophical Magazine: A Journal of Theoretical Experimental and Applied Physics*, 7(73):45–58, 1962.

[74] Derek O Northwood. The development and applications of zirconium alloys. *Materials & design*, 6(2):58–70, 1985.

[75] Gordon B Skinner and Herrick L Johnston. Thermal expansion of zirconium between 298 K and 1600 K. *The Journal of Chemical Physics*, 21(8):1383–1384, 1953.

[76] D G Westlake. The habit planes of zirconium hydride in zirconium and zircaloy. *Journal of Nuclear Materials*, 26(2):208–216, 1968.

[77] K Linga Murty. Applications of crystallographic textures of zirconium alloys in the nuclear industry. In *Zirconium in the Nuclear Industry: Eighth International Symposium*. ASTM International, 1989.

[78] R D Doherty, D A Hughes, F J Humphreys, J Juul Jonas, D Juul Jensen, M E Kassner, W E King, T R McNelley, H J McQueen, and A D Rollett. Current issues in recrystallization: a review. *Materials Science and Engineering: A*, 238(2):219–274, 1997.

[79] D L Gray. Recovery and recrystallization of zirconium and its alloys. *Report HW-69679*, 1961.

[80] D F Washburn. The formation of large grains in alpha Zircaloy-4 during heat treatment after small plastic deformations. Technical report, 1964.

[81] C S Smith. Grains, phases, and interphases: An interpretation of microstructure: Transactions of the American Institute of Mining and Metallurgical Engineers, v. 175. 1948.

[82] Clarence Zener. Theory of growth of spherical precipitates from solid solution. *Journal of applied physics*, 20(10):950–953, 1949.

[83] P M Hazzledine and R D J Oldershaw. Computer simulation of Zener pinning. *Philosophical Magazine A*, 61(4):579–589, 1990.

[84] M Hillert. On the theory of normal and abnormal grain growth. *Acta metallurgica*, 13(3):227–238, 1965.

[85] J C Clayton. Internal hydriding in irradiated defected Zircaloy fuel rods. In *Zirconium in the nuclear industry: Eighth international symposium*. ASTM International, 1989.

[86] A Couet, A T Motta, and R J Comstock. Hydrogen pickup measurements in zirconium alloys: Relation to oxidation kinetics. *Journal of Nuclear Materials*, 451(1-3):1–13, 2014.

[87] H Weidinger. Raman Spectroscopy Study of the Tetragonal-to-Monoclinic Transition in Zirconium Oxide Scales and Determination of Overall Oxygen Diffusion by Nuclear Microanalysis of O18. In *Zirconium in the Nuclear Industry: Proceedings of the... International Conference*, volume 9, page 416. ASTM, 1991.

[88] A Yilmazbayhan, E Breval, A T Motta, and R J Comstock. Transmission electron microscopy examination of oxide layers formed on Zr alloys. *Journal of Nuclear Materials*, 349(3):265–281, 2006.

[89] H Anada and K Takeda. Microstructure of oxides on Zircaloy-4, 1.0 Nb Zircaloy-4, and Zircaloy-2 formed in 10.3-MPa steam at 673 K. In *Zirconium in the Nuclear Industry: Eleventh International Symposium*. ASTM International, 1996.

[90] B H Lim, H S Hong, and K S Lee. Measurements of hydrogen permeation and absorption in zirconium oxide scales. *Journal of nuclear materials*, 312(2-3):134–140, 2003.

[91] B D Warr, M B Elmoselhi, S B Newcomb, N S McIntyre, A M Brennenstuhl, and P C Lichtenberger. Oxide characteristics and their relationship to hydrogen uptake in zirconium alloys. In *Zirconium in the Nuclear Industry: Ninth International Symposium*. ASTM International, 1991.

[92] D Franklin. Performance of Zirconium Alloys in Light Water Reactors with a Review of Nodular Corrosion. In *Zirconium in the Nuclear Industry: 16th International Symposium*. ASTM International, 2012.

[93] M Lindgren and I Panas. Impact of additives on zirconium oxidation by water: mechanistic insights from first principles. *RSC Advances*, 3(44):21613–21619, 2013.

[94] K Kakiuchi, N Itagaki, T Furuya, A Miyazaki, Y Ishii, S Suzuki, T Terai, and M Yamawaki. Role of iron for hydrogen absorption mechanism in zirconium alloys. In *Zirconium in the Nuclear Industry: Fourteenth International Symposium*. ASTM International, 2005.

[95] F Garzarolli, B Cox, and P Rudling. Optimization of Zry-2 for high burnups. In *Zirconium in the Nuclear Industry: 16th International Symposium*. ASTM International, 2012.

[96] G Lelievre, C Tessier, X Iltis, B Berthier, and F Lefebvre. Impact of intermetallic precipitates on hydrogen distribution in the oxide layers formed on zirconium alloys in a steam atmosphere: a 2D (3He, p) α nuclear analysis study in microbeam mode. *Journal of alloys and compounds*, 268(1-2):308–317, 1998.

[97] T Murai, T Isobe, Y Takizawa, and Y Mae. Fundamental Study on the Corrosion Mechanism of Zr-0.2 Fe, Zr-0.2 Cr, and Zr-0.1 Fe-0.1 Cr Alloys. In *Zirconium in the Nuclear Industry: Twelfth International Symposium*. ASTM International, 2000.

[98] Peter Rudling and Gunnar Wikmark. A unified model of Zircaloy BWR corrosion and hydriding mechanisms. *Journal of Nuclear Materials*, 265(1-2):44–59, 1999.

[99] Y Hatano, K Isobe, R Hitaka, and M Sugisaki. Role of intermetallic precipitates in hydrogen uptake of Zircaloy-2. *Journal of nuclear science and technology*, 33(12):944–949, 1996.

[100] P Tägstrom, M Limbäck, M Dahlbäck, T Andersson, and H Pettersson. Zirconium in the Nuclear Industry: Thirteenth International Symposium. *ASTM STP*, 1423:96, 2002.

[101] P Tägtstrom, M Limbäck, M Dahlbäck, T Andersson, and H Pettersson. Effects of hydrogen pickup and second-phase particle dissolution on the in-reactor corrosion performance of BWR claddings. In *Zirconium in the Nuclear Industry: Thirteenth International Symposium*. ASTM International, 2002.

[102] M Yao, J Wang, J Peng, B Zhou, and Q Li. Study on the role of second phase particles in hydrogen uptake behavior of zirconium alloys. In *Zirconium in the Nuclear Industry: 16th International Symposium*. ASTM International, 2012.

[103] P A Burr, S T Murphy, S C Lumley, M R Wenman, and R W Grimes. Hydrogen accommodation in Zr second phase particles: Implications for H pick-up and hydriding of Zircaloy-2 and Zircaloy-4. *Corrosion Science*, 69:1–4, 2013.

[104] J M Markowitz. Internal zirconium hydride formation in zircaloy fuel element cladding under irradiation. Technical report, 1963.

[105] S Banerjee and P Mukhopadhyay. *Phase transformations: examples from titanium and zirconium alloys*, volume 12. Elsevier, 2010.

[106] A T Motta and L Chen. Hydride formation in zirconium alloys. *Jom*, 64(12):1403–1408, 2012.

[107] W H Erickson. Hydrogen Solubility in Zirconium Alloys. *Electrochemical Technology (US) Absorbed by J. Electrochem. Soc.*, 4, 1966.

[108] L Espagno, P Azou, and P Bastien. Dilatometric Study of the Zirconium-Hydrogen System. *Compt. rend.*, 247, 1958.

[109] T B Douglas. The Zirconium-Hydrogen System: Some Thermodynamic Properties from a Heat Content Study1. *Journal of the American Chemical Society*, 80(19):5040–5046, 1958.

[110] M W Mallett and W Me Albrecht. Low-Pressure Solubility and Diffusion of Hydrogen in Zirconium. *Journal of The Electrochemical Society*, 104(3):142–146, 1957.

[111] E A Gulbransen and K F Andrew. The kinetics of oxidation of high purity nickel. *Journal of the Electrochemical Society*, 101(3):128–140, 1954.

[112] C M Schwartz and M W Mallett. Observations on the behavior of hydrogen in zirconium. Technical report, 1953.

[113] A Pebler and E A Gulbransen. Thermochemical and structural aspects of the reaction of hydrogen with alloys and intermetallic compounds of zirconium. *Electrochemical Technology (US) Absorbed by J. Electrochem. Soc.*, 4, 1966.

[114] R Westerman. Charging Zircaloy-2 with hydrogen beyond the solubility limit. *Journal of Nuclear Materials*, 18(1):31–38, 1966.

[115] G Östberg. Determination of hydride solubility in alpha phase zirconium, zircaloy-2 and zircaloy 4. *Journal of Nuclear Materials*, 5(2):208–215, 1962.

[116] A Sawatzky. Hydrogen in Zircaloy-2: Its distribution and heat of transport. *Journal of Nuclear Materials*, 2(4):321–328, 1960.

[117] G K Shek and D B Graham. Effects of loading and thermal maneuvers on delayed hydride cracking in Zr-2.5 Nb alloys. In *Zirconium in the Nuclear Industry: Eighth International Symposium*. ASTM International, 1989.

[118] P Vizcaino, A D Banchik, and J P Abriata. Solubility of hydrogen in Zircaloy-4: irradiation induced increase and thermal recovery. *Journal of nuclear materials*, 304(2-3):96–106, 2002.

[119] S R MacEwen, C E Coleman, C E Ells, and J Faber Jr. Dilation of hcp zirconium by interstitial deuterium. In *Perspectives in Hydrogen in Metals*, pages 185–189. Elsevier, 1986.

[120] T B Flanagan, N B Mason, and H K Birnbaum. The effect of stress on hydride precipitation. *Scripta Metallurgica*, 15(1):109–112, 1981.

[121] S-Q Shi, G K Shek, and M P Puls. Hydrogen concentration limit and critical temperatures for delayed hydride cracking in zirconium alloys. *Journal of nuclear materials*, 218(2):189–201, 1995.

[122] S Yamanaka, T Tanaka, and M Miyake. Effect of oxygen on hydrogen solubility in zirconium. *Journal of nuclear materials*, 167:231–237, 1989.

[123] B F Kammenzind, D G Franklin, H R Peters, and W J Duffin. Hydrogen pickup and redistribution in alpha-annealed Zircaloy-4. In *Zirconium in the Nuclear Industry: Eleventh International Symposium*. ASTM International, 1996.

[124] D Setoyama, J Matsunaga, M Ito, H Muta, K Kurosaki, M Uno, S Yamanaka, K Takeda, and Y Ishii. Influence of additive elements on the terminal solid solubility of hydrogen for Zirconium alloy. *Journal of nuclear materials*, 344(1-3):291–294, 2005.

[125] M Christensen, W Wolf, C Freeman, E Wimmer, R B Adamson, L Hallstadius, P E Cantonwine, and E V Mader. H in α-Zr and in zirconium hydrides: solubility, effect on dimensional changes, and the role of defects. *Journal of Physics: Condensed Matter*, 27(2):25402, 2014.

[126] C E Coleman, S Sagat, and K F Amouzouvi. Control of microstructure to increase the tolerance of zirconium alloys to hydride cracking. In *Proceedings of the Metallurgical Society of the Canadian Institute of Mining and Metallurgy*, pages 293–304. Elsevier, 1988.

[127] R L Beck and W M Mueller. Mechanical properties of solid zirconium hydride. Technical report, 1960.

[128] R Khoda-Bakhsh and D K Ross. Determination of the hydrogen site occupation in the α phase of zirconium hydride and in the α and β phases of titanium hydride by inelastic neutron scattering. *Journal of Physics F: Metal Physics*, 12(1):15, 1982.

[129] S C Lumley, R W Grimes, S T Murphy, P A Burr, Alexander Chroneos, P R Chard-Tuckey, and M R Wenman. The thermodynamics of hydride precipitation: The importance of entropy, enthalpy and disorder. *Acta Materialia*, 79:351–362, 2014.

[130] S C Lumley, S T Murphy, P A Burr, R W Grimes, P R Chard-Tuckey, and M R Wenman. The stability of alloying additions in Zirconium. *Journal of nuclear materials*, 437(1-3):122–129, 2013.

[131] P A Burr, S T Murphy, S C Lumley, M R Wenman, and R W Grimes. Hydrogen solubility in zirconium intermetallic second phase particles. *Journal of Nuclear Materials*, 443(1-3):502–506, 2013.

[132] L O Jernkvist. Multi-field modelling of hydride forming metals Part II: Application to fracture. *Computational materials science*, 85:383–401, 2014.

[133] L O Jernkvist and A R Massih. Multi-field modelling of hydride forming metals. Part I: Model formulation and validation. *Computational materials science*, 85:363–382, 2014.

[134] Y Zhang, C Jiang, and X Bai. Anisotropic hydrogen diffusion in α-Zr and Zircaloy predicted by accelerated kinetic Monte Carlo simulations. *Scientific reports*, 7:41033, 2017.

[135] W Hoffelner. *Materials for nuclear plants: from safe design to residual life assessments*. Springer Science & Business Media, 2012.

[136] M S Blackmur, J D Robson, M Preuss, O Zanellato, R J Cernik, S-Q Shi, F Ribeiro, and J Andrieux. Zirconium hydride precipitation kinetics in Zircaloy-4 observed with synchrotron X-ray diffraction. *Journal of nuclear materials*, 464:160–169, 2015.

[137] Z Zhao, M Blat-Yrieix, J Morniroli, A Legris, L Thuinet, Y Kihn, A Ambard, and L Legras. Characterization of zirconium hydrides and phase field approach to a mesoscopic-scale modeling of their precipitation. In *Zirconium in the Nuclear Industry: 15th International Symposium*. ASTM International, 2009.

[138] E Zuzek, J P Abriata, A San-Martin, and F D Manchester. The H-Zr (hydrogen-zirconium) system. *Bulletin of alloy phase diagrams*, 11(4):385–395, 1990.

[139] J. S. Bradbrook, G. W. Lorimer, and N. Ridley. The precipitation of zirconium hydride in zirconium and zircaloy-2. *Journal of Nuclear Materials*, 1972.

[140] B Nath, G W Lorimer, and N Ridley. Effect of hydrogen concentration and cooling rate on hydride precipitation in α-zirconium. *Journal of Nuclear Materials*, 58(2):153–162, 1975.

[141] J B Bai, C Prioul, and D Francois. Hydride embrittlement in Zircaloy-4 plate: Part I. Influence of microstructure on the hydride embrittlement in Zircaloy-4 at 20 C and 350 C. *Metallurgical and materials transactions A*, 25(6):1185–1197, 1994.

[142] N A P K Kumar, J A Szpunar, and Z He. Preferential precipitation of hydrides in textured zircaloy-4 sheets. *Journal of Nuclear Materials*, 403(1-3):101–107, 2010.

[143] K B Colas, A T Motta, J D Almer, M R Daymond, M Kerr, A D Banchik, P Vizcaino, and J R Santisteban. In situ study of hydride precipitation kinetics and re-orientation in Zircaloy using synchrotron radiation. *Acta Materialia*, 58(20):6575–6583, 2010.

[144] K Sakamoto and M Nakatsuka. Stress reorientation of hydrides in recrystallized Zircaloy-2 sheet. *Journal of nuclear science and technology*, 43(9):1136–1141, 2006.

[145] G J C Carpenter. The dilatational misfit of zirconium hydrides precipitated in zirconium. *Journal of Nuclear Materials*, 48(3):264–266, 1973.

[146] G C Weatherly. The precipitation of γ-hydride plates in zirconium. *Acta Metallurgica*, 29(3):501–512, 1981.

[147] V S Arunachalam, B Lehtinen, and G Östberg. The orientation of zirconium hydride on grain boundaries in zircaloy-2. *Journal of Nuclear Materials*, 21(3):241–248, 1967.

[148] J W Christian. *The theory of transformations in metals and alloys*. Newnes, 2002.

[149] R Birch, S Wang, V S Tong, and T B Britton. The effect of cooling rate and grain size on hydride microstructure in Zircaloy-4. *Journal of Nuclear Materials*, 513:221–225, 2019.

[150] Ju-Seong Kim, Sung-Dae Kim, and Jonghun Yoon. Hydride formation on deformation twin in zirconium alloy. *Journal of Nuclear Materials*, 482:88–92, 2016.

[151] M P Puls, San-Qiang Shi, and J Rabier. Experimental studies of mechanical properties of solid zirconium hydrides. *Journal of nuclear materials*, 336(1):73–80, 2005.

[152] P H Davies and C P Stearns. Fracture toughness testing of Zircaloy-2 pressure tube material with radial hydrides using direct-current potential drop. In *Fracture Mechanics: Seventeenth Volume*. ASTM International, 1986.

[153] C J Simpson, O A Kupcis, and D V Leemans. Hydride reorientation and fracture in zirconium alloys. In *Zirconium in the Nuclear Industry*. ASTM International, 1977.

[154] J J Kearns and C R Woods. Effect of texture, grain size, and cold work on the precipitation of oriented hydrides in Zircaloy tubing and plate. *Journal of Nuclear Materials*, 20(3):241–261, 1966.

[155] D Hardie and M W Shanahan. Stress reorientation of hydrides in zirconium 2.5% niobium. *Journal of Nuclear Materials*, 55(1):1–13, 1975.

[156] R L Eadie, D R Metzger, and M Léger. The thermal ratchetting of hydrogen in zirconium-niobium: An illustration using finite element modelling. *Scripta metallurgica et Materialia*, 29(3):335–340, 1993.

[157] C J Simpson and C E Ells. Delayed hydrogen embrittlement in Zr-2.5 wt% Nb. *Journal of nuclear materials*, 52(2):289–295, 1974.

[158] Young Suk Kim. Driving force for delayed hydride cracking of zirconium alloys. *Metals and Materials International*, 11(1):29–38, 2005.

[159] R W Balluffi, S M Allen, and W C Carter. *Kinetics of materials*. John Wiley & Sons, 2005.

[160] H B Callen. Thermodynamics New York. *NY Wiley*, 1960.

[161] S-Q Shi. Diffusion-controlled hydride growth near crack tip in zirconium under temperature transients. *Journal of nuclear materials*, 275(3):318–323, 1999.

[162] D A Scarth and T Smith. Developments in flaw evaluation for CANDU reactor Zr-Nb pressure tubes. *J. Pressure Vessel Technol.*, 123(1):41–48, 2001.

[163] M Jedrychowski, B Bacroix, O U Salman, J Tarasiuk, and S Wronski. Investigation of SIBM driven recrystallization in alpha Zirconium based on EBSD data and Monte Carlo modeling. In *IOP Conference Series: Materials Science and Engineering*, volume 89, page 12029. IOP Publishing, 2015.

[164] H Chandler. *Hardness testing*. ASM international, 1999.

[165] J R Cahoon, W H Broughton, and A R Kutzak. The determination of yield strength from hardness measurements. *Metallurgical transactions*, 2(7):1979–1983, 1971.

[166] G E Dieter. Mechanical Metallurgy, Mc. *GrawHill Kogakusha Ltd, Tokyo*, 1988.

[167] Standard Test Method for Determination of Hydrogen in Titanium and Titanium Alloys by Inert Gas Fusion Thermal Conductivity/Infrared Detection Method.

[168] A A Holston and J Stjärnsäter. On the effect of temperature on the threshold stress intensity factor of delayed hydride cracking in light water reactor fuel cladding. *Nuclear Engineering and Technology*, 49(4):663–667, 2017.

[169] J Cui, G K Shek, D A Scarth, and Z Wang. Delayed hydride cracking initiation at notches in Zr-2.5 Nb alloys. *Journal of Pressure Vessel Technology*, 131(4):41407, 2009.

[170] Hiroshi Tada, P Paris, and G Irwin. The analysis of cracks handbook. *New York: ASME Press*, 2:1, 2000.

[171] M Creager and P C Paris. Elastic field equations for blunt cracks with reference to stress corrosion cracking. *International Journal of Fracture Mechanics*, 3(4):247–252, 1967.

[172] G A McRae, C E Coleman, and B W Leitch. The first step for delayed hydride cracking in zirconium alloys. *Journal of Nuclear Materials*, 396(1):130–143, 2010.

[173] M Smith. ABAQUS/Standard User's Manual, Version 6.9. *Providence, RI: Simulia*, 2009.

[174] S Wang, F Giuliani, and T B Britton. Microstructure and formation mechanisms of δ-hydrides in variable grain size Zircaloy-4 studied by electron backscatter diffraction. *Acta Materialia*, 169:76–87, 2019.

[175] M Patel, S Waheed, M R Wenman, A P Sutton, and D S Balint. Discrete Dislocation Plasticity Modeling of Hydrides in Zirconium under Thermal Cycling. *MRS Advances*, 2(55):3353–3358, 2017.

[176] F J Humphreys and M Hatherly. *Recrystallization and related annealing phenomena*. Elsevier, 2012.

[177] J Dennis, P S Bate, and F J Humphreys. Abnormal grain growth in Al–3.5 Cu. *Acta materialia*, 57(15):4539–4547, 2009.

[178] W Qin, N A P Kiran Kumar, J A Szpunar, and J Kozinski. Intergranular δ-hydride nucleation and orientation in zirconium alloys. *Acta Materialia*, 59(18):7010–7021, 2011.

[179] S E Chamaa, M Patel, C M Davies, and M R Wenman. The Effect of Grain Boundaries and Second-Phase Particles on Hydride Precipitation in Zirconium Alloys. *MRS Advances*, 3(31):1749–1754, 2018.

[180] C E Ells. Hydride precipitates in zirconium alloys (A review). *Journal of Nuclear Materials*, 28(2):129–151, 1968.

[181] I L Bramwell, T J Haste, D Worswick, and P D Parsons. An experimental investigation into the oxidation of Zircaloy-4 at elevated pressures in the 750 to 1000 C temperature range. In *Zirconium in the Nuclear Industry: Tenth International Symposium*. ASTM International, 1994.

[182] D G Westlake. Disposition of hydrogen in quenched zirconium-hydrogen alloys. *Journal of Nuclear Materials*, 16(2):215–219, 1965.

[183] A J Breen, I Mouton, W Lu, S Wang, A Szczepaniak, P Kontis, L T Stephenson, Y Chang, A K da Silva, and C H Liebscher. Atomic scale analysis of grain boundary deuteride growth front in Zircaloy-4. *Scripta Materialia*, 156:42–46, 2018.

[184] M Christensen, W Wolf, C M Freeman, E Wimmer, R B Adamson, L Hallstadius, P E Cantonwine, and E V Mader. Effect of alloying elements on the properties of Zr and the Zr–H system. *Journal of nuclear materials*, 445(1-3):241–250, 2014.

[185] J Bair, M A Zaeem, and M Tonks. A review on hydride precipitation in zirconium alloys. *Journal of Nuclear Materials*, 466:12–20, 2015.

[186] L Reali, D Balint, A Sutton, and M Wenman. Stress Profile Quantification of Second Phase Particles in Zirconium. 2020.

[187] M Griffiths, R W Gilbert, and G J C Carpenter. Phase instability, decomposition and redistribution of intermetallic precipitates in Zircaloy-2 and-4 during neutron irradiation. *Journal of Nuclear Materials*, 150(1):53–66, 1987.

[188] R L Eadie and R R Smith. Modelling delayed hydride cracking in zirconium alloys. *Canadian Metallurgical Quarterly*, 27(3):213–223, 1988.

[189] J Crank. *The mathematics of diffusion*. Oxford university press, 1979.

[190] B A Bilby, A H Cottrell, and K H Swinden. The spread of plastic yield from a notch. *Proceedings of the Royal Society of London. Series A. Mathematical and Physical Sciences*, 272(1350):304–314, 1963.

[191] D S Dugdale. Yielding of steel sheets containing slits. *Journal of the Mechanics and Physics of Solids*, 8(2):100–104, 1960.

[192] D M Barnett and R J Asaro. The fracture mechanics of slit-like cracks in anisotropic elastic media. *Journal of the Mechanics and Physics of Solids*, 20(6):353–366, 1972.

[193] E Tenckhoff. *Deformation mechanisms, texture, and anisotropy in zirconium and zircaloy*, volume 966. ASTM International, 1988.

[194] W T Read and W Shockley. Dislocation models of crystal grain boundaries. *Physical review*, 78(3):275, 1950.

[195] V Perovic, G C Weatherly, and C J Simpson. The role of elastic strains in the formation of stacks of hydride precipitates in zirconium alloys. *Scripta Metallurgica*, 16(4):409–412, 1982.

[196] V Perovic, G C Weatherly, and C J Simpson. Hydride precipitation in α/β zirconium alloys. In *Perspectives in Hydrogen in Metals*, pages 469–479. Elsevier, 1986.

[197] R Nazarov, J S Majevadia, M Patel, M R Wenman, D S Balint, J Neugebauer, and A P Sutton. First-principles calculation of the elastic dipole tensor of a point defect: Application to hydrogen in α-zirconium. *Physical Review B*, 94(24):241112, 2016.

[198] J D Eshelby. The continuum theory of lattice defects. In *Solid state physics*, volume 3, pages 79–144. Elsevier, 1956.

[199] M P Puls. Review of the thermodynamic basis for models of delayed hydride cracking rate in zirconium alloys. *Journal of nuclear materials*, 393(2):350–367, 2009.